NASA CR-672

NASA CONTRACTOR REPORT

NASA CR-672

NASA CR-6

C. 1

A THEORETICAL INVESTIGATION OF INFORMATION LIMITS OF SCANNING OPTICAL SYSTEMS

by Edward J. Farrell, C. Duane Zimmerman, Donald F. Nickel, and Richard C. Borden

RECEIVED
16 FEB 1967
Technical Library
AF Weapons
Laboratory

NATIONAL AERONAUTICS AND SPACE ADMINISTRATION • WASHINGTON, D. C. • JANUARY 1967

NASA CR-672

A THEORETICAL INVESTIGATION OF INFORMATION LIMITS

OF SCANNING OPTICAL SYSTEMS

By Edward J. Farrell, C. Duane Zimmerman,
Donald F. Nickel, and Richard C. Borden

TABLE OF CONTENTS

TABLE OF CONTENTS (Cont.)

LIST OF FIGURES

LIST OF FIGURES (Cont.)

LIST OF FIGURES (Cont.)

LIST OF FIGURES (Cont.)

LIST OF TABLES

I. INTRODUCTION

Prior to the 1960's, most of the work on celestial sensing devices involved the study and development of star tracking systems using photomultipliers. The possibilities of celestial sensing without closed loop tracking were not extensively considered. Probably the significant exception to this was the work which was done with image tubes in which the gimballed optical system was approximately pointed at the target and the final measurement was made by the image tube.

Since image tubes do not provide an accuracy better than about 1/1000 of the field of view, it was necessary to use fields of view which were not greater than 3.6 degrees to achieve an accuracy of ten seconds of arc. It was for this reason that crude pointing was necessary even though the final determination of star position was made on an open loop basis in which only position sensing was required.

Subsequently, a number of investigators who were interested in the general problem of attitude determination in space considered using image tubes with wide angle optical systems. With this type of system, a sufficient number of bright stars could be detected to achieve automatic pattern recognition for a random orientation. A system of this type was suggested by Rosenfeld (1960). Employing a field of view of about ten degrees, he achieved an accuracy of a few minutes of arc and detected stars down to the sixth magnitude. Another system described by Potter (1960) employed a field of view of 30 degrees, achieved an accuracy of approximately seven minutes of arc, and detected stars down to the third magnitude. Both of these systems had the decided advantage

of requiring no closed loop tracking, but were somewhat lacking in either accuracy or in requiring the detection of very faint stars.

More recently efforts have been made to develop mosaic or grid type celestial sensors, which would avoid the need for an image tube, and which employ no moving parts. Systems of this type have not provided adequate resolution to be competitive with star trackers while providing a sufficiently large field of view. An interesting system described by Lally (1961) uses a mosaic of solid-state detectors. The accuracy expected from a ten by ten detector of this type is seven seconds of arc with a scanning resolution of 1/50 of each detector and optics providing a one degree field of view. A related grid-type system is the electroluminescent panel, Harmon (1962), in which a solid-state cross grid of wires produces a light source which is projected onto a beam coincidence detector. When the star image and the beam from the panel coincide, the conductance of the detector increases sharply. Another mosaic-type system has been described by Viglione and Wolf (1962), in which 400 photovoltaic cells were considered. With a field of view of 25 degrees, a limiting magnitude of 4.5, and two sight lines orthogonal to one another and to a line to the sun, an accuracy of 0.2 degree was predicted.

A partial solution to the problem of achieving a high resolution has been achieved by a novel device described by Snowman (1962) in which a highly accurate attitude measurement (30 arc seconds) was achieved for all three axes with a 46 degree field of view. In this case, various reference star fields were mechanically fabricated and mounted at the focal plane of the optical system. This device requires, however, that it be pointed within ten degrees

of the center of the reference field, and the problem of randomly pointing the

sensor in any direction relative to the celestial sphere was not solved.

A study of the various system trade-offs led Lillestrand and Carroll (1961)

to conclude that wide field of view systems offer considerable promise, if the

problem of achieving a sufficiently high resolution can be solved. By employing

a narrow optical slit to scan the star field, the position of the star images

can be found to an accuracy of at least 1/10,000 of the field of view of the

optical system. This means that optical systems with a 30 degree field of

view can provide an accuracy of ten seconds of arc, as described by Harrington

(1963). In the case of spinning spacecraft, systems of this type can be fab-

ricated with no moving parts, as described by Kenimer and Walsh (1964). In

the case of inertially stabilized spacecraft, provision must be made for

rotating the slit.

The use of a narrow slit mounted at the focal surface permits the accuracy

of the attitude measurement to approach the optical resolution. Resolutions

better than one part in 10^4 can be achieved, whereas other techniques of atti-

tude measurement seem to be limited at about one part in 10^3. Furthermore,

using the techniques described in Section VI, it is possible to interpolate

the star image and to determine its position with more accuracy than the

angular width of the blur circle.

A recent program at Control Data has involved the fabrication and test of

a celestial sensing system. The system can be randomly pointed at the sky,

recognize the pattern of stars, and then solve the three axis attitude deter-

mination problem. They system is composed of a wide angle celestial reference,

(WACR) and a digital computer. The program was sponsored by Air Force Avionics Laboratory, Wright-Patterson Air Force Base, (Contract No. AF 33(615)-1428). One of the sensor design objectives was the measurement of pointing direction relative to the celestial sphere to an accuracy of one minute of arc.

Using an optical system which has a two inch aperture and scan periods ranging from roughly 1.0 to 10 seconds, rms pointing errors of less than 30 seconds of arc were achieved using actual stars. The basis for these tests was a comparison of the known location of the observatory and the location measurements provided by an accurately leveled sensor, which was pointed directly overhead.

Since atmospheric scintillation degraded the quality of the outdoor measurements, a parallel series of tests were made using artificial stars with the result that pointing accuracies of the order of ten seconds of arc were achieved. When multiple scans were averaged the pointing accuracy increased roughly in proportion to the square root of the number of scans. Because of extraneous sources of error in the test set-up, this process of statistical refinement could not be continued below two seconds of arc.

In addition to the accuracy objective, a second major program objective was that of on-line pattern recognition. The first system design, WACR-I, was not able to reliably achieve this objective because of the dependence of the pattern recognition process on the measurement of star intensities. During this phase of the work, in addition to problems presented by large background radiation from city lights, it was found that scintillation caused rms intensity variations of twenty to fifty percent from scan to scan.

As a result of these problems an improved pattern recognition technique was then developed and the original sensor design was modified. The modified system (WACR-II) did not require the measurement of star intensity, and pattern recognition was done on the basis of geometry only. This system was extremely successful and it was found that pattern recognition could be unambiguously achieved when background radiation from city lights was sufficiently small to permit the detection of three or more stars. This technique of pattern recognition is completely general in that no assumption whatsoever regarding sensor orientation need be made.

To be really useful the pattern recognition process must be capable of giving correct three axis attitude determination in the presence of various sources of noise--as well as in the presence of nonstellar targets which fall within the field of view. This capability exists in the present system. For example, pattern recognition has been achieved with nine signal pulses (three stars with three pulses per star) and 50 noise pulses. At a later stage of the pattern recognition process, angular separation matching permits the system to discriminate against nonstellar targets. At various times during the rooftop measurement program, airplanes, earth satellites, and planetary targets have have been detected and have been separated from the data generated by stellar targets.

A. Basic System Parameters

In developing a three axis attitude sensor, a problem which immediately presents itself is the selection of the optimum field of view, which determines the magnitude of the dimmest star we must detect. In the following discussion we assume the sensor is to have the capability of determining its attitude when pointed in a random direction. The factors affecting the selection of the field of view are illustrated by Figure 1. For purposes of simplification we assume that the stars are uniformly distributed on the celestial sphere and that an average of three stars are required within the field of view of the optical system. For example, if the optical system has a ten degree field of view, one must be able to detect about 1500 stars in order to have an average of three stars in the field of view. This means that the system must be able to detect stars down to about 5.5 visual magnitude. If, in this example, we assume that each axis of the three axis attitude sensor must be accurate to ten seconds of arc, then a resolution of one part in 3600 is required in the determination of the position of the stars within the field of view. If a computer memory is to be used to store star position and brightness data, allowing 36 bits for position and 6 bits for brightness, then 63,000 bits of memory are required. Table 1 summarizes the design problems resulting from the decision to use either a small, an intermediate, or a large field of view optical system. The factors shown on this table lead one to conclude that three axis attitude sensors for space navigation and guidance should employ fields of view in the range: $40^{\circ} \leq FOV \leq 60^{\circ}$.

From an operational point of view the design will depend on the dominant

Y-axis labels (left to right):
NUMBER OF BITS OF COMPUTER MEMORY REQUIRED TO STORE STAR DATA (42/STAR): 10^6, 10^5, 10^4, 10^3

LIMITING MAGNITUDE: 8, 7, 6, 5, 4, 3, 2, 1

NUMBER OF STARS: 10^5, 10^4, 10^3, 10^2, 10

ATTITUDE POINTING ACCURACY IS 10 ARC SECONDS

AVERAGE NUMBER OF STARS IN FOV = 3

FIELD OF VIEW (DEGREES): 1, 10, 100

REQUIRED RESOLUTION OF FIELD OF VIEW: 1/1000, 1/3000, 1/10000, 1/30000, 1/100000
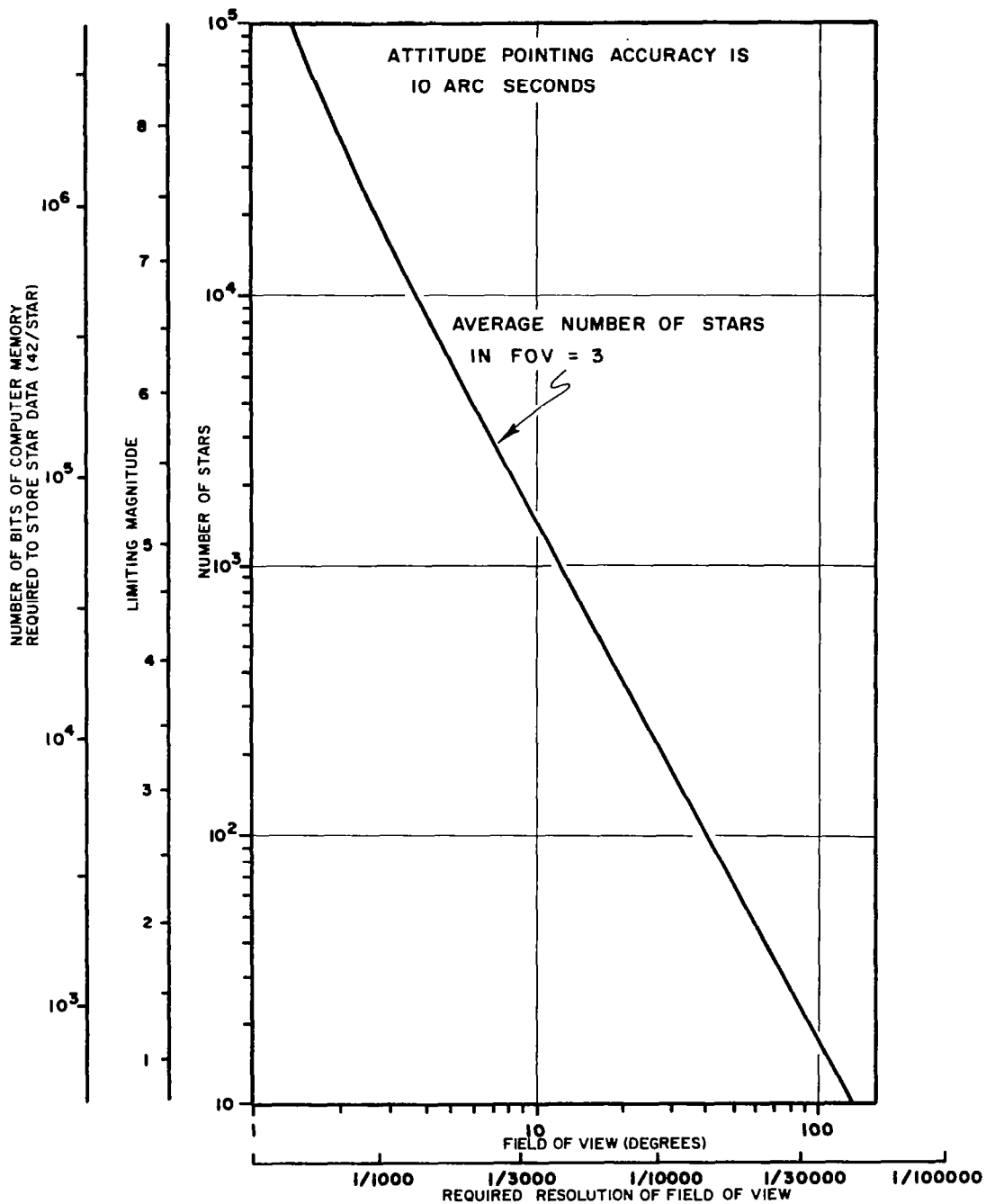
FIGURE I : DESIGN TRADE-OFFS FOR THREE AXIS ATTITUDE SYSTEM

TABLE 1

Field of View Comparison

Size of FOV	Disadvantages
Small (FOV < 10°)	1. Large computer memory is a requirement. 2. Star pattern recognition is difficult because of large number of stars. 3. Detection of faint celestial targets requires large diameter optics. 4. Only two out of three axes are accurately defined.
Intermediate (30° $\leq$ FOV $\leq$ 60°)	1. Detection electronics must be capable of measureing positions of stars within field of view with high resolution. 2. Design of high resolution camera requires more complex lens train. 3. Large FOV requires more carefully designed shield to minimize detrimental effects of sun and nearby planets.
Large (FOV > 90°)	1. High resolution, small f number systems are very difficult--if not impossible-- to design optically. 2. With reasonable apertures, size of optical elements becomes very large. 3. Difficult to find pointing direction not containing bright or extended objects such as sun, earth, and moon.

stabilization mode of the spacecraft. Three modes might logically be considered: (1) spinning spacecraft, (2) inertially stabilized spacecraft, and (3) a spacecraft stabilized relative to local vertical. In Figure 2 these various cases are considered. The major differentiating factor concerns the scan field itself; two cases are shown--a strip scan and a conical scan. Various focal plane slit arrangements have been used and this figure schematically shows the projection of these slits outside the three axis attitude sensor in the direction of pointing. In some of the cases shown, the motion of the spacecraft itself suffices to provide the scan and no moving parts are necessary; in others, a scan must be provided by rotating the slit itself or by rotating the entire sensor.
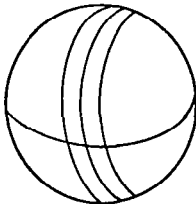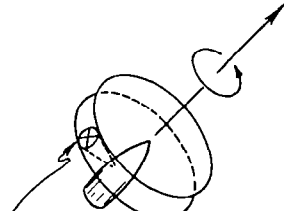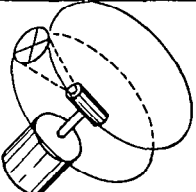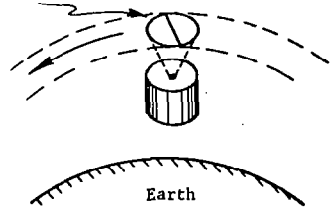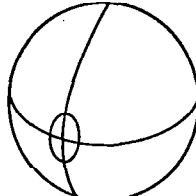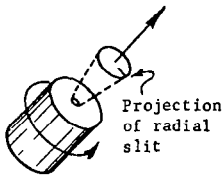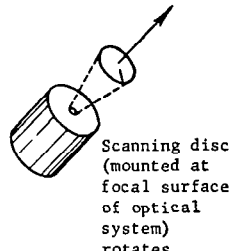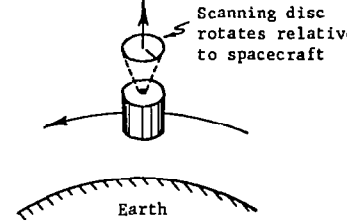
Type of Scan Field (Relative to Celestial Sphere)	Spacecraft Motion		
	Spinning	Inertially Stabilized	Stabilized Relative to Local Vertical
Strip	Projection of crossed slit located at focal plane of optical system	Sensor rotates relative to spacecraft	Projection of radial and circular slits. No moving parts needed Earth
Conical	Projection of radial slit	Scanning disc (mounted at focal surface of optical system) rotates	Scanning disc rotates relative to spacecraft Earth
Comments	No moving parts required relative to spacecraft	One degree of rotational freedom enables sensor to determine all three attitude axes	In case of conical scan, a "running" attitude fix provides time-varying orientation of spacecraft

FIGURE 2 : OPERATIONAL CONFIGURATIONS OF THREE AXIS ATTITUDE SENSORS

B. <u>Information Limits of Scanning Optical Systems</u>

In view of the potential usefulness of scanning optical systems for celestial attitude determination, a theoretical investigation of the information limits of scanning optical systems was initiated by NASA Langley Research Center at Control Data. This report presents our analysis and results.

The investigation had two basic objectives,

(1) to improve the accuracy of current methods of predicting system performance, and

(2) to develop better techniques of signal processing.

The first objective was met by developing complete models for the radiation, optical image, and photodetector. The second objective was met by carefully investigating various operating situations and selecting the most "efficient" processing technique for each situation. To optimize the sensor design a computer program was developed that automates the design. Also techniques for multiple observations were investigated.

In Figure 3, various sections of this report are related to the basic elements of the sensor. In Section II we discuss the effect of image shape, photoemission statistics, and stellar spectrum on the signal generated by the photodetector. Section III contains several statistical models of the background radiation which predict the number of weak star detections. The amount of information that can be extracted from the two-dimensional photoelectric image of a star is limited by the background radiation, optical aberrations, quantum efficiency, etc. The intrinsic limitations are developed in Section IV. In Section V, the characteristics of various photodetectors are discussed in relation to the requirements of scanning optical systems. To

Lens

I.   Introduction

II.   Star Radiation

III.   Background Radiation

IV.   Information Content of
Photoelectric Star Images

Slit

Photomultiplier

V.   Photodetectors for Space
Navigation Systems

VIII.   System
Design

Pulse Height
Discriminator

VI.   Signal Processing

Electronics

VII.   Multiple Observation
Techniques

Star detection
Background discrimination
Blur circle interpolation
Intensity estimation

Position and Intensity
Measurements

Figure 3: Report Organization

efficiently use the detected signal, we must carefully describe the operating situation and select the optimum signal processing technique. This approach was developed in Section VI. Multiple observation techniques are considered in Section VII.

In designing a scanning optical system we must manipulate several system parameters that are interdependent. The system design has been automated with a computer program, Section VIII. The program facilitates the design analysis. Several alternative designs can be developed in a relatively short time.

This report was prepared so that each section is essentially self-contained. An extensive bibliography is included as Section XI.

II. STAR RADIATION

The design of a scanning optical system depends upon the objects being viewed, how the optical system will distort the information being received from the objects in the field of view and how the system transforms this information into a usable electronic signal.

Subsection A discusses the effect that image shape has on the output of a passing slit. All the results are compared to scanning a two-dimensional Gaussian intensity distribution.

Many types of scanning systems already existing use a moving-spot. For example, image orthicons, deflectable photomultipliers and photographic plate scanners. Subsection B shows that the results for a moving slit can be a applied directly to a moving-spot scanner.

In Subsection C we discuss the statistical distribution of photon arrivals and photoelectric emissions. The emission distribution is Poisson for most cases of interest.

The amount of energy received from a light source and its interaction with an electro-optical system is greatly dependent upon the spectral energy distribution of the light source and the wavelength dependent response of the electro-optical system. Subsection D discusses the interaction between specific photoemissive surfaces and starlight.

A. Intensity Distribution Patterns

Imperfections in the optical system result in a distortion of the star image. Common lens aberrations and distortions result in an image which is symmetric about a line from the center of the field of view.

Consider the situation in which a point source image crosses a radial slit. We will compare the relative energy transmitted by the slit for different intensity distributions, such as a two-dimensional Gaussian, uniform triangle, uniform rhombus, uniform ellipse, and a Fraunhofer diffraction pattern.

If $I(x, y)$ describes the intensity distribution on the focal plane, then we will compute

$$G(t) = \frac{\int_{t - \frac{T_s}{2}}^{t + \frac{T_s}{2}} \int_{-\infty}^{\infty} I(x, y) \, dy \, dx}{\int_{-\infty}^{\infty} \int_{-\infty}^{\infty} I(x, y) \, dy \, dx}$$

where T_s is the time it takes a point image to cross the slit and $t = 0$ when maximum energy is being transmitted by the slit. The volume enclosed by the grid lines in Figure 1 is proportional to $G(t)$.

In order to make our results comparable, set $G(0) = 0.8$; i.e., eighty percent of the energy is transmitted at the point of maximum energy transmission.
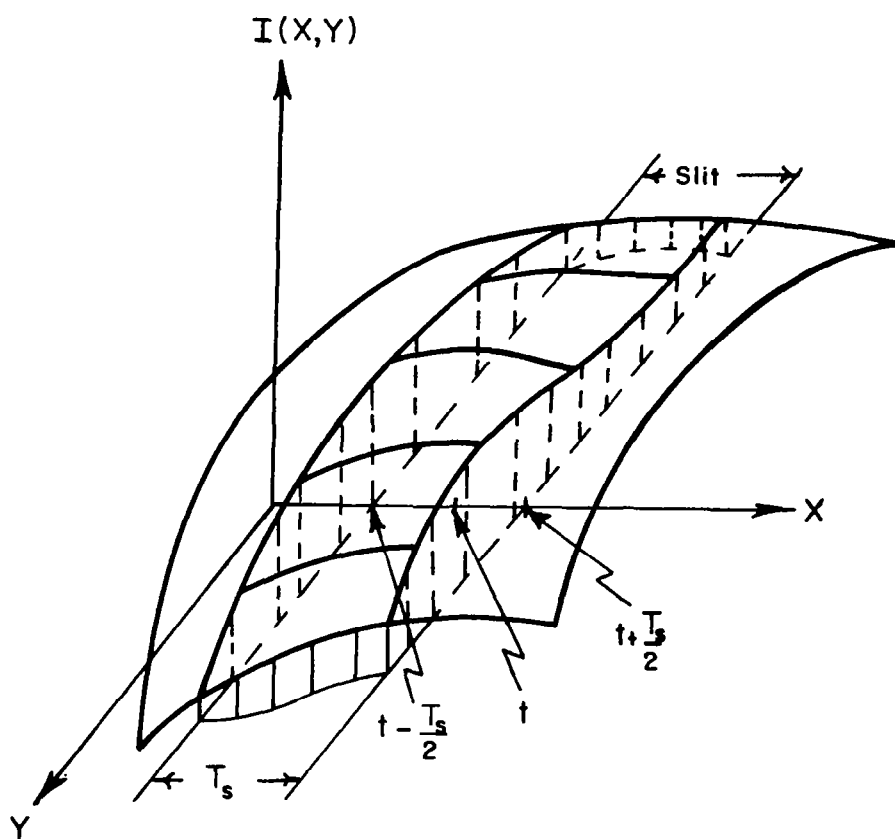
FIGURE 1: ENERGY TRANSMITTED BY SLIT FROM
INTENSITY SURFACE I(X,Y)

When

$$I(x,y) = \frac{k}{2\pi\sigma^2} \, e^{-\frac{1}{2}(x^2+y^2)/\sigma^2}$$

, K = constant

we say that the intensity distribution is two-dimensional Gaussian. The energy passing the slit relative to the total energy is

$$G(t) = \Phi\left(\frac{t}{\sigma} + \frac{T_s}{2\sigma}\right) - \Phi\left(\frac{t}{\sigma} - \frac{T_s}{2\sigma}\right)$$

where

$$\Phi(t) = \frac{1}{\sqrt{2\pi}} \int_{-\infty}^{t} e^{-\frac{1}{2}x^2} dx$$

The geometrical intensity distributions we will consider are:

a. Two dimensional Gaussian

b. Uniform isosceles triangle

c. Uniform rhombus

d. Uniform rectangle

e. Uniform ellipse

f. Fraunhofer diffraction pattern.

Figure 2 shows the relative outputs for the intensity distributions a, b, c, d, and e. The Fraunhofer diffraction pattern is considered at the end of this subsection. Figures 3, 4, 6, and 7 show how closely a Gaussian intensity distribution can approximate the other intensity distributions with respect to

% Radiatiation Passing
Through Slit

Normal

Rectangle

Ellipse

Triangle
Rhombus

·8

·6

·4

·2

·5   1·0   1·5   2·0 $\frac{t}{\sigma}$
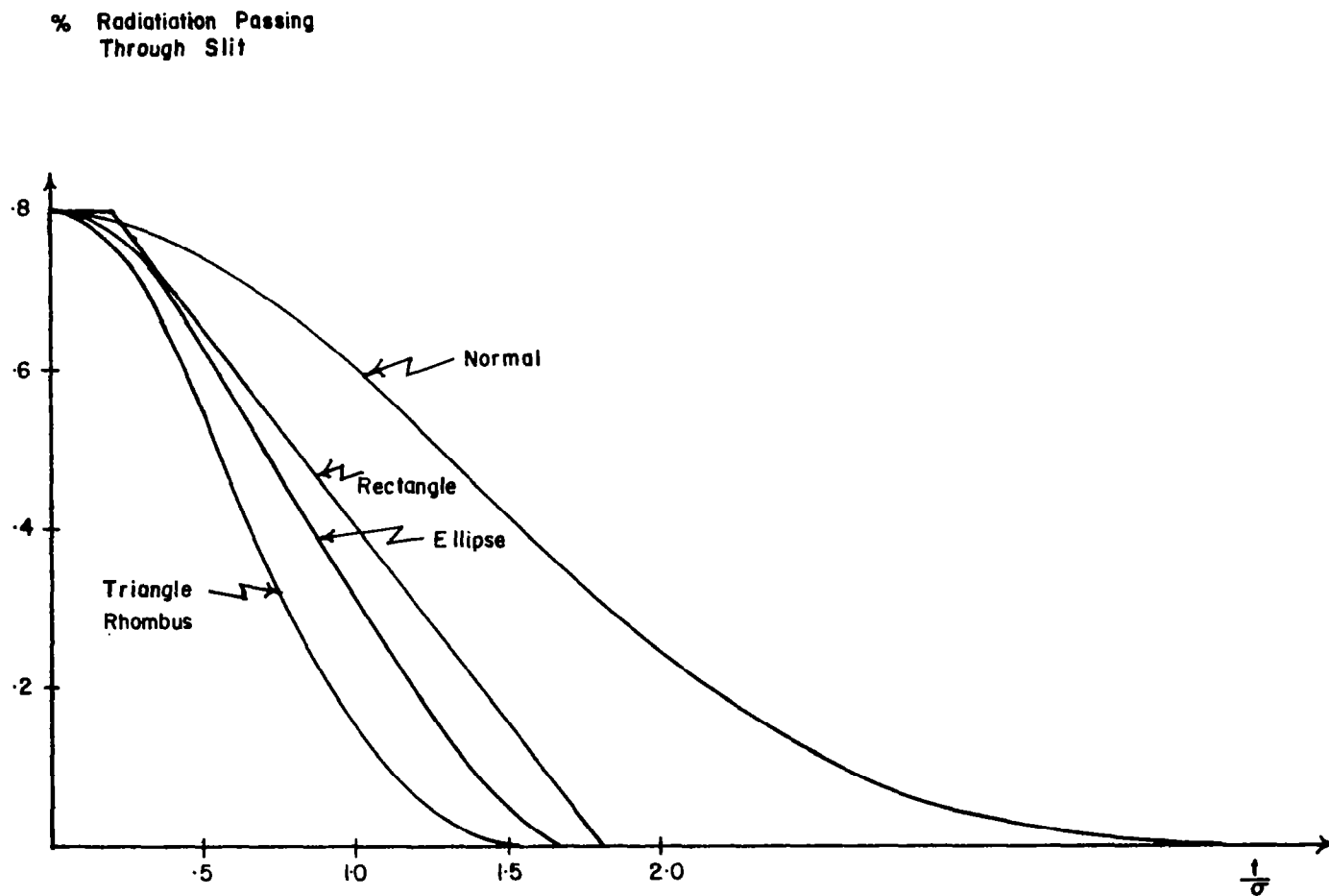
FIGURE 2 : RADIATION TRANSMITTED BY SLIT AS A FUNCTION OF TIME
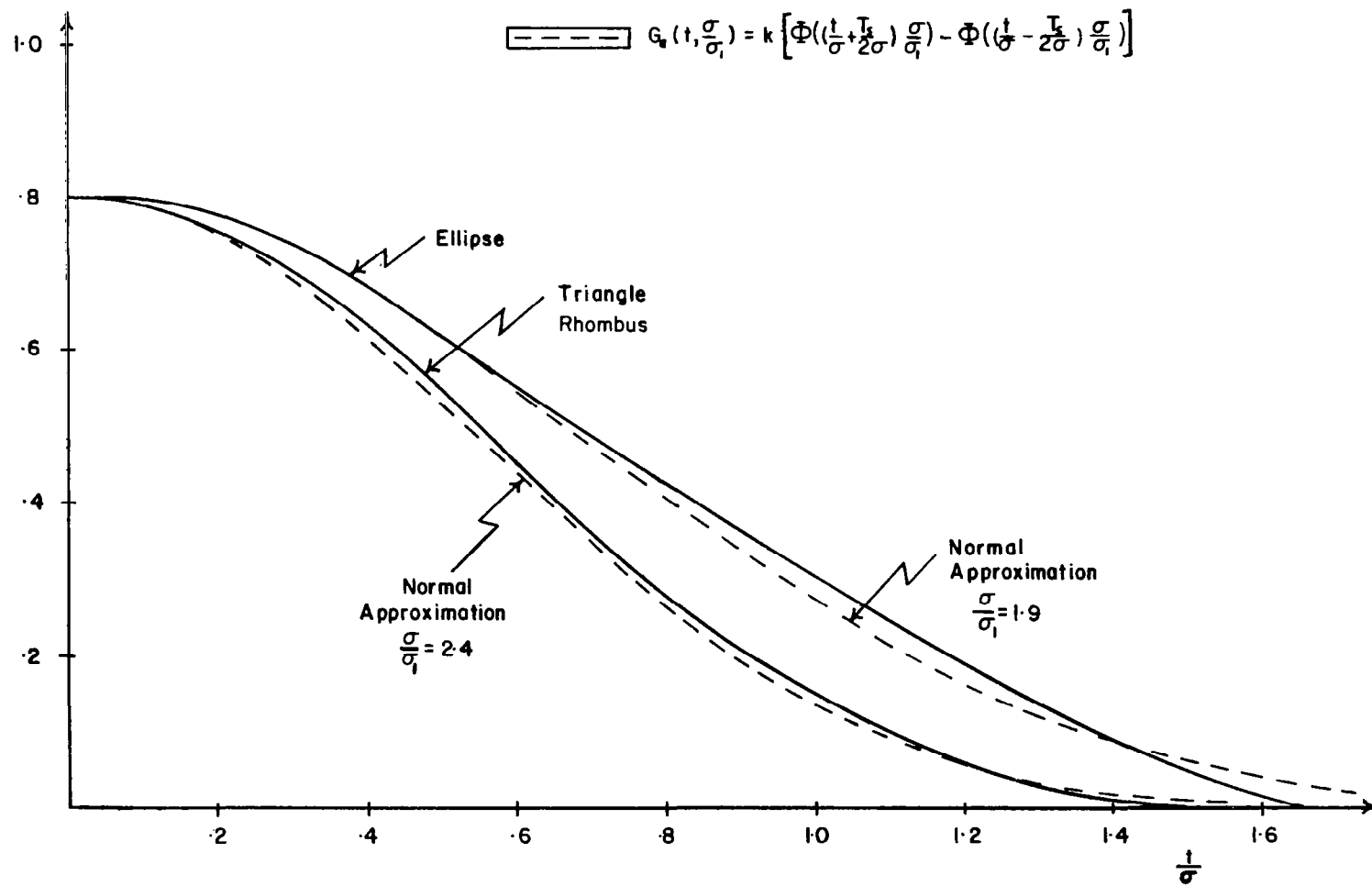
FIGURE 3 : COMPARISON OF ELLIPTICAL AND TRIANGULAR OUTPUT WITH A GAUSSIAN
BLUR CIRCLE OUTPUT
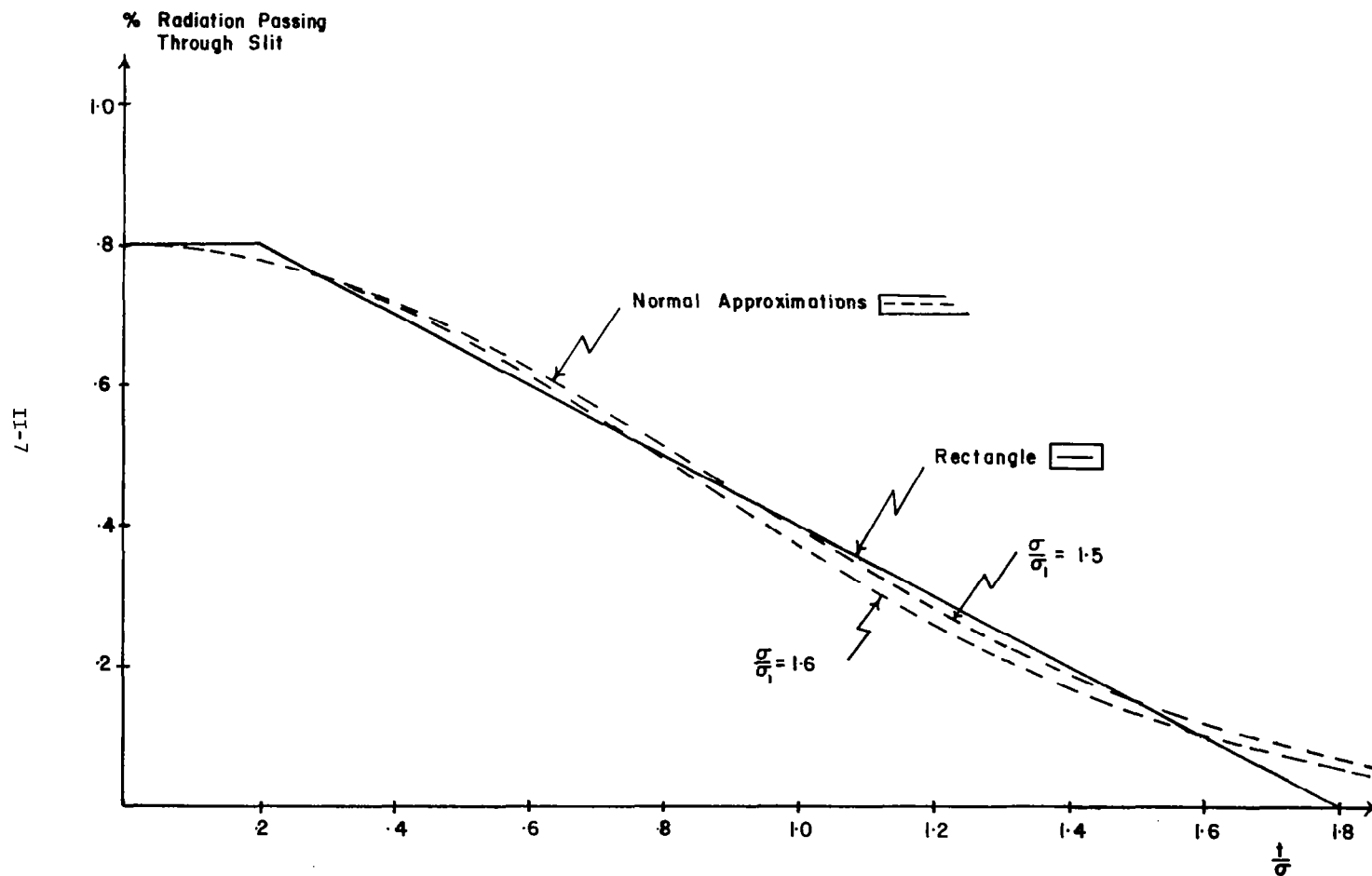
FIGURE 4 : COMPARISON OF RECTANGULAR OUTPUT WITH A GAUSSIAN BLUR CIRCLE OUTPUT

slit output. These comparisons indicate that if the intensity distribution is reasonably symmetric the output from a scanning slit can be thought of as coming from a two-dimensional Gaussian intensity distribution. The Gaussian approximations to the slit outputs are of the form

$$G_0\left(t; \frac{\sigma}{\sigma_1}, k\right) = k\left[\Phi\left(\left(\frac{t}{\sigma} + \frac{T_s}{2\sigma}\right)\frac{\sigma}{\sigma_1}\right) - \Phi\left(\left(\frac{t}{\sigma} - \frac{T_s}{2\sigma}\right)\cdot\frac{\sigma}{\sigma_1}\right)\right]$$

$$= k\left[\Phi\left(\frac{t}{\sigma_1} + \frac{T_s}{2\sigma_1}\right) - \Phi\left(\frac{t}{\sigma_1} - \frac{T_s}{2\sigma_1}\right)\right]$$

K and σ/σ_1 are parameters chosen so as to make a "good" fit.

The analytic derivations of the equations for the slit outputs follow. We first determine the slit width relative to the intensity distribution so that eighty percent of the energy is transmitted when the slit is centered on the intensity distribution. For the uniform intensity distributions, one needs only consider the "base" and its interaction with the slit (volume is reduced to area). Thus, to determine the slit width, $A_S = (0.8)(A_T)$ where A_S = area enclosed by slit and

A_T = total area of geometrical figure.

Isosceles Triangle:
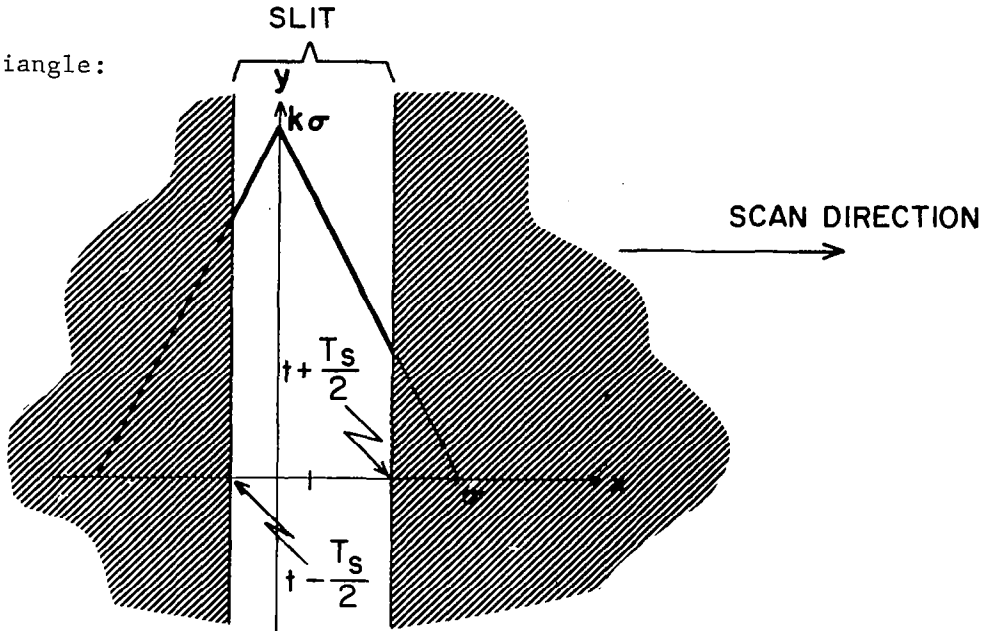
Determination of slit width:

$$A_s = 2 \cdot \frac{T_s}{2} \cdot k \cdot \frac{1}{2}\left(2\sigma - \frac{T_s}{2}\right)$$

$$A_T = k\sigma^2$$

Then

$$\frac{T_s}{2\sigma} = .553$$

Hence,

$$G(t) = \begin{cases} 2\left(\dfrac{T_s}{2\sigma}\right) - \left(\dfrac{T_s}{2\sigma}\right)^2 - \left(\dfrac{t}{\sigma}\right)^2 & 0 \le \left|\dfrac{t}{\sigma}\right| \le 1 - \dfrac{T_s}{2\sigma} \\[2ex] \dfrac{1}{2}\left[1 - \left(\dfrac{t}{\sigma} - \dfrac{T_s}{2\sigma}\right)\left(2 - \dfrac{T_s}{2\sigma} + \dfrac{t}{\sigma}\right)\right] & 1 - \dfrac{T_s}{2\sigma} < \left|\dfrac{t}{\sigma}\right| \le \dfrac{T_s}{2\sigma} \\[2ex] \dfrac{1}{2}\left[1 - \left(\dfrac{t}{\sigma} - \dfrac{T_s}{2\sigma}\right)\left(2 + \dfrac{T_s}{2\sigma} - \dfrac{t}{\sigma}\right)\right] & \dfrac{T_s}{2\sigma} < \left|\dfrac{t}{\sigma}\right| \le 1 + \dfrac{T_s}{2\sigma} \\[2ex] 0 & 1 + \dfrac{T_s}{2\sigma} < \left|\dfrac{t}{\sigma}\right| \end{cases}$$

Rhombus:
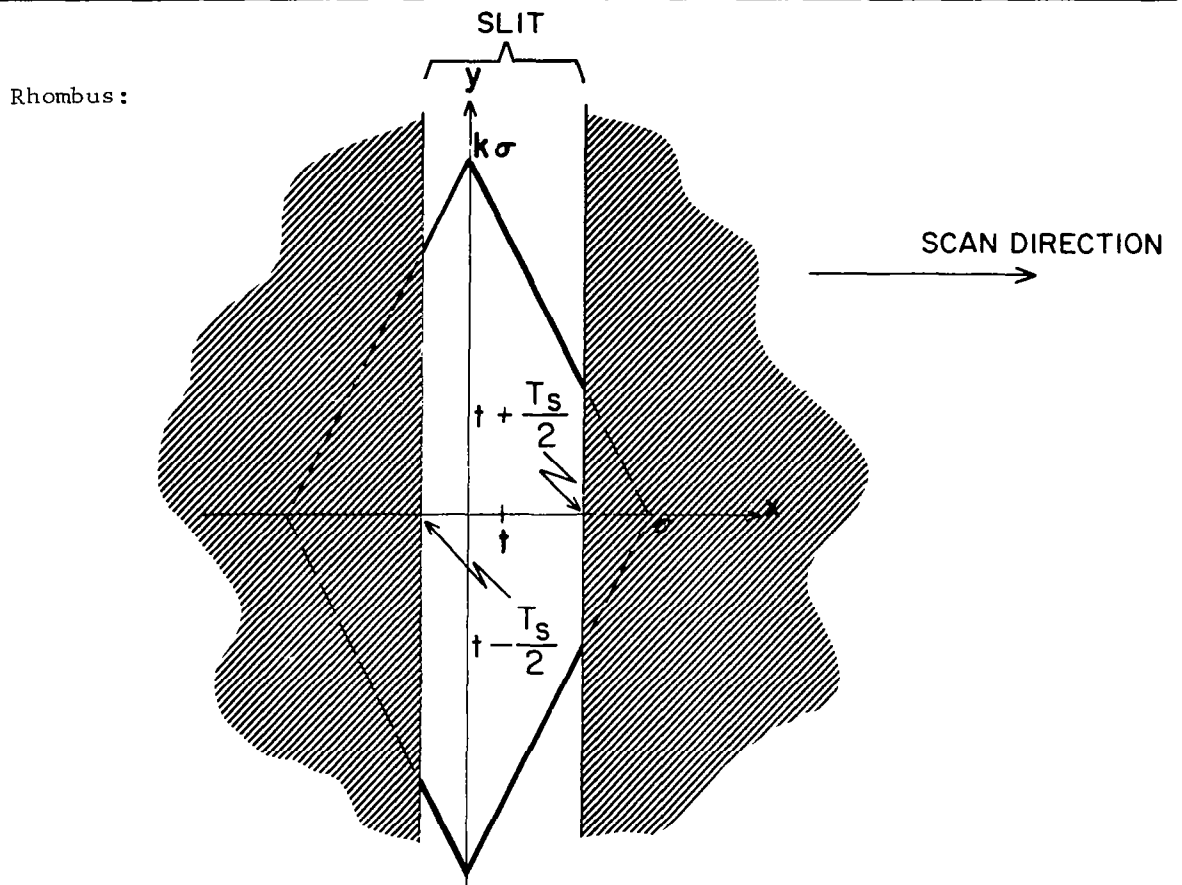
The results for this case are exactly the same as for the isosceles triangle.

Rectangle:
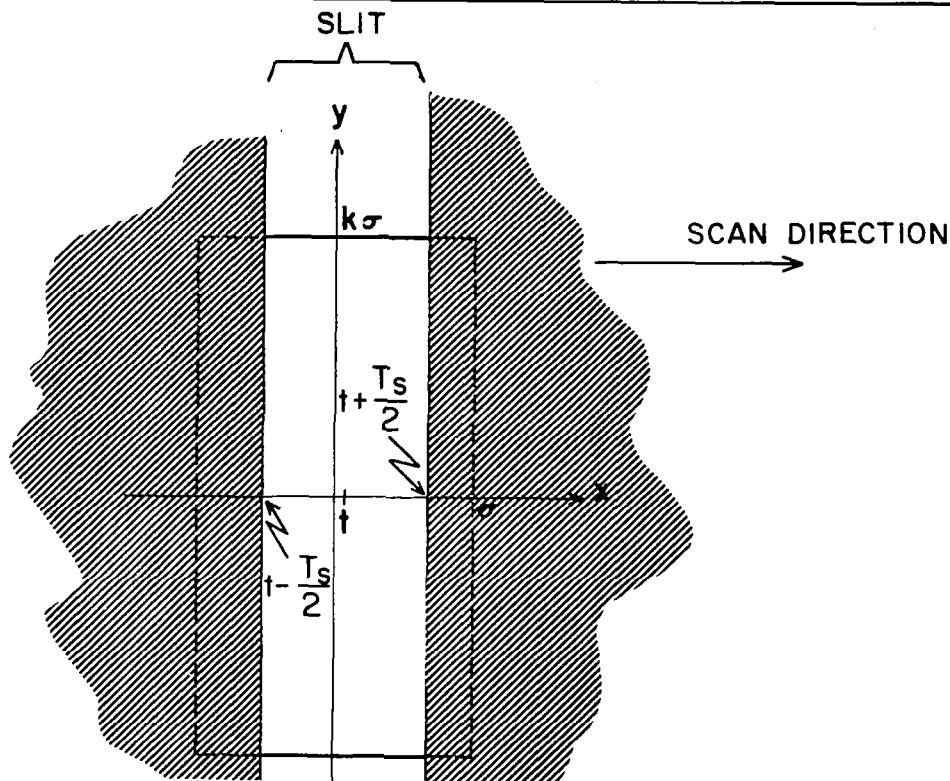
Determination of slit width:

$$A_s = T_s \cdot 2k\sigma$$

$$A_T = 2\sigma(2k\sigma)$$

Then

$$\frac{T_s}{2\sigma} = .8$$

Hence,

$$G(t) = \begin{cases} \dfrac{T_s}{2\sigma} & 0 \le \left|\dfrac{t}{\sigma}\right| \le 1 - \dfrac{T_s}{2\sigma} \\[2ex] \dfrac{1}{2}\left(1 + \dfrac{T_s}{2\sigma} - \dfrac{t}{\sigma}\right) & 1 - \dfrac{T_s}{2\sigma} < \left|\dfrac{t}{\sigma}\right| \le 1 + \dfrac{T_s}{2\sigma} \\[2ex] 0 & 1 + \dfrac{T_s}{2\sigma} < \left|\dfrac{t}{\sigma}\right| \end{cases}$$

II-11

Ellipse:
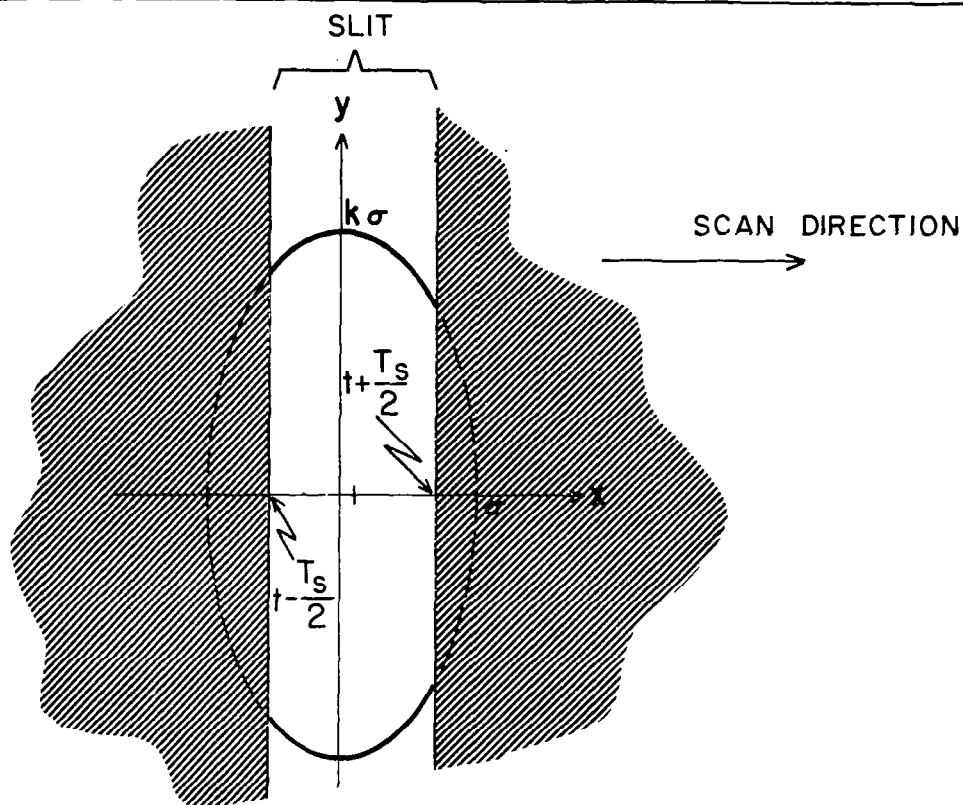
Determination of slit width:

$$A_s = 2k \left\{ \frac{T_s}{2} \sqrt{\sigma^2 - \left(\frac{T_s}{2}\right)^2} + \sigma^2 \; Sin^{-1}\left(\frac{T_s}{2\sigma}\right) \right\}$$

$$A_T = k \pi \sigma^2$$

Then

$$\frac{T_s}{2\sigma} = .69$$

Hence,

$$
G(t) = \begin{cases}
\frac{1}{\pi}\left\{\left(\frac{t}{\sigma}+\frac{T_s}{2\sigma}\right)\sqrt{1-\left(\frac{t}{\sigma}+\frac{T_s}{2\sigma}\right)^2}\ +\ \sin^{-1}\left(\frac{t}{\sigma}+\frac{T_s}{2\sigma}\right)\right.\\
\qquad\left.-\left(\frac{t}{\sigma}-\frac{T_s}{2\sigma}\right)\sqrt{1-\left(\frac{t}{\sigma}-\frac{T_s}{2\sigma}\right)^2}\ -\ \sin^{-1}\left(\frac{t}{\sigma}-\frac{T_s}{2\sigma}\right)\right\}\\
\qquad\qquad\qquad\qquad\qquad 0 \le \left|\frac{t}{\sigma}\right| \le 1 - \frac{T_s}{2\sigma}\\[2mm]
\frac{1}{2}-\frac{1}{\pi}\left\{\left(\frac{t}{\sigma}-\frac{T_s}{2\sigma}\right)\sqrt{1-\left(\frac{t}{\sigma}-\frac{T_s}{2\sigma}\right)^2}\ +\ \sin^{-1}\left(\frac{t}{\sigma}-\frac{T_s}{2\sigma}\right)\right\}\\
\qquad\qquad\qquad\qquad\qquad 1 - \frac{T_s}{2\sigma} < \left|\frac{t}{\sigma}\right| \le 1 + \frac{T_s}{2\sigma}\\[2mm]
0 \qquad\qquad\qquad\qquad\qquad 1 + \frac{T_s}{2\sigma} < \left|\frac{t}{\sigma}\right|
\end{cases}
$$

Diffraction Pattern:

The energy distribution resulting from a point source using a circular aperture results in a relative light intensity distribution function of the form

$$
F(r) = \left(\frac{2\,J_1(r)}{r}\right)^2
$$

where r is proportional to the distance from the center of the image. A basic problem is to determine the accumulated energy to one side of a knife edge. From this function one can then determine the energy transmitted by a slit of finite width but infinite length. This is done by evaluating the cumulative energy function at the two edges of the slit and taking their difference. At the end of this subsection the function G is determined from G_1 in this manner.

To determine the energy to one side of a knife edge we must integrate I(x, y) over the region

$$R = \left\{ (x,y) \mid x \leq a \right\}$$

where

$$I(x, y) = F\left(\sqrt{x^2+y^2} \right).$$

Let

$$G_1(a) = \iint_R I(x, y)\, dx\, dy.$$

From the symmetry of F,
$$G_1(a) + G_1(-a) = 2 \cdot G_1(0) = G_1(\infty).$$

Let

$$H(a) = \iint_{R'} I(x,y)\, dx\, dy$$

where

$$R' = \left\{ (x,y) \mid 0 \leq x \leq a, \ 0 \leq y \right\}.$$

Then

$$H(a) = 4 \int_0^{\pi/2} \int_0^{a \cdot \sec \theta} \left[J_1^2(r)/r^2 \right] \cdot r\, dr\, d\theta$$

$$= 4 \int_0^{\pi/2} \left(-\tfrac{1}{2}\right) \left[J_0^2(r) + J_1^2(r) \right]_0^{a \cdot \sec \theta} d\theta$$

$$= 2 \int_0^{\pi} \left[1 - J_0^2(a \cdot \sec \theta) - J_1^2(a \cdot \sec \theta) \right] d\theta.$$

If we let $t = a \sec \theta$, then

$$H(a) = 2 \int_a^\infty \left(1 - J_0^2(t) - J_1^2(t)\right) \frac{a}{t\sqrt{t^2 - a^2}} \, dt$$

$$= \pi - 2a \int_a^\infty \frac{J_0^2(t) + J_1^2(t)}{t\sqrt{t^2 - a^2}} \, dt$$

Note that

$$\lim_{a \to \infty} H(a) = \pi$$

Hence

$$G_1(0) = \frac{1}{2} G(\infty) = 2 \cdot H(\infty) = 2\pi$$

From the symmetry of F we have for $a \geq 0$,

$$G_1(a) = G(0) + 2 \cdot H(a)$$

$$= 4 \left\{ \pi - a \int_a^\infty \frac{J_0^2(t) + J_1^2(t)}{t\sqrt{t^2 - a^2}} \, dt \right\}$$

If $\nu = \dfrac{a}{t}$, then

$$G_1(a) = 4 \left\{ \pi - \int_0^1 \frac{J_0^2\left(\frac{a}{\nu}\right) + J_1^2\left(\frac{a}{\nu}\right)}{\sqrt{1 - \nu^2}} \, d\nu \right\} \qquad a \geq 0$$

To evaluate the integral a Chebyshev-Gauss quadrature formula was used, namely, for f even

$$\int_0^1 \frac{f(x)}{\sqrt{1-x^2}} \, dx = \frac{\pi}{2m} \sum_{k=1}^{m} f(x_k)$$

where

$$x_k = \cos\left[\frac{(2k-1)\pi}{4m} \right] \quad ; \quad k = 1, \cdots, m$$

Figure 5 shows the graph of the function G_1. Figure 6 shows the graph of

$$G(t) = G_1\left(t + \frac{T_s}{2}\right) - G_1\left(t - \frac{T_s}{2}\right)$$

where T_s represents the slit width. Note that Gaussian approximations are very good except in the "tails". Figure 7 shows how G and Gaussian approximations compare for cases when the slit passes ninety percent and ninety-five percent of the energy when the star is in the slit center.

The averaging affect of the slit again tends to obliterate the variations of the image, so that the output of a slit crossing a two-dimensional Gaussian intensity distribution approximates the diffraction pattern output.

graph of $G_1(u)/G_1(\infty)$

where $G_1(u) = \displaystyle\int_{-\infty}^{\infty}\int_{-\infty}^{u} \left[\frac{2 J_{01}(\sqrt{x^2+y^2})}{\sqrt{x^2+y^2}} \right]^2 dx\,dy$

PERCENT

DISTANCE FROM CENTER OF PATTERN   U

U
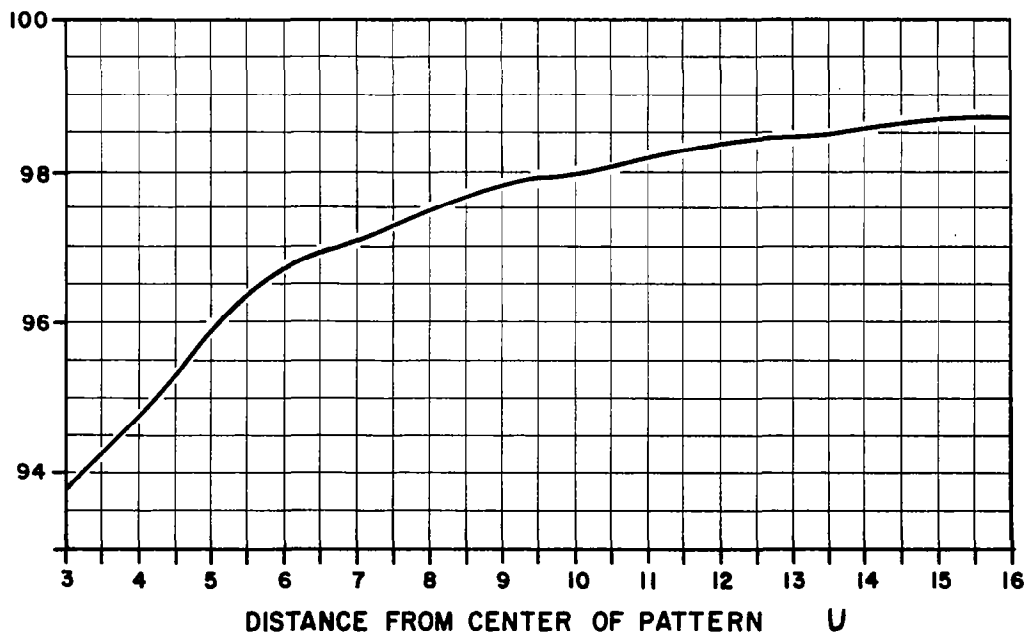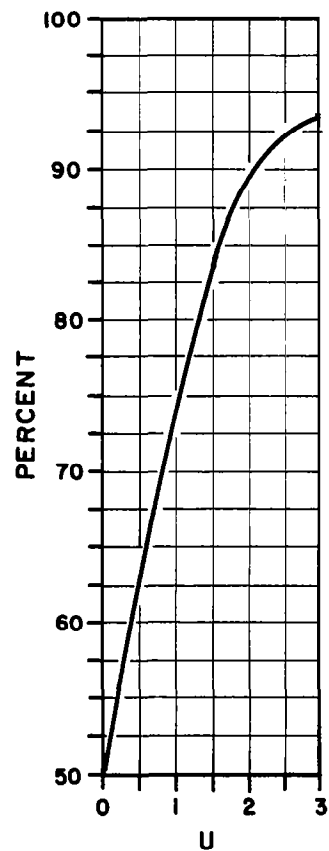
FIGURE 5 : RADIATION OF A DIFFRACTION PATTERN PASSING A
KNIFE EDGE
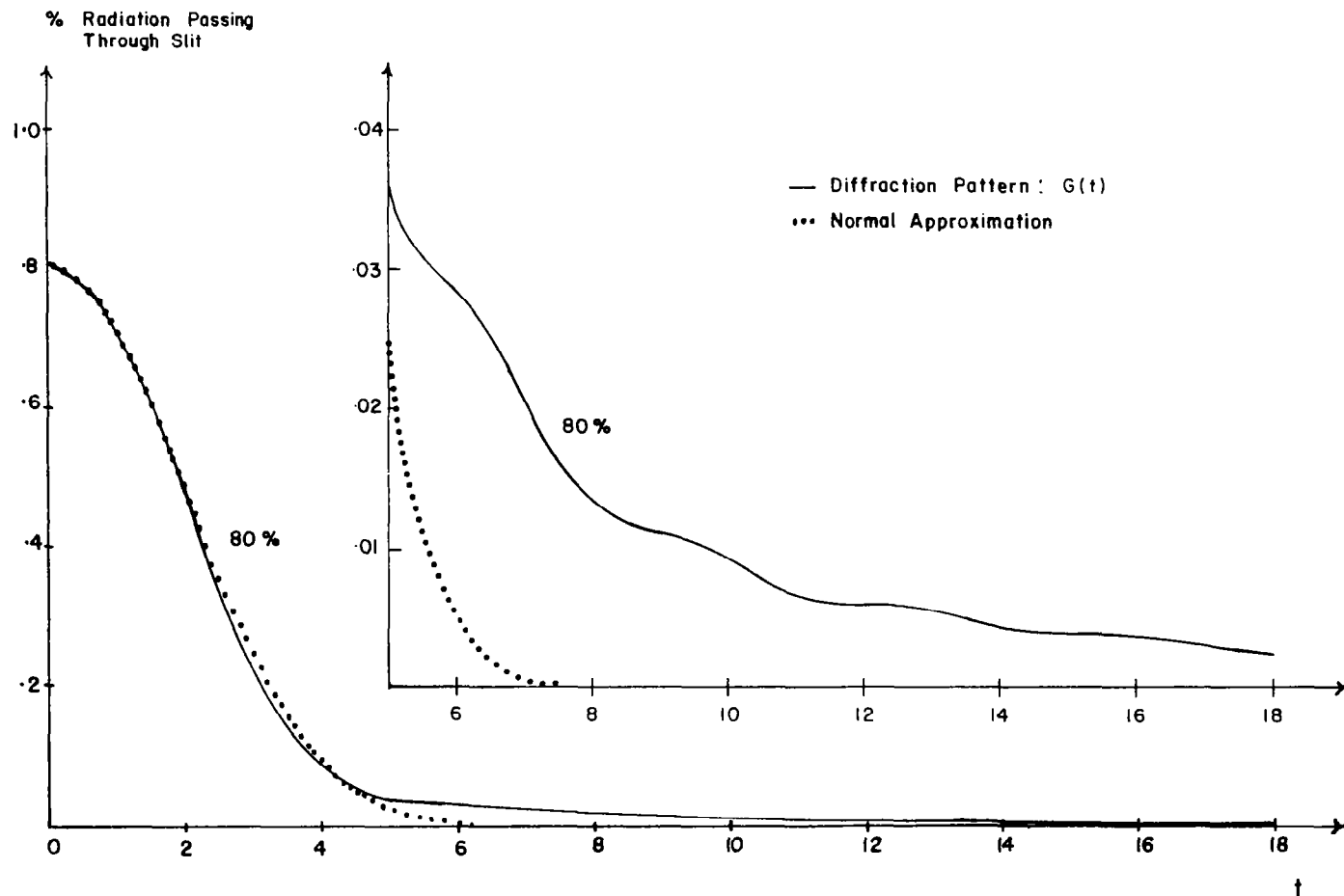
FIGURE 6 : COMPARISON OF DIFFRACTION PATTERN OUTPUT WITH A GAUSSIAN BLUR CIRCLE
OUTPUT, WHEN THE MAXIMUM RADIATION PASSING THE SLIT IS 80%
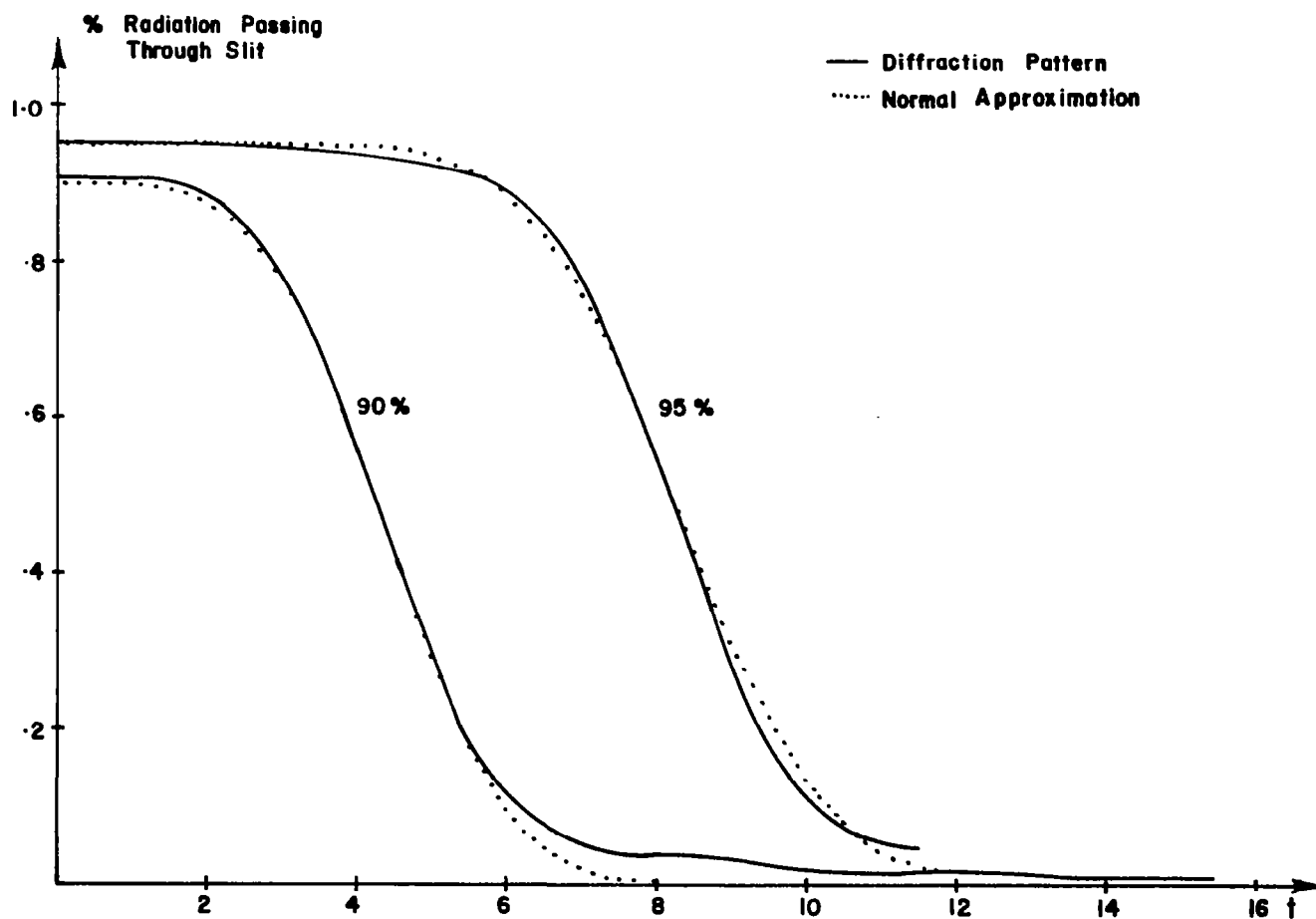
FIGURE 7: NORMAL APPROXIMATIONS TO THE OUTPUT OF A DIFFRACTION PATTERN
WHEN THE MAXIMUM RADIATION PASSING THE SLIT IS 90% AND 95%

B. Comparison to Moving-Spot Scanning

In this section we wish to contrast the output of a moving-spot scanning system and that of a moving slit. The spot is assumed to be rectangular in shape. A rectangular spot can reasonably approximate the scanning spots used in image orthocons, deflectable photomultipliers, and photographic plate scanners. Suppose **the optical system** produces a diffraction pattern that is two-dimensional Gaussian. The energy density in the focal plane is given by

$$I(x,y) = \frac{k}{2\pi \sigma^2}\, e^{-\frac{1}{2}(x^2+y^2)/\sigma^2}$$

where K is a constant.

Then the outputs of the slit and spot are

$$P_{SLIT}(t) = \int_{R_{SLIT}} I(x,y)\, dx\, dy$$

$$P_{SPOT}(t,u) = \int_{R_{SPOT}} I(x,y)\, dx\, dy$$

where

$$R_{SLIT} = \left\{ (x,y) \,\Big|\, t - \frac{T_s}{2} \le x \le t + \frac{T_s}{2} \right\}$$

$$R_{SPOT} = \left\{ (x,y) \,\Big|\, t - \frac{T_s}{2} \le x \le t + \frac{T_s}{2} \,,\, u - \frac{L_s}{2} \le y \le u + \frac{L_s}{2} \right\}$$

   See Figure 8 for symbol explanation.

The star is in the center of the slit when t = 0 and is in the center of the

spot when (t, u) = (0, 0).

   The results of the above integration are

$$P_{SLIT}(t) = K' \cdot G_{T_s}(t)$$

$$P_{SPOT}(t,u) = K' \cdot G_{T_s}(t) \, G_{L_s}(u) \quad , \quad K' = CONSTANT$$

where

$$G_w(t) = \Phi\left(\frac{t}{\sigma} + \frac{w}{2\sigma}\right) - \Phi\left(\frac{t}{\sigma} - \frac{w}{2\sigma}\right)$$

and

$$\Phi(t) = \frac{1}{\sqrt{2\pi}} \int_{-\infty}^{t} e^{-\frac{1}{2}x^2} \, dx$$
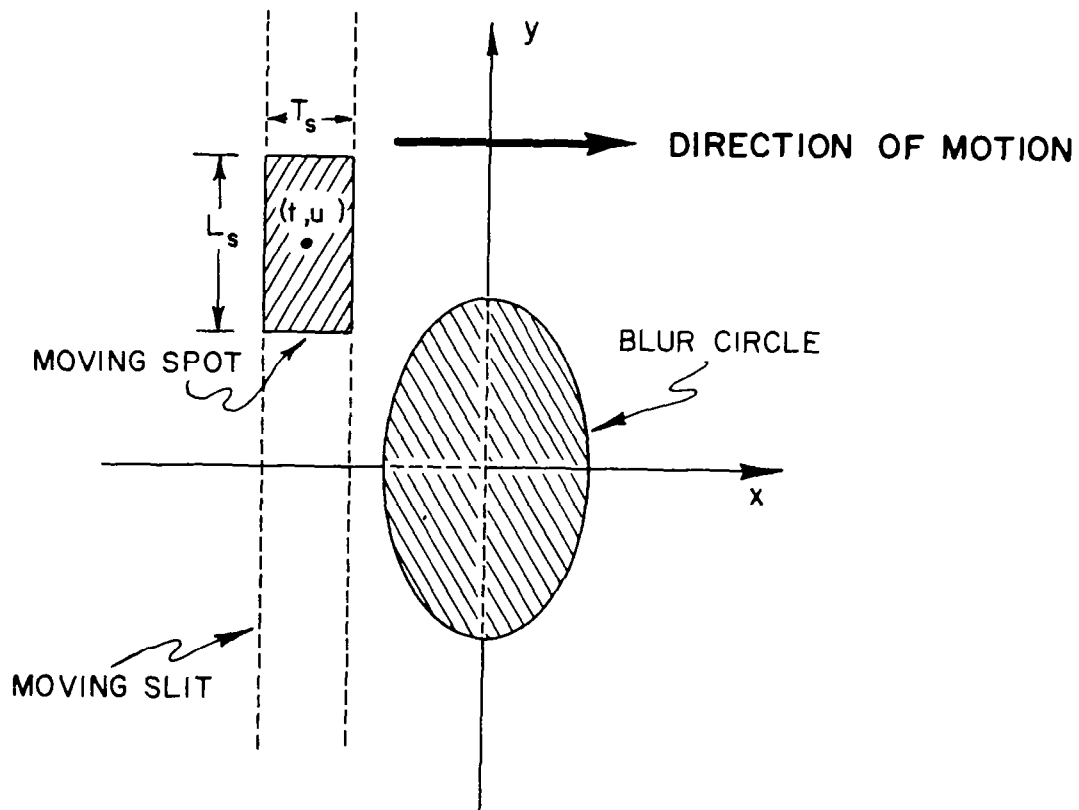
FIGURE 8 : MOVING - SPOT SCANNING OF A
BLUR CIRCLE

The point to be made here is that for fixed u, $P_{slit}(t)$ is proportional to $P_{spot}(t, u)$.

These results can be slightly generalized. If the star image is elliptical then the energy distribution is of the form

$$I(x, y) = \frac{K}{2\pi \sigma_1 \sigma_2} e^{-\frac{1}{2}\left(\frac{x^2}{\sigma_1^2} + \frac{y^2}{\sigma_2^2}\right)}$$

If the slit and spot move in a direction that is orthogonal to one of the axes of the ellipse, the output for the slit and spot are still proportional in the same sense as used previously.

For an arbitrary direction of motion across an elliptical image we do not have any conclusive results regarding the relation between the slit and spot output. Thus, results derived for a moving slit can be applied directly to a moving-spot scanner.

C. Statistics of Photoemissions

To select a reasonable technique of processing photoelectric measurements, we must consider the statistics of the photoemissions. There are basically two approaches, or models, to describe the statistical distribution of the number of photoelectric emissions in a fixed time period. The first model describes the radiation incident on the photodetector as a stochastic sequence of photon arrivals. The second model describes the radiation incident on the photodetector as a stochastic wave. The wave model has three advantages.

(1) The wave model applies directly to radiation which has a wide frequency spectrum.

(2) The wave model yields "classical equations" for dim and bright radiation.

(3) The results obtained with the photon model are special cases of the results obtained with the wave model.

In the following discussion we will restrict our attention to the wave model. The statistical characteristics of photon beams and photoemissions have been discussed by Stern (1960), Jones (1962), Hisdal (1965), Fried (1965), Grau (1965), Hodora (1965), Bolgiano (1964), Harwit (1960), Jones (1953), and Fellgett (1949, 1959).

The following discussion of the wave model is based on results presented by Mandel (1958, 1959). If one observes an average of $\bar{n}$ emissions in a period T, the probability of obtaining n emissions is

$$p(n,T) = \frac{\Gamma\left(n + T/\xi\right)}{n!\, \Gamma\left(T/\xi\right)} \; q^{n} \left(1 - q\right)^{T/\xi}$$

where

$$q = \frac{1}{1 + T/\bar{n}\,\xi}$$

The parameter ξ is defined in terms of the normalized correlation function $\gamma(\tau)$ of the incident wave $y(t)$. In particular,

$$\gamma(\tau) = \frac{E\left[y(\tau+t)\,y(t)\right]}{E\left[y(t)\right]^2}$$

$$\xi = \frac{4}{T}\int_0^T (T-\tau)\,\gamma^2(\tau)\,d\tau$$

The parameter ξ has the dimension of time and can be interpreted as the coherence time, and T/ξ represents the number of "degrees of freedom." The quantity $\bar{n}\,\xi/T$ is a basic parameter; it is the average number of photoemissions in one coherence time. For a system in thermal equilibrium we can show that

$$\frac{\bar{n}\,\xi}{T} = \left(e^{h\nu/kT_0} - 1\right)^{-1}$$

where $h\nu$ is the quantum energy, k is Boltzmann's constant, and T_o is the temperature in degrees Kelvin, see Garbuny (1965), p. 418.

We can show directly that $p(n, T)$ approaches a Poisson distribution as $\bar{n}\,\xi/T$ approaches zero. This is the case in most stellar applications. On the other hand, $p(n, T)$ approaches a "gamma distribution" for large values of

$\bar{n}$ ξ/T. This limiting form represents the distribution of intensity of the incident wave, since Mandel assumes the incident waves are Gaussian random processes.

The variance of the number of emissions is

$$\bar{n}\left(1 + \bar{n}\,\xi/T\right).$$

For a dim source, the variance becomes $\bar{n}$. For a bright source, the variance becomes $\bar{n}^2\,\xi/T$.

For stellar radiation, $\Delta\lambda$ is the order of 0.1 micron and $\xi \approx 1/\Delta\nu$ is the order of 10^{-15}. (The effective response with an S-4 detector and a Type A star is presented in Figure 4 of Section V.) Consequently, we may assume the photoemissions form a Poisson process. Note that the output from a photomultiplier may deviate from Poisson even though the primary emissions are Poisson, see Gadsden (1965). This deviation can be attributed to a loss of electrons between the cathode and anode. In most cases, we can neglect this effect.

D.   Effective Intensity of Star Radiation

The response of a star being observed with a photomultiplier is dependent
on a multitude of factors among which are the spectral energy distribution of
the star and the spectral response of the photoemissive surface.

The spectral energy distribution of a star has been studied using two
types of photometry, wide-band and narrow-band. In the first type, the radiant
energy from a star is integrated over several hundred angstroms by a combina-
tion of filters and a detector. Clearly, much of the detail of the spectral
energy distribution is lost in wide-band photometry. However, extensive data
exists in this form[*] and if one is interested in only the gross features of
the spectral energy distribution, this is quite adequate.

In narrow-band photometry the radiant energy from a star is integrated
over regions less than 20 angstroms in width. Much more information is
gathered in this way and as yet, only a limited number of stars have been
studied.[**]

In order to study the gross features of star spectra it is necessary to
classify the stars according to their spectral response. A common classifi-
cation according to temperature is readily available. The classes considered
here are B, A, F, G, K, M.

The spectral responses of the UBV color system are shown in Figure 9.[***]

---

[*]   Iriarte, et al., (1965), pp. 21-31.

[**]   Norton (1964), and Code (1960).

[***]   Taken from Allen, C. W. (1963), p. 195.
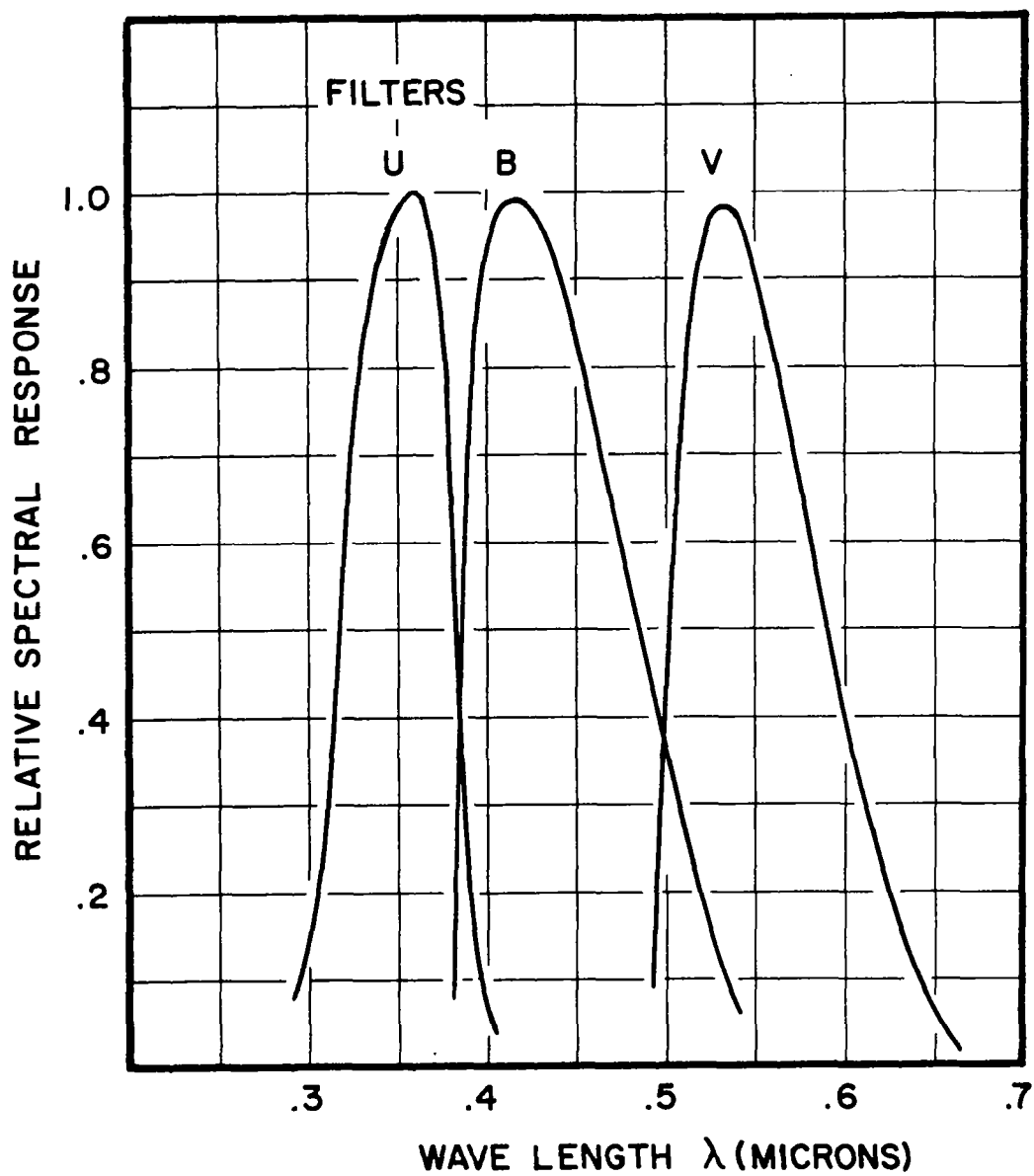
FIGURE 9 : RELATIVE SPECTRAL RESPONSE OF THE
U, B AND V FILTERS

The magnitude of a star is thus obtained at three different wavelengths, namely, .36 micron, .43 micron, .54 micron. These values are the wavelengths at which the U, B, and V spectral responses are maximum. Figures 10 and 11 show how the U-V and B-V magnitudes vary as a function of spectral class. The list of stars used was a list published in Sky and Telescope by Iriarte, et al., (1965). Using this data an average value for the U-V and B-V magnitudes as a function of spectral class was obtained.

In the following discussion we assume the U, B, and V spectral responses are simple bandpass filters. The effective intensity of a star in spectral C (C = 0, B, A, F, G, K, or M) is then

$$\int I_c(\lambda) \cdot R(\lambda) \, d\lambda \approx I_c(\lambda_0) \cdot R(\lambda_0) \cdot \Delta\lambda$$

where $I_C(\lambda)$ is the spectral energy density of a star in class C, and where $R(\lambda)$ is the response of the filter. In the present problem, λ_0 is the wavelength of the peak of the U, B, or V response. Also $R(\lambda_0)$ and $\Delta\lambda$ are assumed to be the same for each response. Therefore, the values of the spectral energy density at the peak wavelength of the U, B, V responses are related to the U, B, V magnitudes (denoted by $M_C(U)$, $M_C(B)$, $M_C(V)$) through the following equations

$$I_c(\lambda_u) = a \cdot 10^{-.4 M_c(U)}$$
$$I_c(\lambda_B) = a \cdot 10^{-.4 M_c(B)}$$
$$I_c(\lambda_v) = a \cdot 10^{-.4 M_c(V)}$$
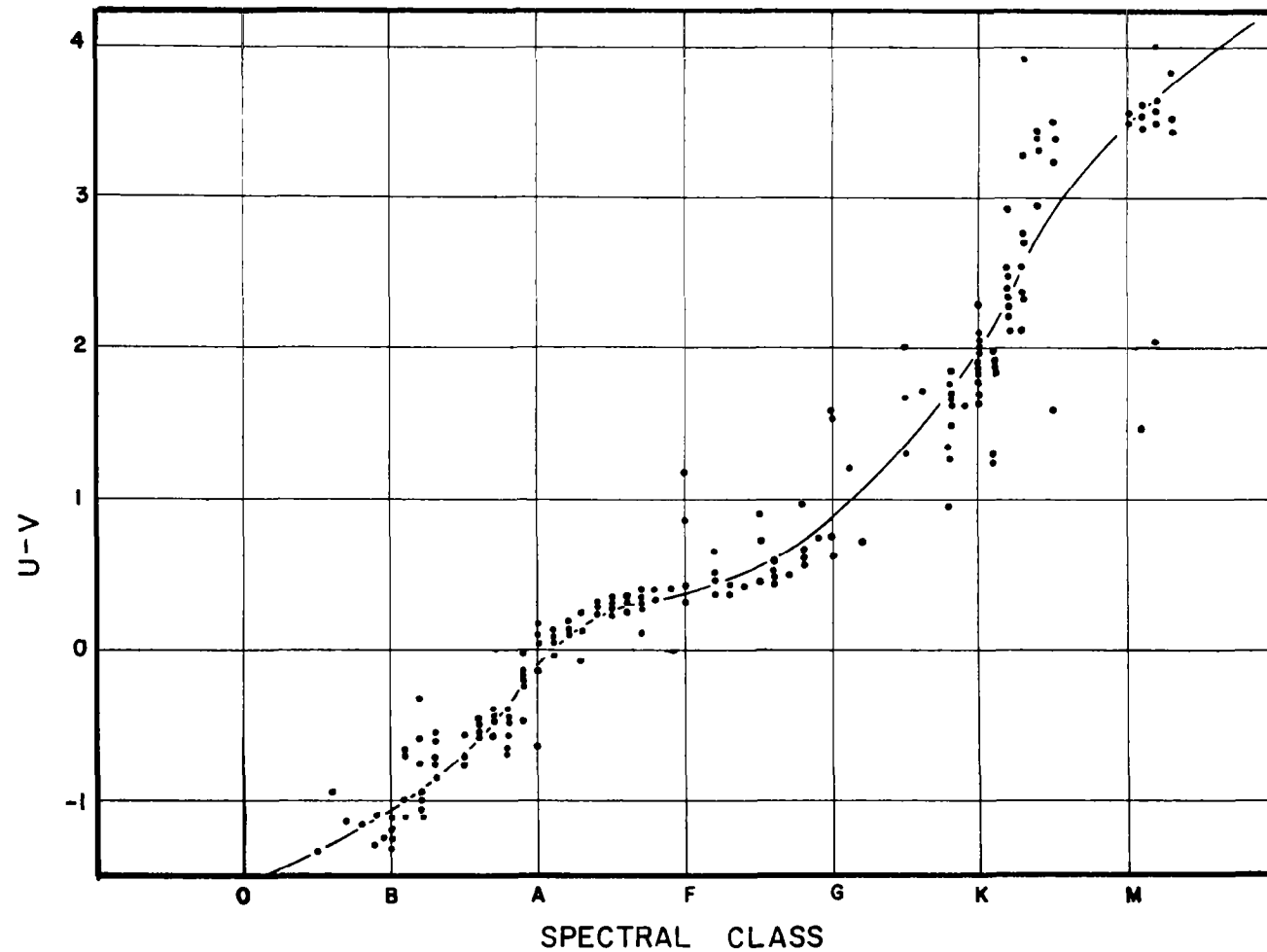
FIGURE 10: U-V MAGNITUDES AS A FUNCTION OF SPECTRAL CLASS
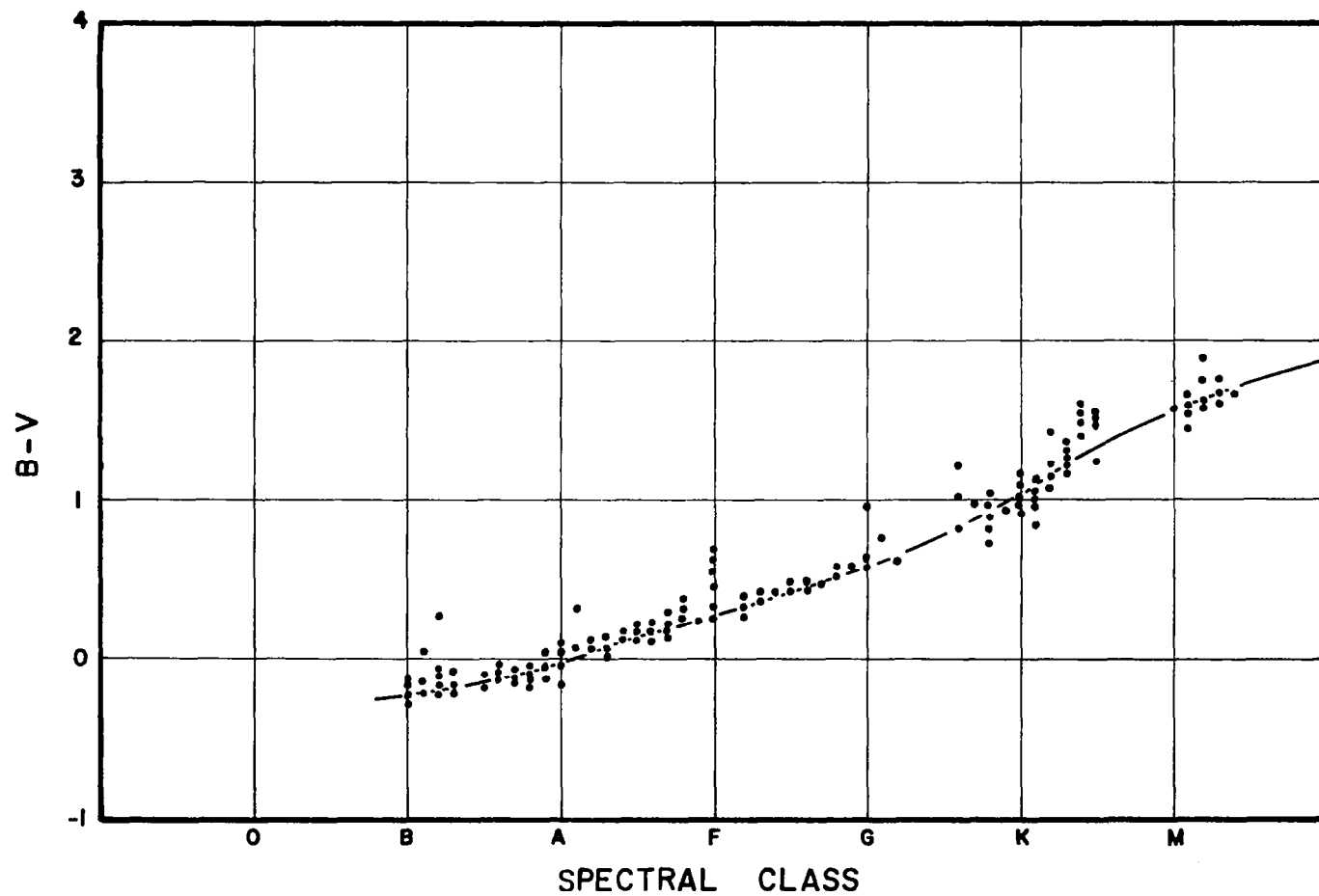
FIGURE II : B−V MAGNITUDES AS A FUNCTION OF SPECTRAL CLASS

where a is a constant of·proportionality.

It is then necessary to extrapolate and interpolate in order to "complete" the curve $I_c(\lambda)$. For wavelengths below the Balmer cutoff .36 micron, $I_c(\lambda)$ is assumed to be constant. *The attenuation at the Balmer cutoff is based on data given by Greaves (1956).* For values of $\lambda \geq .36$, an interpolation function of the form

$$I_c(\lambda) = e^{(a_1 + b_1\lambda + c_1\lambda^2)} \lambda^N$$

was used. N is initially chosen to be zero. For this value the data points sometimes yield an approximation with c_1 positive. For extrapolation in the .54 to .70 micron range this yields poor results. Thus, we let N take on the successive values of -1, -2, ... until the approximation gave us $c_1 < 0$.

We will determine the relative photoelectric intensity and magnitude of stars in several spectral classes and for S-4, S-11, S-20 detector responses; see Figure 12.[*] The photoelectric intensity is

$$F(c,P) = \beta \int_{\lambda_1}^{\lambda_2} I_c(\lambda) \cdot S_p(\lambda)\, d\lambda \quad ; \quad P = S\text{-}4, S\text{-}11, S\text{-}20$$

where β is a constant of proportionality and where $S_p(\lambda)$ is the spectral response for the particular photoemissive device. The wavelengths λ_1, λ_2 are practical limits of the response $S_p(\lambda)$. The above integral is evaluated

---

[*] Typical Absolute Spectral Response Characteristics of Photoemissive Devices, ITT Components and Instrument Laboratory.
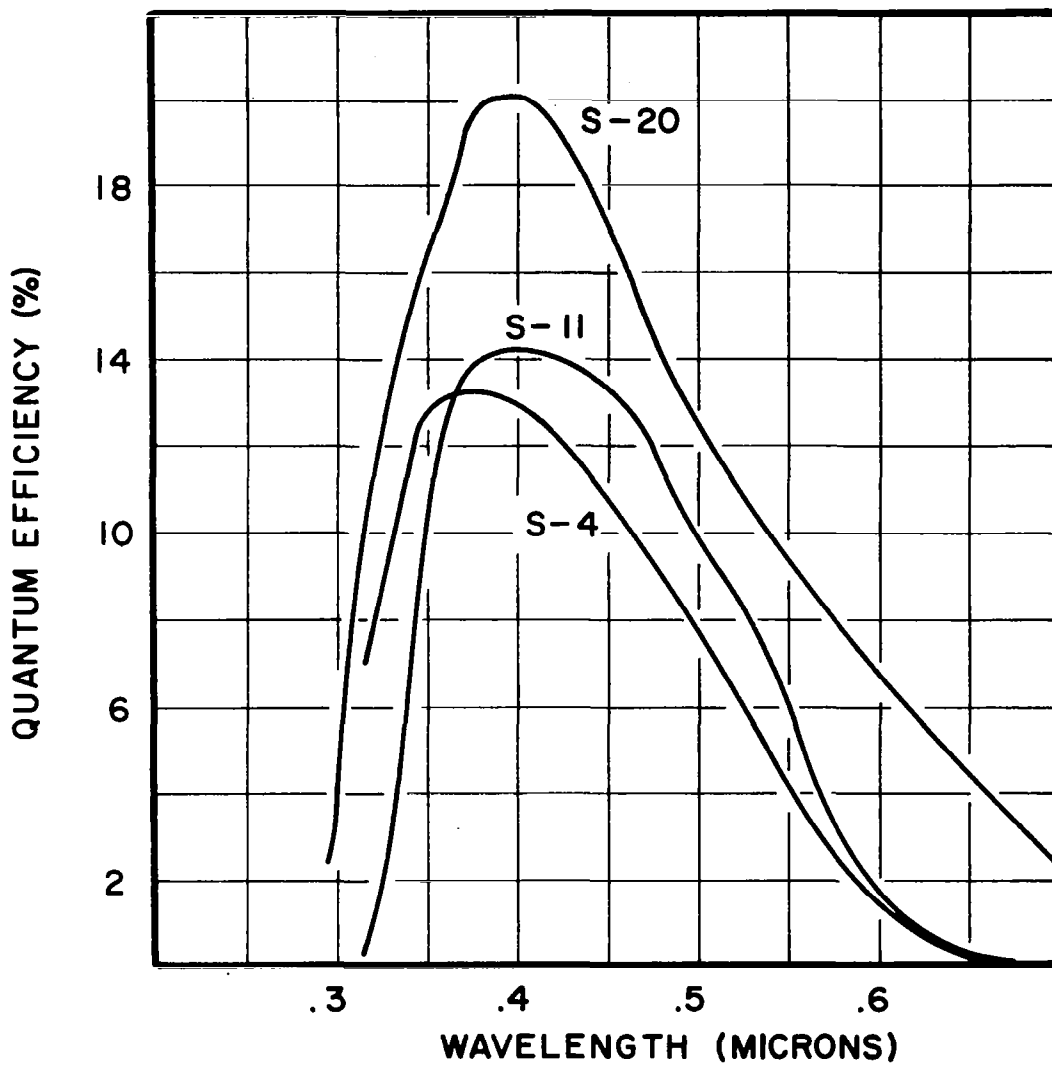
FIGURE 12: SPECTRAL RESPONSE OF PHOTOEMISSIVE
DEVICES

approximately by means of Simpson's rule with an interval length of .02 micron Note that absolute values are given in V.B for an S-4 response and a Type Ao star.

Since Ao stars are frequently detected with S-4 photodetectors it is convenient to evaluate the relative intensity and magnitudes:

$$F^*(C,P) = \frac{F(C,P)}{F(Ao, S-4)}$$

$$M^*(C,P) = -2.5 \ \log_{10} F^*(C,P)$$

These values are graphed in Figures 13 and 14.

Suppose stars of spectral class c_1 and c_2 are viewed by photoemissive surfaces p_1 and p_2, respectively. The ratio of their intensities is

$$\frac{F^*(C_1,P_1)}{F^*(C_2,P_2)} = \frac{F(C_1,P_1)}{F(C_2,P_2)}$$

and their difference in magnitude is

$$M^*(C_1,P_1) - M^*(C_2,P_2) = -2.5 \ \log_{10} \frac{F^*(C_1,P_1)}{F^*(C_2,P_2)}$$
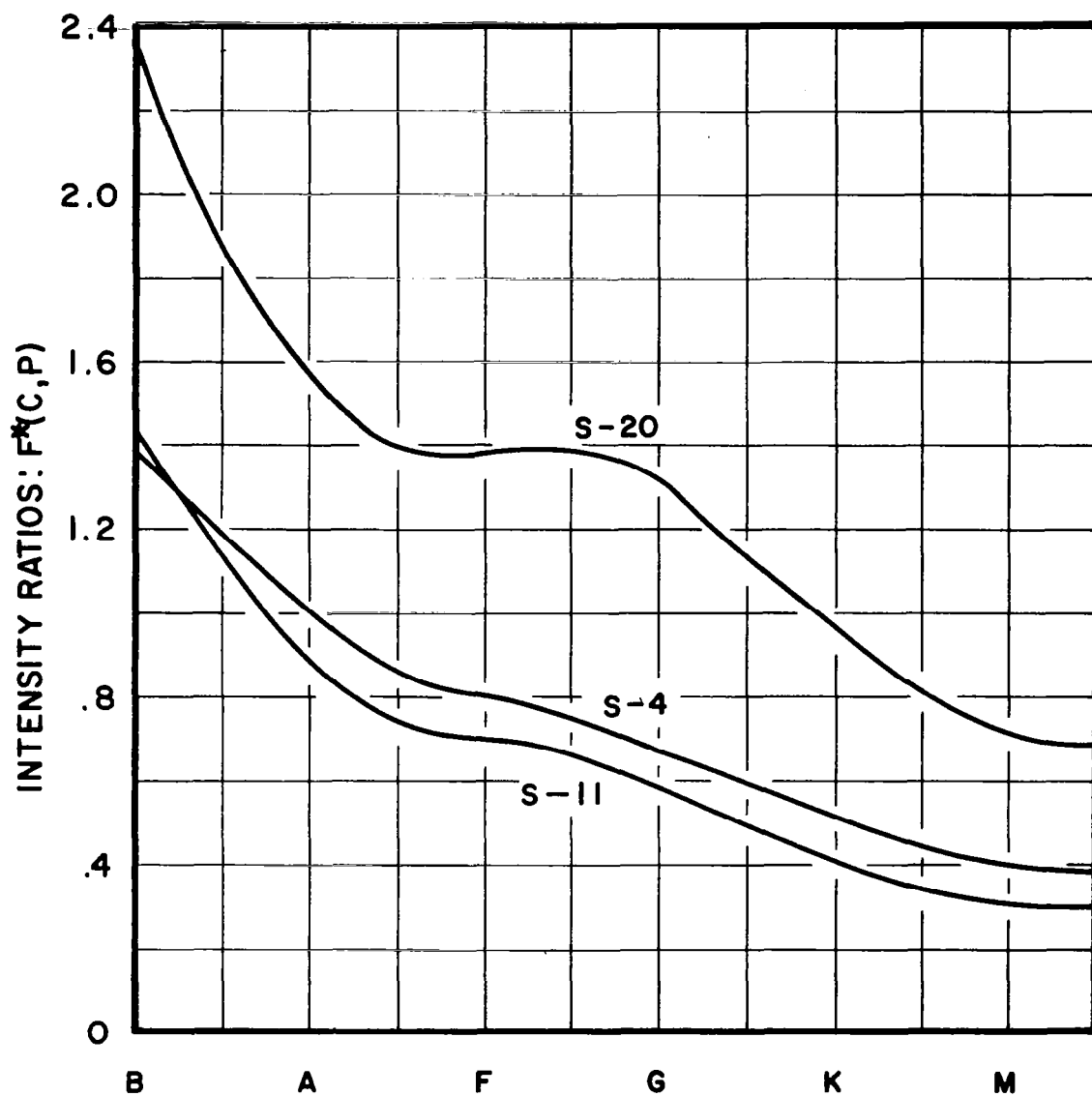
FIGURE 13: INTENSITY RATIOS AS A FUNCTION OF
SPECTRAL CLASS (C) AND PHOTOEMISSIVE
SURFACE (P)
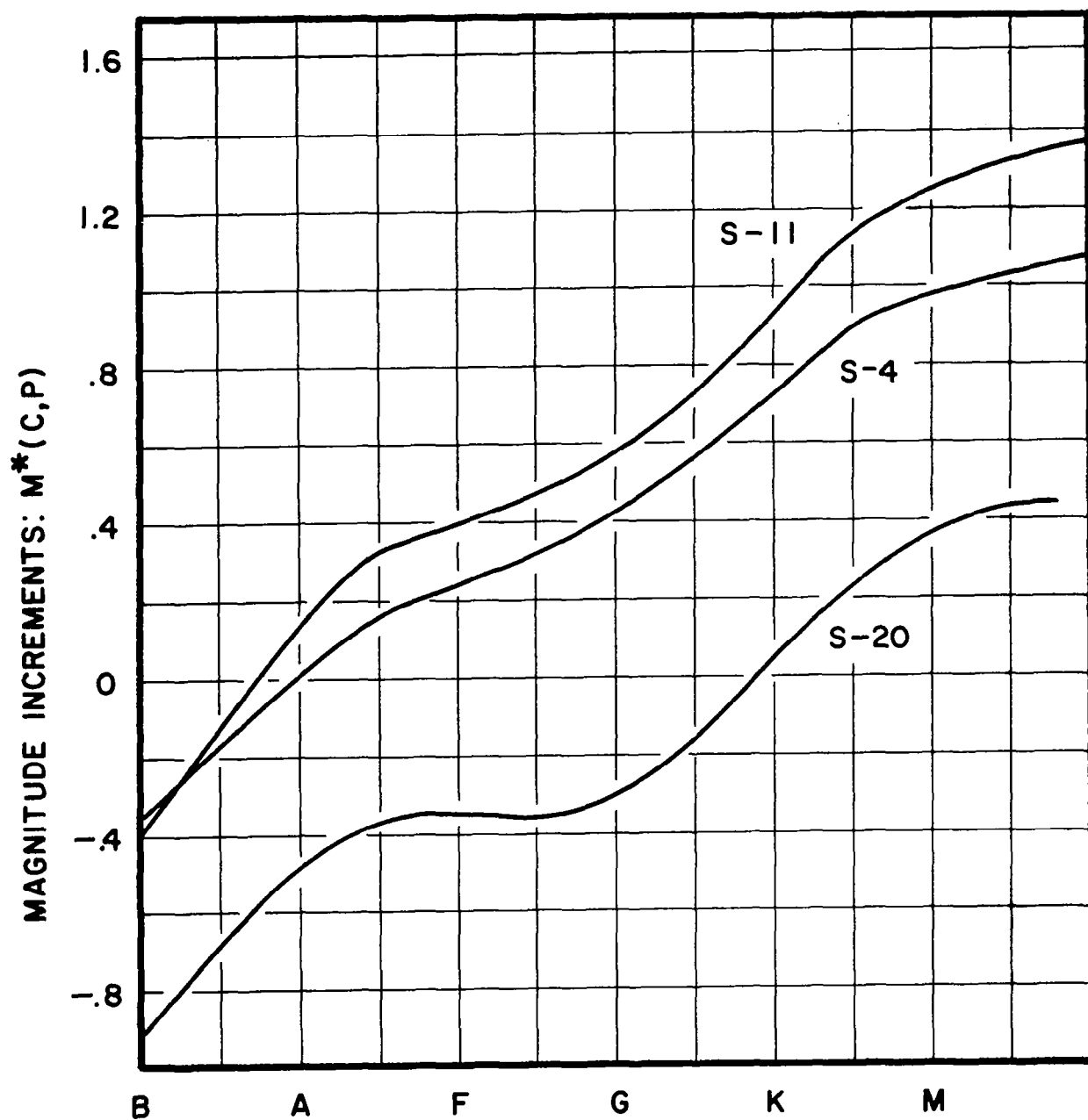
FIGURE 14 : MAGNITUDE INCREMENTS AS A FUNCTION OF
SPECTRAL CLASS (C) AND PHOTOEMISSIVE
SURFACE (P)

III. STELLAR BACKGROUND RADIATION

A. Introduction

A celestial frame of reference can be obtained by observing star transits through a scanning slit. The characteristics of such systems with respect to star detection and location have been previously investigated by Farrell and Zimmerman.[*] This section is primarily concerned with developing models for the stellar background noise in such systems.

In particular, the scanning system consists of lens, slotted reticle, and photomultiplier. A star field is focussed on the reticle, which is fixed relative to the lens and photomultiplier. The entire system rotates; consequently the star field moves across the slit. See Figure 1. The following results apply equally to systems in which the reticle moves, with a fixed lens and photomultiplier.

As the star field moves across the slit, the amount of radiation reaching the photomultiplier fluctuates, with a corresponding variation in its output. The output from a bright star represents a "signal"; the output from weak stars represents background "noise." See Figure 2. The background noise has two components: photon noise and spatial noise. The photon noise results from the quantum character of the photoelectric emissions. The spatial noise results from scanning the random spatial distribution of weak stars.

Other sources of interferring radiation include zodiacal light and airglow. Zodiacal light is sunlight reflected by meteoric material and by dust grains

---

[*] Farrell, E. J. and C. D. Zimmerman (1965).
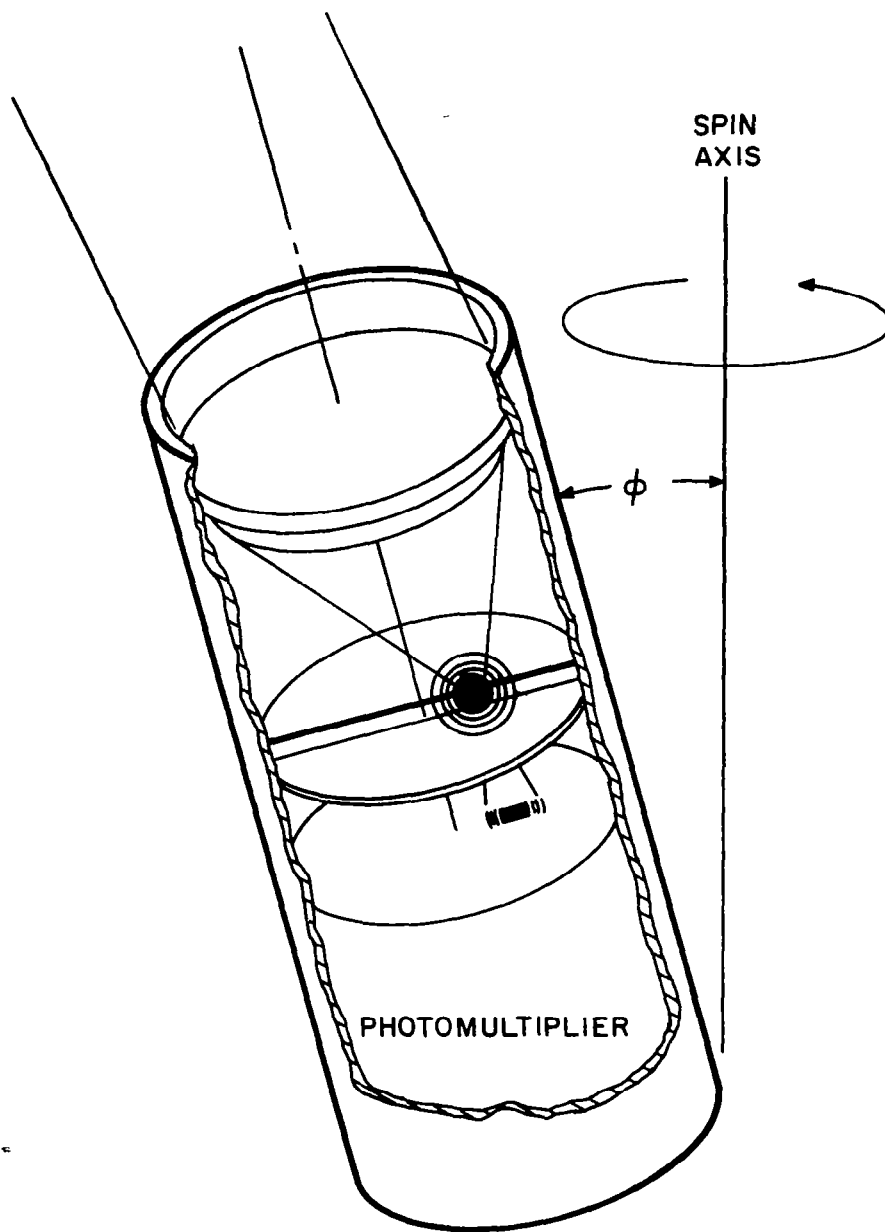
SPIN
AXIS

ϕ

PHOTOMULTIPLIER

FIGURE I: SCANNING SYSTEM

SLIT

MOTION OF

STAR FIELD

FIELD OF VIEW

RADIATION TRANSMITTED BY SLIT

BRIGHT STAR

TIME

SPATIAL NOISE

SIGNAL

SPATIAL NOISE
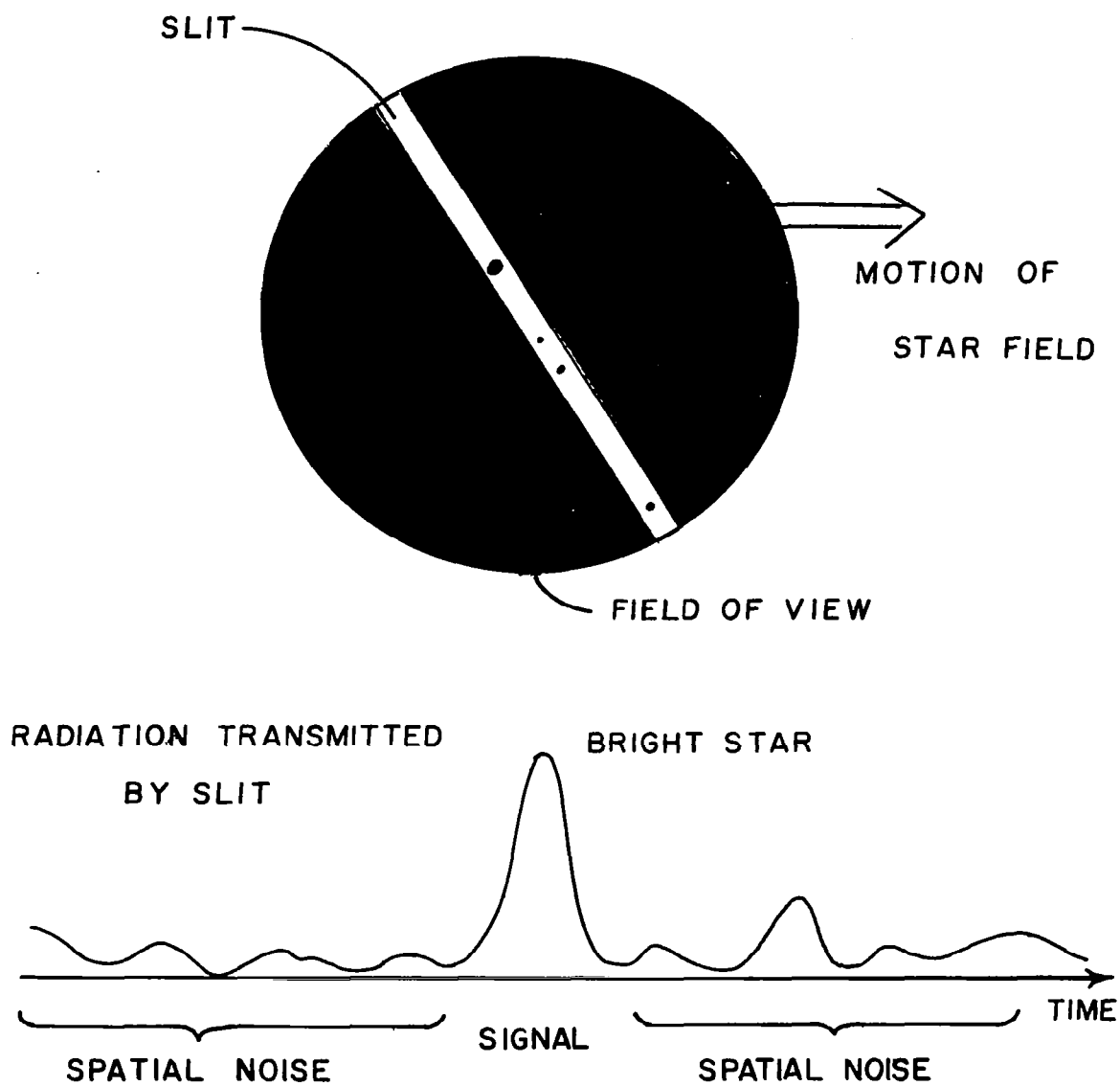
FIGURE 2: NOISE MODEL

of uncertain origin, which form a ring around the sun in the ecliptic plane. Measured in units of equivalent tenth magnitude stars per square degree zodiacal light varies from 30,000 (points near the sun) to 160 (points away from the sun).[*] Airglow is an illumination suffused over the sky which originates in the atmosphere and occurs mainly at altitudes of from 60 to 120 miles. The most intense radiation appears to be in the infrared. Airglow places a limit on the faintest celestial objects that can be detected photo-electrically and photographically from the surface of earth. In the total night sky radiation (no moon present), the contributions from zodiacal light and airglow have been estimated to be as much as 65 percent.[**] Special techniques must be used to minimize the effect of this radiation for scanning systems which encounter the earth's atmosphere and the ecliptic plane.

A basic problem is to discriminate between the desired signals and un-desired signals from the background. The optimum detection technique depends on the characteristics of the signals. In scanning optical systems, we en-counter three operating situations.

In the first situation, the detection technique must discriminate against "false" star detections, i.e., detections resulting from dark current, zodiacal light, "very weak" stars (stars with intensities several stellar magnitudes below that of the weakest star of interest), and radiation from the atmosphere, when observations are made from Earth. The sporadic detections of "weak"

---

[*]   Allen, C. W. (1963), p. 159.

[**] Chapman, R. M. and R. O'B. Carpenter (1959).

stars (i.e., stars with stellar magnitudes near that of the weakest star of interest) are acceptable in this operating situation. The optimum technique maximizes the probability of detecting the weakest star of interest with a fixed probability of detecting a false star. Several detection techniques for this situation are described in Subsection VI.B. The expected number of false star detections in one scan period is approximately equal to the product of (1) the number of "slit positions" in one scan and (2) the probability of detecting a false star. In this section we are primarily interested in the second and third operating situations.

In the second operating situation, the detection technique must discriminate against weak stars. False star detections can be neglected. The stars of interest are relatively bright. Hence, weak star detections are widely spaced in time and are statistically independent. The optimum technique maximizes the probability of detecting the weakest star of interest with a fixed probability of detecting the brightest weak star that we must discriminate against. Detection techniques for this situation are described in Subsection VI.B. The optimum technique uses a holding filter, i.e., a filter with a rectangular impulse response. If the filter output exceeds a pre-assigned threshold, a star is present. In the following paragraphs (Subsections B, C, D, and E) we develop two models for the weak star background, and determine the expected number of weak star detections in one scan period. A holding filter is used.

In the third operating situation the detection technique must discriminate against weak stars; but in this case, the detections are not independent.

The stars of interest are relatively weak. The primary cause of variability in the photomultiplier output (in the absence of a bright star) is the variability in the spatial distribution of weak stars. In this situation the goal is to select a detection filter that maximizes the ratio of the output signal level to output rms noise level. Detection techniques for this situation are described in Subsection VI.B. In the following paragraphs (Subsections F and G), we describe the characteristics of the background noise in the filter output. The dependence of spatial noise on the slit width and optical resoultion is derived; also the magnitude of the photon noise and spatial noise are compared. A similar problem has been studied for scanning photographic plates.[*] Because of the random variations in granularity across the plate, one obtains a scanning noise like that obtained in scanning a stellar background. On the other hand, there are several differences. In photographs the "elements" one scans are the photographic grains, which are opaque with sharp edges. Also, the scanning aperture is generally circular; photon noise is neglected. When scanning photoelectric star images, the basic elements are nebulous due to optical aberrations. Also, the aperture is rectangular and photon noise is very significant.

---

[*]   For a more complete discussion see O'Neil, E. L., (1963), pp. 109-121.

B.   Weak Star Background: Statistical Model

In this subsection we will describe a statistical model of the weak star background for the second operating situation described above. Weak star detections are widely separated in time and are statistically independent. False star detections can be neglected. Also we assume that the detection filter has a rectangular impulse response. In addition to the weak stars, the background radiation has a homogeneous component from the very weak stars. The homogeneous component varies across the celestial sphere. In the next subsection, C, we will describe a "simulation model" of the background using the same assumptions. In evaluating the expected number of star detections in one scan, we assume a statistical distribution for the weak stars. In subsection C, however, a star map determines the affect of the weak stars.

Let a two-dimensional surface S have points distributed at random with intensity function $v_s(\theta, \phi)$. The probability of N points being contained in $S_1 \subseteq S$ is

$$e^{-\mu(S_1)} \frac{\mu^N(S_1)}{N!}$$

where

$$\mu(S_1) = \iint_{S_1} v_s(\theta, \phi) \, d\theta \, d\phi$$

Also, the number of points in non-overlapping areas are independent random variables.

For our applications, S will be a unit sphere representing the galactic sphere (equator coincides with the Milky Way) and ν_s will depend only on galactic latitude.[*] In this section, ν_s will be latitude symmetric. However, in Subsection C, latitude asymmetries are introduced in the homogeneous component. The field of view of the scanning system in general is a spherical cap with the center deleted. See Figure 3.

Let $N(\theta_s)$ be the number of points encountered by scanning through an angle θ_s. See Figure 3 for definitions. We will show that $N(\theta_s)$ is a non-homogeneous Poisson process.[**] There are five conditions that must be satisfied for this to be true.

(0) $N(0) = 0$ because of the definition of N.

(1) $N(\theta_s)$, $\theta_s > 0$ has independent increments since for

$0 < \theta_1 < \theta_2 < \theta_3 < \theta_4$, $S(\theta_4 - \theta_3)$ $S(\theta_2 - \theta_1)$ are non-overlapping areas. See Figure 3 for the definition of $S(\theta)$.

(2) For $\theta_s > 0$, $0 < P[N(\theta_s) > 0] < 1$ since $P[N(\theta_s) > 0] = 1 - e^{-\mu_s}$ where

$$\mu_s = \iint\limits_{S(\theta_s)} \nu_s(\theta, \varphi)\, d\theta\, d\varphi \quad > 0$$

(3) For simplicity, let $\mu(\theta_s) = \mu(S(\theta_s))$. If

$$\mu^*(\Delta\theta) = \mu(\theta_s + \Delta\theta) - \mu(\theta_s)$$

---

[*] See Trumpler, R. J. and H. F. Weaver, (1953), Chapter 5.1.

[**] Parzen, E., (1962), Chapter 4.
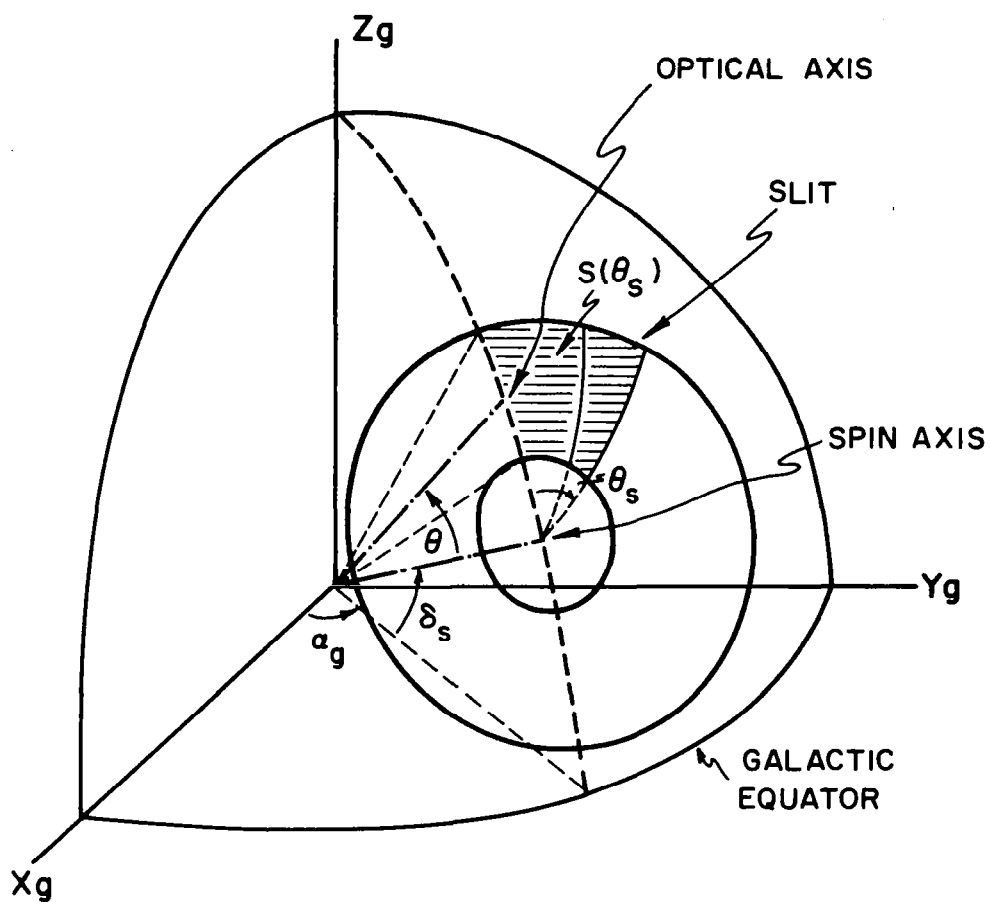
FIGURE 3 : A CONICAL SCAN ON THE GALACTIC SPHERE

then
$$\lim_{\Delta\theta\to 0} \frac{P\left[N(\theta_s+\Delta\theta)-N(\theta_s)\geq 2\right]}{P\left[N(\theta_s+\Delta\theta)-N(\theta_s)=1\right]}$$

$$=\lim_{\Delta\theta\to 0} \frac{1-e^{-\mu^*(\Delta\theta)}\left[1-\mu^*(\Delta\theta)\right]}{e^{-\mu^*(\Delta\theta)}\mu^*(\Delta\theta)}$$

$$=\lim_{m\to 0} \frac{1-e^{-m}(1+m)}{m\,e^{-m}}=0$$

$$(4)\quad \lim_{\Delta\theta\to 0}\frac{1-P\left[N(\theta_s+\Delta\theta)-N(\theta_s)=0\right]}{\Delta\theta}=\lim_{\Delta\theta\to 0}\frac{1-e^{-\mu^*(\Delta\theta)}}{\Delta\theta}$$

$$=\lim_{\Delta\theta\to 0} e^{-\mu(\theta_s+\Delta\theta)}\frac{e^{\mu(\theta_s+\Delta\theta)}-e^{\mu(\theta_s)}}{\Delta\theta}$$

$$=e^{-\mu(\theta_s)}\frac{d}{d\theta_s}e^{\mu(\theta_s)}$$

$$=\mu'(\theta_s)$$

Thus, the mean of the process $N(\theta_s)$ is

$$\mu(\theta_s)=\iint_{S(\theta_s)}\nu_s(\theta,\varphi)\,d\theta\,d\varphi$$

$\nu_s(\theta,\phi)$ depends on the magnitude of the point source. For the sake of analytic simplicity $\nu(z)=\nu_s(\theta,\sin^{-1}z)$ has been assumed to be quadratic in z. In particular, let ν_M and ν_b be the functions describing the densities of stars of magnitude M and the homogeneous background respectively. By a star of magnitude M we mean any star with magnitude between $M-\frac{1}{2}$ and $M+\frac{1}{2}$.

One of the fundamental quantities to determine is the probability of

detecting a star of magnitude M. The probability of detecting an Mth magnitude star when the star occurs at angle θ in the scan plane is

$$P_M(\theta) = \sum_{n \geq \tau} \frac{\bar{\mu}_M^n(\theta)}{n!} e^{-\bar{\mu}_M(\theta)}$$

where

$$\bar{\mu}_M(\theta) = \alpha \varepsilon_q \varepsilon_o \lambda_M H_{max} + \alpha \varepsilon_q \varepsilon_o \lambda_{10} \gamma_b(\theta) T_f + T_f \cdot \lambda_d \alpha$$

α = fraction of photoelectric pulses transmitted by a threshold clamp

ε_q = quantum efficiency of photomultiplier

ε_o = optical efficiency of lens system

λ_M = number of photons per second being received from an Mth magnitude star at the photocathode

   = $(5.06 \times 10^6) e^{-.921 \cdot M} \cdot D^2$

D = diameter of aperture in inches

$H_{max} = \max_t (H(t))$

H(t) = output of holding filter relative to the rate at which pulses are being received

T_f = time duration of holding filter

T_s = time for star to cross slit

λ_d = rate at which noise pulses are being generated by the photomultiplier

$$\gamma_b(\theta) = \mu_b(\theta + \theta_{sw}/2) - \mu_b(\theta - \theta_{sw}/2)$$

$$\mu_b(\theta) = \iint_{S(\theta)} \nu_b \, d\sigma$$

θ_{sw} = slit width

A diagram of the detection electronics is presented in Figure 4. The output of the photomultiplier is a sequence of pulses with random amplitudes and separations. Since the amplitude variations do not contain information about the stars, the output pulses are clamped to a fixed level when they exceed a minimum amplitude. A detailed discussion of this technique is given in Subsection VI.B.

Let $\nu_M(\theta) = \mu_M'(\theta)$ be the intensity of the non-stationary Poisson process which describes the number of Mth magnitude stars crossed while scanning through an angle θ. Then $P_M(\theta) \cdot \nu_M(\theta)$ is the intensity of a non-stationary Poisson process which describes the number of star detections while scanning through an angle θ. Thus, the expected number of Mth magnitude star detections in one scan is

$$\int_0^{2\pi} P_M(\theta) \, \nu_M(\theta) \, d\theta$$

A numerical method of integration will be used to evaluate this latter integral. See Subsection D.1.

An alternative and more exact approach can be used to find the expected number of star detections. We propose to use a star map which includes all
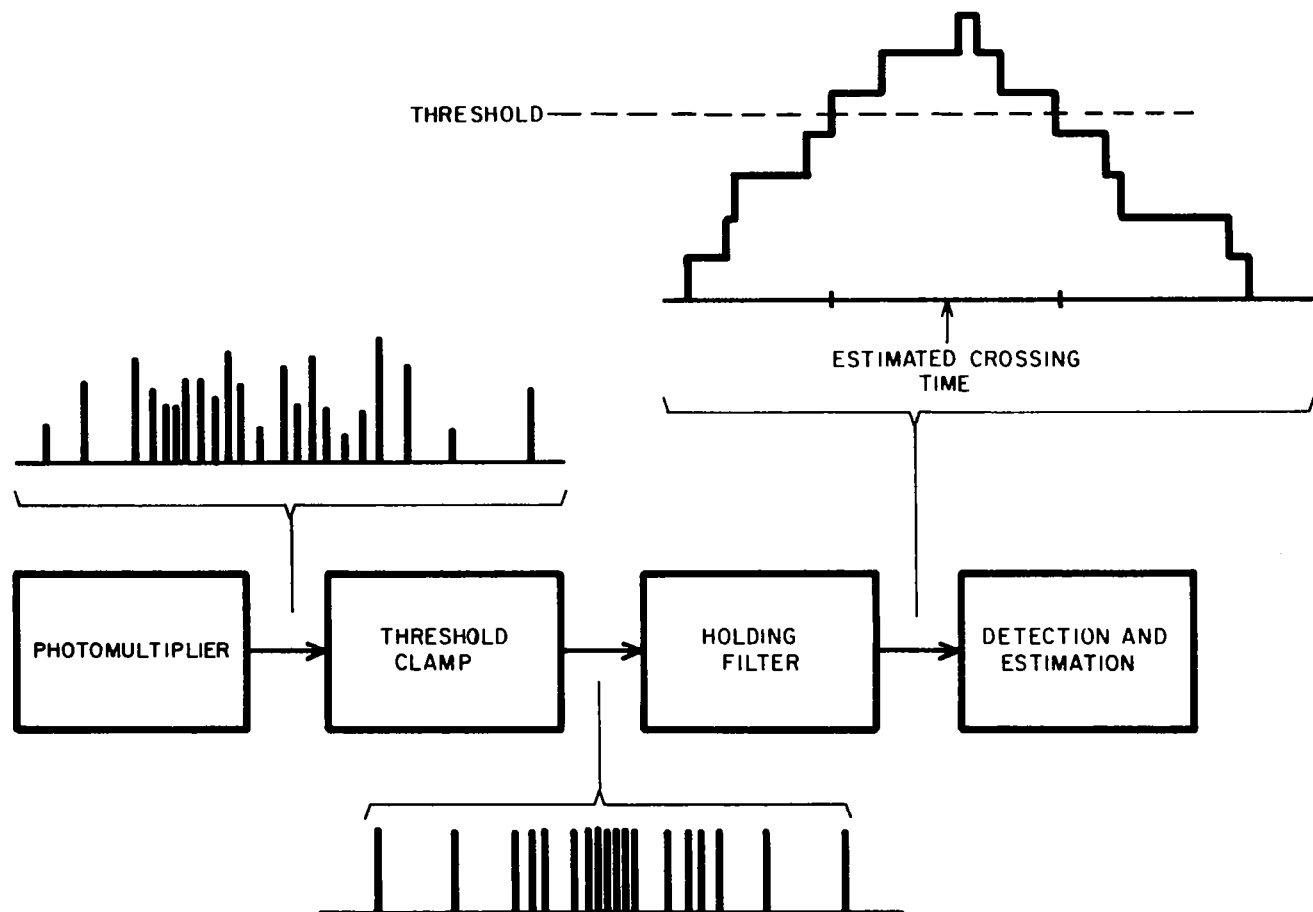
FIGURE 4: PROCESSING SYSTEM

stars of photographic magnitude 7.5 and brighter along with their position.

See Subsection E.1 for star map information. To find the expected number of

star detections, we simply sum their probabilities of detection.

C. Weak Star Background: Simulation Model

In many applications of a conical scanner, the sensor remains at essentially the same galactic longitude for many scans. In this case, the averaging effect of the strip type scan is not exhibited and a stored star map is necessary to evaluate the effect of weak stars on the number of detections.

The following model is used to evaluate the weak star component. The system parameters and data handling capability define a limiting magnitude (M_L). We wish to detect all stars brighter than M_L and to keep other detections resulting from stars with magnitude greater than M_L smaller than some number specified by the data handling capability of the system. If we detect a limiting star with probability .9, any star of magnitude larger than $M_L + 2$ would have essentially zero probability of detection. We, thus, assume that all stars of magnitude greater than $M_L + 2$ form the homogeneous component of the background and that the weak stars have magnitudes between M_L and $M_L + 2$.

In practice, we initially assume that all stars of magnitude greater than 7.5 form the homogeneous component. Our stored star map includes all stars of photographic magnitude smaller than 7.5 ordered by magnitude; a total of 15173 stars. Once a limiting magnitude has been determined, the homogeneous component of the background is adjusted so as to include all the weak stars with magnitude between $M_L + 2$ and 7.5. Probabilities of detection are then computed on the basis of this adjusted homogeneous component.

FLOWCHART

Input

System Parameters
Program Constants
Star Map

Pointing Direction
Specified in Galactic
Direction Cosines

From Limiting
Magnitude Construct
a New Set of Homogeneous
Background Density
Points

I = LST where
LST is the Index of
the First Weak Star

Is Star I in the
Field of View

Compute Background
for Weak Star

Yes

Compute Probability
of Detection

Cumulatively Sum
These Probabilities

No

Is List
Exhausted

No

I = I + 1

Yes

Return to Main
Program

1. Coordinate Transformation

Let $F(z_g)$ be the function describing the homogeneous background. $z_g = \sin \phi$ where ϕ is the galactic latitude. For a particular scanning system we wish to determine the homogeneous background entering the slit at an arbitrary position in the scan.

Let ϕ_L and ϕ_H be lower and upper limits on the scanned region. I.e.,

$$\phi_L = \phi - \frac{FOV}{2}$$

$$\phi_H = \phi + \frac{FOV}{2}$$

where FOV is the field of view (see Figures 3 and 5). Two successive rotations will place the spin axis on one of the coordinate axes. The required transformation is

$$\begin{pmatrix} x_g \\ y_g \\ z_g \end{pmatrix} = \begin{pmatrix} \cos \delta_g \cos \alpha_g & -\sin \alpha_g & -\cos \alpha_g \sin \delta_g \\ \sin \alpha_g \cos \delta_g & \cos \alpha_g & -\sin \alpha_g \sin \delta_g \\ \sin \delta_g & 0 & \cos \delta_g \end{pmatrix} \begin{pmatrix} x \\ y \\ z \end{pmatrix}$$

Thus, the homogeneous background as a function of the angle θ_s and slit width SW is
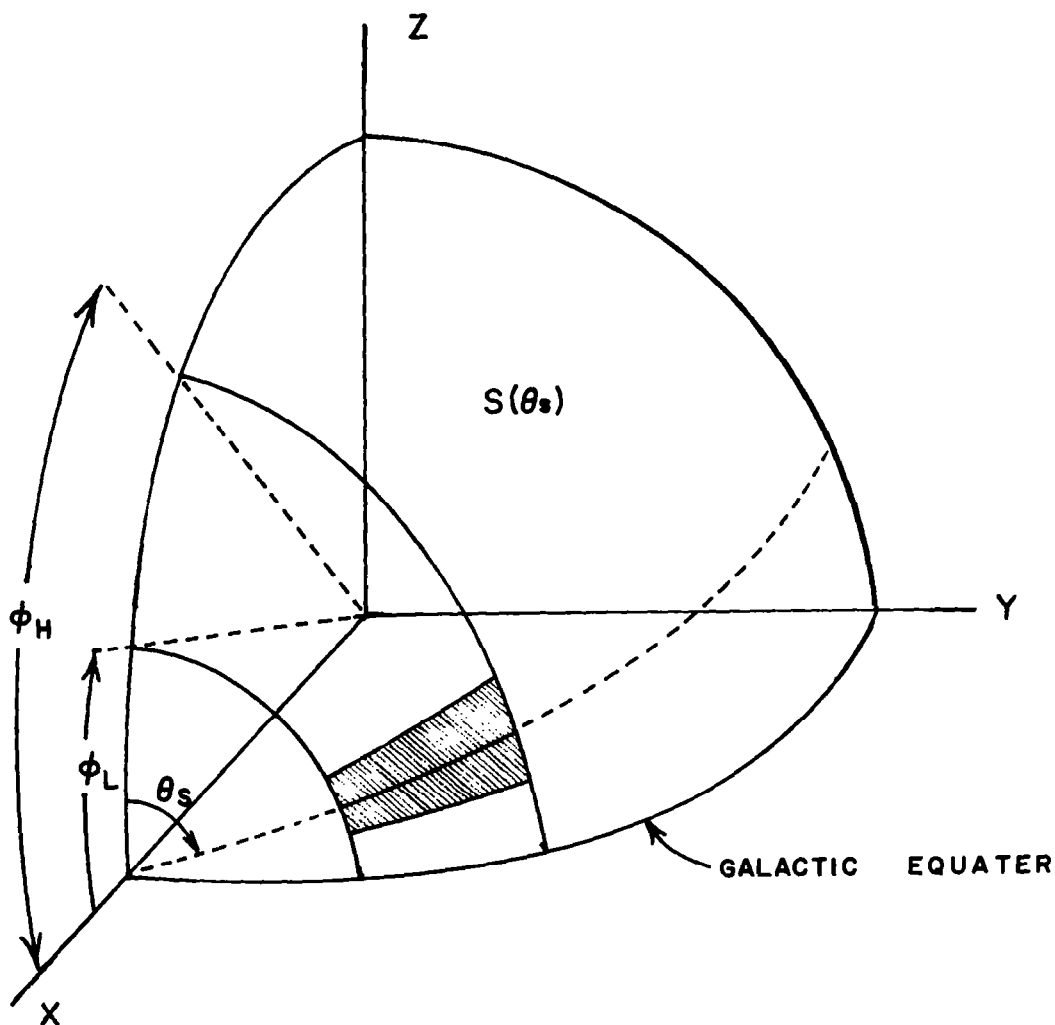
FIGURE 5 : RESULT OF ROTATION THROUGH
ANGLES α_g AND δ_g

$$\mu_{sw}(\theta_s) = \iint\limits_{S_{sw}(\theta_s)} F(z_g)\,d\sigma = \int\limits_{|\theta_s|-\frac{sw}{2}}^{|\theta_s|+\frac{sw}{2}} \int\limits_{\phi_L}^{\phi_H} F(x\sin S_g + z\cos S_g)\cdot \sin\phi\,d\phi\,d\theta.$$

where $x = \cos\phi$

$y = \sin\phi\sin\theta$

$z = \sin\phi\cos\theta$

$0 \le |\theta_s| \le \pi$

$0 < \phi_L < \phi_H \le \pi$

Since SW is very small (a few minutes of arc) relative to the field of view

$$\mu_{sw}(\theta_s) \doteq SW\cdot \int\limits_{\phi_L}^{\phi_H} F(\cos\phi\sin S_g + \sin\phi\cos\theta_s\cos S_g)\cdot\sin\phi\,d\phi.$$

The latter integral is evaluated numerically using Simpson's rule with approximately 1.75 points per degree.

2. Determination of Reference Angle θ_c

Figure 6 shows the geometrical relationship between the necessary vectors to determine the angle (θ_c) at which a star occurs in the scan.

The galactic sphere is assumed to have radius one. Thus $\hat{s}_t$ and $\hat{s}_p$ are unit position vectors of the star and spin axis respectively. $\vec{r}_1$ is a vector in the z_g direction. $\vec{r}_2$ is a vector orthogonal to $\hat{s}_p$ and in the plane of $\hat{s}_p$ and $\hat{s}_t$. Hence,
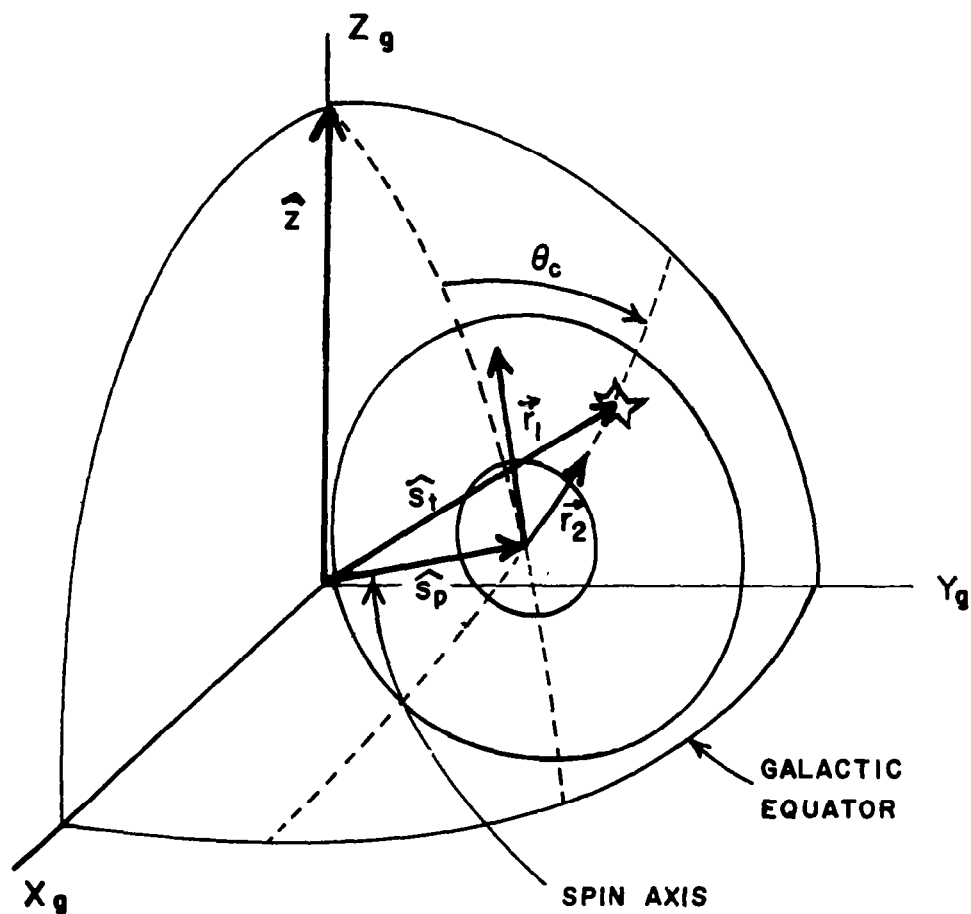
FIGURE 6: VECTORS NECESSARY TO DETERMINE

REFERENCE ANGLE θ_c

$$\vec{r_1} = \hat{z} - (\hat{z} \ \hat{s}_p) \hat{s}_p$$

$$\vec{r_2} = \hat{s}_t - (\hat{s}_t \ \hat{s}_p) \hat{s}_p$$

Then

$$\cos \theta_c = \frac{\vec{r_1} \cdot \vec{r_2}}{|\vec{r_1}| \, |\vec{r_2}|}$$

$$= \frac{\hat{z} \cdot \hat{s}_t - (\hat{s}_t \cdot \hat{s}_p)(\hat{z} \ \hat{s}_p)}{\left\{ [1 - (\hat{z} \cdot \hat{s}_p)^2][1 - (\hat{s}_t \cdot \hat{s}_p)^2] \right\}^{1/2}}$$

3. Program Description

The program is an assembly of several subroutines which in several cases use the same constants. To describe some of these constants a description of the star map and homogeneous background construction is necessary.

The star tape contains 15173 stars ordered by photographic magnitude. Each record on the tape contains the general catalog number, photographic magnitude, and the three direction cosines on the galactic sphere. The right handed coordinate system (x_g, y_g, z_g) imposed on the galactic sphere is one in which the z_g axis passes through the galactic north pole and the x_g axis passes through the point of intersection of the galactic and celestial equators which has the smallest celestial right ascension angle (descending node). By the index of a star we mean the position of the star in the magnitude ordered list. Index 1 is the brightest star and index 15173 the dimmest star.

For background purposes the galactic sphere is divided into 21 latitude classes.

Class	Galactic Latitude Range
1	(-90, -85)
2	(-85, -75)
3	(-75, -65)
.	.
.	.
.	.
8	(-25, -15)
9	(-15, -7.5)
10	(-7.5, -2.5)
11	(-2.5, 2.5)

Class	Galactic Latitude Range
12	(2.5, 7.5)
.	.
.	.
.	.
21	(85, 90)

We originally started out with the homogeneous background generated by stars of 7.5 magnitude and weaker. The data used was latitude symmetric and is expressed in number of tenth magnitude stars per square degree. Since the resolution of the system determines the homogeneous background component, the background density list is altered by including in it stars which are brighter than 7.5 magnitude. To augment a group of weak stars to the list, they are first put through a sieve to determine which latitude class they belong in and then their magnitude is converted to an equivalent number of tenth magnitude stars. We thus generate a homogeneous background which is latitude asymmetric.

Definition of Symbols:

NOSTAR

WMAG

GX

GY

GZ : These symbols stand for arrays which hold respectively the star general catalog number, photographic magnitude and the three direction cosines.

DPTSAG : The array giving the number of tenth magnitude stars per square degree for each of the 21 latitude classes.

INDAG : Index of the star list for which DPTSAG is computed. I.e., all stars of magnitude > WMAG(INDAG) are used in determining DPTSAG.

DLBDS

ZLAT   :   These arrays are used only to determine the latitude classes
                and class boundaries.

4.   Description of Subroutines

a.   Call Statement: DPTSCP(PRMAG)

This subroutine updates the star density list for a new limiting magnitude.
PRMAG is the magnitude limit for computing the new background list. All
stars with magnitude > PRMAG are to be included in the list. The subroutine
assumes that it is given an initial density points list. To each of the
21 latitude classes there corresponds a number which represents the equivalent
number of tenth magnitude stars per square degree for that class (array DPTSAG).
Suppose stars of a certain magnitude range are to be added to the density list.
A sieve determines that a given star belongs in latitude class I. The star is
then converted to the equivalent number of tenth magnitude stars. This
number is added to the number in CLSLAT(I). Thus CLSLAT is an array whose
members represent the total number of tenth magnitude stars that are to be
added to the respective latitude classes.

FLOWCHART: UPDATING STAR DENSITY LIST

```
  ⎛ INDAG = Starting ⎞
  ⎜ Index of Present ⎟ ────────┐
  ⎝  Density List    ⎠         │          ┌─────────────────┐
                               ├─────────►│   Set Array     │
  ⎛    PRMAG = New    ⎞        │          │ CLSLAT to Zero  │
  ⎜ Limiting Magnitude⎟ ───────┘          └────────┬────────┘
  ⎜  for Which we     ⎟                            │
  ⎝  Wish to Adjust   ⎠                            ▼
                          ≤                                    >
                          =  ◄─── WMAG(INDAG):   PRMAG ───►

            ┌──────────────────────┐
         ┌─►│  INDAG = INDAG + 1   │
         │  └──────────┬───────────┘
         │             ▼
         │       ╱ INDAG:  15173 ╲ ──── >
         │       ╲               ╱
         │          ≤ ↓ =
         │      ╱                 ╲ ──── >
         │     ╱ WMAG(INDAG): PRMAG ╲
         │     ╲                    ╱
         │          ≤ ↓ =                        ┌──────────────────┐
         │  ┌──────────────────────┐             │  Add WMAG(INDAG)  │
         └──│ Subtract WMAG(INDAG) │             │    to CLSLAT      │
            │    from CLSLAT       │             └─────────┬────────┘
            └──────────────────────┘                       ▼
                                                 ┌──────────────────┐
                                                 │ INDAG = INDAG - 1 │
                                                 └─────────┬────────┘
                                     >                     ▼
                                            ╱ WMAG(INDAG):  PRMAG ╲
                                            ╲                     ╱
            ┌──────────────────────┐                   ≤ =
            │  INDAG = INDAG - 1   │
            └──────────┬───────────┘
                       ▼
            ┌──────────────────────┐
            │   Update Star        │◄───────────
            │   Density List       │
            └──────────┬───────────┘
                       ▼
                  ⎛ Return ⎞
```

III-25
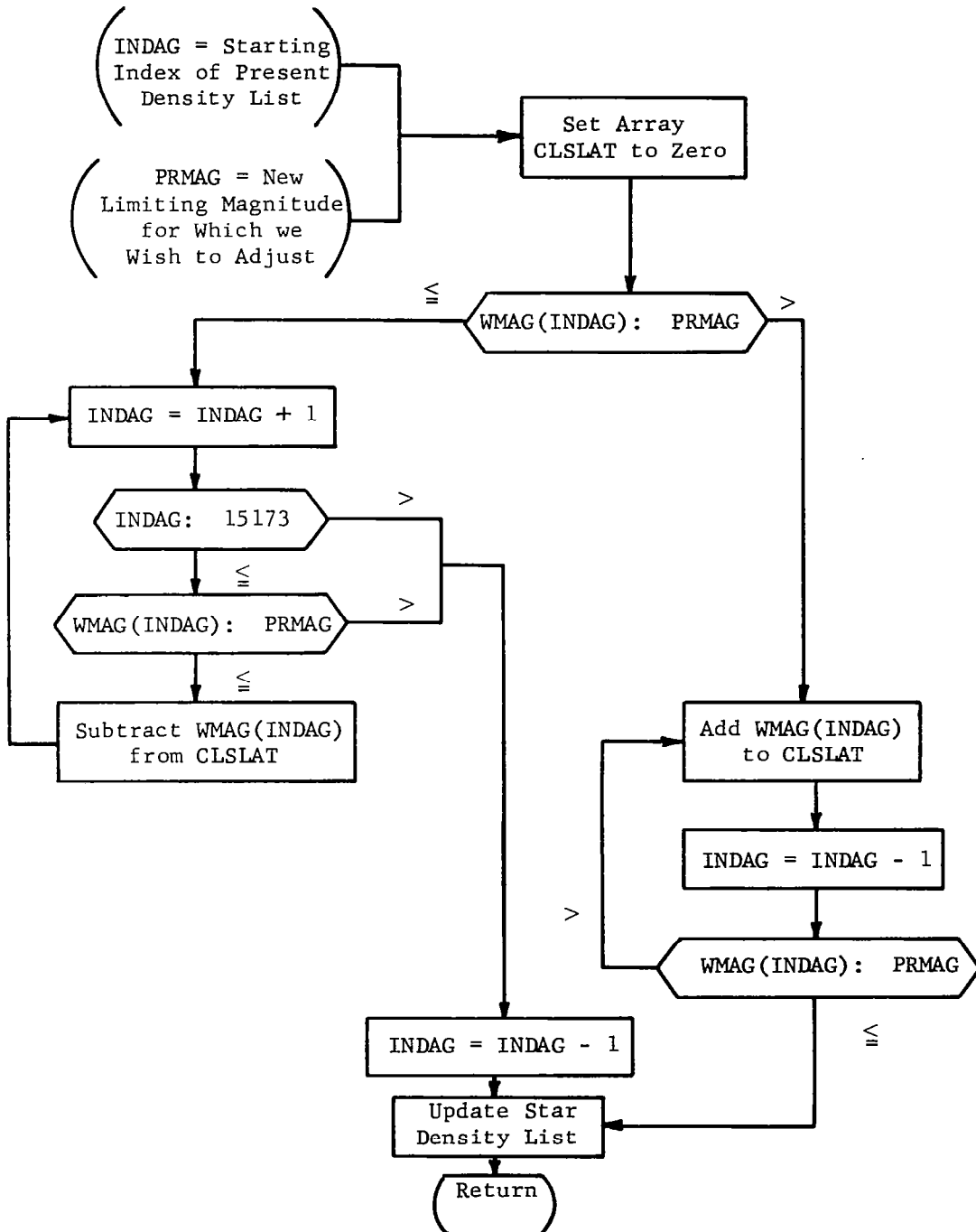
b. Call Statement: DENFN(ZARG, VALUE)

This subroutine interpolates between the points given in DPTSAG. ZARG is

the argument of the function and VALUE is the interpolated value. Given ZARG

the routine determines the latitude class that ZARG belongs to and then chooses

the density point for that class along with the density points on either side.

Thus given the three points $x_1 < x_2 < x_3$ the form of the quadratic interpolating

polynomial due to Lagrange is

$$F(x) = \frac{x-x_2}{x_1-x_2} \cdot \frac{x-x_3}{x_1-x_3} F(x_1) + \frac{x-x_1}{x_2-x_1} \cdot \frac{x-x_3}{x_2-x_3} \cdot F(x_2)$$

$$+ \frac{x-x_1}{x_3-x_1} \cdot \frac{x-x_2}{x_3-x_2} \cdot F(x_3)$$

c. Call Statement: BKGDPD(NUMSTR, PTDIRC, PHIS, PHIL, BKVAL)

This subroutine computes the average homogeneous background passing the

slit when the star with index NUMSTR is being observed. In particular, it

approximates

$$\int_{\phi_L}^{\phi_H} F(\cos\phi \, \sin\delta_q + \sin\phi \, \cos\theta_s \, \cos\delta_q) \cdot \sin\phi \, d\phi$$

by the use of Simpson's rule.

PTDIRC is an array giving the direction cosines of the pointing direction.

PHIS = ϕ_L

PHIL = ϕ_H

BKVAL gives the number of tenth magnitude stars per arc minute passing
the slit.

The other subroutines present in the program are assembly or service routines.

Their function is explained via common statements.

5. Program Usage

The program uses two data input media. A magnetic tape with the star

list and a set of two cards which give the initial values of DPTSAG and INDAG.

All statements through number 35 must be present to compute the necessary

constants and to read in the data. The next ten constants can be altered to

present different systems to the program.

LISTNO = ordered list number of the limiting magnitude star.

LTAU   = detection threshold.

APED   = aperture diameter in inches.

DARK   = number of dark current pulses from the photomultiplier.

TTS   = transit time of star (seconds).

SW   = slit width in minutes of arc.

SPHIS
SPHIL = the smallest and largest angles of the field of view as measured
from the spin axis (degrees).

TRAS
DECA   = celestial right ascension and declination of the spin axis
(degrees).

A program listing appears in E.2.

D. Applications of Models

In this subsection we compare the different background models on the basis of the expected number of star detections in one scan. Two different scanning systems are examined.

1. Strip Type Scan With No Stored Star Map

The basic scanning geometry is shown in Figure 7. The assumption that the density of weak stars of a given magnitude and the homogeneous background can be approximated by quadratic functions enables one to compute most of the resulting integrals analytically. See E.3 for derivations.

The data for homogeneous background and star densities aere taken from Allen.[*] Figure 8 shows the graph of the star background versus the galactic latitude.

Figures 9 and 10 show the relations between the cumulative background, the scan plane angle (θ_s), the scan plane inclination (α), and the field of view (ϕ).

In particular, the quadratic functions used to approximate the homogeneous background and weak star densities are

$$\gamma_b(z) = 128 - 232\, z + 116\, z^2$$
$$\gamma_4(z) = .0188 - .0294\, z + .0157\, z^2$$
$$\gamma_5(z) = .0553 - .0882\, z + .0487\, z^2$$
$$\gamma_6(z) = .151 - .231\, z + .124\, z^2$$
$$\gamma_7(z) = .332 - .372\, z + .156\, z^2$$

[*] Allen, C. W. (1955), pp. 213, 214.
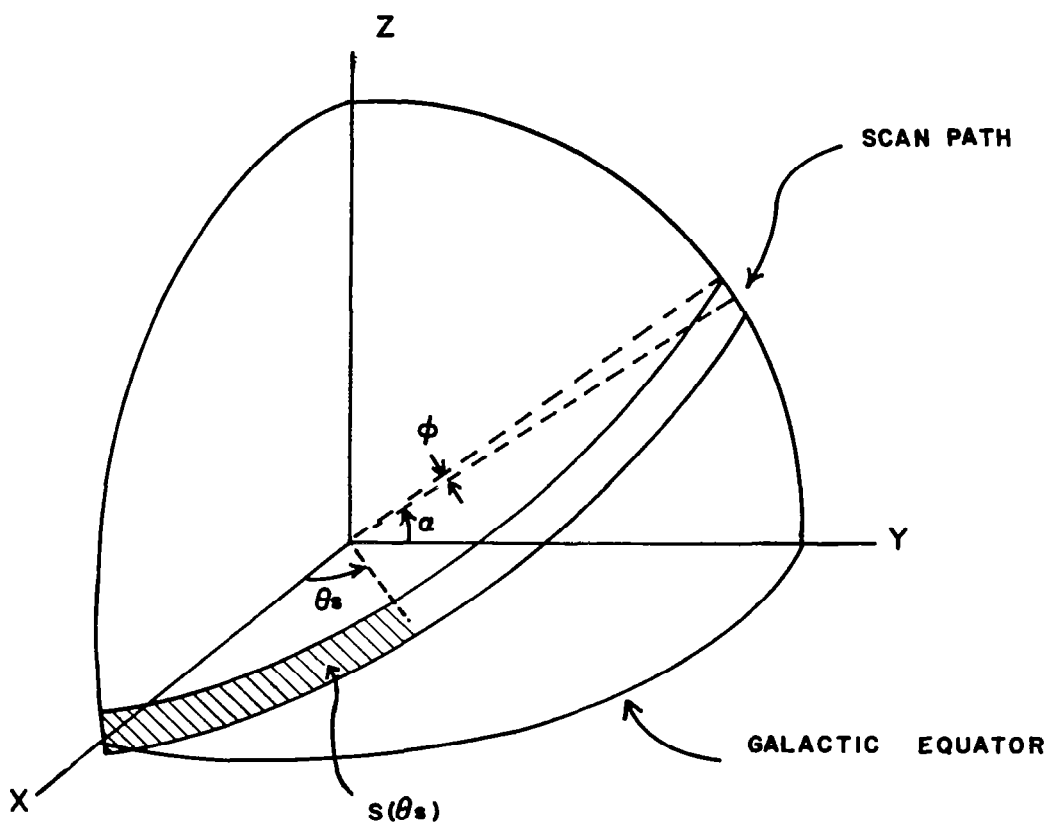
FIGURE 7 : THE GALACTIC SPHERE WITH A STRIP SCAN

BACKGROUND: 7.5 MAGNITUDE AND DIMMER
(NO. OF 10th MAGNITUDE
STARS PER SQ DEG.)

GALACTIC LATITUDE (DEG)
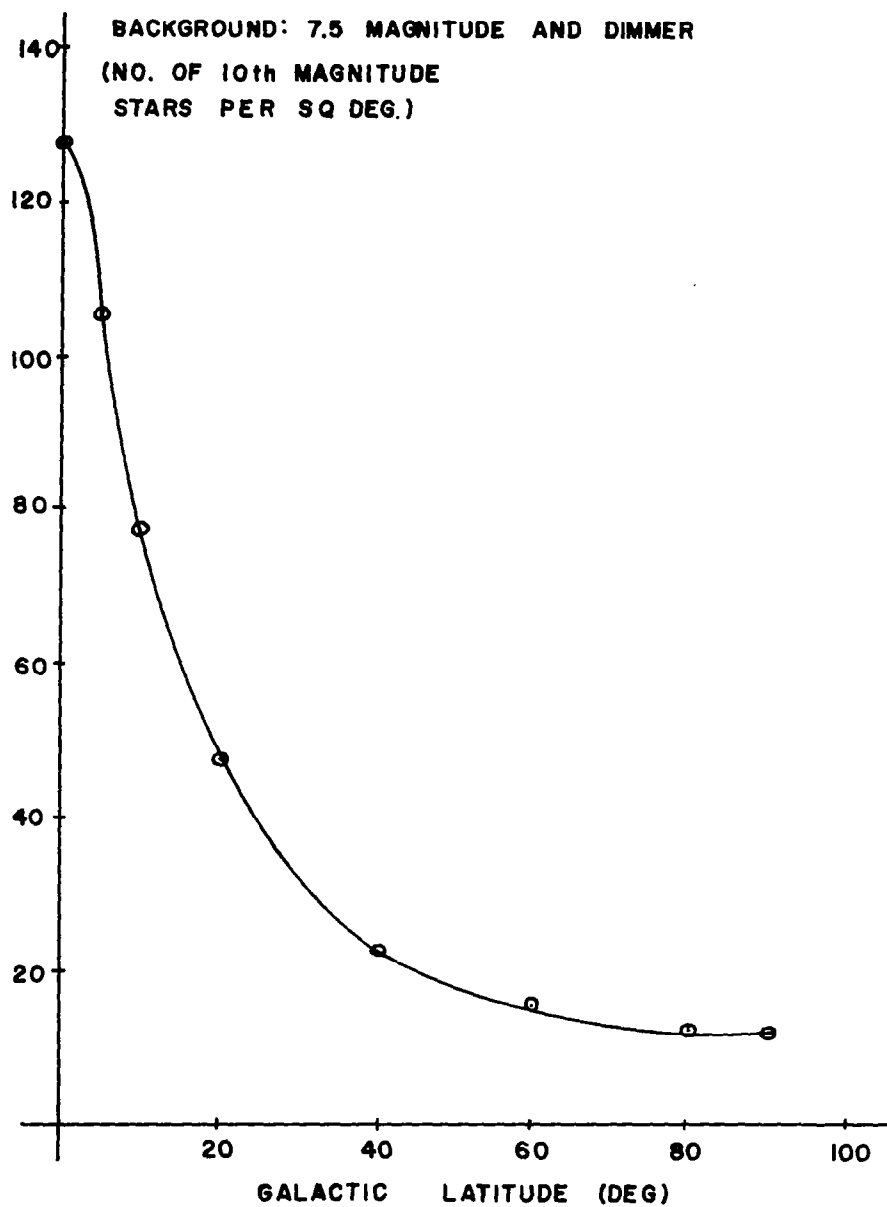
FIGURE 8 : BACKGROUND RADIATION DENSITY
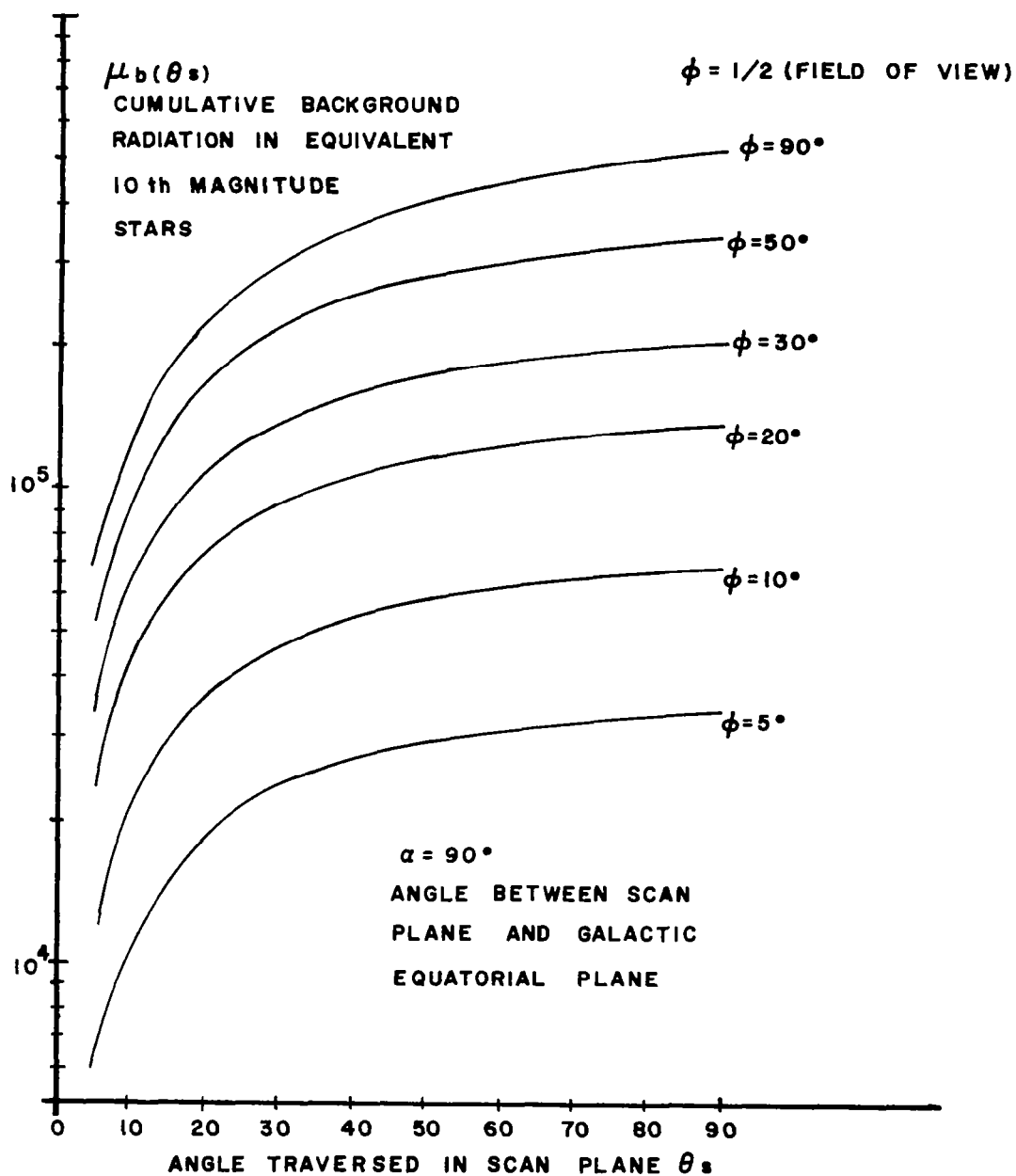
FIGURE 9 : CUMULATIVE BACKGROUND WITH
INITIAL POINT ON GALACTIC EQUATOR
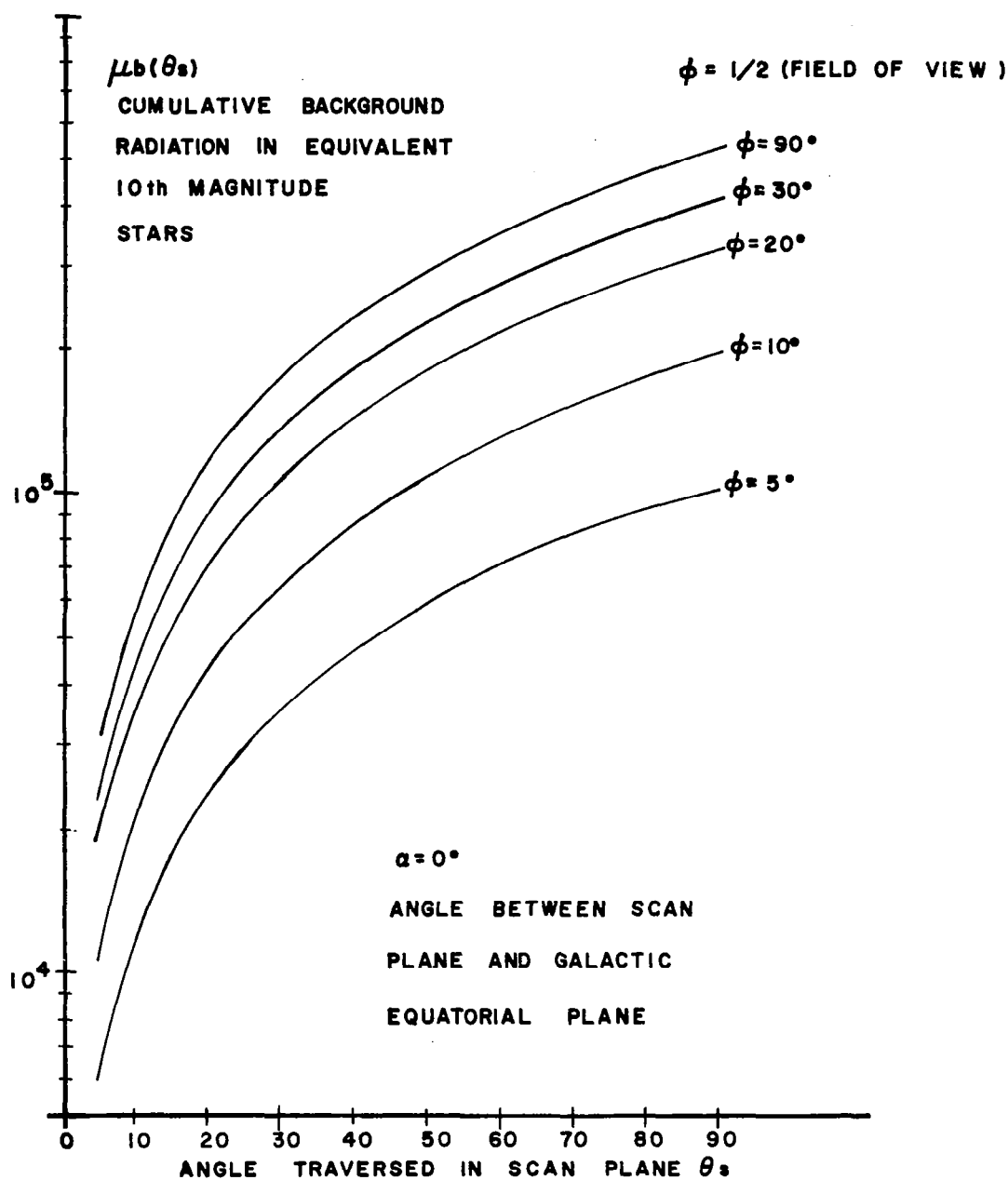
FIGURE 10 : CUMULATIVE BACKGROUND WITH INITIAL POINT ON GALACTIC EQUATOR

where $z = \sin \delta_g$ and δ_g is the galactic latitude.

The system parameters for this example are for a spinning rocket sensor considered by Kenimer, R. L. and T. M. Walsh, (1964).

Aperture diameter: 5.08 inches

Field of View: 6° x 6° rectangular

Optical efficiency: .5

Quantum efficiency: .12

Slit size: 6° x $.015^o$ (8 slits)

Spin rate: 270° per second

The threshold is set so that a third magnitude star occurring in a minimum homogeneous background field will be detected with probability 0.9. The homogeneous background includes all stars of 7.5 magnitude and weaker.

The simulation used pointing direction galactic right ascension and declinations of

$(0^o, 90^o)$

$(0^o, 60^o), (30^o, 60^o), \ldots, (330^o, 60^o)$

$(0^o, 30^o), (30^o, 30^o), \ldots, (330^o, 30^o)$

$(0^o, 0^o), (30^o, 0^o), \ldots, (330^o, 0^o)$

For each pointing direction a star map was searched to find the stars with magnitudes between 3.5 and 7.5 that occurred in the field of view. The slit was then superimposed over the star to determine the homogeneous background component. Finally, the probability of detection was computed. The expected number of weak star detections is the sum of these probabilities. Figure 11 indicates the relationship between the statistical model and the simulation.
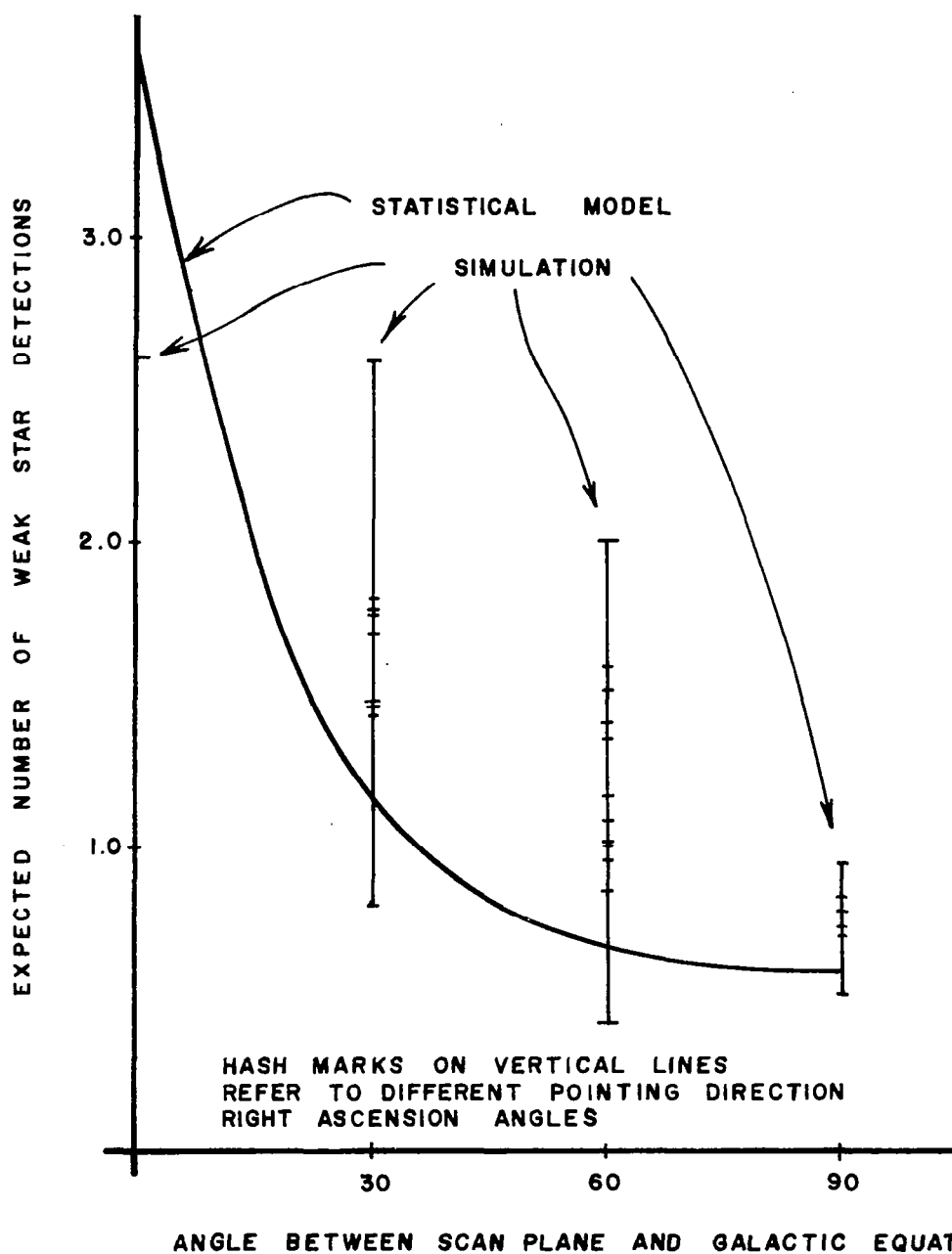
FIGURE II: COMPARISON OF THE STATISTICAL MODEL AND A SIMULATION FOR WEAK STAR DETECTION EXPECTATION

A relatively small computer is needed for the computations involved in the statistical model, whereas, a large amount of storage is needed for the simulation.

2. Comparison to Simple Model

One of the proposed Tiros satellites makes use of a scanning optical system in which the optical axis is inclined 14 degrees from the spin axis. In order to meet accuracy and data handling requirements, the following system and design parameters were chosen:

aperture diameter	.411 inch
scan period	6 seconds
slit width	6 minutes of arc
optical efficiency	.75
photomultiplier	EMR 541A-01-14
dark current equivalent photoelectron rate	2540 per second
quantum efficiency	.15

Figure 12 shows how the statistical simulation model compares with a simple magnitude dependent weak star detection model. This latter model assumes that stars with magnitudes between $M - \frac{1}{2}$ and $M + \frac{1}{2}$ are distributed uniformly over the sphere. The homogeneous background value was taken as the average of the minimum and maximum values as indicated in an integrated star light map which is latitude and longitude dependent.[*]

---

[*] Megill, L. R. and F. E. Roach (1961).
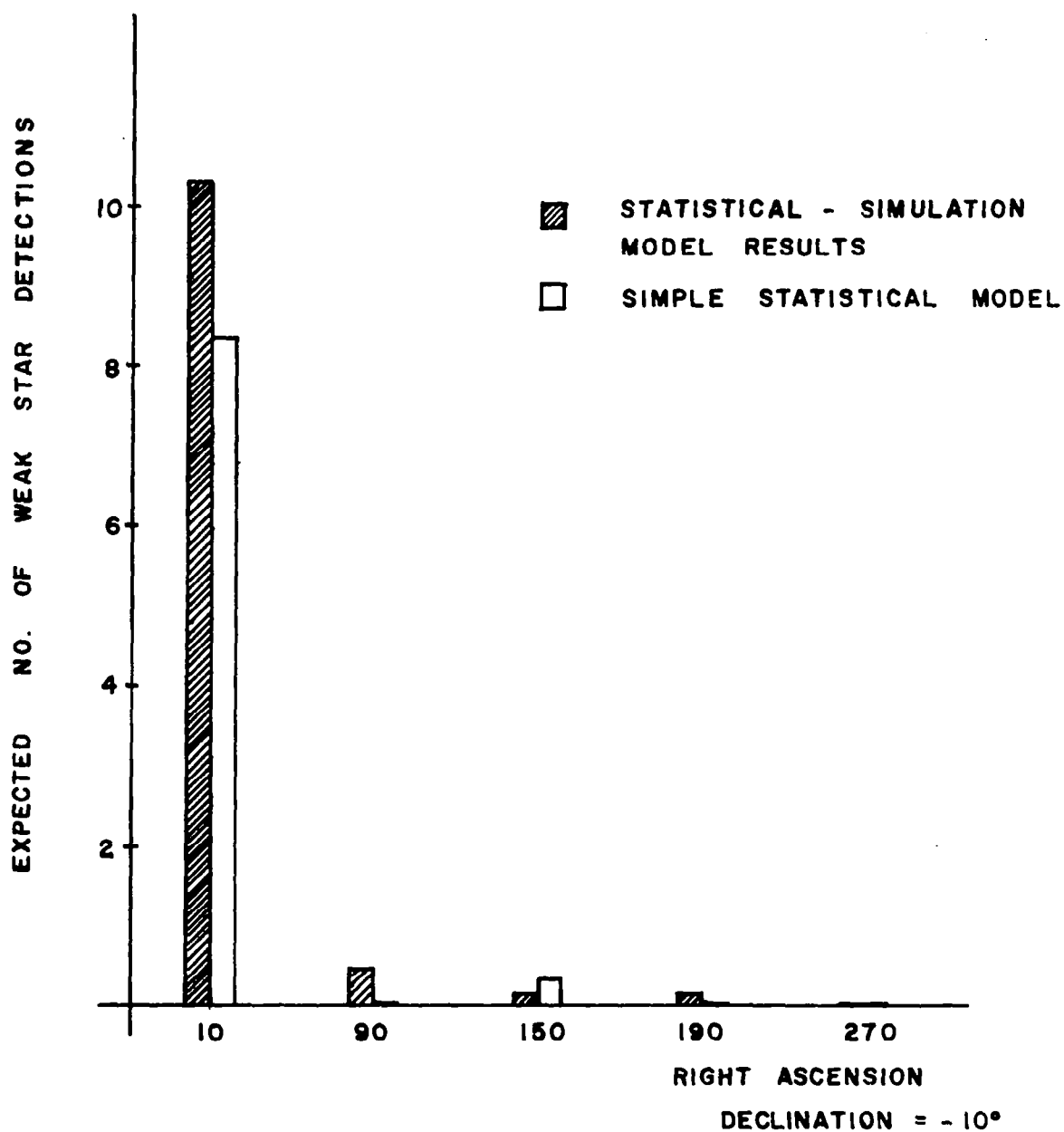
FIGURE 12 : COMPARISON OF TWO METHODS OF
COMPUTING EXPECTED NUMBER OF
WEAK STAR DETECTIONS

The latter model does not compute the homogeneous background component and is not subject to weak star density variations. The first model, however, is completely automatic and does account for weak star density variations. Figure 12 indicates that the two models agree reasonably well for the case considered, but greater variability will most likely be exhibited in further cases.

The optical designer must know the slit width as measured from the lens. Figure 13 shows the relationship between the slit width as measured from the spin axis (SW) and from the lens (SW'). Note that $SW' = SW \sin \gamma$. Thus, SW' is a function of distance from the spin axis, whereas, SW is constant.
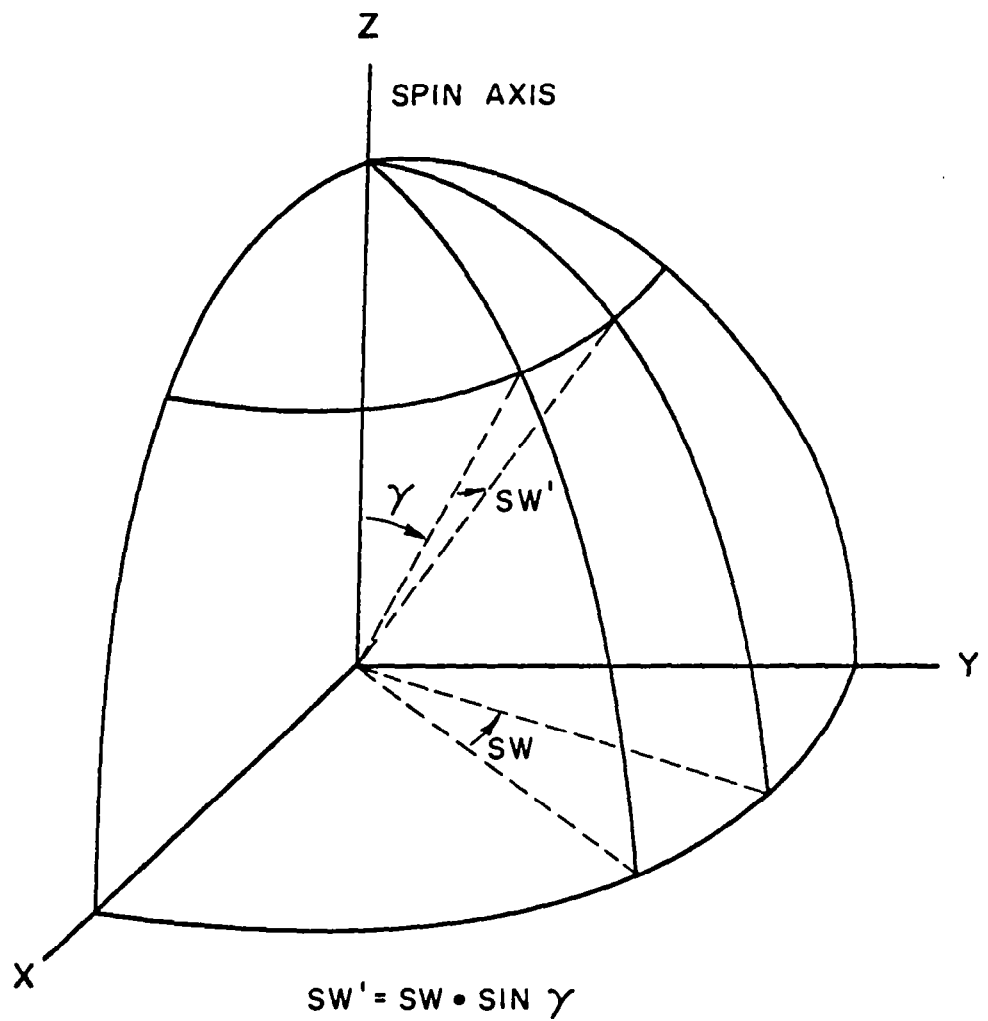
FIGURE 13: RELATION BETWEEN SLIT WIDTH AS
MEASURED FROM SPIN AXIS (SW) AND
LENS (SW')

E.   Special Results and Derivations

This subsection contains some special calculations and data necessary for the listing of the previous results. It includes the details of the construction of the star tape and computer program used in the simulation model. E.4 contains a table of star background radiation along with a coordinate conversion chart.

1.   Construction of Star Tape

The original data was in the form of punched cards. The data on these cards was taken from the Albany General Star Catalog which lists 33,342 stars, ordered by celestial right ascension. Each card contained the catalog number, visual magnitude, spectral class, right ascension and declination angles of the given star.

The visual magnitude of the stars was transformed to photographic magnitudes by using the spectral class of each star. The transformation used was

$$\text{photographic magnitude} = (B - V) - .11 + \text{visual magnitude}$$

where B - V is the color index of the star.[*] Only stars whose photographic magnitudes were 7.5 or less were used.

---

[*]   Allen, C. W. (1963), p. 197.

The color index and spectral class exhibit a strong quadratic correlation. See Figure 14. A quadratic polynomial was used to estimate this correlation with the fifty brightest stars providing the data points. The polynomial used was

$$B - V = -.43 + S (-.06 + .04 S)$$

where S is the spectral code used. See Figure 14.

The celestial direction cosines were computed using a right-handed xyz triad with z-axis passing through the celestial North Pole and the x-axis passing through the First Point of Aries (0° right ascension). The galactic direction cosines were then computed by a series of two rotations. First rotate 102° about the z-axis to produce an x'y'z' system. Then rotate -62° about the y'-axis to produce the $x_g y_g z_g$ system. The composite transformation is

$$\begin{pmatrix} x_g \\ y_g \\ z_g \end{pmatrix} = \begin{pmatrix} -\cos 78^\circ & \sin 78^\circ & 0 \\ -\sin 78^\circ \cos 62^\circ & -\cos 78^\circ \cos 62^\circ & -\sin 62^\circ \\ -\sin 78^\circ \sin 62^\circ & -\cos 62^\circ \cos 78^\circ & \cos 62^\circ \end{pmatrix} \begin{pmatrix} x \\ y \\ z \end{pmatrix}$$

The final tape contains a list of the brightest 15173 stars ordered by photographic magnitude (7.5 magnitude and brighter). Each record also contains the star catalog number and its three galactic direction cosines.
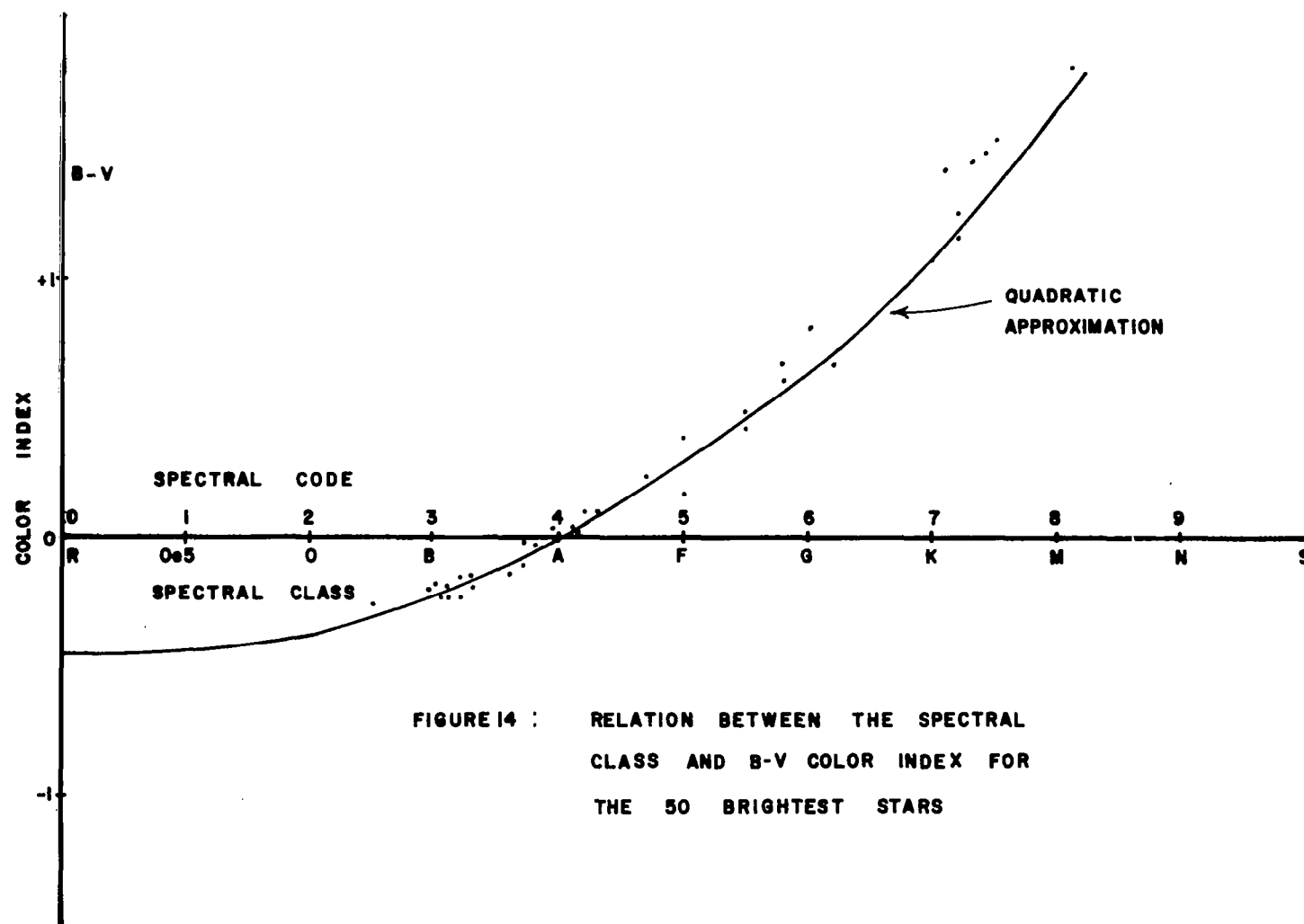
FIGURE 14 : RELATION BETWEEN THE SPECTRAL CLASS AND B-V COLOR INDEX FOR THE 50 BRIGHTEST STARS

2. Program Listing

```
PROGRAM SIMUL2
DIMENSION DCP(3)
1,DPTSAG(21),CLBDS(21),ZLAT(21)
2,NOSTAR(16000),WMAG(16000),GX(16000),GY(16000),GZ(16000)
COMMON DPTSAG,INDAG,CLBDS,ZLAT
COMMON/1/ GX
COMMON/2/ GY,GZ
COMMON/3/ WMAG,NOSTAR
DTR=.017453292520
CLBDS(1)=SINF(2.5*DTR)
CLBDS(2)=SINF(7.5*DTR)
DO 45 I=3,10
ALAT=10*I-15
45 CLBDS(I)=SINF(ALAT*DTR)
CLBDS(11)=1
DO 50 I=1,9
FI=I
ZLAT(I+12)=SINF(FI*10.*DTR)
M1=-I+10
50 ZLAT(M1   )=-ZLAT(I+12)
ZLAT(12)=SINF(5.*DTR)
ZLAT(10)=-ZLAT(12)
ZLAT(11)=0
READ 60,(DPTSAG(I),I=1,21),INDAG
60 FORMAT(11F7.2/10F7.2,I10)
INDTO=15174
REWIND 3
READINPUTTAPE3,90,(NOSTAR(I),WMAG(I),GX(I),GY(I),GZ(I),I=1,INDTO)
90 FORMAT(3X,I5,F9.2,3F13.8)
PRINT 95,NOSTAR(1),WMAG(1)
PRINT 95,NOSTAR(INDTO),WMAG(INDTO)
95 FORMAT(3X,I5,F9.2)
PRINT 35,INDAG,(I,DPTSAG(I),I=1,21)
35 FORMAT(//,5X,6HINDAG=I7/(I20,E20.10))
APED=.411
DARK=2540
TTS=.00688927
SW=6
SPHIS=4
SPHIL=24
DO 100 NPD=1,5
READ 105,RTAS,DECA,LISTNO,LTAU
105 FORMAT(2F10.5,2I10)
CALL DIRCOS(RTAS,DECA,DCP(1),DCP(2),DCP( 3))
PRINT 15,RTAS,DECA
15 FORMAT(//,5X,20HPOINTING DIR RT AS =F4.0,/,5X
1,         20HPOINTING DIR  DEC  =F4.0)
CALL EXPWSD(LISTNO,DCP,SPHIS,SPHIL,APED,TTS,SW,DARK,LTAU,ANS)
PRINT 25,ANS
25 FORMAT(10X,27HEXPECTED NO. OF DETECTIONS=E17.9)
100 CONTINUE
END
```

```
      SUBROUTINE EXPWSD(LSTNOS,DRCOPT,DPHIS,DPHIL,APEDIA,TTSC,SWMN,DKCR
     1,NETAU,EXPNO)
      DIMENSION DRCOPT(3)
     1,DPTSAG(21),CLBDS(21),ZLAT(21)
     2,NOSTAR(16000),WMAG(16000),GX(16000),GY(16000),GZ(16000)
      COMMON DPTSAG,INDAG,CLBDS,ZLAT
      COMMON/1/ GX
      COMMON/2/ GY,GZ
      COMMON/3/ WMAG,NOSTAR
C EXPECTED NO OF WEAK STAR DETECTIONS
C LSTNOS=INDEX OF LIMITING MAG.,DRCOPT=DIR COS OF POINTING DIR.,DPHIS,DPHIL=SLIT
C LENGTH IN DEG FROM SPIN AXIS,,APEDIA=APERTURE DIA IN INCHES,,TTSC=TRANSIT
C TIME IN SEC,,SWMN=SLIT WIDTH IN MIN OF ARC,,DKCR=DARK CURRENT IN PULSES/SEC,,
C NETAU=THRESHOLD,,EXPNO=EXPECTED NO OF WEAK STAR DETECTIONS
      YI=TIMEF(XX)
      NOOSTS=15174
      EXPNO=0
      DTR=.017453292520
      RPHIS=DTR*DPHIS
      RPHIL=DTR*DPHIL
      CLIMS=COSF(RPHIS)
      CLIML=COSF(RPHIL)
   50 FLMP2=WMAG(LSTNOS)+2.
   40 CALL DPTSCP(FLMP2)
      KTR=0
      LST=LSTNOS+1
      DO 10 I=LST,NOOSTS
      IF(WMAG(I)-FLMP2) 20,20,30
   30 PRINT 35,KTR
   35 FORMAT(10X,26HTOTAL NO OF STARS IN SCAN=I7)
      YT=TIMEF(XX)
      TTIME=YT-YI
      PRINT 45,TTIME
   45 FORMAT(2X,13HTIME IN MSEC=E17.9)
      RETURN
   20 COSANG=DRCOPT(1)*GX(I)+DRCOPT(2)*GY(I)+DRCOPT(3)*GZ(I)
      IF(COSANG-CLIMS) 60,10,10
   60 IF(CLIML-COSANG) 70,10,10
   70 CALL PRODET(I,DRCOPT,RPHIS,RPHIL,APEDIA,TTSC,SWMN,DKCR,NETAU
     1,PRDET)
      KTR=KTR+1
      EXPNO=EXPNO+PRDET
      PRINT 95, I,NOSTAR(I),WMAG(I),PRDET
   95 FORMAT(2I10,F9.2,E20.9)
      IF(PRDET-.00001) 80,10,10
   80 PRINT 85,I,WMAG(I)
   85 FORMAT(//,2X,34HPROB OF DETECTION LESS THEN .00001,/,
     12X,5HWMAG(I5,2H)=F7.2)
      GO TO 90
   10 CONTINUE
   90 CONTINUE
      PRINT 35,KTR
      YT=TIMEF(XX)
      TTIME=YT-YI
      PRINT 45,TTIME
      RETURN
      END
```

```
      SUBROUTINEPRODET(NUMBST,DIRCPT,PPHIS,PPHIL,APDIAM,TTSEC,SWMIN,DRKC
     1UR,NWTAU,PRDECT)
      DIMENSION DIRCPT(3)
     1,DPTSAG(21),CLBDS(21),ZLAT(21)
     2,NOSTAR(16000),WMAG(16000),GX(16000),GY(16000),GZ(16000)
      COMMON DPTSAG,INDAG,CLBDS,ZLAT
      COMMON/1/ GX
      COMMON/2/ GY,GZ
      COMMON/3/ WMAG,NOSTAR
C PROBABILITY OF DETECTION
C NUMBST=INDEX OF STAR..DIRCPT=DIR COS OF POINTING DIR..PPHIS,PPHIL=SLIT LENGTH
C IN RAD FROM SPIN AXIS..APDIAM=APERTURE DIAM IN IN..TTSEC=TRANSIT TIME IN SEC.
C SWMIN=SLIT WIDTH IN MIN OF ARC..DRKCUR=DARK CURRENT PULSES/SEC..
C NWTAU=THRESHOLD..PRDECT=PROB OF DECT.
      CALL BKGDPD(NUMBST,DIRCPT,PPHIS,PPHIL,BKTENM)
      FFACT=.1125
C FFACT IS THE PRODUCT OF CLAMP LEVEL,OPTICAL EFFICIENCY,QUANTUM EFFICIENCY
      BKMEAN=BKTENM*SWMIN*1.20E7*APDIAM**2*EXPF(-9.21)*TTSEC*FFACT
      STMEAN=1.20E7*APDIAM**2*EXPF(-.921*WMAG(NUMBST))*TTSEC*FFACT
      FALPHA=1.
C FALPHA IS THE CLAMP LEVEL
      DCMEAN=DRKCUR*TTSEC*FALPHA
      TOTMEN=STMEAN+BKMEAN+DCMEAN
      CALL POSTAL(TOTMEN,NWTAU,PRDECT)
      RETURN
      END




      SUBROUTINE POSTAL(FMPT,NTAU,VPT)
C FMPT=MEAN  NTAU=THRESHOLD        VPT=TAIL VALUE
C  SUMS THE TAIL STARTING AT NTAU+1
      IF(FMPT-50.) 30,30,40
   40 FTAU=NTAU
      SDV=SQRTF(FMPT)
      CALL CUMNOR(FTAU,1.,FMPT,SDV,VPTC)
      VPT=1.-VPTC
      RETURN
   30 CONTINUE
      TERM=1
      DO 10 J=1,NTAU
      DIV=NTAU-J+1
   10 TERM=TERM*FMPT/DIV+1.
      VPT=1.-EXPF(-FMPT)*TERM
      IF(VPT-.1E-7) 15,20,20
   15 VPT=0
   20 RETURN
      END
```

```
      SUBROUTINE BKGDPD(NUMSTR,PTDIRC,PHIS,PHIL,BKVAL)
      DIMENSION PTDIRC(3)
     1,DPTSAG(21),CLBDS(21),ZLAT(21)
     2,NOSTAR(16000),WMAG(16000),GX(16000),GY(16000),GZ(16000)
      COMMON DPTSAG,INDAG,CLBDS,ZLAT
      COMMON/1/ GX
      COMMON/2/ GY,GZ
      COMMON/3/ WMAG,NOSTAR
   COMPUTES THE BACKGROUND DENSITY IN NO OF 10TH MAG STARS/ARC MINUTE
      ZDP=PTDIRC(3)
      IF(ABSF(ZDP)-1.) 100,200,300
 300  PRINT 350,ZDP,NUMSTR
 350  FORMAT(39HERROR IN POINTING DIRECTION COORDINATES,E19.9,I10)
      RETURN
 200  COTHEC=0
      GO TO 60
 100  ZDT=GZ(NUMSTR)
      PDT=PTDIRC(1)*GX(NUMSTR)+PTDIRC(2)*GY(NUMSTR)+PTDIRC(3)*GZ(NUMSTR)
      IF(ABSF(PDT)-1.) 600,400,400
 400  PRINT 450,PDT,NUMSTR,(PTDIRC(I),I=1,3)
 450  FORMAT(35HERROR OR STAR AT POINTING DIRECTION,/,E19.9,I10,3E19.9)
 600  COTHEC=(ZDT-PDT*ZDP)/SQRTF((1.-ZDP**2)*(1.-PDT**2))
  60  SIDLG=PTDIRC(3)
      CODLG=SQRTF(1.-SIDLG**2)
      NN=(PHIL-PHIS)*100
      NN=NN/2*2+3
      ZN=NN
      HINT=(PHIL-PHIS)/(ZN-1.)
      N4=NN-1
      S4=0
      DO 10 I=2,N4,2
      ZI=I
      ARGU=(ZI-1.)*HINT+PHIS
      SIPHI=SINF(ARGU)
      FARG=COSF(ARGU)*SIDLG+SIPHI*COTHEC*CODLG
      CALL DENFN(FARG,FNV)
  10  S4=S4+FNV*SIPHI
      S4=4.*S4
      S2=0
      N2=NN-2
      DO 20 I=3,N2,2
      YI=I
      ARGU=(YI-1.)*HINT+PHIS
      SIPHI=SINF(ARGU)
      FARG=COSF(ARGU)*SIDLG+SIPHI*COTHEC*CODLG
      CALL DENFN(FARG,FNV)
  20  S2=S2+FNV*SIPHI
      S2=2.*S2
      SIPHIS=SINF(PHIS)
      FARGS=COSF(PHIS)*SIDLG+SIPHIS*COTHEC*CODLG
      CALL DENFN(FARGS,FNVS)
      SIPHIL=SINF(PHIL)
      FARGL=COSF(PHIL)*SIDLG+SIPHIL*COTHEC*CODLG
      CALL DENFN(FARGL,FNVL)
      BKVAL=HINT*(FNVS*SIPHIS+S4+S2+FNVL*SIPHIL)/3.
      BKVAL=BKVAL*.9549296586
      RETURN
      END
```

```
      SUBROUTINE DPTSCP(       PRMAG)
      DIMENSION CLSLAT(21)
     1,DPTSAG(21),CLBDS(21),ZLAT(21)
     2,NOSTAR(16000),WMAG(16000),GX(16000),GY(16000),GZ(16000)
      COMMON DPTSAG,INDAG,CLBDS,ZLAT
      COMMON/1/ GX
      COMMON/2/ GY,GZ
      COMMON/3/ WMAG,NOSTAR
C   INDAG= STARTING INDEX OF LIST     PRMAG=MAGNITUDE FOR NEW LIST
      TI=TIMEF(TTT)
      PRINT 37,INDAG,WMAG(INDAG),NOSTAR(INDAG)
   37 FORMAT(2X,22HINITIAL INDEX AND MAG0 I7,F8.2,10X,7HSTAR NO I10)
      DO 9 I=1,21
    9 CLSLAT(I)=0
      IF(PRMAG-7.5) 40,40,12
   12 PRMAG=7.5
   40 IF(WMAG(INDAG)-PRMAG) 10,10,60
   10 SIGN=-1
   70 INDAG=INDAG+1
      IF(INDAG-15174) 42,42,41
   41 INDAG=INDAG-1
      GO TO 80
   42 IF(WMAG(INDAG)-PRMAG) 50,50,41
   30 INDAG=INDAG-1
      IF(WMAG(INDAG)-PRMAG) 80,80,50
   60 SIGN=1
   50 WMAG10=EXPF(.92103403720*(10.-WMAG(INDAG)))
      ABGZ=ABSF(GZ(INDAG))
      DO 500 K=1,10
      IF(CLBDS(K)-ABGZ) 500,600,600
  500 CONTINUE
      K=11
  600 IF(CLBDS(1)-GZ(INDAG)) 700,800,800
  700 LATC=K+10
      CLSLAT(LATC)=CLSLAT(LATC)+SIGN*WMAG10
      GO TO 400
  800 LATC=12-K
      CLSLAT(LATC)=CLSLAT(LATC)+SIGN*WMAG10
  400 LTEST=1
      IF(SIGN)  70,70,30
   80 SDINSP=41252.961253
      DO 90 I=2,11
      FATRAT=2./((CLBDS(I)-CLBDS(I-1))*SDINSP  )
      MGM=I+10
      DPTSAG(MGM)=FATRAT*CLSLAT(MGM)+DPTSAG(MGM)
      MGM=-I+12
   90 DPTSAG(MGM)=FATRAT*CLSLAT(MGM)+DPTSAG(MGM)
      DPTSAG(11)=CLSLAT(11)/(CLBDS(1)*SDINSP)+DPTSAG(11)
      PRINT 38,INDAG,WMAG(INDAG),NOSTAR(INDAG)
   38 FORMAT(2X,23HTERMINAL INDEX AND MAG0 I7,F8.2,10X,7HSTAR NO I10)
      PRINT 39,DPTSAG
   39 FORMAT(E20.10)
      TT=TIMEF(TTT)
      TTTIME=TT-TI
      PRINT 36,TTTIME
   36 FORMAT(2X,30HDPTSCP SUB - TIME IN MIL SEC = E17.9)
      RETURN
      END
```

```
      SUBROUTINE DENFN(ZARG,VALUE)
      DIMENSION DUMMY(2)
     1,DPTSAG(21),CLBDS(21),ZLAT(21)
     2,NOSTAR(16000),WMAG(16000),GX(16000),GY(16000),GZ(16000)
      COMMON DPTSAG,INDAG,CLBDS,ZLAT
      COMMON/1/ GX
      COMMON/2/ GY,GZ
      COMMON/3/ WMAG,NOSTAR
      ABZ=ABSF(ZARG)
      DO 10 K=1,10
      IF(CLBDS(K)-ABZ) 10,20,20
   10 CONTINUE
      K=11
   20 IF(CLBDS(1)-ZARG) 30,40,40
   30 LATF=K+10
      GO TO 50
   40 LATF=12-K
   50 IF(LATF-1) 60,70,60
   60 IF(LATF-21)80,90,80
   70 LATF=2
      GO TO 80
   90 LATF=20
   80 NUMPT1  =LATF-1
      NUMPT2  =LATF
      NUMPT3  =LATF+1
  100 X12=ZLAT(NUMPT1   )-ZLAT(NUMPT2   )
      X13=ZLAT(NUMPT1   )-ZLAT(NUMPT3   )
      X23=ZLAT(NUMPT2   )-ZLAT(NUMPT3   )
      X1=ZARG-ZLAT(NUMPT1   )
      X2=ZARG-ZLAT(NUMPT2   )
      X3=ZARG-ZLAT(NUMPT3   )
      VALUE=X2/X12*X3/X13*DPTSAG(NUMPT1   )-X1/X12*X3/X23*DPTSAG(NUMPT2
     1)+X1/X13*X2/X23*DPTSAG(NUMPT3   )
      RETURN
      END
C


      SUBROUTINE  CUMNOR(X,C,FM,FS,V)
C   V=C*PHI((X-FM)/FS)
C     C*(VALUE OF CUM. NORMAL WITH MEAN FM AND S.D. FS)
      PX=X
      PY=((PX-FM)/FS)*.7071067811.9
      Y=ABSF(PY)
      D=((((((.0000430638*Y+.0002765672)*Y+.0001520143)*Y+.0092705272)*Y
     1+.0422820123)*Y+.0705230784)*Y+1.)**16
      ERF=1.-1./D
      V=.5*(1.+ERF)*C
      IF(PY) 20,30,30
   20 V=C-V
   30 RETURN
      END
```

```
      SUBROUTINE DIRCOS (RA, DEC, X, Y, Z)
      DTR=.017453292520
      RAD=RA*DTR
      DECD=DEC*DTR
      CDEC=COSF(DECD)
      XT=COSF(RAD)*CDEC
      YT=SINF(RAD)*CDEC
      ZT=SINF(DECD)
      X = -.20791169*XT + .97814760*YT
      Y = -.45921248*XT - .09760863*YT - .88294759*ZT
      Z = -.86365307*XT - .18357513*YT + .46947156*ZT
      RETURN
      END
         SCOPE
  15.73   16.82   18.89   21.23   24.03   29.03   39.11   58.99   91.39 121.13 146.21
 118.52   88.19   56.55   38.42   28.76   23.49   21.07   18.09   18.82   16.63        1179
         10.     -10.       490        40
         90.     -10.        20       461
        150.     -10.       249        70
        190.     -10.       129       102
        270.     -10.        74       176
```

3. Computation of Surface Integral $\mu_b(\theta_s)$

For integration purposes ν_b is assumed to be quadratic, i.e.,
$\nu_b(z) = p_1 + p_2 z^2$. Also $\nu_b(-z) = \nu_b(z)$.

The method used is to rotate the xyz system about the x-axis through
an angle α. This can be accomplished by the transformation

$$\begin{pmatrix} x' \\ y' \\ z' \end{pmatrix} = \begin{pmatrix} 1 & 0 & 0 \\ 0 & \cos\alpha & \sin\alpha \\ 0 & -\sin\alpha & \cos\alpha \end{pmatrix} \begin{pmatrix} x \\ y \\ z \end{pmatrix}$$
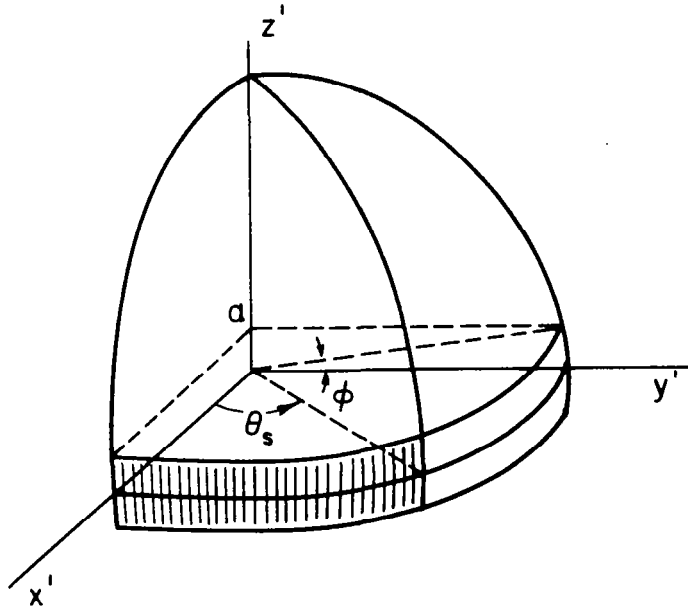
If we parametrically represent this surface by

$$x' = r\cos\theta \qquad y' = r\sin\theta \qquad z' = \pm\sqrt{1-r^2}$$

then
$$x = r \cos \theta$$

$$y = r \sin \theta \cos \alpha \mp \sqrt{1 - r^2} \sin \alpha$$

$$z = r \sin \theta \sin \alpha \pm \sqrt{1 - r^2} \cos \alpha$$

Using this representation, we have

$$J_1^2 + J_2^2 + J_3^2 = \left[\frac{\partial(y,z)}{\partial(r,\theta)} \right]^2 + \left[\frac{\partial(z,x)}{\partial(r,\theta)} \right]^2 + \left[\frac{\partial(x,y)}{\partial(r,\theta)} \right]^2$$

$$= \frac{r^2}{1 - r^2}$$

Thus

$$\mu_b(\theta_s) = \iint_{\mathcal{D}} F(r \sin\theta \cdot \sin\alpha + \sqrt{1-r^2} \cos\alpha) \frac{r}{\sqrt{1-r^2}} \, d\theta \, dr$$

$$+ \iint_{\mathcal{D}} F(r \sin\theta \cdot \sin\alpha - \sqrt{1-r^2} \cos\alpha) \frac{r}{\sqrt{1-r^2}} \, d\theta \, dr$$

where

$$\mathcal{D} = \left\{ (r,\theta) \,\middle|\, \sqrt{1-a^2} \leq r \leq 1 \quad 0 \leq \theta \leq \theta_s \right\}$$

Since
$$r \sin\theta \cdot \sin\alpha + \sqrt{1-r^2} \cos\alpha \geq 0 \quad \text{for} \quad (r,\theta) \in \mathcal{D}$$

$$\iint_{\mathcal{D}} F(r\sin\theta \cdot \sin\alpha + \sqrt{1-r^2}\,\cos\alpha)\,\frac{r}{\sqrt{1-r^2}}\,d\theta\,dr$$

$$= \int_{\sqrt{1-a^2}}^{1} \int_{0}^{\theta_s} \Big[\, P_1 + P_2\,r\sin\theta\cdot\sin\alpha + P_2\sqrt{1-r^2}\,\cos\alpha + P_3\,r^2\sin^2\theta\,\sin^2\alpha$$

$$+ P_3(1-r^2)\cos^2\alpha + P_3\,r\sqrt{1-r^2}\,\sin\theta\sin 2\alpha \Big]\cdot\frac{r}{\sqrt{1-r^2}}\,d\theta\,dr$$

$$= P_1\,\theta_s \int_{\sqrt{1-a^2}}^{1} \frac{r}{\sqrt{1-r^2}}\,dr + P_2\sin\alpha\,(1-\cos\theta_s)\int_{\sqrt{1-a^2}}^{1}\frac{r^2}{\sqrt{1-r^2}}\,dr$$

$$+ P_2\,\theta_s\cdot\cos\alpha \int_{\sqrt{1-a^2}}^{1} r\,dr + P_3\sin^2\alpha\cdot\frac{1}{2}(\theta_s - \frac{1}{2}\sin 2\theta_s)\int_{\sqrt{1-a^2}}^{1}\frac{r^3}{\sqrt{1-r^2}}\,dr$$

$$+ P_3\,\theta_s\cos^2\alpha \int_{\sqrt{1-a^2}}^{1} r\sqrt{1-r^2}\,dr + P_3\sin 2\alpha\,(1-\cos\theta_s)\int_{\sqrt{1-a^2}}^{1} r^2\,dr$$

$$= P_1\,\theta_s\,a + P_2\sin\alpha\,(1-\cos\theta_s)\left(\frac{\pi}{4} + \frac{a}{2}\sqrt{1-a^2} - \frac{1}{2}\sin^{-1}\sqrt{1-a^2}\right)$$

$$+ P_2\,\theta_s\cos\alpha\cdot\frac{1}{2}a^2 + P_3\sin^2\alpha\cdot\frac{1}{2}(\theta_s - \frac{1}{2}\sin 2\theta_s)(1 - \frac{a^2}{3})a$$

$$+ P_3\,\theta_s\cos^2\alpha\cdot\frac{1}{3}a^3 + P_3\sin 2\alpha\,(1-\cos\theta_s)\cdot\frac{1}{3}\left(1 - (1-a^2)^{3/2}\right)$$

The second integral is not quite so easy. First, we determine

where A $= r \sin\theta \cdot \sin\alpha - \sqrt{1-r^2} \cos\alpha$ is positive.

$$r \sin\theta \cdot \sin\alpha - \sqrt{1-r^2} \cos\alpha > 0$$
$$r^2 > 1/[1+\tan^2\alpha \sin^2\alpha] = u^2(\theta).$$
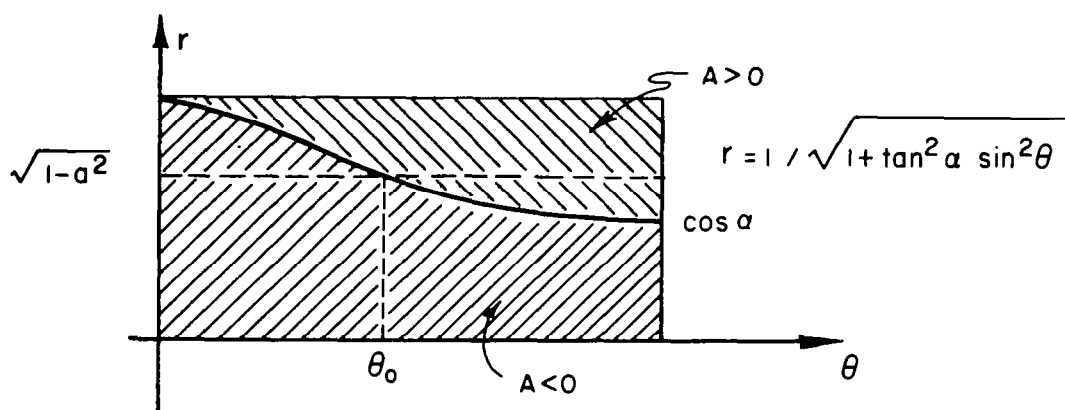
θ is the value of θ which satisfies

$$\frac{1}{1+\tan^2\alpha \sin^2\theta} = 1-a^2$$

$$\theta_0 = \sin^{-1}\left(\cot\alpha \cdot a/\sqrt{1-a^2}\right)$$

This integral can be broken up into several cases.

Case I: $\cos\alpha \geqslant \sqrt{1-a^2}$ $\quad \{\cos\alpha < \sqrt{1-a^2}, \theta_s \leq \theta_0\}$

Case II:

$$\cos \alpha \; < \sqrt{1-a^2}\,, \quad \theta_s > \theta_o$$

In Case I

$$\iint\limits_{\theta} F(r\sin\theta\cdot\sin\alpha - \sqrt{1-r^2}\,\cos\alpha)\;\frac{r}{\sqrt{1-r^2}}\;d\theta\,dr$$

$$= \int_0^{\theta_s}\left\{\int_{\sqrt{1-a^2}}^{\mu(\theta)} F(-A)\cdot\frac{r}{\sqrt{1-r^2}}\,dr + \int_{\mu(\theta)}^{1} F(A)\,\frac{r}{\sqrt{1-r^2}}\,dr\right\}d\theta$$

Note that

$$F(A) = p_1 + p_2\,r\sin\theta\cdot\sin\alpha - p_2\sqrt{1-r^2}\,\cos\alpha + p_3\,r^2\sin^2\theta\,\sin^2\alpha$$

$$+ p_3(1-r^2)\cos^2\alpha - p_3\,r\sqrt{1-r^2}\,\sin\theta\,\sin 2\alpha$$

$$F(-A) = p_1 - p_2\,r\sin\theta\cdot\sin\alpha + p_2\sqrt{1-r^2}\,\cos\alpha + p_3\,r^2\sin^2\theta\,\sin^2\alpha$$

$$+ p_3(1-r^2)\cos^2\alpha - p_3\,r\sqrt{1-r^2}\,\sin\theta\,\sin 2\alpha.$$

Let

$$I_1(\theta_s) = \iint\limits_{\theta} p_1\,\frac{r}{\sqrt{1-r^2}}\,dr\,d\theta$$

$$I_2(\theta_s) = \iint\limits_{\theta} p_2\,\sin\theta\,\sin\alpha\,\frac{r^2}{\sqrt{1-r^2}}\,dr\,d\theta$$

$$I_3(\theta_s) = \iint\limits_{\theta} p_2\,\cos\alpha\cdot r\,dr\,d\theta$$

$$I_4(\theta_s) = \iint_{\vartheta} P_3 \sin^2\theta \sin^2\alpha \cdot \frac{r^3}{\sqrt{1-r^2}} \, dr \, d\theta$$

$$I_5(\theta_s) = \iint_{\vartheta} P_3 \cos^2\alpha \cdot r \cdot \sqrt{1-r^2} \, dr \, d\theta$$

$$I_6(\theta_s) = \iint_{\vartheta} P_3 \sin\theta \sin 2\alpha \cdot r^2 \, dr \, d\theta$$

$$I_7(\theta_s) = \iint_{\vartheta'(\theta_s)} P_2 \sin\theta \cdot \sin\alpha \cdot \frac{r^2}{\sqrt{1-r^2}} \, dr \, d\theta$$

$$I_8(\theta_s) = \iint_{\vartheta'(\theta_s)} P_2 \cos\alpha \cdot r \cdot dr \, d\theta$$

where

$$\vartheta'(\theta_s) = \left\{ (r,\theta) \mid \mu(\theta) \le r \le 1, \; 0 \le \theta \le \theta_s \right\}$$

Thus, in Case I

$$\mu_b(\theta_s) = \sum_{i=1}^{6} I_i + (I_1 + I_4 + I_5 - I_6)$$

$$- \int_0^{\theta_s} \int_{\sqrt{1-a^2}}^{\mu(\theta)} P_2 \sin\theta \cdot \sin\alpha \cdot \frac{r^2}{\sqrt{1-r^2}} \, dr \, d\theta + \int_0^{\theta_s} \int_{\sqrt{1-a^2}}^{\mu(\theta)} P_2 \cos\alpha \cdot r \cdot dr \, d\theta$$

$$+ \int_0^{\theta_s} \int_{\mu(\theta)}^{1} P_2 \sin\theta \sin\alpha \cdot \frac{r^2}{\sqrt{1-r^2}} \, dr \, d\theta - \int_0^{\theta_s} \int_{\mu(\theta)}^{1} P_2 \cos\alpha \cdot r \, dr \, d\theta$$

$$= \sum_{i=1}^{6} I_i + I_1 + I_4 + I_5 - I_6 + (-I_2 + I_3)$$

$$+ 2 \int_0^{\theta_S} \int_{\mu(\theta)}^{1} P_2 \, \sin\theta \cdot \sin\alpha \cdot \frac{r^2}{\sqrt{1-r^2}} \, dr \, d\theta - 2 \int_0^{\theta_S} \int_{\mu(\theta)}^{1} P_2 \, \cos\alpha \cdot r \, dr \, d\theta.$$

$$= 2 \left[I_1 + I_3 + I_4 + I_5 + I_7 - I_8 \right]$$

where the I's are all evaluated at θ_S.

In Case II

$$\iint_{\mathcal{D}} F(A) \cdot \frac{r}{\sqrt{1-r^2}} \, dr \, d\theta$$

$$= \int_0^{\theta_0} \int_{\frac{\mu(\theta)}{\sqrt{1-a^2}}}^{\mu(\theta)} F(-A) \, \frac{r}{\sqrt{1-r^2}} \, dr \, d\theta + \int_0^{\theta_0} \int_{\mu(\theta)}^{1} F(A) \cdot \frac{r}{\sqrt{1-r^2}} \, dr \, d\theta$$

$$+ \int_{\theta_0}^{\theta_S} \int_{\frac{1}{\sqrt{1-a^2}}}^{1} F(A) \, \frac{r}{\sqrt{1-r^2}} \, dr \, d\theta$$

$$= I_1(\theta_0) + I_4(\theta_0) + I_5(\theta_0) - I_6(\theta_0) \quad - I_2(\theta_0) + 2 I_7(\theta_0)$$

$$+ I_3(\theta_0) - 2 I_8(\theta_0)$$

$$+ \left[I_1(\theta_S) - I_1(\theta_0) \right] - \left[I_2(\theta_S) - I_2(\theta_0) \right] + \left[I_3(\theta_S) - I_3(\theta_0) \right]$$

$$+ \left[I_4(\theta_S) - I_4(\theta_0) \right] + \left[I_5(\theta_S) - I_5(\theta_0) \right] - \left[I_6(\theta_S) - I_6(\theta_0) \right]$$

$$= I_1(\theta_S) + I_4(\theta_S) + I_5(\theta_S) - I_6(\theta_S)$$

$$- I_2(\theta_s) \quad + 2I_7(\theta_o)$$

$$+ I_3(\theta_s) \quad - 2I_8(\theta_o)$$

Thus, for Case II

$$\mu_b(\theta_s) = 2\left[I_1(\theta_s) + I_3(\theta_s) + I_4(\theta_s) + I_5(\theta_s) + I_7(\theta_o - I_8(\theta_o)\right]$$

Integrals

For $\sin\phi = a$

$$I_1(\theta_s) = P_1 \theta_s a = P_1 \theta_s \sin\phi$$

$$I_2(\theta_s) = P_2 \sin\alpha \, (1 - \cos\theta_s)\left(\frac{\pi}{4} + \frac{a}{2}\sqrt{1-a^2} - \frac{1}{2}\sin^{-1}\sqrt{1-a^2}\right)$$

$$= P_2 \sin\alpha \, (1 - \cos\theta_s)\left(\frac{1}{4}\sin 2\phi + \frac{1}{2}\phi\right)$$

$$I_3(\theta_s) = P_2 \theta_s \cos\alpha \, \frac{1}{2}a^2 = P_2 \theta_s \cos\alpha \, \frac{1}{2}\sin^2\phi$$

$$I_4(\theta_s) = P_3 \sin^2\alpha \, \frac{1}{2}(\theta_s - \frac{1}{2}\sin 2\theta_s)(1 - a^2/3)\, a$$

$$I_5(\theta_s) = P_3 \theta_s \cos^2\alpha \, a^3/3$$

$$I_6(\theta_s) = P_3 \sin 2\alpha \, (1 - \cos\theta_s)(1 - (1-a^2)^{3/2})/3$$

$$I_7(\theta_s) = P_2\left\{\sin\alpha\left(-\frac{\pi}{4}\cos\theta_s + \frac{1}{2}\cos\theta_s \sin^{-1}(u(\theta_s))\right)\right.$$

$$-\frac{1}{2}\cos^2\alpha \, \tan^{-1}(\sec\alpha \tan\theta_s) - \frac{1}{2}\tan^{-1}(\cos\alpha \cot\theta_s)$$

$$\left. + \frac{\pi}{4}\right\}$$

$$I_8(\theta_s) = P_2 \cos\alpha \cdot \frac{1}{2}\left[\theta_s - \cos\alpha \cdot \tan^{-1}(\sec\alpha \cdot \tan\theta_s)\right]$$

$I_7(\theta_s):$

$$\int_0^{\theta_s}\int_{u(\theta)}^{1} \sin\theta \, \frac{r^2}{\sqrt{1-r^2}} \, dr\,d\theta$$

$$= \int_0^{\theta_s} \sin\theta \left[-\frac{r}{2}\sqrt{1-r^2} + \frac{1}{2}\sin^{-1}r\right]_{u(\theta)}^{1} d\theta$$

$$= \int_0^{\theta_s} \sin\theta \left[\frac{\pi}{4} + \frac{u(\theta)}{2}\sqrt{1-u^2(\theta)} - \frac{1}{2}\sin^{-1}(u(\theta))\right] d\theta$$

$$= \int_0^{\theta_s}\left\{\frac{\pi}{4}\sin\theta + \frac{1}{2}\frac{\tan\alpha \sin^2\theta}{1+\tan^2\alpha \sin^2\theta} - \frac{\sin\theta}{2}\sin^{-1}\left(\frac{1}{\sqrt{1+\tan^2\alpha \sin^2\theta}}\right)\right\}d\theta$$

$$= -\frac{\pi}{4}\cos\theta_s - \frac{1}{2}\cot\alpha\,\cos\alpha\,\tan^{-1}(\sec\alpha\,\tan\theta_s)$$

$$- \frac{1}{2}\csc\alpha\,\tan^{-1}\left(\frac{1}{\sec\alpha\,\tan\theta_s}\right)$$

$$+ \frac{1}{2}\cos\theta_s\,\sin^{-1}(u(\theta_s)) + \frac{\pi}{4}\csc\alpha.$$

$I_8(\theta_s):$

$$\int_0^{\theta_s}\int_{u(\theta)}^{1} r\,dr\,d\theta = \int_0^{\theta_s}\left[\frac{1}{2} - \frac{1}{2}\frac{1}{1+\tan^2\alpha \sin^2\theta}\right] d\theta$$

$$= \frac{1}{2}\left[\theta_s - \cos\alpha\,\tan^{-1}(\sec\alpha\,\tan\theta_s)\right].$$

4.   Background Tables and Coordinate Conversions

Table 1 gives the total integrated starlight for stars of sixth magnitude and weaker.[*] Photographic magnitude is used throughout. The entries are in terms of tenth magnitude stars per square degree. The coordinates are old galactic coordinates.[**] A coordinate conversion graph follows the background table.

The following indicates the relations between the celestial and galactic spheres.
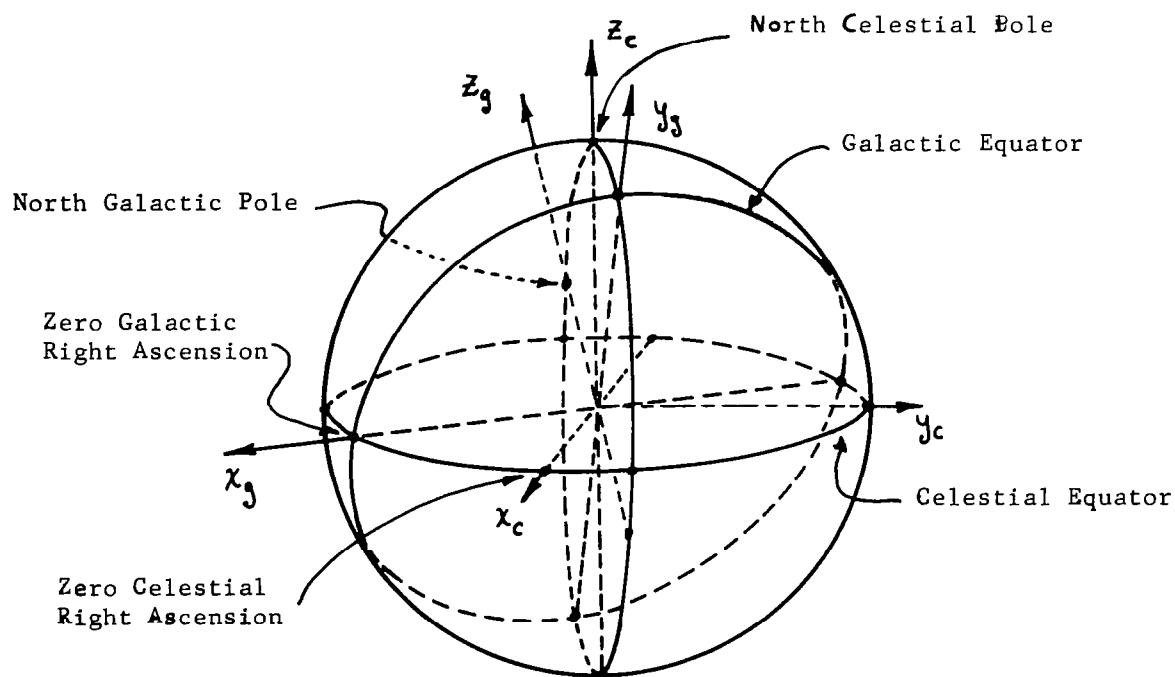
*   Megill, L. R. and F. E. Roach (1961).

**   See Allen (1963), p. 17.

TABLE 1

INTEGRATED STARLIGHT

ℓ^I\\b^I	00	05	10	15	20	30	40	50	60	70	80
000	99	62	54	55	51	40	28	22	19	17	16
010	102	65	60	68	62	43	30	22	19	17	15
020	117	74	68	81	72	45	30	22	19	16	15
030	144	89	77	85	74	44	30	23	19	16	15
040	171	106	82	78	66	42	30	22	18	16	15
050	187	114	80	65	55	38	29	22	18	16	15
060	174	106	70	53	45	34	27	22	18	16	15
070	141	87	58	44	38	31	26	21	18	16	15
080	106	65	47	39	35	29	25	21	18	16	15
090	80	49	39	38	35	28	24	21	18	16	15
100	66	41	35	38	36	28	24	21	18	16	15
110	62	38	34	40	37	28	24	21	18	17	16
120	68	42	37	41	38	28	23	20	18	17	16
130	83	52	43	42	38	29	23	20	18	17	15
140	102	69	52	43	37	29	23	19	17	16	15
150	125	90	62	45	38	30	23	18	16	15	15
160	140	107	72	49	41	31	22	18	16	15	14
170	147	112	78	56	45	31	22	17	15	14	14
180	147	105	80	64	51	32	22	17	15	14	14
190	147	98	78	70	55	33	22	17	15	14	14
200	159	97	76	71	56	33	23	18	16	15	15
210	189	106	78	66	53	33	23	19	17	16	15
220	239	127	82	60	48	33	24	20	17	17	16
230	290	152	89	54	43	32	25	20	18	17	16
240	321	176	98	53	42	33	26	21	19	17	16
250	323	191	109	58	45	35	28	22	19	17	15
260	306	191	118	68	52	38	29	23	19	17	15
270	282	182	124	82	61	40	30	24	19	16	15
280	263	170	125	94	69	41	30	24	19	16	15
290	254	158	120	96	70	40	29	24	20	17	15
300	251	148	109	86	62	37	29	24	20	17	16
310	235	134	94	70	52	34	27	23	20	17	16
320	206	116	79	55	43	33	27	23	20	18	16
330	167	94	65	45	38	32	26	22	20	18	16
340	132	76	56	43	38	34	26	22	19	18	16
350	109	66	52	46	42	36	27	22	19	17	16

ℓ^I = galactic right ascension

b^I = galactic declination

TABLE 1 (cont.)

ℓ^I \ b^I	-02	-05	-10	-15	-20	-30	-40	-50	-60	-70	-80
000	111	95	81	77	65	42	31	25	21	19	18
010	114	95	79	70	56	38	29	24	21	19	18
020	129	106	83	67	50	34	27	24	21	20	18
030	154	122	91	68	47	32	26	23	21	20	19
040	179	136	99	72	48	32	25	21	20	20	18
050	190	140	102	76	52	33	25	20	19	19	18
060	177	131	98	79	58	36	25	20	18	19	18
070	147	113	90	79	62	39	26	19	18	18	18
080	115	95	80	74	60	40	27	19	17	17	17
090	91	80	70	66	54	38	27	20	17	16	17
100	76	70	62	55	45	34	26	20	17	16	17
110	72	64	55	46	36	30	25	20	17	16	17
120	76	63	50	39	30	26	23	20	18	16	17
130	86	63	46	35	27	24	22	20	18	17	17
140	99	65	44	35	27	23	21	19	18	17	17
150	111	67	44	36	30	25	22	19	18	17	17
160	122	71	46	41	36	28	23	19	18	17	17
170	130	80	54	50	44	32	25	20	18	17	17
180	127	92	66	62	55	37	27	21	18	17	17
190	148	113	85	76	64	40	29	22	18	17	17
200	168	139	110	91	68	42	29	23	19	17	17
210	206	169	131	99	67	41	29	23	19	18	18
220	255	197	144	101	63	38	28	22	19	18	18
230	303	214	142	94	57	35	26	21	20	19	18
240	323	208	128	83	52	33	25	21	20	19	18
250	308	187	108	73	48	32	25	21	20	19	18
260	281	168	94	66	45	31	25	22	21	19	18
270	259	161	91	65	44	32	27	24	21	19	18
280	251	168	100	69	46	33	28	25	22	19	18
290	253	186	119	79	49	34	30	27	22	19	18
300	258	203	141	92	56	37	32	27	22	19	18
310	251	205	153	104	63	40	33	27	22	19	18
320	228	186	148	110	72	43	33	27	21	19	18
330	185	155	129	108	78	46	33	26	21	18	18
340	147	124	108	99	79	47	33	25	20	18	18
350	122	104	91	87	73	46	32	25	20	19	18

ℓ^I = galactic right ascension

b^I = galactic declination

TRANSFORMATION FROM CELESTIAL COORDINATES TO OLD GALACTIC COORDINATES

CELESTIAL DECLINATION

CELESTIAL RIGHT ASCENSION

---- GALACTIC RIGHT ASCENSION
—— GALACTIC DECLINATION
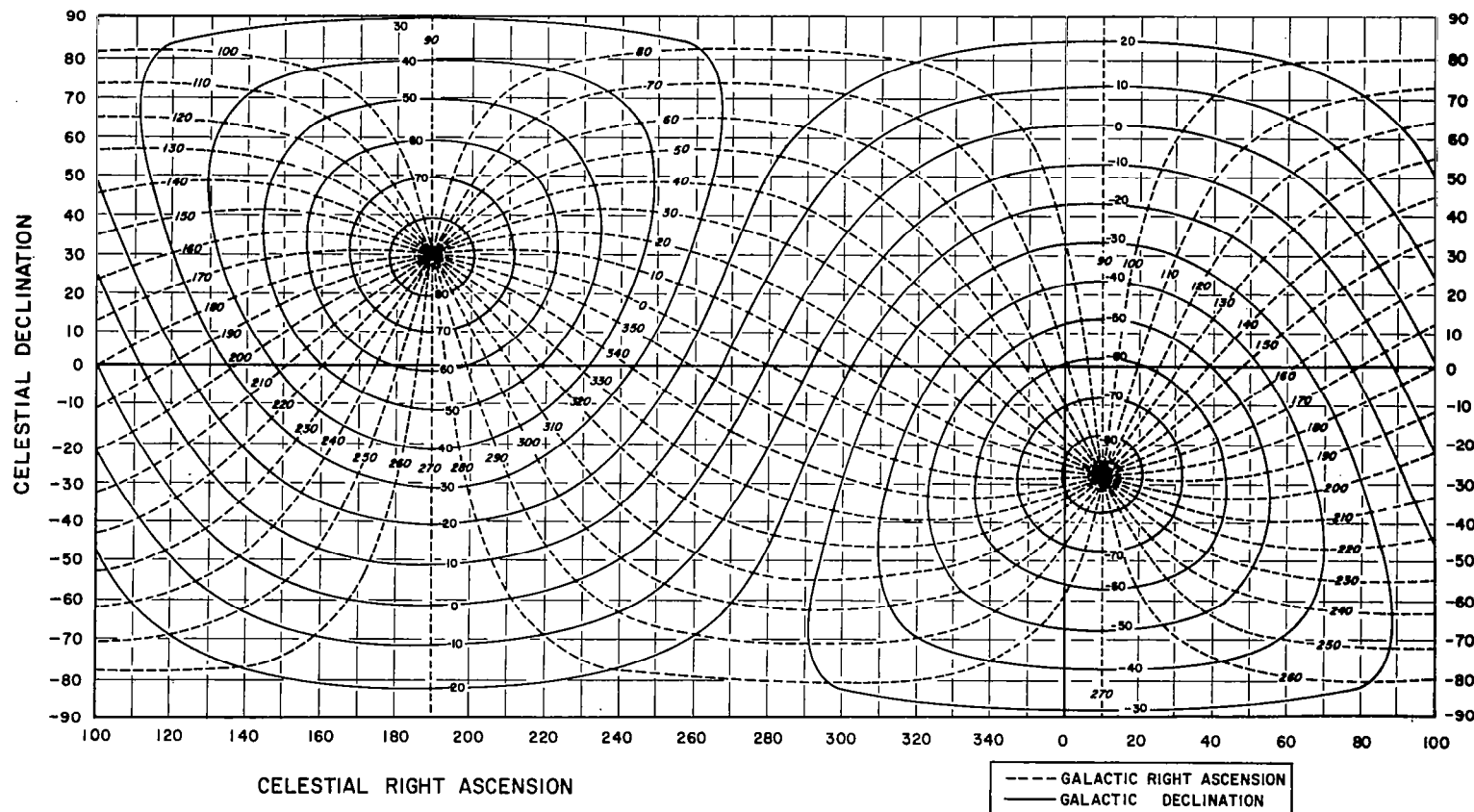
F.   Statistical Model for Spatial Noise

In this subsection, F, we describe a statistical model of the weak star background for the third operating situation. The weak stars are closely spaced in time, and their detections are statistically dependent. In the next subsection, G, we evaluate the spatial noise power, and describe the characteristics of two typical filters.

A weak star background is used in the following discussion; the very weak stars are not combined to form a homogeneous component. The weak star images are assumed to be randomly distributed across the reticle with a homogeneous, two-dimensional Poisson distribution. The gross variation in star density between the galactic pole and equator can be neglected in the following. Hence, the times at which weak stars enter the slit form a stationary Poisson process. Let ν denote the average rate of star transits, and t_1, t_2, t_3, ... denote the times when weak stars are in the center of the slit. Let $I_j(\lambda) \, \Delta\lambda$ be the amount of radiation from the jth star in the wavelength interval $(\lambda, \lambda + \Delta\lambda)$ entering a unit area of the optical aperture. Assume $I_j(\lambda)$ is expressed in photons per second. The variation of $I_j(\lambda)$ between successive stars, and the rate ν, depend on the region of the sky one is scanning.

The optical system produces an aberrated image. Assume it is Gaussian in shape; i.e., the radiation per unit area on the reticle is given by

$$\frac{A T(\lambda) \, I_j(\lambda) \, \Delta\lambda}{2\pi \sigma^2} \, \exp\left[-\frac{1}{2} \frac{x^2 + y^2}{\sigma^2} \right]$$

in the wavelength interval $(\lambda, \lambda + \Delta\lambda)$, where A is the aperture area, where $T(\lambda)$ is the transmittance of the optical system for wavelength λ, and where σ defines the optical resolution.

III-63

STELLAR BACKGROUND RADIATION

1. Radiation Passed Slit

Let T_s be the time required for a star to cross the slit. The radiation passing the slit at time t from the jth star is $AT(\lambda)\ I_j(\lambda)\ G(t - t_j)\ \Delta\lambda$ in the wavelength interval $(\lambda, \lambda + \Delta\lambda)$, where

$$G(t) = \phi\left(\frac{t}{\sigma} + \frac{T_s}{2\sigma}\right) - \phi\left(\frac{t}{\sigma} - \frac{T_s}{2\sigma}\right)$$

$$\phi(t) = \frac{1}{\sqrt{2\pi}} \int_{-\infty}^{t} e^{-x^2/2}\,dx$$

With the star centered in the slit, eighty percent of the star radiation passes the slit when $T_s/2 = 1.28\sigma$. It follows that the total background radiation passing the slit at time T is

$$I_b(t, \lambda)\Delta\lambda = AT(\lambda)\sum_j I_j(\lambda)G(t-t_j) + I_o(\lambda)T(\lambda)\Delta\lambda$$

in the wavelength interval $(\lambda, \lambda + \Delta\lambda)$. The constant term $I_o(\lambda)$ is introduced for generality. One may make observations from the earth's surface; in which case $I_o(\lambda)$ is the airglow radiation. Also if one is scanning near the ecliptic, $I_o(\lambda)$ can include zodiacal radiation. In general $I_o(\lambda)$ will depend on the optical aperture and field of view.

2. Filter Output

The radiation $I_b(t, \lambda)$ on the photocathode produces electron emissions. These emissions form a non-stationary Poisson process with an instantaneous emission rate of
$$\int_{-\infty}^{\infty} Q(\lambda)I_b(t,\lambda)\,d\lambda.$$

where $Q(\lambda)$ is the quantum efficiency at wavelength λ.[*] Substituting

for $I_b(t,\lambda)$ the rate becomes

$$\mu(t) = A \sum_j I_j^* G(t-t_j) + I_o^*$$

where I_j^* and I_o^* are the effective intensities.

$$I_j^* = \int_0^\infty T(\lambda) I_j(\lambda) Q(\lambda) d\lambda$$
$$I_o^* = \int_0^\infty T(\lambda) I_o(\lambda) Q(\lambda) d\lambda$$

Let τ_1, τ_2, ...τ_k denote the times at which emissions occur.
Corresponding to the k-th emission one obtains a pulse at the output of
the photomultiplier $a_k p(t-\tau_k)$, where

$$p(t) = 0 \quad \text{for} \quad t < 0$$

and

$$\int_0^\infty p(t) dt = 1.$$

The pulse amplitude a_k varies between pulses since the electron multiplication
is random.

Assume the filter has an impulse response $w(t)$, with $w(t) = 0$ for

---

For the intensity and spectral characteristics of stellar radiation,
these assumptions are physically reasonable. The characteristics of
photo-electric emissions are discussed by L. Mandel (1958) pp. 1037-
1047 and (1959), pp. 233-243.

$t < 0$. Then the output of the filter is

$$X(t) = \sum_{k} a_k \int_0^\infty p(t - \tau_k - \tau') \, w(\tau') \, d\tau'$$

where the τ_k's form a non-stationary Poisson process with an instantaneous rate $\mu(t)$. The photomultiplier dark current will be omitted in the following discussion since the objective is to describe stellar background noise. The dark current is simply additive since the filter in linear.

G. Spatial Noise Power

At time t the uncertainty in X(t) results from photon noise. The instantaneous "dc level" is expected value X(t): viz.,[*]

$$\overline{X(t)} = \bar{a} \int_{-\infty}^{\infty} \mu(T'') \int_{-\infty}^{\infty} P(t-T''-T') W(T') dT' dT''$$

$$= \bar{a} A \sum_j I_j^* \int_{-\infty}^{\infty} G(T''-t_j) \int_{-\infty}^{\infty} P(t-T''-T') W(T') dT' dT''$$

$$+ \bar{a} I_o^* \int_{-\infty}^{\infty} W(T') dT'$$

The uncertainty in X(t) about $\overline{X(t)}$ corresponds to the photon noise. The variance of X(t) is the power in the photon noise at time t, call it $P_{pn}(t)$. It is

$$P_{pn}(t) = \overline{a^2} A \sum_j I_j^* \int_{-\infty}^{\infty} G(T''-t_j) \left[\int_{-\infty}^{\infty} P(t-T''-T') W(T') dT' \right]^2 dT''$$

$$+ \overline{a^2} I_o^* \int_{-\infty}^{\infty} \left[\int_{-\infty}^{\infty} P(t-T''-T') W(T') dT' \right]^2 dT''$$

---

[*] In the following discussion extensive use is made of relationships developed for Poisson processes by E. Parzen (1962), Chapter 4.

Since $P_{pn}(t)$ changes with time, $X(t)$ is not stationary, even in the wide sense. It is natural to measure the photon noise power by the time average of $P_{pn}(t)$: viz.,

$$\langle P_{pn}(t) \rangle = \lim_{T \to \infty} \frac{1}{2T} \int_{-T}^{T} P_{pn}(t) \, dt$$

In practical cases, the above limit converges in mean square to the expected value of $P_{pn}(t)$ with respect to the ensemble generated by the t_j's and I_j^*'s. Hence

$$\langle P_{pn}(t) \rangle = \overline{a^2} \left(A \overline{I^+} \nu T_s + I_o^* \right) \int_{-\infty}^{\infty} \left[\int_{-\infty}^{\infty} p(\tau'' - \tau') w(\tau') \, d\tau' \right]^2 d\tau''$$

To obtain this result one must use the identity

$$\int_{-\infty}^{\infty} G(t) \, dt = T_s$$

Note that νT_s is the expected number of stars in the slit. The double integral in $\langle P_{pn}(t) \rangle$ can be written in a simpler form;

$$\int_{-\infty}^{\infty} \left[\int_{-\infty}^{\infty} p(\tau'' - \tau') w(\tau') \, d\tau' \right]^2 d\tau'' = \int_{-\infty}^{\infty} |\wp(f)|^2 |\mathscr{W}(f)|^2 \, df,$$

where $\mathcal{P}(f)$ and $\mathcal{W}(f)$ are the Fourier transforms of $p(t)$ and $w(t)$. In cases of interest, the band width of the filter determines the value of this integral since the band width corresponding to $|\mathcal{P}(f)|$ is much greater.

The spatial noise is the variation of $\overline{X(t)}$ as a function of time. The dc component of the spatial noise is simply the time average of $\overline{X(t)}$: viz.,

$$\langle X(t) \rangle = \lim_{T \to \infty} \frac{1}{2T} \int_{-T}^{T} \overline{X(t)} \, dt \ .$$

In practical cases, the above limit converges in mean square to the expected value of $\overline{X(t)}$ with respect to the ensemble generated by the T_j's and I_j^*'s. Hence

$$\langle \overline{X(t)} \rangle = \overline{a} \left[A \overline{I^*} \nu T_s + I_o^* \right] \int_{0}^{\infty} w(\tau) \, d\tau$$

The ac component of the spatial noise is the variation of $\overline{X(t)}$ about the dc level $\langle \overline{X(t)} \rangle$. The power in ac component is therefore

$$\left\langle \left(\overline{X(t)} - \langle \overline{X(t)} \rangle \right)^2 \right\rangle =$$

$$\lim_{T \to \infty} \frac{1}{2T} \int_{-T}^{T} \left(\overline{X(t)} - \langle \overline{X(t)} \rangle \right)^2 \, dt \ .$$

As before, the limit converges in mean square to the ensemble average

which is the variance of $\overline{X(t)}$. Therefore,

$$\left\langle \left(\overline{X(t)} - \left\langle \overline{X(t)} \right\rangle \right)^2 \right\rangle =$$

$$\overline{a}^2 A^2 \overline{I^{*2}} \nu \int_{-\infty}^{\infty} \left[\int_{-\infty}^{\infty} G(\tau''-\tau''') \int_{-\infty}^{\infty} p(t-\tau''-\tau') \, w(\tau') \, d\tau' d\tau'' \right]^2 dt$$

$$= \overline{a}^2 A^2 \overline{I^{*2}} \nu \int_{-\infty}^{\infty} |\mathcal{G}(f)|^2 |\mathcal{P}(f)|^2 |\mathcal{W}(f)|^2 \, df$$

Where $\mathcal{G}(f)$ is the Fourier transform of $G(t)$.

The average power in the filter output is defined as the time

average of $X^2(t)$. Applying the ergodic theorem, one can show that the

average power $\langle X^2(t) \rangle$ is equal to the sum of the average power in the

photon noise and the power in the spatial noise, i.e.,

$$\langle X^2(t) \rangle = \overline{a^2} \left(A \overline{I^*} \nu T_s + I_o^* \right) \int_{-\infty}^{\infty} |\mathcal{P}(f)|^2 |\mathcal{W}(f)|^2 df$$

$$+ \overline{a}^2 A^2 \overline{I^{*2}} \nu \int_{-\infty}^{\infty} |\mathcal{G}(f)|^2 |\mathcal{P}(f)|^2 |\mathcal{W}(f)|^2 \, df$$

$$+ \overline{a}^2 \left[A \overline{I^*} \nu T_s + I_o^* \right]^2 \left[\int_{-\infty}^{\infty} w(\tau) \, d\tau \right]^2$$

The first term corresponds to the photon noise. The second term corresponds to the ac component of the spatial noise. It is the only term that is dependent on the optical resolution. The third term corresponds to the dc component of the spatial noise. Note that the integrand $|\mathcal{G}(f)|^2 |\mathcal{W}(f)|^2$ corresponds to the power spectrum of the photon noise, and the integrand $|\mathcal{Y}(f)|^2 |\mathcal{G}(f)|^2 |\mathcal{W}(f)|^2$ corresponds to the power spectrum of the spatial noise.

One can evaluate the Fourier transform $\mathcal{Y}(f)$ explicitly. In G.3, $|\mathcal{Y}(f)|^2$ is shown to be

$$\frac{1}{\pi f^2} \sin^2\left(\pi f T_s\right) \exp\left[-4\pi^2 f^2 \sigma^2\right].$$

Also, in cases of interest $|\mathcal{G}(f)|$ is constant relative to and $|\mathcal{W}(f)|$. Neglecting I_o^*, one can now rewrite the average power as

$$\langle X^2(t) \rangle = \overline{a^2} A \overline{I^*} \nu T_s \left[\int_{-\infty}^{\infty} w^2(t)\, dt \right.$$

$$+ A T_s \frac{\overline{a}^2}{\overline{a^2}} \frac{\overline{I^{*2}}}{\overline{I^*}} \int_{-\infty}^{\infty} \frac{1}{(\pi T_s f)^2} \sin^2(\pi T_s f) e^{-4\pi^2 f^2 \sigma^2}$$

$$\cdot |\mathcal{W}(f)|^2\, df$$

$$\left. + \frac{\overline{a}^2}{\overline{a^2}} A \overline{I^*} \nu T_s \left(\int_{-\infty}^{\infty} w(t)\, dt \right)^2 \right]$$

The power in the spatial noise is monotone increasing function of optical resolution. To illustrate the relative magnitude of various noise components, the terms in the brackets will be evaluated for typical systems.

The ratio $\overline{a}^2 / \overline{a^2}$ depends on the photomultiplier; a nominal value is 2/3.[*]

The intensity ratio $\overline{I^{*2}} / \overline{I^*}$ and the average intensity $\overline{I^*} \nu T_S$ can be evaluated directly using previous results developed by Farrell and Zimmerman.[**] Assume one is interested in stars with photographic magnitudes M_0 and smaller. Then the background consists of stars with magnitudes greater than M_0. In the following discussion a mean galactic background is used. One can show that

$$\frac{\overline{I^{*2}}}{\overline{I^*}} = 3.98 \times 10^8 T_0 Q_0 \frac{1 - \Phi(.173 M_0 + 3.53)}{1 - \Phi(.173 M_0 - 1.80)}$$

where T_0 is the nominal optical transmittance and Q_0 is the nominal quantum efficiency, with the aperture area expressed in square inches. This ratio is graphed in Figure 15 with $T_0 = .5$ and $Q_0 = .1$. The average intensity $\overline{I^*} \nu T_S$ is

$$3.85 \times 10^4 \left[1 - \Phi(.173 M_0 - 1.80) \right] A' T_0 Q_0$$

where A' is the slit area in square degrees, with the aperture

[*] R. F. Tusting, Q. Z. Kerms, H. K. Knudsen, (1962), pp. 118-123.

[**] E. J. Farrell and C. D. Zimmerman, (1965), Appendix B.
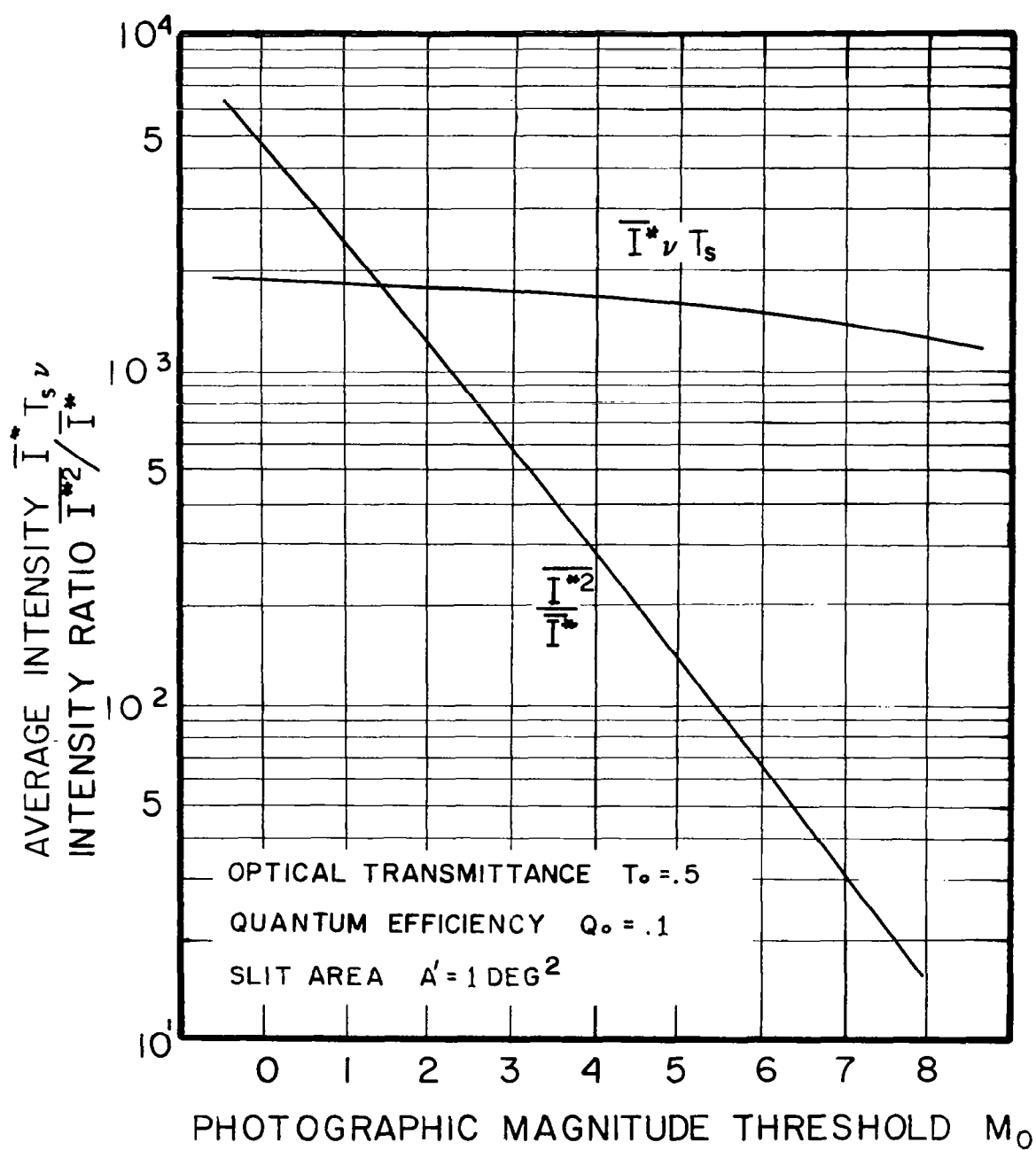
FIGURE 15: INTENSITY RATIO AND AVERAGE INTENSITY

area expressed in square inches. This expression is graphed in Figure 15 with $T_0 = .5$, $A' = 1$, and $Q_0 = .1$.

There are several possible filters that can be used. In the following sections, two filters will be considered in detail. The first is a simple low-pass filter, with an exponential impulse response. The second is a matched filter.

1.   Spatial Noise With a Simple Low Pass Filter

Assume the filter has an exponential impulse response:

$$w(t) = \begin{cases} w_0 \, e^{-t/\tau_c} & t \geq 0 \\ 0 & t < 0. \end{cases}$$

where τ_c is the time constant. The transfer function is

$$|W(f)|^2 = \frac{w_0^2 f^2}{1 + (2\pi f \tau_c)^2}$$

Further, the integral of $w^2(t)$ and the square of the integral of $w(t)$ can be evaluated directly. Namely

$$\int_{-\infty}^{\infty} w^2(t)\, dt = w_0^2 \, \tau_c/2$$

$$\left(\int_{-\infty}^{\infty} w(t)\, dt \right)^2 = w_0^2 \, \tau_c^2$$

The expression for average power $\langle X^2(t) \rangle$ reduces to

$$\langle X^2(t) \rangle = \overline{a^2} A \overline{I^*} \nu T_s \left(\frac{w_o^2 \tau_c}{2} \right).$$

$$\cdot \left[1 + A T_s \frac{\overline{a}^2}{\overline{a^2}} \frac{\overline{I^{*2}}}{\overline{I^*}} \int_{-\infty}^{\infty} \left(\frac{\sin \pi T_s f}{\pi T_s f} \right)^2 e^{-4\pi^2 \sigma^2 f^2} \frac{2\tau_c}{1 + (2\pi \tau_c f)^2} df \right.$$

$$\left. + 2 \frac{\overline{a}^2}{\overline{a^2}} A \overline{I^*} \nu T_s \tau_c \right]$$

Note that the second term is the ratio of the spatial noise power to the photon noise power. The integral in the second term of $\langle X^2(t) \rangle$ can not be evaluated in closed form. It can be rewritten as

$$\frac{4}{\pi} \left(\frac{\tau_c}{T_s} \right)^2 \int_{-\infty}^{\infty} \left[\frac{\sin \left(\frac{1}{2} \frac{T_s}{\tau_c} v \right)}{v} \right]^2 e^{-(\sigma/\tau_c)^2 v^2} \frac{1}{1+v^2} dv$$

which only depends on the ratio of image diameter to slit width, and the ratio of the star transit time to the filter time constant. The image diameter is defined as the slit width that passes eighty percent of the image radiation. The diameter D equals 2.56 σ. The following function is graphed in Figures 16 and 17.
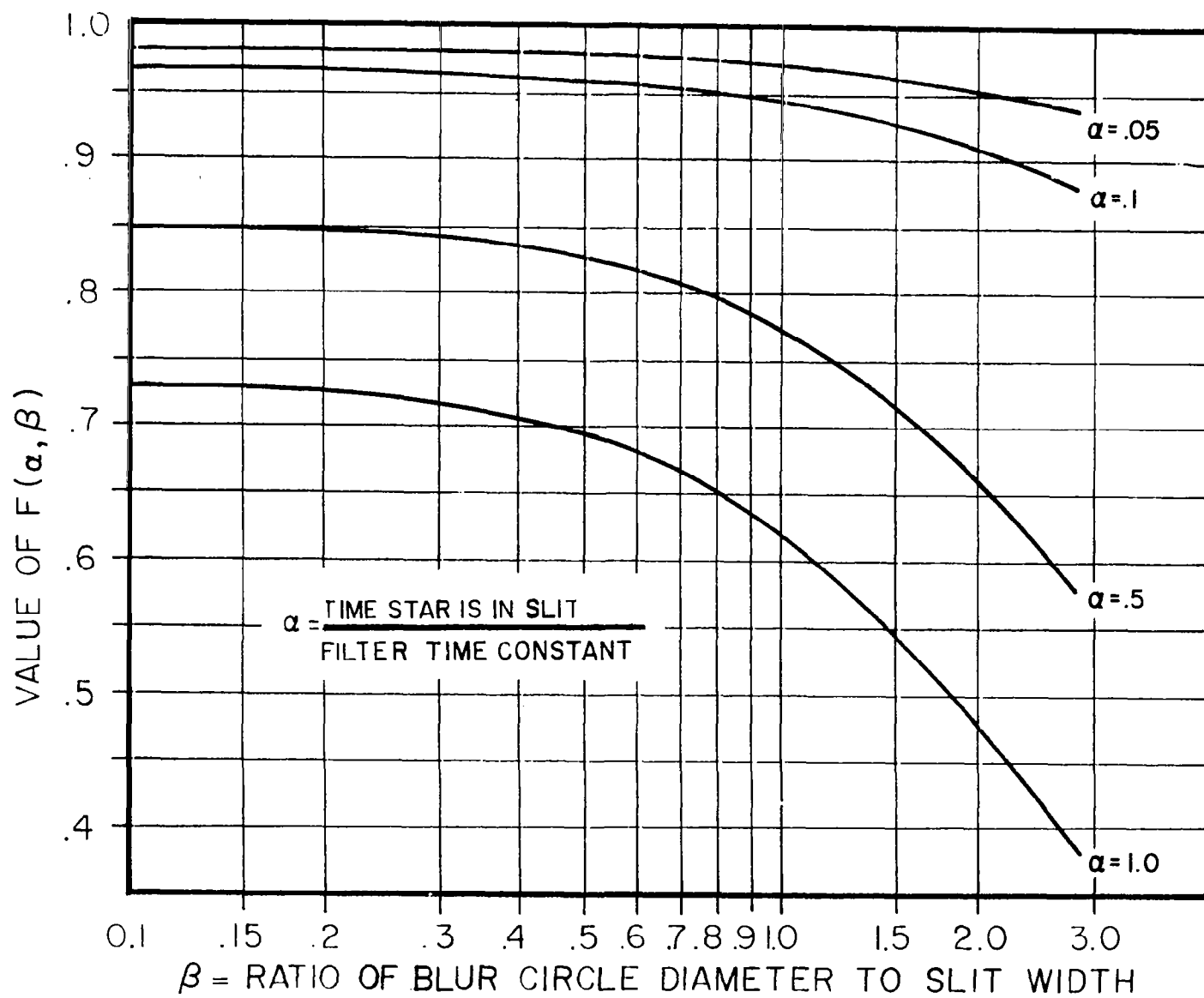
FIGURE 16: GRAPH OF $F(\alpha, \beta)$, $\alpha = .05$ TO 1.0

Axis labels (within figure):

VALUE OF $F(\alpha, \beta)$

$\alpha = \dfrac{\text{TIME STAR IS IN SLIT}}{\text{FILTER TIME CONSTANT}}$

β = RATIO OF BLUR CIRCLE DIAMETER TO SLIT WIDTH

Curve labels: $\alpha = .05$, $\alpha = .1$, $\alpha = .5$, $\alpha = 1.0$

$\alpha = \dfrac{\text{TIME STAR IS IN SLIT}}{\text{FILTER TIME CONSTANT}}$

$\alpha = 2$

$\alpha = 4$

$\alpha = 6$

$\alpha = 8$

$\alpha = 10$

VALUE OF $F(\alpha, \beta)$

$\beta =$ RATIO OF BLUR CIRCLE DIAMETER TO SLIT WIDTH
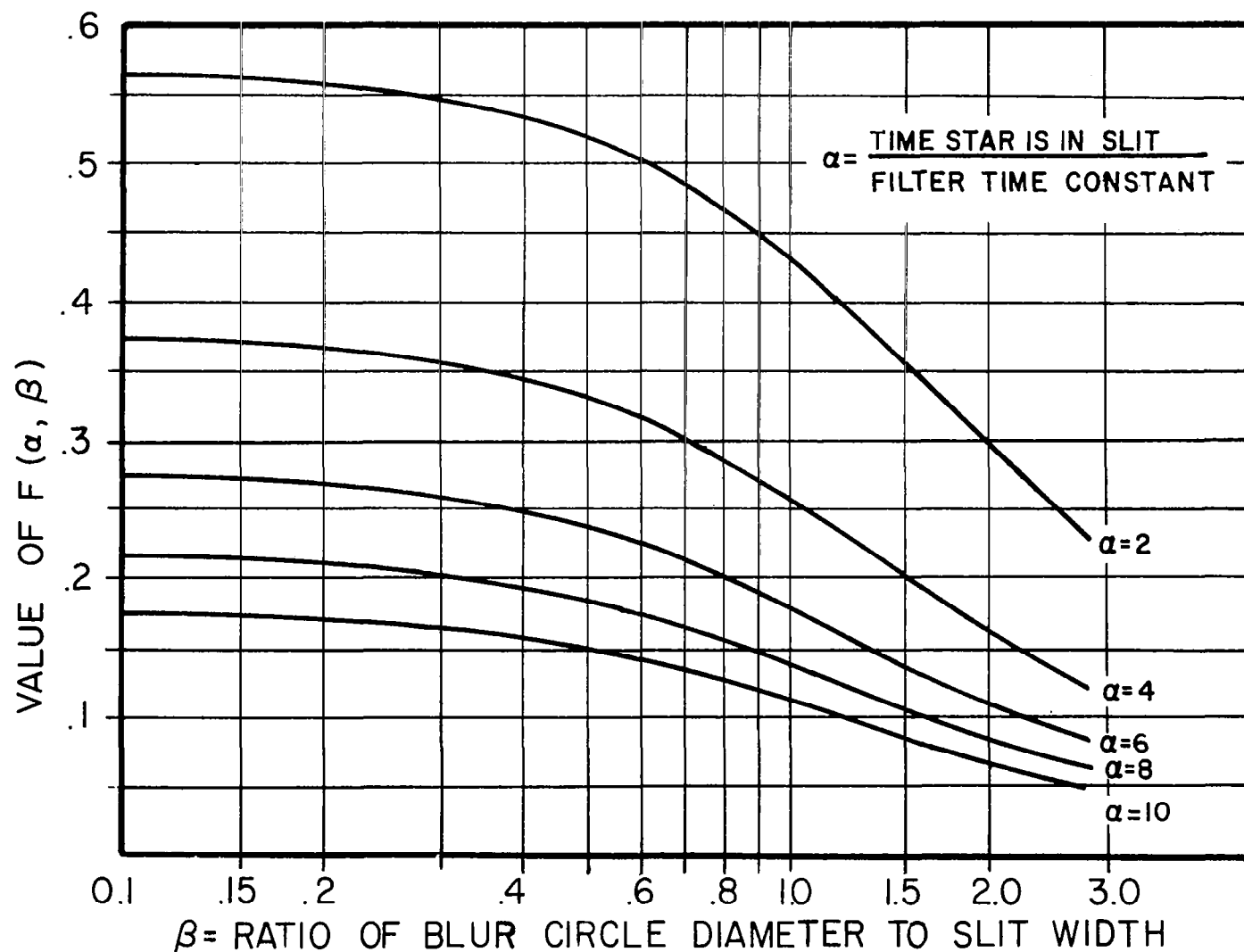
FIGURE 17: GRAPH OF $F(\alpha, \beta)$, $\alpha = 2$ TO 10

$$F(\alpha, \beta) = \frac{4}{\pi \alpha^2} \int_{-\infty}^{\infty} \left[\frac{\sin \alpha v/2}{v} \right]^2 \exp\left[-\frac{\alpha^2 \beta^2 v^2}{(2.56)^2} \right] \frac{1}{1+v^2} \, dv$$

where α corresponds to T_s/τ_c and β corresponds to D/T_s.

The "efficiency" of the filter can be measured by the ratio of rms output ripple to dc level. This ratio is

$$E = \frac{\left[1 + \frac{\overline{a}^2}{\overline{a^2}} \frac{\overline{I^{*2}}}{\overline{I^*}} A T_s F\left(\frac{T_s}{\tau_c}, \frac{D}{T_s}\right) \right]^{1/2}}{\left[2 \frac{\overline{a}^2}{\overline{a^2}} A \overline{I^*} \nu T_s \tau_c \right]^{1/2}}$$

To illustrate the effect of increasing the time constant τ_c, the ripple ratio is evaluated for a particular system using different time constants. Assume $\overline{a}^2/\overline{a^2}$ is 2/3; aperture area A is 20 square inches; limiting magnitude M_o is 3; transit time T_s is 5.6×10^{-5} seconds; the image diameter is equal to the slit width; slit area is .7 square degrees; optical efficiency is .5; quantum efficiency is .1. The ratio of rms ripple to dc level is graphed in Figure 18. Note that the star signal will be significantly distorted when the time constant is greater than the star transit time T_s.
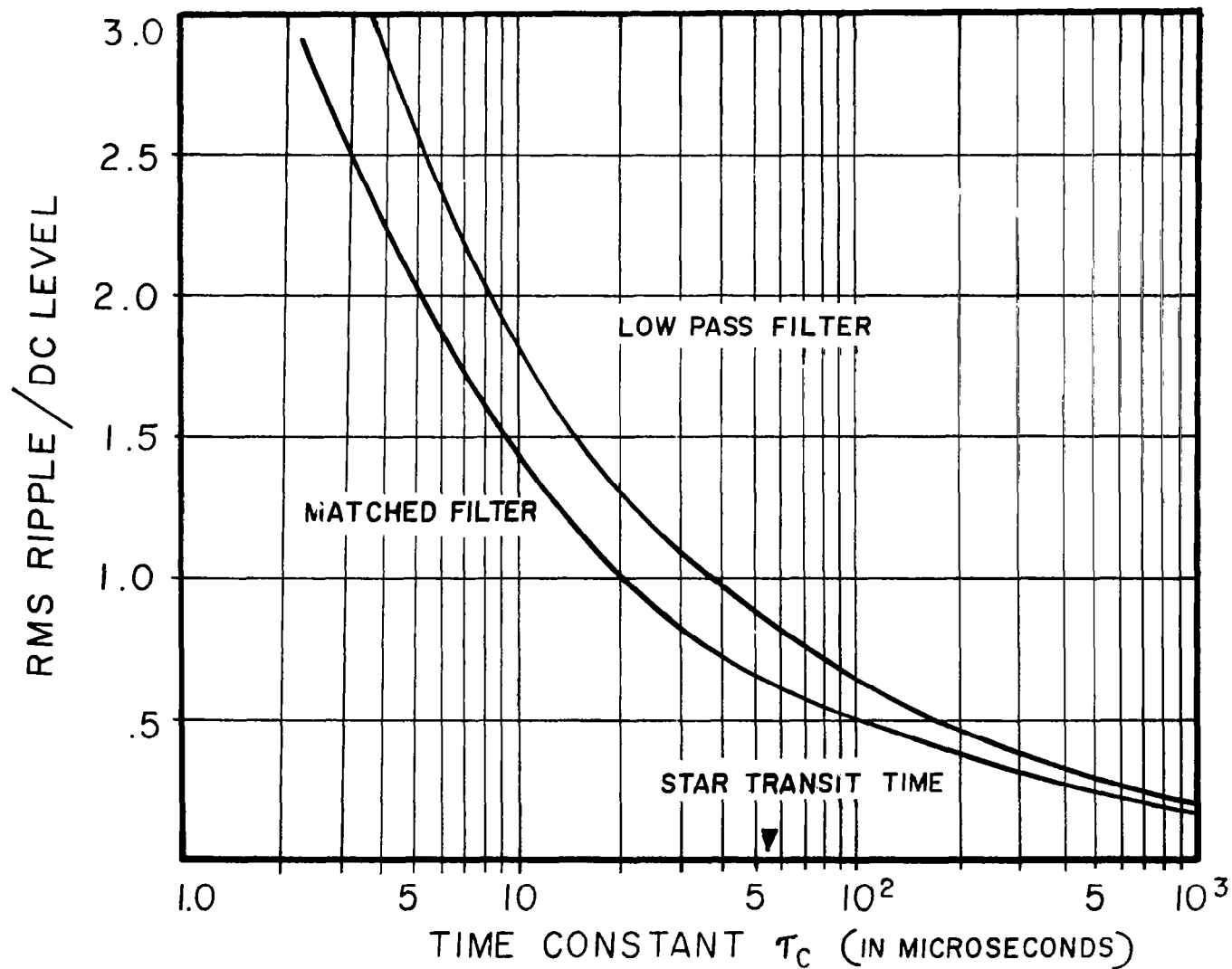
FIGURE 18: RATIO OF RMS RIPPLE TO DC LEVEL

2.   Spatial Noise With a Matched Filter

The signal from a bright star is described by $G(t)$. Hence a matched filter is one which has an impulse response proportional $G(t)$. In many cases of interest, $G(t)$ can be approximated by a Gaussian density. In addition, it is mathematically convenient to use a Gaussian density for the impulse response. Set

$$w(t) = w_o \, e^{-\frac{1}{2}(t/\tau_c)^2}$$

where w_o and τ_c are the filter parameters. The transfer function is

$$|W(f)|^2 = 2\pi \, w_o^2 \, \tau_c^2 \, e^{-(2\pi f \tau_c)^2}$$

The integral of $w^2(t)$ and the square of the integral of $w(t)$ can be evaluated directly. Namely,

$$\int_{-\infty}^{\infty} w^2(t)\, dt = \sqrt{\pi} \; \tau_c \, w_o^2$$

$$\left[\int_{-\infty}^{\infty} w(t)\, dt \right]^2 = 2\pi \, \tau_c^2 \, w_o^2$$

The integral involved in the ac component of the spatial noise can also be evaluated, namely,

$$\int_{-\infty}^{\infty} \left[\frac{\sin \pi T_s f}{\pi T_s f} \right]^2 e^{-4\pi^2 f^2 \sigma^2} |W(f)|^2 df$$

$$= 2\pi W_o^2 \tilde{T}_c^2 \int_{-\infty}^{\infty} \left[\frac{\sin \pi T_s f}{\pi T_s f} \right]^2 e^{-4\pi^2 f^2 (\sigma^2 + \tilde{T}_c^2)} df$$

$$= 4\pi W_o^2 \frac{T_c^2}{T_s} \left\{ \Phi\left(\frac{T_s}{\sqrt{2} \sqrt{\sigma^2 + \tilde{T}_c^2}} \right) - \frac{1}{2} \right.$$

$$+ \frac{\sqrt{2} \sqrt{\sigma^2 + \tilde{T}_c^2}}{T_c} \left[\phi\left(\frac{T_s}{\sqrt{2} \sqrt{\sigma^2 + \tilde{T}_c^2}} \right) - \phi(0) \right] \right\}$$

Hence, the noise power is

$$\langle X^2(t) \rangle = \sqrt{\pi}\ \overline{a^2}\ A \overline{I^*} \nu T_s \tilde{T}_c W_o^2$$

$$\cdot \left\{ 1 + 4\sqrt{\pi}\ A \tilde{T}_c\ \frac{\overline{a}^2}{\overline{a^2}}\ \frac{\overline{I^{*2}}}{\overline{I^*}} \left[\Phi\left(\frac{T_s}{\sqrt{2} \sqrt{\sigma^2 + \tilde{T}_c^2}} \right) - \frac{1}{2} \right.\right.$$

$$\left. + \frac{\sqrt{2} \sqrt{\sigma^2 + \tilde{T}_c^2}}{T_s} \left(\phi\left(\frac{T_s}{\sqrt{2} \sqrt{\sigma^2 + \tilde{T}_c^2}} \right) - \phi(0) \right) \right]$$

$$\left. + 2\sqrt{\pi}\ \frac{\overline{a}^2}{\overline{a^2}}\ A \overline{I^*} \nu T_s \tilde{T}_c \right\}$$

To illustrate the effect of increasing the time constant τ_c, the ripple ratio E is evaluated with the specific set of system parameters used above, for different time constant values τ_c. The ratio is graphed in Figure 6. The ripple is smaller with the matched filter since it has a smaller band width for the same time constant.

3. Special Derivations

The Fourier transform of G(t) is

$$\mathcal{J}(f) = \int_{-\infty}^{\infty} G(t)\, e^{i2\pi ft}\, dt = \int_{-\infty}^{\infty} G(t)\, \cos(2\pi ft)\, dt$$

Substituting for G(t)   and integrating by parts, one obtains

$$\mathcal{J}(f) = \lim_{a \to \infty} \left\{ \int_{-a}^{a} \Phi\left(\frac{t}{\sigma} + \frac{T_s}{2\sigma}\right) \cos(2\pi ft)\, dt \right.$$

$$\left. - \int_{-a}^{a} \Phi\left(\frac{t}{\sigma} - \frac{T_s}{2\sigma}\right) \cos(2\pi ft)\, dt \right.$$

$$= \frac{1}{2\pi f} \lim_{a \to \infty} \left\{ \left[\Phi\left(\frac{t}{\sigma} + \frac{T_s}{2\sigma}\right) \sin(2\pi ft) \right]_{-a}^{a} \right.$$

$$- \int_{-a}^{a} \phi\left(\frac{t}{\sigma} + \frac{T_s}{2\sigma}\right) \sin(2\pi ft)\, dt \; - \left[\Phi\left(\frac{t}{\sigma} - \frac{T_s}{2\sigma}\right) \sin(2\pi ft) \right]_{-a}^{a}$$

$$\left. + \int_{-a}^{a} \phi\left(\frac{t}{\sigma} - \frac{T_s}{2\sigma}\right) \sin(2\pi ft)\, dt \right\}$$

$$= \frac{1}{2\pi f} \lim_{a \to \infty} \left\{ \int_{-a}^{a} \phi\left(\frac{t}{\sigma} - \frac{T_s}{2\sigma}\right) \sin(2\pi ft)\, dt \right.$$

$$\left. - \int_{-a}^{a} \phi\left(\frac{t}{\sigma} + \frac{T_s}{2\sigma}\right) \sin(2\pi f \quad dt \right\}$$

III-82

With a linear change of variables and application of the trigonometric

identity for the sum of two angles, one obtains

$$
\mathcal{Q}(f) = \frac{1}{2\pi f} \lim_{a \to \infty} \left\{ \int_{-a/\sigma - T_s/2\sigma}^{a/\sigma - T_s/2\sigma} \phi(x) \sin 2\pi f\left(\sigma x + \frac{T_s}{2}\right) dx \right.
$$

$$
- \int_{-a/\sigma + T_s/2\sigma}^{a/\sigma + T_s/2\sigma} \phi(x) \sin 2\pi f\left(\sigma x - \frac{T_s}{2}\right) dx
$$

$$
= \frac{1}{2\pi f} \lim_{a \to \infty} \left\{ \int_{-a/\sigma - T_s/2\sigma}^{a/\sigma - T_s/2\sigma} \phi(x) \sin(2\pi f \sigma x) \cos(\pi f T_s) dx \right.
$$

$$
+ \int_{-a/\sigma - T_s/2\sigma}^{a/\sigma - T_s/2\sigma} \phi(x) \cos(2\pi f \sigma x) \sin(\pi f T_s) dx
$$

$$
- \int_{-a/\sigma + T_s/2\sigma}^{a/\sigma + T_s/2\sigma} \phi(x) \sin(2\pi f \sigma x) \cos(\pi f T_s) dx
$$

$$
+ \int_{-a/\sigma + T_s/2\sigma}^{a/\sigma - T_s/2\sigma} \phi(x) \cos(2\pi f \sigma x) \sin(\pi f T_s) dx
$$

$$
= \frac{1}{\pi f} \sin(\pi f T_s) \int_{-\infty}^{\infty} \phi(x) \cos(2\pi f \sigma x) dx
$$

$$
= \frac{1}{\pi f} \sin(\pi f T_s) \, e^{-2(\pi f \sigma)^2}
$$

This is the required result.

IV.   INFORMATION CONTENT OF PHOTOELECTRIC STAR IMAGES

Celestial navigation sensors and certain types of astronomical techniques use photoelectric imaging of star fields. In particular, navigation sensors use image tubes or special phototubes, others use moving slits with a simple photomultiplier.[*] Astronomical techniques using image orthicons and image converters are currently being developed, as described by Hiltner (1960). In these applications, stars must be detected against a noise background. In most applications, one must also accurately locate the star image in the field of view and estimate its intensity.

The sensor introduces randomness at three different points in the image sensing, see Figure 1. The phototube has internal noise that limits its information capacity and detecting ability.[**] The scanning process also has certain intrinsic limitations.[***] Third, the photon noise, optical aberrations, and

---

[*]   Lillestrand and Carroll (1961) and Kenimer and Walsh (1964).

[**]   Jones (1960 a, b)

[***]   Beall (1964) and Farrell and Zimmerman (1965).
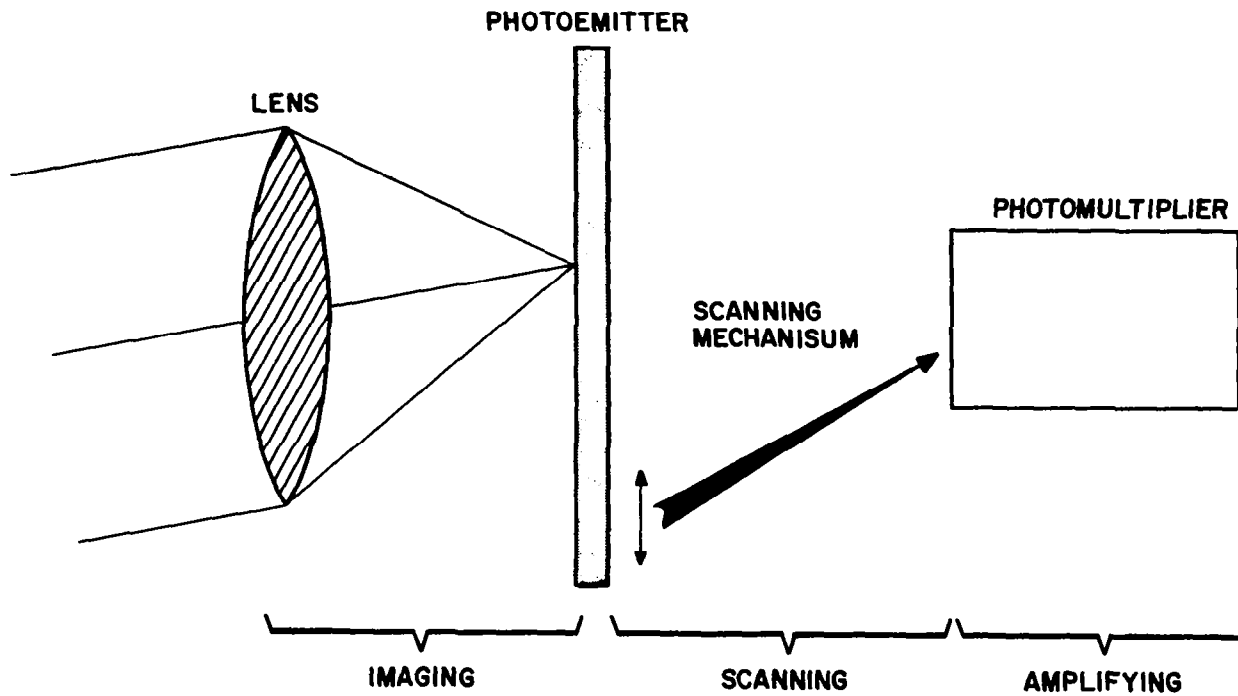
FIGURE I: BASIC ELEMENTS OF SENSOR

stellar background limit the information one can extract from the photo-
electric star image. This third source of randomness is the primary concern
in the following discussion. The basic problem can be stated as follows.
Starlight is focused on a photoemissive surface to form an aberrated image.
For a fixed exposure time one obtains a charge distribution. The distri-
bution is different for each exposure because of the quantum nature of the
emissions. In addition, the stellar background produces an overall charge.
The basic problem is to detect the presence of a star and estimate its
position and intensity. The objective of this section is to determine the
detectability of such two dimensional photoelectric images, and to determine
the limiting accuracy of position and intensity estimation. These limits
represent the "information content" of the image and describe the ultimate
capability of any sensor, independent of the phototube and scanning method.

Detection and resolution limits have been discussed previously by Helstrom
(1964). Most of his results on detection are derived for a signal-to-
noise ratio much less than one. This is not the case in most stellar appli-
cations. Also, he assumes the observation interval is sufficiently long to
obtain a large number of emissions. In stellar applications of interest,
one does not have a large number of counts. In the following discussion,
both large and small signal-to-noise ratios are considered; and the average
number of counts is not restricted. Helstrom briefly describes accuracy
limits of parameter estimation for a large signal-to-noise ratio. In the
following discussion of estimation, the signal-to-noise ratio is not restricted.

Preliminary results on the information content of quantized random surfaces have been developed by Swerling (1962). His objective is to determine the number of bits required to describe a random surface. Extending this analysis, one could obtain a second bound on the limiting accuracy of position and intensity estimation.

The basic statistical models used in this section are presented in Subsection A. Detectability is discussed in Subsection B; the accuracy limits of estimation are developed in Subsection C. A numerical example is given in Subsection D. The results are developed with star images in mind; nevertheless, several of the basic results can be applied to general images and background.

A. Radiation Model

Before discussing the information content of photoelectric images, it is necessary to select a statistical model for the radiation. Let V denote the region in the focal plane corresponding to the field of view, see Figure 2. Consider a particular star image in the field of view, with coordinates (x_0, y_0). Let λ_s denote the intensity of the star radiation entering the optical system. The intensity λ_s is expressed in photons per second (relative to the frequency at which the sensor has peak sensitivity). The star image can be described by an energy density function $G_s(x, y)$: vix., the energy falling in the small rectangle $(x, x + \Delta x)$ $(y, y + \Delta y)$ for a period T is

$$\lambda_s \, \epsilon_0 \, G_s(x - x_0, y - y_0) \, \Delta x \, \Delta y$$

where ϵ_0 is the optical efficiency.

The density $G_s(x, y)$ is normalized so that

$$\iint_V G_s(x, y) \, dx \, dy = 1$$

Hence, G_s describes the optical aberrations.

The "background" is all radiation entering the optical system that does not emanate from the star being considered. In most cases, the background consists of "randomly positioned" stars which are much weaker than the star being considered. Let λ_b denote the intensity of the background radiation entering the optical system. The intensity λ_b is expressed in photons per second (relative to the frequency at which the sensor has its peak sensitivity). The background image can be described by an energy density function

INTENSITY
DISTRIBUTION $G_s(x,y)$

$(x_1 y_1)$

Y

X

(x_2, y_2)

FIELD OF
VIEW V

(not to scale)

PHOTOEMITTER
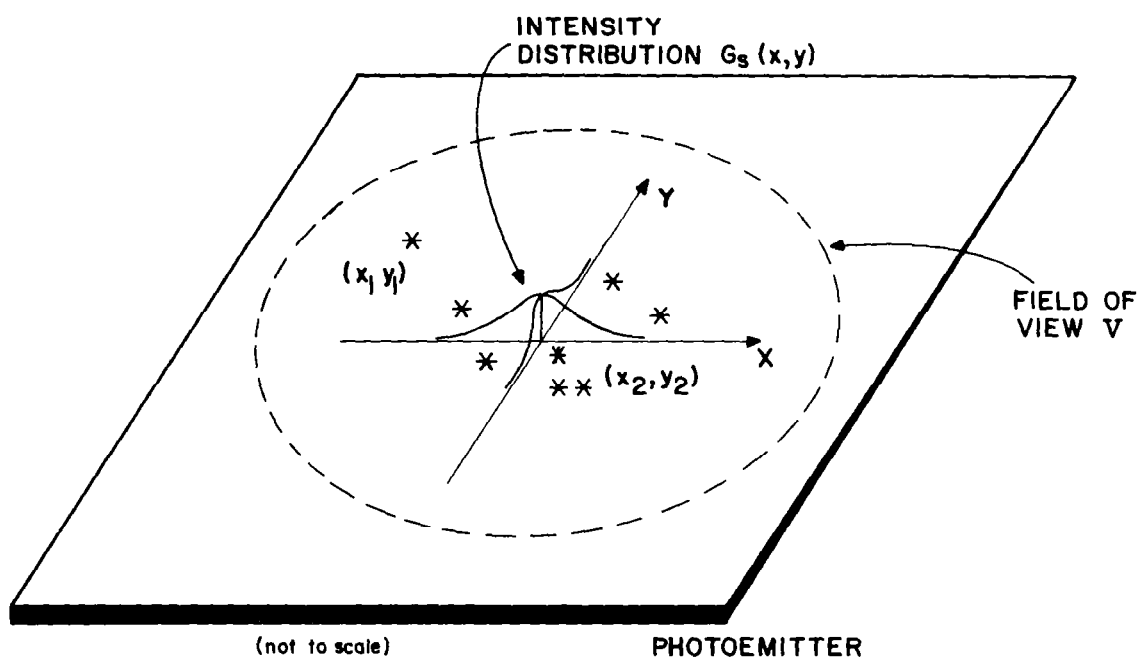
FIGURE 2: STATISTICAL MODEL

$G_b(x, y)$: viz., the energy falling in a small rectangle $(x, x + \Delta x)$

$(y, y + \Delta y)$ for a period T is

$$\lambda_b \epsilon_o T G_b(x, y) \; \Delta x \; \Delta y$$

The density $G_b(x, y)$ is normalized so that

$$\iint_V G_b(x, y) \; dx \; dy = 1$$

A photoemissive surface is placed at the focal plane. Let ϵ_q be the quantum efficiency, i.e., number of electrons emitted per incident photon.[*] The statistical model of the photoelectric emissions over the field of view is defined by the following assumptions:

(i) the number of photoelectric emissions from disjoint regions are statistically independent

(ii) the number of photoelectric emissions in T seconds from a region R is a Poisson random variable with mean[**]

$$\epsilon_o \epsilon_q T \iint_R \left[\lambda_s G_s(x - x_o, y - y_o) + \lambda_b G_b(x, y) \right] dx \; dy$$

---

[*] In practice, the overall efficiency $\epsilon_o \, \epsilon_q$ must be corrected for spectral characteristics of the optical system, the spectral response of the sensor, and the stellar spectrum.

[**] For the intensity and spectral characteristics of stellar radiation, these assumptions are physically reasonable. The characteristics of photo-electric emissions are discussed by L. Mandel (1958, 1959).

The mean number of photoelectric emissions over the entire field of view is

$$\bar{N} = \epsilon_o \epsilon_q [\lambda_s + \lambda_b] T$$

for a period of T seconds.

To determine the "information content" of the star image, assume the position of each photoelectric emission can be measured. Let N denote the number of emissions in the period (O, T); and let (X_1, Y_1), (X_2, Y_2)---denote the positions of the first, second, --- photoemission in period (O, T). See Figure 2. One can determine the joint probability density function of (X_1, Y_1)---(X_N, Y_N) conditional on obtaining N photoemissions. Consider the "small" rectangles defined by

$$r_1 ; (x_1, x_1 + \Delta x_1) (y_1, y_1 + \Delta y_1)$$

$$r_2 ; (x_2, x_2 + \Delta x_2) (y_2, y_2 + \Delta y_2)$$
$$\cdot$$
$$\cdot$$
$$\cdot$$
$$r_N ; (x_N, x_N + \Delta x_N) (y_N, y_N + \Delta y_N).$$

Let P_N denote probability of obtaining N photoemissions, and let p_j denote the probability of obtaining one photoemission in r_j. Let p_o be the probability of obtaining no emissions outside of the N rectangles.

Then

$$\frac{1}{N!} \prod_{j=0}^{N} p_j$$

is the probability of obtaining exactly N photoemissions with the jth

emission in r_j during the period (O, T). Hence, the joint density function

of $(X_1, Y_1)---(X_N Y_N)$ conditional on obtaining N photoemissions is

$$\lim_{\substack{\Delta x_k \to 0 \\ \Delta y_k \to 0}} \left\{ \frac{\frac{1}{N!} \prod_{j=0}^{N} P_j}{P_N \prod_{j=1}^{N} (\Delta x_j \, \Delta y_j)} \right\}$$

Further, $p_j = \mu_j \, e^{-\mu_j}$ where

$$\mu_j = \epsilon_o \epsilon_q T \iint_{r_j} \left[\lambda_s G_s(x - x_o, y - y_o) + \lambda_b G_b(x, y) \right] \, dx \, dy$$

and $P_N = \frac{(\bar{N}_o)^N}{N!} e^{-\bar{N}}$.

Then

$$\frac{\frac{1}{N!} \prod_{j=0}^{N} P_j}{P_N \prod_{k=1}^{N} (\Delta x_k \, \Delta y_k)} = \frac{\prod_{j=0}^{N} \mu_j}{(\bar{N})^N \prod_{k=1}^{N} (\Delta x_k \, \Delta y_k)}$$

Since

$$\lim \left[\frac{\mu_j}{\Delta x_j \, \Delta y_j} \right] = \epsilon_o \epsilon_q T \left[\lambda_s G_s(x_j - x_o, y_j - y_o) + \lambda_b G_b(x_j, y_j) \right]$$

the joint density of (x_i, y_i)'s is

$$f_N(x_1, y_1, \cdots, x_N, y_N) = \prod_{j=1}^{N} \left[\frac{\lambda_s G_s(x_j - x_o, y_j - y_o) + \lambda_b G_b(x_j, y_j)}{\lambda_s + \lambda_b} \right]$$

Note that the density is independent of the duration of the observation. The position coordinates can be interpreted as N independent, identically random variables with a density function

$$\frac{\lambda_s G_s(x - x_o, y - y_o) + \lambda_b G_b(x, y)}{\lambda_s + \lambda_b}$$

Also the distribution of the ith emission and the number of emissions N are independent random variables, provided $N \geq i$.

For a given "image" (x_1, y_1), (x_2, y_2),...(x_N, y_N), one must decide whether or not a star is present; and if a star is present, estimate its position (x_o, y_o) and intensity λ_s. The background intensity $\lambda_b G_b(x, y)$ is assumed to be known near the star image. In most cases of interest $\lambda_b G_b(x, y)$ is small compared to λ_s. Also $G_b(x, y)$ is assumed to be relatively constant near the star image. Using these assumptions, detectability is discussed in the next section.

B. **Detectability**

Detectability of signals in noise has been studied extensively for simple time dependent signals, such as radar returns. These problems are essentially one dimensional. On the other hand, detection of star images in a noise background is essentially a two dimensional problem. Spatial filters can be used to detect two dimensional images similar to the way in which temperal filters are used to detect one dimensional signals. Lugt (1964) describes a technique for image detection which is intrinsically two-dimensional. A spatial filter is used that maximizes the output signal-to-noise ratio. Montgomery and Broome (1962) have used a similar technique based on sampling data from the image. In particular, the image is sampled at regular intervals over the field of view. If the spacing of the sampling points is comparable to the optical resolution, the image is accurately represented by the sampled values; detection is based on the sampled values. These two detection techniques are developed with bright images in mind. The following results are based on individual photoelectric emissions, and thus represent the detection limits for strong as well as weak stars. To determine the detectability of a star image the position and intensity of the star are assumed to be known (when the star is present), say (x_o, y_o) and λ_1. Later this restriction is removed.

Detection is basically a statistical problem of testing the hypothesis that $\lambda_s = 0$ as opposed to $\lambda_s = \lambda_1$. There are two types of errors: Type I-- a star is "detected" when no star is present, Type II--a star is not detected when a star is present. In practice, most false star detections can be eliminated by comparison to stored star charts. On the other hand, if a star is missed, the system accuracy is reduced; and it may be impossible to obtain the required results. Hence, the goal is to select a detection method that minimizes the probability of a Type II error for a fixed probability of a Type I error.

The optimum detection method is based on the likelihood ratio test statistic $\mathcal{J}$, which is a function of (x_1, y_1), $(x_2, y_2),\ldots,$ (x_N, y_N).[*] If $\mathcal{J}$ is larger than a specified constant C_P, a star is said to be present. If $\mathcal{J}$ is less than C_P, no star is detected. The constant C_P is selected so that the probability of a Type I error is P. The probability of a Type II error is then minimized; a proof is given in subsection IV.E.1. The likelihood ratio is

$$\frac{\left[f_N(x_1, y_1, \ldots, x_N, y_N) \, P_N\right]_{\lambda_s = \lambda_1}}{\left[f_N(x_1, y_1, \ldots, x_N, y_N) \, P_N\right]_{\lambda_s = 0}} .$$

---

[*] Likelihood detection techniques are discussed in detail by L. A. Wainstein and V. D. Zubakov (1962), Chapter 5.

The corresponding test statistic is

$$\mathcal{J} = \prod_{j=1}^{N} \left[\frac{\lambda_1 G_s(x_j-x_o, y_j-y_o) + \lambda_b G_b(x_j, y_j)}{\lambda_b G_b(x_j, y_j)} \right]$$

Note that $\mathcal{J}$ is independent of the observation duration T, the optical efficiency ϵ_o and the quantum efficiency ϵ_q. A test based on $\ln \mathcal{J}$ is equivalent to a test based on $\mathcal{J}$. Namely, a star is present if $\ln \mathcal{J}$ is greater than $\ln C_p$. In this section we will discuss the test based on $\mathcal{J}' = \ln \mathcal{J}$, with $\ln C_p = C_p'$. It is interesting to note that the test statistic $\mathcal{J}'$ can be expressed in terms of a spatial filter

$$\mathcal{J}' = \iint_{-\infty}^{\infty} h(x,y) \sum_{j=1}^{N} \delta(x_j - x, y_j - y) \, dx \, dy$$

where $\delta(x, y)$ is the Dirac delta function. The impulse response of the spatial filter is

$$h(x,y) = \ln \left[\frac{\lambda_1 G_s(x-x_o, y-y_o) + \lambda_b G_b(x, y)}{\lambda_b G_b(x, y)} \right]$$

To determine the threshold C_p and the probability of a Type II error, it is necessary to use the distribution function of $\mathcal{J}'$. In general, one can not determine the distribution function of $\mathcal{J}'$ explicitly. On the other hand, the characteristic function of $\mathcal{J}'$ can be evaluated. In subsection IV.E.2,

we show that the logarithm of the characteristic function of $\mathcal{J}'$ is[*]

$$\bar{N} \iint\limits_{\infty}^{\infty} \left(\frac{\lambda_s \, G_s(x-x_o, y-y_o) + \lambda_b G_b(x,y)}{\lambda_s + \lambda_b} \right)$$

$$\cdot \left[\left(\frac{\lambda_1 \, G_s(x-x_o, y-y_o) + \lambda_b G_b(x,y)}{\lambda_b G_b(x,y)} \right)^{iu} - 1 \right] dx \, dy$$

where $\lambda_s = \lambda_1$ or 0. The mean and variance of $\mathcal{J}'$ are

$$E \, \mathcal{J}' = \bar{N} \iint\limits_{-\infty}^{\infty} \left(\frac{\lambda_s \, G_s(x-x_o, y-y_o) + \lambda_b G_b(x,y)}{\lambda_s + \lambda_b} \right)$$

$$\cdot \ln \left[\frac{\lambda_1 \, G_s(x-x_o, y-y_o) + \lambda_b G_b(x,y)}{\lambda_b G_b(x,y)} \right] \, dx \, dy$$

$$Var \, \mathcal{J}' = \bar{N} \iint\limits_{-\infty}^{\infty} \left(\frac{\lambda_s \, G_s(x-x_o, y-y_o) + \lambda_b G_b(x,y)}{\lambda_s + \lambda_b} \right)$$

$$\cdot \ln^2 \left[\frac{\lambda_1 G_s(x-x_o, y-y_o) + \lambda_b G_b(x,y)}{\lambda_b G_b(x,y)} \right] dx \, dy$$

This characteristic function is very similar to the characteristic function of a non-stationary temporial Poisson process. See E. Parzen (1962), p. 156.

One can approximate the distribution of $\mathcal{J}'$ by a gamma distribution with the same mean and variance, and then determine C_p' and the probability of a Type II error. In some applications, $\overline{N}$ is relatively small so the central limit theorem does not apply to the sum $\mathcal{J}'$, particularly when no star is present. Also $\mathcal{J}'$ is strictly positive. Hence, a gamma distribution is a better approximation to the distribution of $\mathcal{J}'$ than a normal distribution, in general. In some cases, a normal approximation is reasonable, and it may simplify the calculations. The probability that $\mathcal{J}' > C_p'$, when a star is present, is a measure of the detectability of a star image. Note that the above results can be applied to an arbitrary image and background since G_s and G_b are general intensity functions.

The test statistic $\mathcal{J}'$ can be simplified. For data points (x_j, y_j) with

$$\lambda_1 G_s(x_j - x_o, y_j - y_o) \ll \lambda_b G_b(x_j, y_j)$$

the corresponding term in $\mathcal{J}'$ is essentially zero. In general, the star image is localized to a small region about (x_o, y_o), and the background intensity $G_b(x, y)$ is slowly changing over the field of view. Hence, only data points near (x_o, y_o) effect the value of $\mathcal{J}'$. (A quantitative measure of nearness will be given below.) Further, $G_b(x_j, y_j)$ can be assumed to be constant in the region near (x_o, y_o). With these assumptions the test statistic reduces to

$$\mathcal{J}' = \sum_{j=1}^{N'} \ln\left[\frac{\lambda_1}{\lambda_b G_b} G_s(x_j - x_o, y_j - y_o) + 1 \right]$$

where N' is the number of data points near (x_0, y_0) and $G_b = G_b(x_0, y_0)$. This detection technique is similar to the technique described by Montgomery, in that detection is based on localized data points.

In the remainder of this section, $G_s(x, y)$ is assumed to be a Gaussian density function with zero mean and a covariance matrix[*]

$$\Sigma = \begin{pmatrix} \sigma_x^2 & \sigma_x \sigma_y \rho \\ \sigma_x \sigma_y \rho & \sigma_y^2 \end{pmatrix} .$$

Let

$$R^2 = \frac{1}{1 - \rho^2} \left[\frac{(x - x_0)^2}{\sigma_x^2} - \frac{2 \rho (x - x_0)(y - y_0)}{\sigma_x \sigma_y} + \frac{(y - y_0)^2}{\sigma_y^2} \right] .$$

The ellipse $R^2 \leq 1$ contains forty per cent of the star radiation. It is convenient to define the signal-to-noise ratio

$$r_1 = \frac{\lambda_1}{\pi |\Sigma|^{1/2} \lambda_b G_b} ,$$

which is the ratio of the total star radiation to the background radiation in the ellipse $R^2 \leq 1$ centered at (x_0, y_0). With these assumptions the

---

[*]   In practice the shape of the star image is not Gaussian. The characteristics of the image change across the field of view, and from one lens to another. A Gaussian model has the advantage of being functionally simple, and yet having three shape parameters σ_x, σ_y, ρ.

test statistic becomes

$$J' = \sum_{j=1}^{N'} \ln\left[\frac{r_1}{2} e^{-R_j^2/2} + 1 \right] , \qquad (1)$$

where R_j is the value of R at (x_j, y_j).

Further, one can now easily evaluate the moments of J' and then the approximate distribution of J' , see IV.E.2. The mean of J' becomes

$$\epsilon_o \epsilon_q T \lambda_s \left[F_1(r_1) + F_2(r_1)/r \right]$$

when $\lambda_s \neq 0$ and

$$\epsilon_o \epsilon_q T \lambda_1 F_2(r_1)/r_1$$

when $\lambda_s = 0$. The functions $F_1(r_1)$ and $F_2(r_1)$ are

$$F_1(r_1) = \left(1 + \frac{2}{r_1}\right) \ln\left(\frac{r_1}{2} + 1\right) - 1$$

$$F_2(r_1) = 2 \int_0^\infty \ln\left[\frac{r_1}{2} e^{-z} + 1 \right] dz$$

These functions are graphed in Figure 3.

IV-17
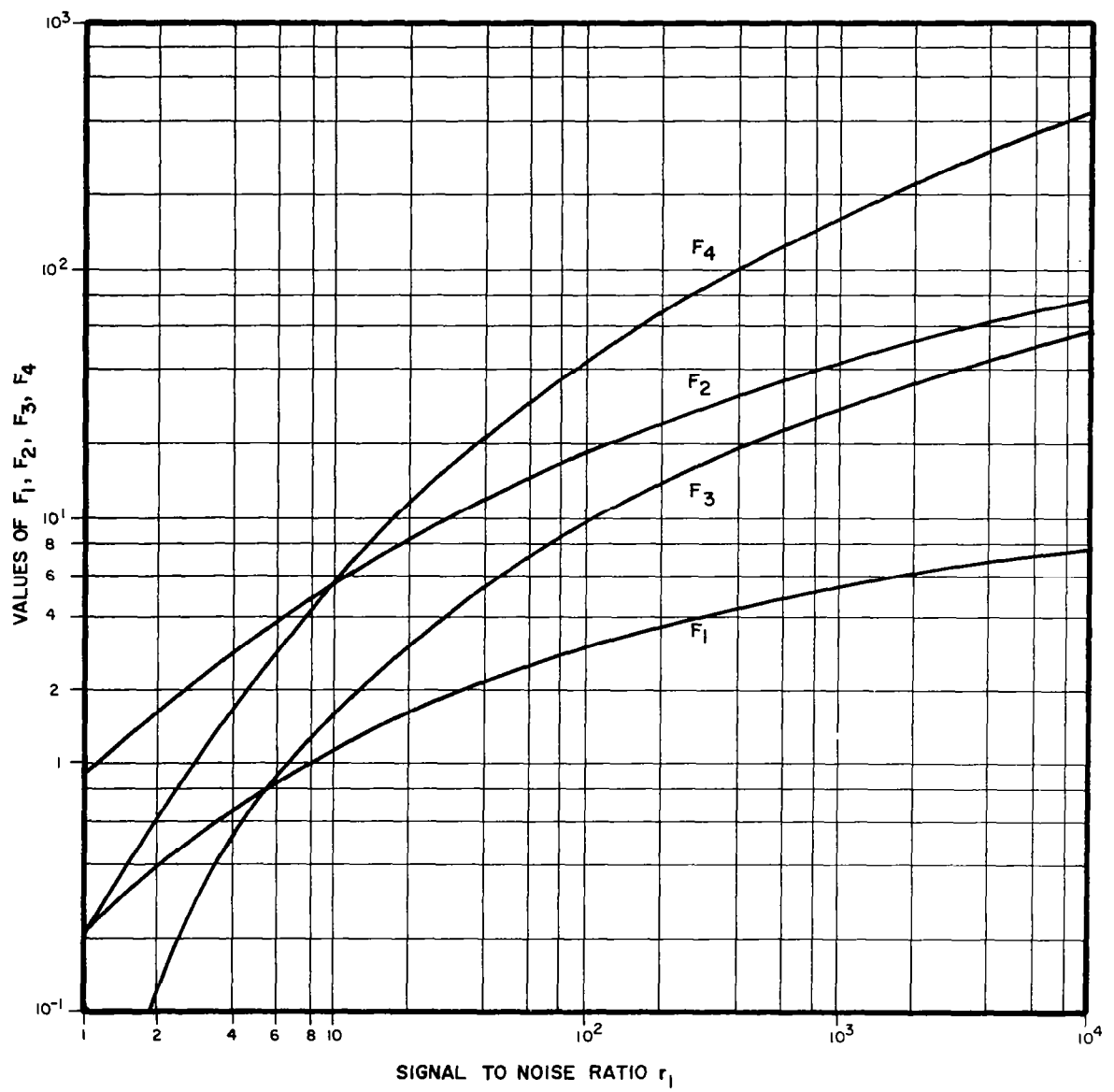
FIGURE 3: GRAPH OF F_1, F_2, F_3, F_4

Similarly, the variance of $\mathcal{J}'$ becomes

$$\epsilon_o \epsilon_q T \lambda_s \left[F_3(r_1) + F_4(r_1)/r \right]$$

when $\lambda_s \neq 0$ and

$$\epsilon_o \epsilon_q T \lambda_1 F_4(r_1)/r_1$$

when $\lambda_s = 0$. The functions $F_3(r_1)$ and $F_4(r_1)$ are

$$F_3(r_1) = \left(1 + \frac{2}{r_1}\right) \left[\ln^2\left(\frac{r_1}{2} + 1\right) - 2 \ln\left(\frac{r_1}{2} + 1\right) \right] + 2$$

$$F_4(r_1) = 2 \int_0^\infty \ln^2\left[\frac{r_1}{2} e^{-2} + 1\right] dz$$

These functions are graphed in Figure 3. Note for $r_1 \geqslant 10$, the variance of $\mathcal{J}'$ is greater than its mean; a normal distribution is not reasonable. The three basic parameters in $E\mathcal{J}'$ and $Var\,\mathcal{J}'$ are the expected number of emissions for the observed star $\epsilon_o \epsilon_q T \lambda_s$, the expected number of emissions for a target star $\epsilon_o \epsilon_q T \lambda_1$, the expected number of emissions

from the background in the ellipse $R^2 \leq 1$, $\pi \lambda_b G_b |\Sigma|^{1/2}$.

With the mean and variance, the distribution of $\mathcal{J}'$ can be approximated with a gamma distribution; the density function is

$$\frac{\alpha}{\Gamma(\beta)} (\alpha x)^{\beta-1} e^{-\alpha x}$$

where

$$\alpha = E\,\mathcal{J}' / Var\,\mathcal{J}'$$

$$\beta = (E\,\mathcal{J}')^2 / Var\,\mathcal{J}'.$$

Using this approximation, one can evaluate C_p and the probability of detecting a star with intensity λ_1. The probability of detection measures the detectability of the star. In addition, one can determine the probability of detecting an arbitrary star when the test is set for a star with intensity λ_1. This measures one's ability to discriminate against weak stars.

When the signal-to-noise ratio r is large or small, one can obtain special approximations to $\mathcal{J}'$. In most stellar applications r is large. In the following paragraphs, these approximations are developed.

1. Large Signal-To-Noise Ratio

To illustrate the relative significance of stellar and background radiation, an example will be presented using a typical set of system parameters. The average integrated starlight on the galactic equator is 184 tenth magnitude (photographic) stars per square degree.[*] The star being

---

[*] This data is from C. W. Allen (1963) p. 235.

observed is at the equator. Assume the area of the star image is one square minute of arc, i.e., $\pi |\Sigma|^{1/2} = 1$. Then the test statistic (1) becomes

$$J' = \sum_{j=1}^{N'} \ln\left[9.80 \times 10^4 \, e^{-.921M - R_j^2/2} + 1\right] \qquad (2)$$

where M is the photographic magnitude of the star observed. Data points with

$$9.80 \times 10^4 \, e^{-.921M - R_j^2/2} \leq 10^{-2}$$

are not "near" (x_o, y_o) and can be neglected. This inequality defines the elliptical region of interest; its "radius" is $R' = \sqrt{32.2 - 1.84M}$, which is graphed in Figure 4. When R_j is small, the second term in $\ln[\cdots]$ of (2) can be neglected. If most of the star data points occur near (x_o, y_o), the test statistic becomes

$$J' = N' \ln\left(9.80^4 \, e^{-.921M}\right) - \frac{1}{2} \sum_{j=1}^{N'} R_j^2 \qquad (3)$$

For data points with

$$9.80 \times 10^4 \, e^{-.941M - R_j^2/2} \geq 10^2$$

the second term in (2) can be neglected. This inequality defines an elliptical region of approximation with "radius" $R'' = \sqrt{13.8 - 1.84M}$
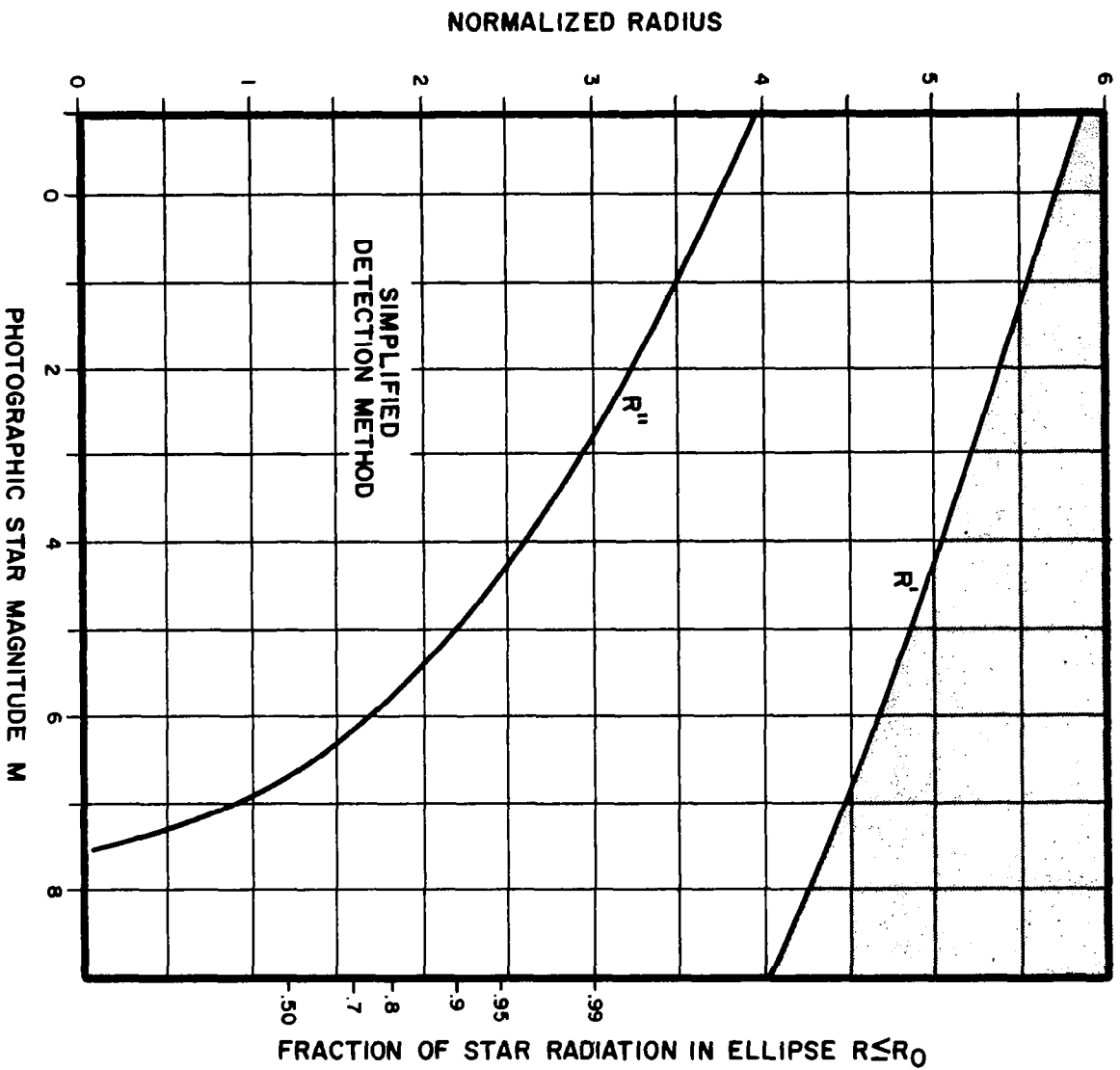
FIGURE 4: CRITICAL RADIUS FOR
APPROXIMATING $\smile$

This "radius" is graphed in Figure 4. For example, if one wished to detect a fourth magnitude star and $\sigma_x = \sigma_y = \frac{1}{\sqrt{\pi}}$ minutes of arc, data points more than 2.8 minutes of arc from the star image do not influence the probability of detection. Further, if one only considers data points 1.4 minutes of arc from (x_0, y_0), then the simple test statistic (3) may be used. This includes 95 per cent of the star data points, see Figure 4.

From the preceding discussion, one concludes that a detection technique based on statistic (3) is reasonable, and optimum in many cases of interest. In the following paragraphs, a detection technique based on (3) will be considered in detail: namely,

$$\left\{ \begin{array}{l} \text{If } J = 2N' \ln(r_1/2) - \sum_{j=1}^{N'} R_j^2 > C_p \qquad (4) \\[2mm] \text{a star is present. Only data points with } R_j \leq R_0 \text{ are considered;} \\[2mm] N' \text{ is the number of these data points.} \end{array} \right.$$

The "radius" R_0 is selected so that the fraction f of star radiation in the ellipse $R \leq R_0$ is near unity (.9 or .95); the fraction f is included in Figure 4.

$$f = \iint\limits_{R \leq R_0} G_s(x,y) \, dx \, dy$$

The constant C_p is selected so that the probability of a Type I error is P. This detection technique will "detect" a star when many closely spaced emissions are observed.

The detection technique (4) has a simple implementation in terms of a spatial filter. The spatial impulse response is

$$h(x,y) = \begin{cases} 2\ln\left(\dfrac{r_1}{2}\right) - R^2(x,y) & R \le R_o \\ 0 & \text{otherwise} \end{cases} \tag{5}$$

where

$$R^2(x,y) = \frac{1}{1+\rho^2}\left[\frac{(x-x_o)^2}{\sigma_x^2} - \frac{2\rho(x-x_o)(y-y_o)}{\sigma_x\,\sigma_y} + \frac{(y-y_o)^2}{\sigma_y^2}\right]$$

Since R_o was selected so that the first term in $\ln[\cdots]$ of (1) is greater than unity, $h(x, y) \ge 0$.

2. Small Signal-To-Noise Ratio

    If r_1 is small, say less than one-fifth, statistic (1) can be approximated by

$$J' \approx \sum_{j=1}^{N'} \frac{r_1}{2}\, e^{-R_j^2/2}$$

The corresponding impulse response function is

$$h(x,y) = \begin{cases} \dfrac{r_1}{2}\, e^{-R^2(x,y)/2} & R(x,y) \le R_o \\ 0 & \text{otherwise} \end{cases}$$

This is essentially a matched filter since the impulse response $h(x, y)$ and signal $G_s(x - x_o, y - y_o)$ are proportional.

It is interesting to compare the impulse response functions for different signal-to-noise ratios. Assume h(x, y) is normalized so that $h(x_0, y_0) = 1$. The function value h is graphed in Figure 5 for different values of r_1, as a function of R. For $r_1 \geq 10$, (5) is graphed. When r_1 is large, the detection technique is primarily dependent on the number of emissions for which $R \leq R_0$. In other words, the optimum detection technique is based on the light intensity in an elliptical region about (x_0, y_0). When r_1 is small, the decision also depends on the spatial distribution of the emissions.

3. Remarks

In practice the star position (x_0, y_0) is unknown, and the detection techniques must be modified. In particular, the likelihood ratio test statistic becomes

$$J^* = \MAX_{(x_0, y_0) \in V} \prod_{j=1}^{N} \left[\frac{\lambda_1 G_s(x_j - x_0, y_j - y_0) + \lambda_b G_b(x_j, y_j)}{\lambda_b G_b(x_j, y_j)} \right]$$

A star is present if $J^* > C_p^*$, where C_p^* is determined by the probability of a Type I error. In many cases of interest, J^* reduces to

$$\MAX_{(x_0, y_0) \in V} \left[2N'\left(\frac{r_1}{2}\right) - \sum_{j=1}^{N'} R_j^2 \right]$$

Only data points with $R_j \leq R_0$ are considered; N' is the number of these
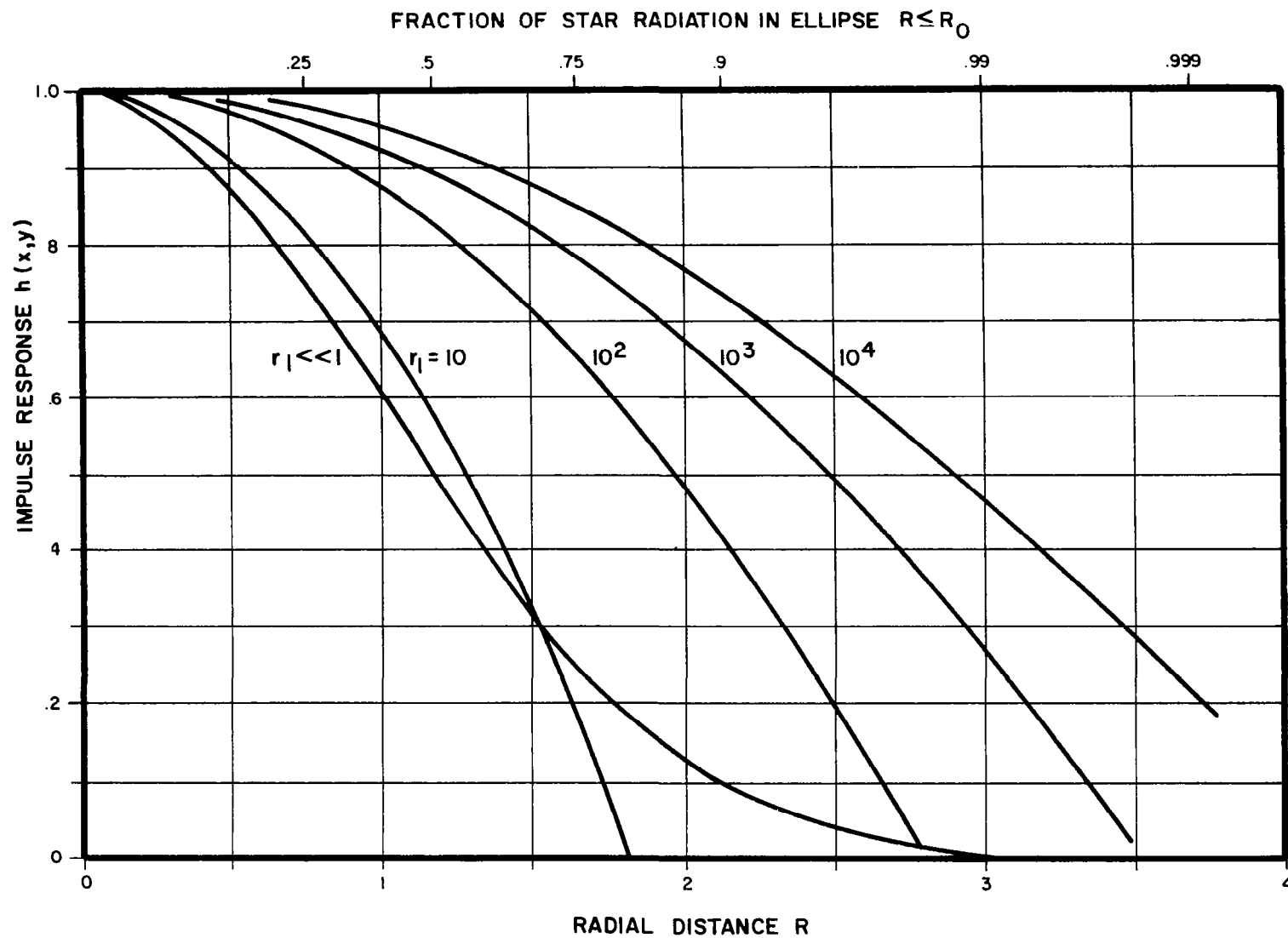
FIGURE 5: IMPULSE RESPONSE

data points. When the signal-to-noise ratio r_1 is large, the optimum detection technique is to scan the field of view with an elliptical region ($R \leq R_0$), and base detection on the peak radiation in this scanning region. When the signal-to-noise ratio r_1 is low, the optimum detection technique is to scan the field of view with the spatial filter (5), and base detection on the peak output from the filter.

The value of (x_0, y_0) that maximizes $\mathcal{J}'$ is the maximum likelihood estimates of (x_0, y_0). Hence, the preceding detection technique yields an estimate of the position of the star image. After detecting a star and estimating its position, one can estimate its intensity. The maximum likelihood estimate of λ_s is

$$\hat{\lambda}_s = \frac{N' - \epsilon_0 \epsilon_q T (\pi \sigma_x \sigma_y \lambda_b G_b)}{\epsilon_0 \epsilon_q f T}$$

where N' is the number of points for which $R_j \leq R_0$. The mean of $\hat{\lambda}_s$ is λ_s; the variance of $\hat{\lambda}_s$ is

$$\frac{\lambda_s f + \pi \sigma_x \sigma_y \lambda_b G_b}{\epsilon_0 \epsilon_q f^2 T} .$$

In the following section, lower bounds are derived for the variance of position and intensity estimates; these bounds represent the ultimate capability of any sensor.

The stellar background has effectively a homogeneous component and a granular component. The homogeneous component results from weak stars

that are closely spaced; this component changes slowly across the field

of view. The granular component results from stars slightly below the

brightness level of interest, λ_1. In the preceding paragraphs, we were

primarily interested in detection techniques to discriminate between the

homogeneous background and star images. To discriminate against the granular

background, one must combine detection and intensity estimation. In parti-

cular, when a star is detected, its intensity is estimated. If the intensity

estimate is not large enough, the detection is ignored.

C.   Accuracy Limits for Position and Intensity Measurements

In this section, the ultimate capability of sensors to estimate the position and intensity of a star image is derived. In particular, lower bounds are derived for the variance of position and intensity estimates using a Cramer-Rao bound.[*] These bounds are independent of the estimation technique, and thus represent the ultimate capability or "information limit" of the sensor.

Assume there is one star image in the field of view. Let $(\hat{x}_0, \hat{y}_0)$ and $\hat{\lambda}_s$ be estimates of the position (x_0, y_0) and intensity λ_s of the star image based on the observed values $(x_1, y_1) \ldots (x_N, y_N)$. Assume the mean value of the estimates are (x_0, y_0) and λ_s, respectively. The variability of the estimates can be measured in several ways. The variability of $\hat{\lambda}_s$ will be measured by its variance, $\mathrm{Var}\,(\hat{\lambda}_s)$. The variability of $(\hat{x}_0, \hat{y}_0)$ will be measured by its generalized variance

$$ S = \mathrm{Var}\,\hat{x}_0 \; \mathrm{Var}\,\hat{y}_0 \; (1 - \hat{\rho}^2) $$

where $\hat{\rho}$ is the correlation between $\hat{x}_0$ and $\hat{y}_0$. The generalized variance S measures the joint variability of $\hat{x}_0$ and $\hat{y}_0$. It increases with $\mathrm{Var}\,\hat{x}_0$ and

[*]   Cramer, H. (1958), p. 477. Also, Swerling (1964) has obtained similar results for waveform parameter estimation.

Var $\hat{y}_0$, and decreases with $|\hat{\rho}|$. Further S is invariant under orthogonal transformations of $(\hat{x}_0, \hat{y}_0)$.

The generalized variance S has an interesting geometrical interpretation. Let $\hat{\Sigma}$ be the covariance matrix of $(\hat{x}_0, \hat{y}_0)$. Note that $|\hat{\Sigma}| = S$. The area of the ellipse defined by

$$E_c = \left\{ (x - x_0, y - y_0) \, \hat{\Sigma}^{-1} \begin{pmatrix} x - x_0 \\ y - y_0 \end{pmatrix} \leq C \right\}$$

is $\pi C |\hat{\Sigma}|^{1/2} = \pi C S^{1/2}$. Further, the probability that $(\hat{x}_0, \hat{y}_0) \in E_c$ is $P(\chi_2^2 \leq C)$, when $(\hat{x}_0, \hat{y}_0)$ are normally distributed. In the following paragraphs a lower bound is derived for S which is independent of the estimators $\hat{x}_0$ and $\hat{y}_0$. Hence, the confidence ellipse E_c has a minimum area, at a fixed level. In other words, one can change the variance of the estimators by using different techniques, but the generalized variance will always be greater than a specified constant.

First consider the variability of $\hat{\lambda}_s$. In subsection IV.E.3 a lower bound is derived for the variance, namely,

$$\text{Var } \hat{\lambda}_s \geq (B_\lambda)^{-1}$$

where

$$B_\lambda = \frac{\bar{N}}{\lambda_s (1 - P_0)(\lambda_s + \lambda_b)} \iint_{-\infty}^{\infty} \frac{G_s^2(x,y)}{G_s(x,y) + \lambda_b G_b(x,y)/\lambda_s} \, dx \, dy \quad (6)$$

Next assume $G_s(x, y)$ is a Gaussian density function with mean zero and a covariance matrix

$$\Sigma = \begin{pmatrix} \sigma_x^2 & \sigma_x \sigma_y \rho \\ \sigma_x \sigma_y \rho & \sigma_y^2 \end{pmatrix}.$$

Since the integrand in (6) is zero except in a small region near the origin, $G_b(x, y)$ is assumed to be constant. Let $G_b = G_b(0, 0)$. Then the value of the integral only depends on the signal-to-noise ratio

$$r = \frac{\lambda_s}{\pi |\Sigma|^{1/2} \lambda_b G_b}$$

Let $H_1(r)$ denote the value of the integral; $H_1(r)$ is graphed in Figure 6. Then

$$Var\left(\frac{\hat{\lambda}_s}{\lambda_s}\right) \geqslant \frac{1 - P_0}{\epsilon_0 \epsilon_q \lambda_s T H_1(r)}$$

Next, consider the variability of $(\hat{x}_0, \hat{y}_0)$. In subsection IV.E.3 a lower bound is derived for the generalized variance S, namely,

$$S \geqslant \left(B_x B_y - B_{xy}^2\right)^{-1}$$

where

$$B_x = \frac{\epsilon_0 \epsilon_q \lambda_s T}{1 - P_0} \iint\limits_{-\infty}^{\infty} \frac{[\partial_1 G_s(x,y)]^2}{G_s(x,y) + \lambda_b G_b(x,y)/\lambda_s} \, dx \, dy \qquad (7)$$
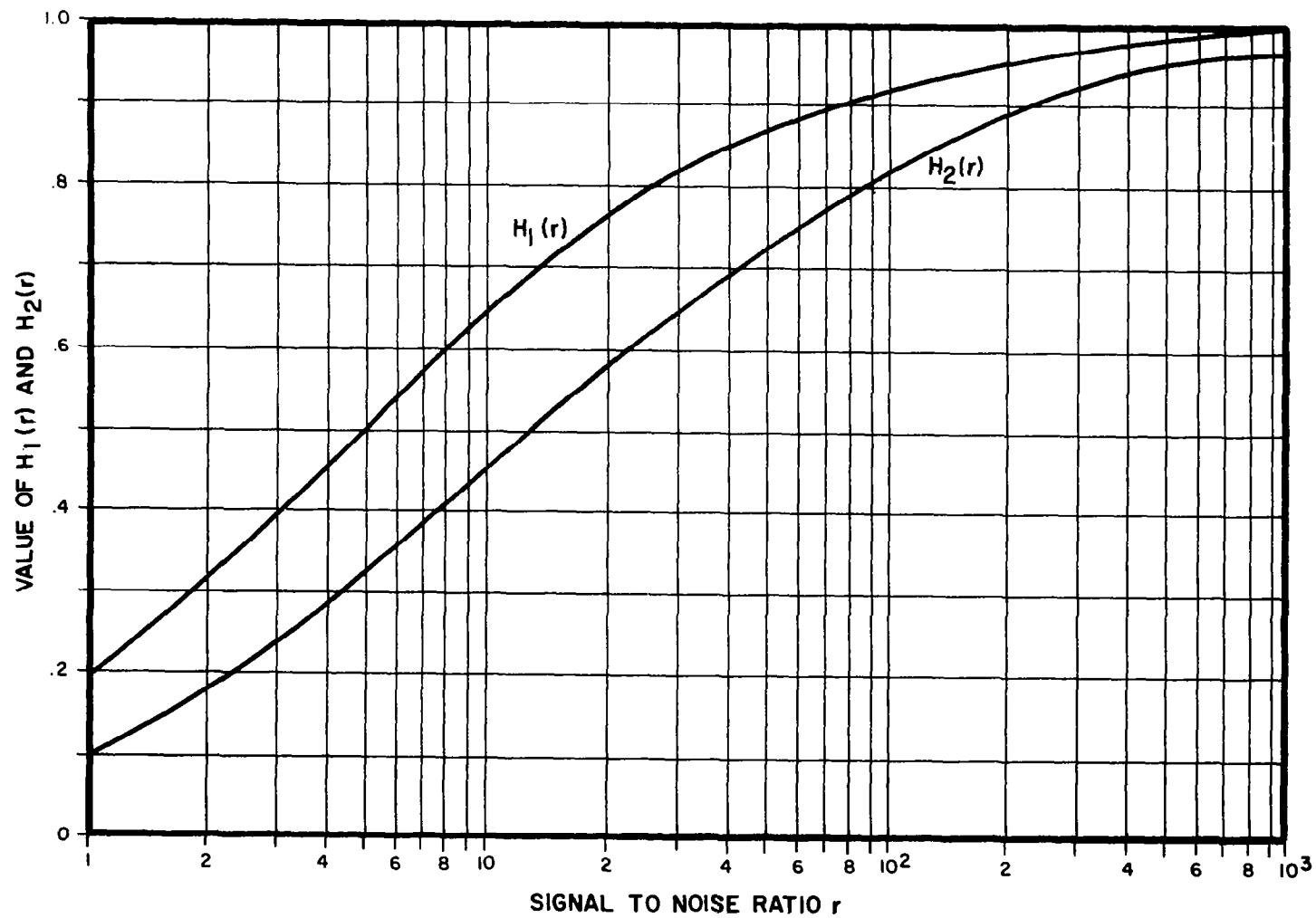
FIGURE 6: GRAPHS OF $H_1(r)$ AND $H_2(r)$

$$B_y = \frac{\epsilon_o \epsilon_q \lambda_s T}{1 - P_o} \iint_{-\infty}^{\infty} \frac{[\partial_2 G_s(x,y)]^2}{G_s(x,y) + \lambda_b G_b(x,y)/\lambda_s} \, dx \, dy$$

$$(8)$$

$$B_{xy} = \frac{\epsilon_o \epsilon_q \lambda_s T}{1 - P_o} \iint_{-\infty}^{\infty} \frac{\partial_1 G_s(x,y) \, \partial_2 G_s(x,y)}{G_s(x,y) + \lambda_b G_b(x,y)/\lambda_s} \, dx \, dy$$

$$(9)$$

where

$$\partial_1 G_s(x,y) = \frac{\partial G_s(x,y)}{\partial x} \qquad \partial_2 G_s(x,y) = \frac{\partial G_s(x,y)}{\partial y}$$

Assume $G_s(x, y)$ is a Gaussian density function with mean zero and a covariance matrix

$$\Sigma = \begin{pmatrix} \sigma_x^2 & \sigma_x \sigma_y \rho \\ \sigma_x \sigma_y \rho & \sigma_y^2 \end{pmatrix}$$

Then

$$\partial_1 G_s(x,y) = \frac{-1}{(1-\rho^2)\sigma_x} \left(\frac{x}{\sigma_x} - \rho \frac{y}{\sigma_y} \right) G_s(x,y)$$

$$\partial_2 G_s(x,y) = \frac{-1}{(1-\rho^2)\sigma_y} \left(\frac{y}{\sigma_y} - \rho \frac{x}{\sigma_x} \right) G_s(x,y)$$

The integral in (7) reduces to

$$\frac{1}{(1-\rho^2)^2 \sigma_x^2} \iint\limits_{-\infty}^{\infty} \left[\left(\frac{x}{\sigma_x}\right)^2 + \rho^2 \left(\frac{y}{\sigma_y}\right)^2 - \frac{2\rho xy}{\sigma_x \sigma_y} \right]$$

$$\cdot \frac{G_s^2(x,y)}{G_s(x,y) + \lambda_b G_b(x,y)/\lambda_s} \, dx \, dy \tag{10}$$

The integral in (8) reduces to

$$\frac{1}{(1-\rho^2)^2 \sigma_y^2} \iint\limits_{-\infty}^{\infty} \left[\left(\frac{y}{\sigma_y}\right)^2 + \rho^2 \left(\frac{x}{\sigma_x}\right)^2 - \frac{2\rho xy}{\sigma_x \sigma_y} \right]$$

$$\cdot \frac{G_s^2(x,y)}{G_s(x,y) + \lambda_b G_b(x,y)/\lambda_s} \, dx \, dy \tag{11}$$

The integral in (9) reduces to

$$\frac{-\rho}{(1-\rho^2)^2 \sigma_x \sigma_y} \iint\limits_{-\infty}^{\infty} \left[\left(\frac{x}{\sigma_x}\right)^2 + \left(\frac{y}{\sigma_y}\right)^2 - \frac{xy}{\sigma_x \sigma_y} \left(\frac{1+\rho^2}{\rho}\right) \right]$$

$$\cdot \frac{G_s^2(x,y)}{G_s(x,y) + \lambda_b G_b(x,y)/\lambda_s} \, dx \, dy \tag{12}$$

Since the integrands of (10), (11), and (12) are zero except in a small region near the origin, $G_b(x, y)$ is assumed to be constant. Let $G_b = G_b(0, 0)$.

To evaluate (10) it is convenient to transform the coordinates and diagonalize the quadratic form in $G_s(x, y)$. Let

$$X = u \cos \theta - v \sin \theta$$
$$y = u \sin \theta + v \cos \theta$$

(13)

with
$\theta = 0$ when $\rho = 0$

$\theta = \pi/4$ when $\rho \neq 0$ and $\sigma_x = \sigma_y$

$\theta = 1/2 \ \text{Arctan} \left[\dfrac{2 \rho \sigma_x \sigma_y}{\sigma_x^2 - \sigma_y^2} \right]$

when $\rho \neq 0$ and $\sigma_x \neq \sigma_y$. See Figure 7. Then

$$\frac{G_s^2(x, y)}{G_s(x, y) + \lambda_b G_b / \lambda_s} =$$

$$\frac{\exp\left[-\left(\frac{u}{\sigma_u}\right)^2 - \left(\frac{v}{\sigma_v}\right)^2 \right]}{\exp\left[-\frac{1}{2}\left(\frac{u}{\sigma_u}\right)^2 - \frac{1}{2}\left(\frac{v}{\sigma_v}\right)^2 \right] + \frac{2}{r}} \quad \left[2\pi \sigma_u \sigma_v \right]^{-1}$$
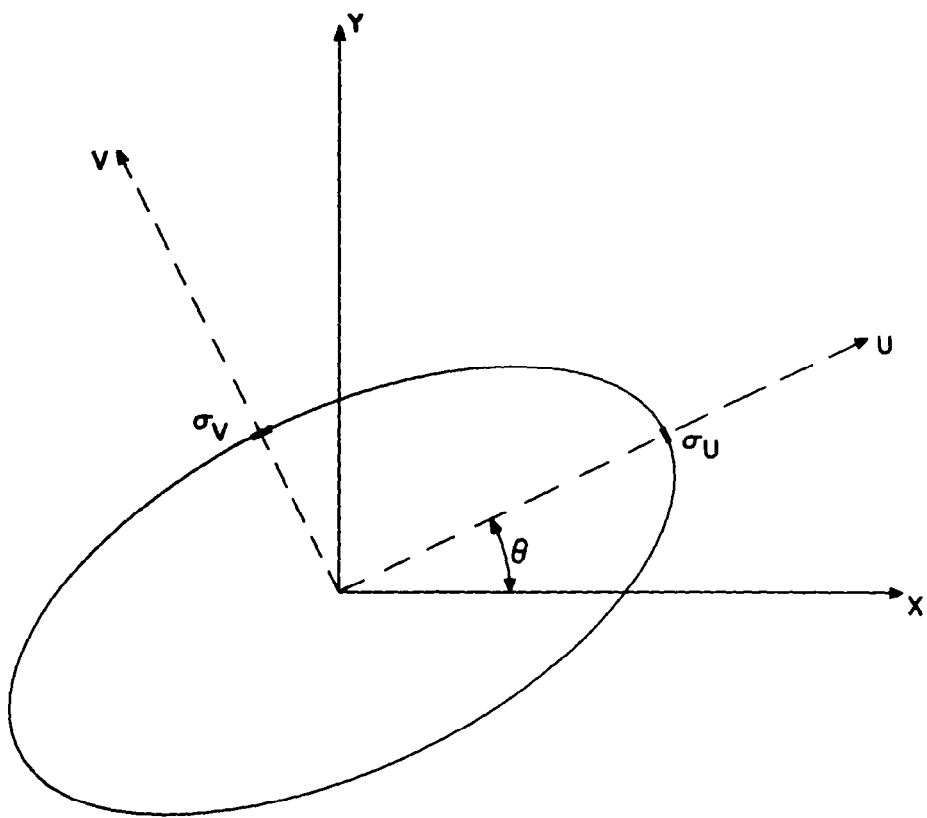
FIGURE 7: COORDINATE GEOMETRY

where

$$\frac{1}{\sigma_u^2} = \frac{1}{1-\rho^2}\left[\frac{\cos^2\theta}{\sigma_x^2} - \frac{2\rho\cos\theta\sin\theta}{\sigma_x\,\sigma_y} + \frac{\sin^2\theta}{\sigma_y^2}\right]$$

$$\frac{1}{\sigma_v^2} = \frac{1}{1-\rho^2}\left[\frac{\sin^2\theta}{\sigma_x^2} + \frac{2\rho\cos\theta\sin\theta}{\sigma_x\,\sigma_y} + \frac{\cos^2\theta}{\sigma_y^2}\right]$$

Also

$$\left[\left(\frac{x}{\sigma_x}\right)^2 + \rho^2\left(\frac{y}{\sigma_y}\right)^2 - \frac{2\rho xy}{\sigma_x\,\sigma_y}\right] =$$

$$\left(\frac{u}{\sigma_u}\right)^2(1-\rho^2)\left[1 - \left(\frac{\sigma_u}{\sigma_y}\right)^2\sin^2\theta\right]$$

$$+ \left(\frac{v}{\sigma_v}\right)^2(1-\rho^2)\left[1 - \left(\frac{\sigma_v}{\sigma_y}\right)^2\cos^2\theta\right] + uv\left[\cdots\right] .$$

Hence

$$B_x = \frac{\epsilon_o\epsilon_q\lambda_s T}{1-P_o} \frac{1}{(1-\rho^2)\,\sigma_x^2} H_2(r)$$

where

$$H_2(r) = \iint_{-\infty}^{\infty} \frac{x^2}{2\pi} \frac{\exp(-x^2-y^2)}{\exp(-x^2/2 - y^2/2) + 2/r} \, dx\, dy .$$

Note that

$$\sigma_x^2 = \sigma_u^2 \cos^2\theta + \sigma_v^2 \sin^2\theta$$

$$\sigma_y^2 = \sigma_u^2 \sin^2\theta + \sigma_v^2 \cos^2\theta$$

$$|\Sigma| = \sigma_x^2 \sigma_y^2 (1-\rho^2) = \sigma_u^2 \sigma_v^2 .$$

The function $H_2(r)$ is graphed in Figure 6. Similarly, one can show that

$$B_y = \frac{\epsilon_0 \epsilon_q \lambda_s T}{1-P_o} \frac{1}{(1-\rho^2)\sigma_y^2} H_2(r) .$$

Next, consider the integral in (12). Using transformation (13), (12) becomes

$$\frac{-\rho}{(1-\rho^2)\sigma_x\sigma_y} H_2(r)$$

and

$$B_{xy} = - \frac{\epsilon_0 \epsilon_q \lambda_s T}{1-P_o} \frac{\rho}{(1-\rho^2)\sigma_x\sigma_y} H_2(r)$$

Therefore,

$$B_x B_y - B_{xy}^2 = \left[\frac{\epsilon_0 \epsilon_q \lambda_s T H_2(r)}{1-P_o}\right]^2 \frac{1}{\sigma_x^2 \sigma_y^2 (1-\rho^2)}$$

and the bound on the generalized variance is

$$S \geqslant |\Sigma| \left[\frac{1-P_o}{\epsilon_0 \epsilon_q \lambda_s T H_2(r)}\right]^2$$

The quantity $|\Sigma|$ measures the spread of the image since $|\Sigma| = \sigma_u^2 \, \sigma_v^2$.

The product $\epsilon_0 \, \epsilon_q \, \lambda_s \, T$ measures the effective star intensity. The function $H_2(r)$ describes the effect of the background on the image.

In subsection IV.E.3 it is shown that B_x^{-1} is a lower bound on Var $\hat{x}_0$. It is informative to express the bound in terms of σ_u^2, σ_v^2, and θ; namely

$$\text{Var } \hat{x}_0 \;\geqslant\; \frac{2\,\sigma_v^2 \sigma_u^2}{\sigma_v^2 + \sigma_u^2 + (\sigma_v^2 - \sigma_u^2)\,\cos 2\theta}$$

$$\cdot \; \frac{1 - P_0}{\epsilon_0 \, \epsilon_q \, \lambda_s T \, H_2(r)}$$

At different points in the field of view, the image size (σ_u, σ_v) and orientation θ are different. Hence, the accuracy to which the image can be located along the x-axis depends on the position of the image. Similarly, B_y^{-1} is a lower bound on the variance of $\hat{y}_0$.

The bound on S can be extended to form

$$\text{Var } \hat{x}_0 \; \text{Var } \hat{y}_0 \;\geqslant\; \text{Var } \hat{x}_0 \; \text{Var } \hat{y}_0 \,(1 - \hat{\rho}^2) \;\geqslant\;$$

$$\left(B_x B_y - B_{xy}^2\right)^{-1} \;\geqslant\; \left(B_x B_y\right)^{-1}.$$

Hence Var $\hat{x}_0$ and Var $\hat{y}_0$ must satisfy three bounds

$$\text{Var } \hat{x}_0 \geqslant B_x^{-1} \qquad \text{Var } \hat{y}_0 \;\geqslant\; B_y^{-1}$$

$$\text{Var } \hat{x}_0 \; \text{Var } \hat{y}_0 \;\geqslant\; \left(B_x B_y - B_{xy}^2\right)^{-1}$$

For fixed σ_u and σ_v, as the orientation θ of the image changes, B_x^{-1} and B_y^{-1} changes. On the other hand, $B_x B_y - B_{xy}^2$ is independent of θ. These bounds are illustrated in Figure 8. When the image axes are parallel to the coordinate axes, only two bounds must be satisfied

$$Var\ \hat{x}_0 \geqslant B_x^{-1} \qquad Var\ \hat{y}_0 \geqslant B_y^{-1}$$

Also note that the accuracy to which x_0 and y_0 can be estimated decreases as the correlation between the estimates increases.
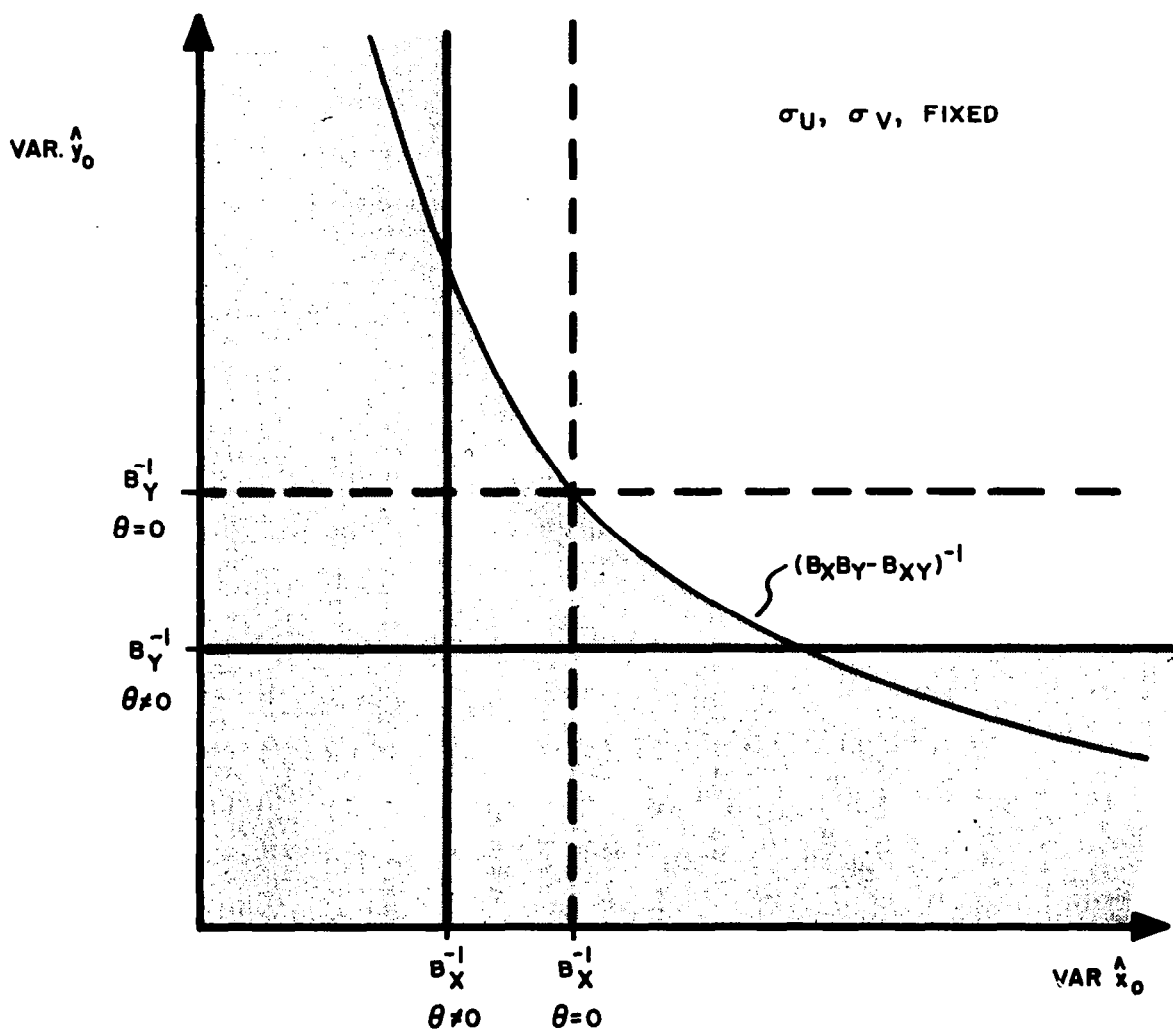
FIGURE 8: BOUNDS ON VAR $\hat{y}_0$ AND VAR $\hat{x}_0$

D.   Numerical Example

In this section a particular system will be considered in detail to illustrate how the preceding theoretical results can be applied. The system parameters are as follows:

(i)   Optical aperture is 3.3 inches with a 46 degree field of view.

(ii)   The energy in the star image can be described by a Gaussian function.

(iii)   Image at the center of the field of view is circular ($\sigma_u = \sigma_v$) with a diameter of twenty seconds of arc.

(iv)   Image at edge is elliptical with a radial size σ_u of 60 seconds of arc, and with a transverse size σ_v of 30 seconds of arc, see Figure 9.

(v)   The image size increases quadratically with distance ρ from the center, both σ_u and σ_v. In particular

$$\sigma_u = 50 \left(\frac{\rho}{23} \right)^2 + 10$$

$$\sigma_v = 20 \left(\frac{\rho}{23} \right)^2 + 10$$

where ρ is the radial distance from the center of the field of view to the star image in degrees, and where σ_u and σ_v are expressed in seconds of arc.

(vi)   Optical efficiency is .5.

(vii)   Quantum efficiency is .1.

(viii) Exposure duration T is 100 micro-seconds.
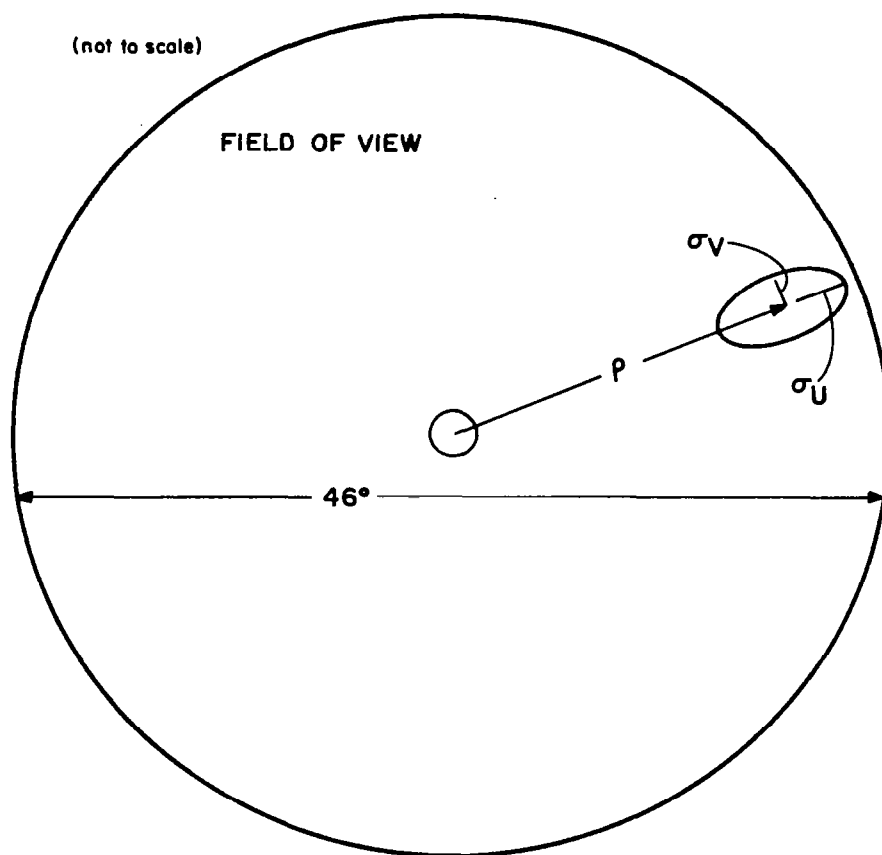
$$\sigma_U = 50 \left(\frac{\rho}{23}\right)^2 + 10 \text{ (SECONDS OF ARC)}$$

$$\sigma_V = 20 \left(\frac{\rho}{23}\right)^2 + 10 \text{ (SECONDS OF ARC)}$$

FIGURE 9: OPTICAL ABERRATION MODEL

(ix)   A fourth magnitude (photographic) star is observed.

(x)   The effective background $\lambda_b \ G_b$ is 300 tenth magnitude stars per square degree, and is constant near the star image.

1.   Detectability

With the above assumptions the optimum detection technique is based on (1). The signal-to-noise ratio is

$$r_1 = \frac{3.48 \times 10^4}{\left[5\left(\rho/23\right)^2 + 1\right]\left[2\left(\rho/23\right)^2 + 1\right]}$$

which is graphed in Figure 10. Three points in the field of view will be considered $\rho = 0°$, $11.5°$, $23°$. The basic problem is to determine C_p' so that the probability of detection at the edge of the field of view is .9, and then to determine the probability of detection at $\rho = 0°$, $11.5°$.

The moments of the test statistic (1) can be evaluated using Figure 3. The mean is 57.1 at $\rho = 0°$, 48.6 at $\rho = 11.5°$, and 39.0 at $\rho = 23°$ when a fourth magnitude star is observed. The variance is 461 at $\rho = 0°$, 356 at $\rho = 11.5°$, and 222 at $23°$. The distribution of $\mathcal{J}'$ will be approximated by a gamma distribution with the same mean and variance. The density is

$$\frac{\alpha}{\Gamma(\beta)} (\alpha x)^{\beta - 1} e^{-\alpha x}$$

where $\rho = 0°$, $11.5°$, $23°$.

$\alpha = .124, .137, .176$

$\beta = 7.12, 6.66, 5.85$
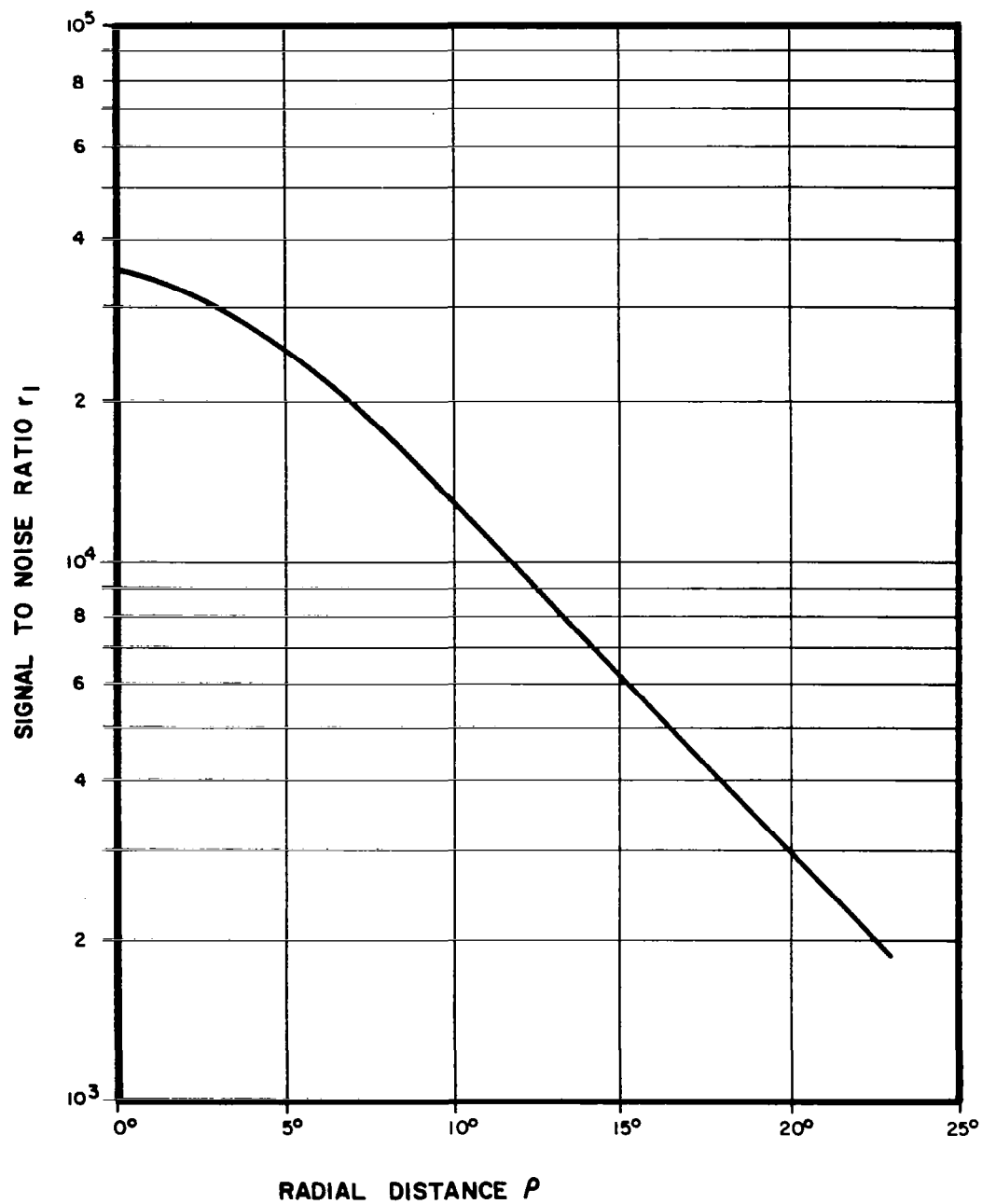
FIGURE 10: SIGNAL TO NOISE RATIO

Then C_P' is defined by

$$.9 = \int_{\alpha C_P'}^{\infty} \frac{1}{\Gamma(\beta)} \, y^{\beta-1} \, e^{-y} \, dy$$

where $\beta = 5.85$ and $\alpha = .176$. Hence $\alpha C_P' = 3.04$ and $C_P' = 17.3$. With this threshold the probability of detecting a fourth magnitude star at $\rho = 11.5^{\circ}$ is .98, and at $\rho = 0^{\circ}$ is .994.

If one observes a star with an intensity below fourth magnitude, the probability of detection is reduced. This probability determines the number of extraneous weak stars one detects. Note that parameter α is essentially independent of the star intensity when $r > 10^3$, and that β is proportional to the star intensity. The probability of detection is graphed in Figure 11 for $C_P' = 17.3$. With $r > 10^3$, the background will not produce a detection.

For the range of signal-to-noise involved in this example, the detection technique in expression (4) is reasonable where R_o is the order of 2.5.

2. Accuracy Limits

From the results in Section IV, one obtains

$$Var\left(\frac{\hat{\lambda}_s}{\lambda_s}\right) \geq \frac{1 - P_o}{\epsilon_o \epsilon_q \lambda_s T \, H_1(r)}$$

The standard deviation of $\hat{\lambda}_s/\lambda_s$ is graphed in Figure 12 as a function of star intensity. Note that the bound is independent of position ρ since $r > 10^3$.

Two position estimates will be considered. First, assume one estimates the position of the star using polar coordinates. The standard deviation
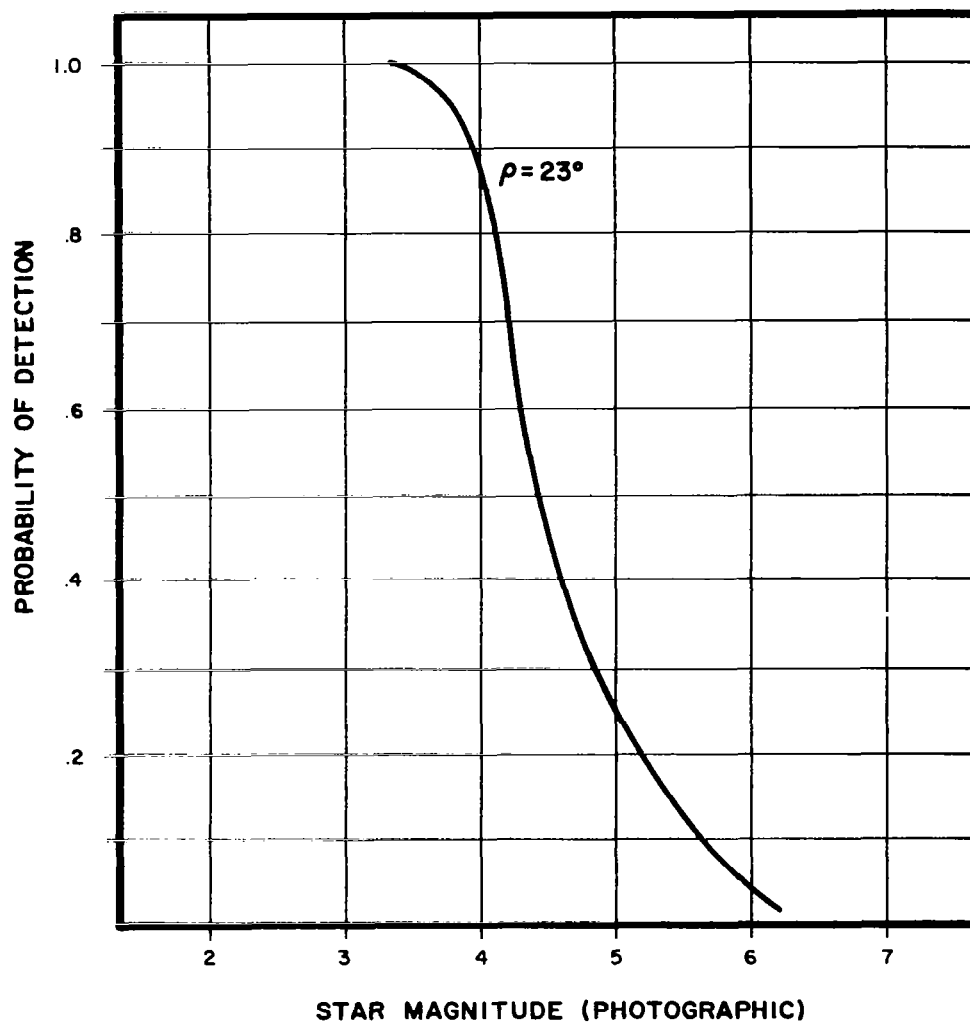
FIGURE II: PROBABILITY OF DETECTION
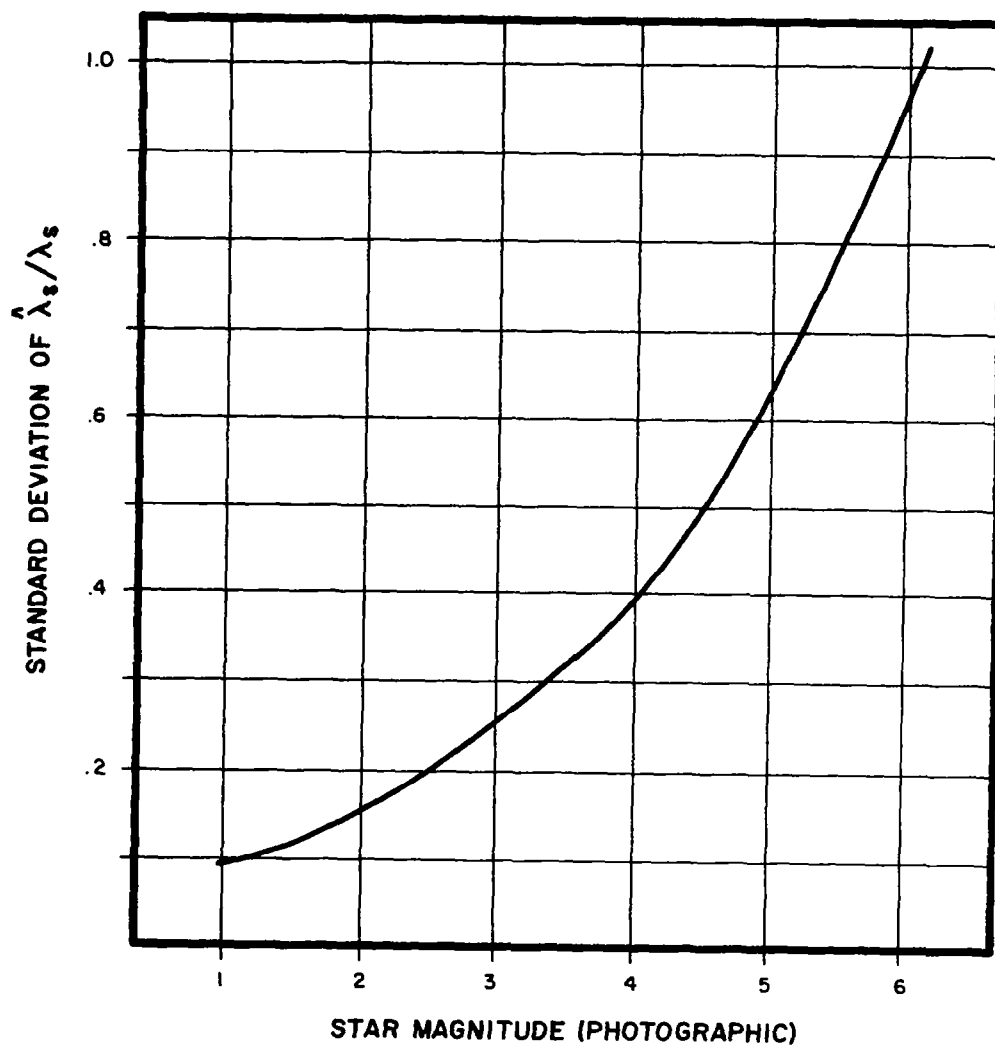
FIGURE 12: INTENSITY ACCURACY

of the radial error is not less than

$$\left[50\left(\frac{\rho}{23}\right)^2 + 10\right]\left[\frac{1 - P_0}{\epsilon_0 \epsilon_q \lambda_1 T\, H(r_1)}\right]^{1/2}$$

The angular error is not less

$$\frac{20\left(\frac{\rho}{23}\right)^2 + 10}{3600\,\rho}\left[\frac{1 - P_0}{\epsilon_0 \epsilon_q \lambda_1 T\, H(r_1)}\right]^{1/2}$$

expressed in radians. These results are graphed in Figure 13 for a fourth magnitude star.

Next, assume one estimates the position of the star using rectilinear coordinates. The standard deviation of the error along the x-axis is not less than

$$\left[\frac{2\sigma_v^2 \sigma_u^2}{\sigma_v^2 + \sigma_u^2 + (\sigma_v^2 - \sigma_u^2)\cos 2\theta} \cdot \frac{1 - P_0}{\epsilon_0 \epsilon_q \lambda_s T\, H_2(r)}\right]^{1/2}$$

Lines of equal accuracy are graphed in Figure 14, for a fourth magnitude star. Note that the bound on the product of the "x-error" and "y-error" increases as ρ^4.
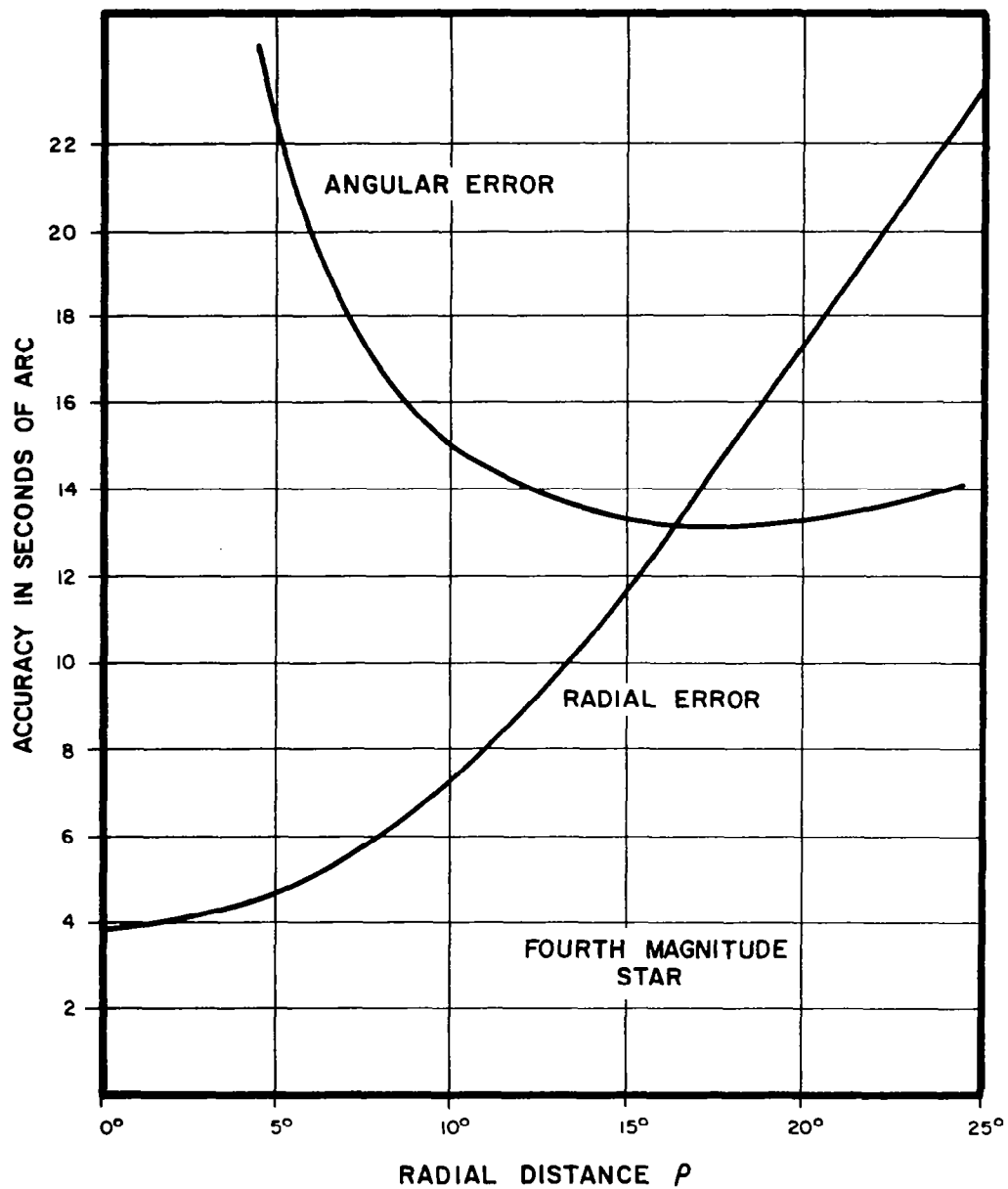
FIGURE 13: POLAR POSITION ACCURACY
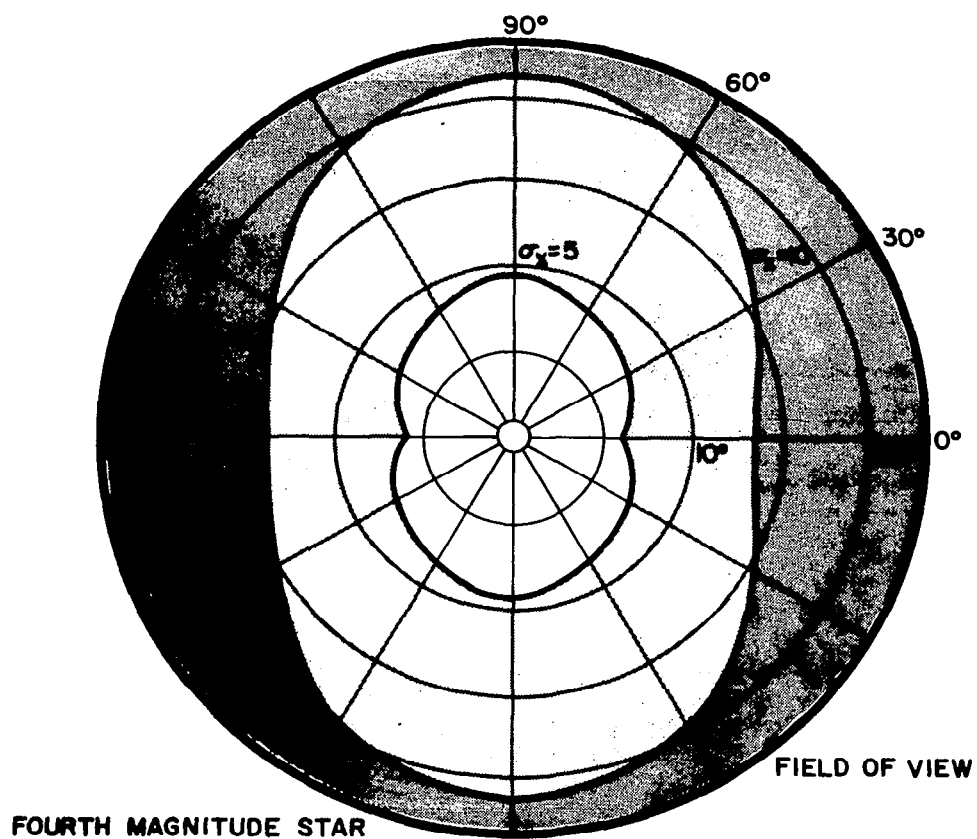
FIGURE 14: LINES OF CONSTANT ERROR IN X-DIRECTION, STANDARD
DEVIATIONS OF 5 AND 10 SECONDS OF ARC.

E.   Special Derivations

1.   Optimality of Detection Method

A detection technique is characterized by a sequence of sets

ω_2, ω_4, ..., ω_{2N}, ... in Euclidian spaces of two dimensions, four dimensions, ..., 2N dimensions, etc.   If N emissions are observed, a star is "present" when

$$\left(x_1, y_1, x_2, y_2, \cdots, x_N, y_N \right) \in \omega_{2N}$$

Let $\underset{\sim}{x}$ denote this (2N)-vector.   The probability of a Type I error is

$$\sum_{N=1}^{\infty} \int_{\omega_{2N}} f_N(\underset{\sim}{x}) \, P_N \Big|_{\lambda_s=0} \, d\underset{\sim}{x} = P$$

and the probability of detection is

$$\sum_{N=1}^{\infty} \int_{\omega_{2N}} f_N(\underset{\sim}{x}) \, P_N \Big|_{\lambda_s=\lambda_1} \, d\underset{\sim}{x}$$

Let ω_{2N}^* be the set such that

$$\frac{f_N(\underset{\sim}{x}) \, P_N \Big|_{\lambda_s=\lambda_1}}{f_N(\underset{\sim}{x}) \, P_N \Big|_{\lambda_s=0}} \geqslant C_p$$

where C_p is selected so that

$$\sum_{N=1}^{\infty} \int_{\omega_{2N}^*} f_N(\underset{\sim}{x}) \, P_N \Big|_{\lambda_s=0} \, d\underset{\sim}{x} = P .$$

The sequence ω_2^*, ω_4^*, ... defines a detection technique that minimizes the

probability of a Type II error, and hence maximizes the probability of detection. Let $\bar{\omega}_N$ denote the compliment ω_N. Then

$$\sum_{N=1}^{\infty} \int_{\omega_{2N}^* \cap \omega_{2N}} f_N(\underset{\sim}{x}) P_N \Big|_{\lambda_s=0} d\underset{\sim}{x} + \sum_{N=1}^{\infty} \int_{\omega_{2N}^* \cap \bar{\omega}_{2N}} f_N(\underset{\sim}{x}) P_N \Big|_{\lambda_s=0} d\underset{\sim}{x} =$$

$$P = \sum_{N=1}^{\infty} \int_{\omega_{2N} \cap \omega_{2N}^*} f_N(\underset{\sim}{x}) P_N \Big|_{\lambda_s=0} d\underset{\sim}{x} + \sum_{N=1}^{\infty} \int_{\omega_{2N} \cap \bar{\omega}_{2N}^*} f_N(\underset{\sim}{x}) P_N \Big|_{\lambda_s=0} d\underset{\sim}{x} .$$

and hence

$$\sum_{N=1}^{\infty} \int_{\omega_{2N}^* \cap \bar{\omega}_{2N}} f_N(\underset{\sim}{x}) P_N \Big|_{\lambda_s=0} d\underset{\sim}{x} = \sum_{N=1}^{\infty} \int_{\omega_{2N} \cap \bar{\omega}_{2N}^*} f_N(\underset{\sim}{x}) P_N \Big|_{\lambda_s=0} d\underset{\sim}{x} .$$

The probability of detection using ω_N^* is then

$$\sum_{N=1}^{\infty} \int_{\omega_{2N}^* \cap \omega_{2N}} f_N(\underset{\sim}{x}) P_N \Big|_{\lambda_s=\lambda_1} d\underset{\sim}{x} + \sum_{N=1}^{\infty} \int_{\omega_{2N}^* \cap \bar{\omega}_{2N}} f_N(\underset{\sim}{x}) P_N \Big|_{\lambda_s=\lambda_1} d\underset{\sim}{x} \geqslant$$

$$\sum_{N=1}^{\infty} \int_{\omega_{2N}^* \cap \omega_{2N}} f_N(\underset{\sim}{x}) P_N \Big|_{\lambda_s=\lambda_1} d\underset{\sim}{x} + \sum_{N=1}^{\infty} C_P \int_{\omega_{2N}^* \cap \bar{\omega}_{2N}} f_N(\underset{\sim}{x}) P_N \Big|_{\lambda_s=0} d\underset{\sim}{x} =$$

$$\sum_{N=1}^{\infty} \int_{\omega_{2N}^* \cap \omega_{2N}} f_N(\underset{\sim}{x}) P_N \Big|_{\lambda_s=\lambda_1} d\underset{\sim}{x} + \sum_{N=1}^{\infty} C_P \int_{\omega_{2N} \cap \bar{\omega}_{2N}^*} f_N(\underset{\sim}{x}) P_N \Big|_{\lambda_s=0} d\underset{\sim}{x} \geqslant$$

$$\sum_{N=1}^{\infty} \int_{\omega_{2N}^* \cap \omega_{2N}} f_N(\underset{\sim}{x}) P_N \Big|_{\lambda_s=\lambda_1} d\underset{\sim}{x} + \sum_{N=1}^{\infty} \int_{\omega_{2N} \cap \bar{\omega}_{2N}^*} f_N(\underset{\sim}{x}) P_N \Big|_{\lambda_s=\lambda_1} d\underset{\sim}{x} =$$

$$\sum_{N=1}^{\infty} \int_{\omega_{2N}} f_N(\underset{\sim}{x}) P_N \Big|_{\lambda_s=\lambda_1} d\underset{\sim}{x} .$$

Therefore, $\left\{ \omega_2^*, \omega_4^*, \ldots \right\}$ maximizes the probability of detection.

2. Characteristic Function of $\mathcal{J}'$

The basic test statistic is

$$\mathcal{J}' = \sum_{j=1}^{N} \ln \left[\frac{\lambda_1 G_s(x_j - x_o, y_j - y_o) + \lambda_b G_b(x_j, y_j)}{\lambda_b G_b(x_j, y_j)} \right]$$

where the (x_j, y_j)'s are independent and identically distributed with the density

$$\frac{\lambda_s G_s(x - x_o, y - y_o) + \lambda_b G_b(x, y)}{\lambda_s + \lambda_b}$$

and where N has a Poisson distribution with mean $\bar{N}$. To evaluate the characteristic function of $\mathcal{J}'$, the first step is to evaluate the characteristic function $\mathcal{J}'$ for a fixed value of N. In particular,

$$E\left\{ e^{iu\mathcal{J}'} \mid N \right\} =$$
$$\left\{ E \exp\left[iu \ln \left(\frac{\lambda_1 G_s(x - x_o, y - y_o) + \lambda_b G_b(x, y)}{\lambda_b G_b(x, y)} \right) \right] \right\}^N$$

since (x_j, y_j)'s are independent and identically distributed. Let ϕ denote the quantity inside the braces. Then

$$E\left\{ e^{iu\mathcal{J}'} \right\} = \sum_{N=0}^{\infty} \phi^N \frac{\bar{N}^N}{N!} e^{-\bar{N}} = e^{\bar{N}(\phi - 1)}$$

and the logarithm of the characteristic function is

$$\bar{N} \iint\limits_{-\infty}^{\infty} \frac{\lambda_s G_s(x-x_o, y-y_o) + \lambda_b G_b(x,y)}{\lambda_s + \lambda_b}$$

$$\cdot \left\{ \exp\left[iu \ln\left(\frac{\lambda_1 G_s(x-x_o, y-y_o) + \lambda_b G_b(x,y)}{\lambda_b G_b(x,y)} \right) \right] - 1 \right\} dx\, dy$$

Expanding the exponential, one obtains the semi-invariants

$$\mathcal{K}_n = \bar{N} \iint\limits_{-\infty}^{\infty} \frac{\lambda_s G_s(x-x_o, y-y_o) + \lambda_b G_b(x,y)}{\lambda_s + \lambda_b}$$

$$\cdot \left[\ln\cdot\left(\frac{\lambda_1 G_s(x-x_o, y-y_o) + \lambda_b G_b(x,y)}{\lambda_b G_b(x,y)} \right) \right]^n dx\, dy$$

with $n = 1, 2, 3, \ldots$.

Next, assume $G_s(x, y)$ is a Gaussian density function and $G_b(x, y)$ is slowly changing. The nth semi-invariant becomes

$$\mathcal{K}_n = \epsilon_o \epsilon_q T \lambda_s \iint\limits_{-\infty}^{\infty} G_s(x,y) \left[\ln\left(\frac{\lambda_1 G_s(x,y)}{\lambda_b G_b} + 1 \right) \right]^n dx\, dy$$

$$+ \epsilon_o \epsilon_q T \lambda_b G_b \iint\limits_{-\infty}^{\infty} \left[\ln\left(\frac{\lambda_1 G_s(x,y)}{\lambda_b G_b} + 1 \right) \right]^n dx\, dy$$

The first integral reduces to

$$\iint\limits_{-\infty}^{\infty} \frac{1}{2\pi|\Sigma|^{1/2}} e^{-\frac{1}{2}R^2} \left[\ln\left(\frac{r_1}{2} e^{-\frac{1}{2}R^2} +1\right)\right]^n dx\, dy =$$

$$\iint\limits_{-\infty}^{\infty} \frac{1}{2\pi} e^{-\frac{1}{2}(x^2+y^2)} \left[\ln\left(\frac{r_1}{2} e^{-\frac{1}{2}(x^2+y^2)} +1\right)\right]^n dx\, dy =$$

$$\int_0^{2\pi}\int_0^{\infty} \frac{1}{2\pi} e^{-\frac{1}{2}\rho^2} \left[\ln\left(\frac{r_1}{2} e^{-\frac{1}{2}\rho^2} +1\right)\right]^n \rho\, d\rho\, d\theta =$$

$$\int_0^{\infty} e^{-z} \left[\ln\left(\frac{r_1}{2} e^{-z} +1\right)\right]^n dz$$

Substituting y for

$$\ln\left(\frac{r_1}{2} e^{-z} +1\right)$$

the first integral becomes

$$\frac{2}{r_1} \int_0^{\ln(r_1/2 +1)} y^n e^y\, dy$$

The second integral reduces to

$$\iint\limits_{-\infty}^{\infty} \left[\ln\left(\frac{r_1}{2} e^{-R^2/2} +1\right)\right]^n dx\, dy =$$

$$|\Sigma|^{1/2} \iint\limits_{-\infty}^{\infty} \left[\ln\left(\frac{r_1}{2} e^{-\frac{1}{2}(x^2+y^2)} +1\right)\right]^n dx\, dy =$$

$$|\Sigma|^{1/2} \int_0^{2\pi}\int_0^{\infty} \left[\ln\left(\frac{r_1}{2} e^{-\rho^2/2} +1\right)\right]^n \rho\, d\rho\, d\theta =$$

$$2\pi|\Sigma|^{1/2} \int_0^{\infty} \left[\ln\left(\frac{r_1}{2} e^{-z} +1\right)\right]^n dz$$

3. Lower Bounds for $\hat{\lambda}_s$ and S

To derive the lower bounds for Var $\hat{\lambda}_s$ and S, it is convenient to use a more compact notation. Let $\underset{\sim}{z}_N$ be the vector

$$\underset{\sim}{z}_N = \begin{pmatrix} x_1 \\ y_1 \\ x_2 \\ y_2 \\ \vdots \\ y_N \end{pmatrix}$$

and

$$\underset{\sim}{\theta} = \begin{pmatrix} \theta_1 \\ \theta_2 \\ \theta_3 \end{pmatrix} = \begin{pmatrix} x_0 \\ y_0 \\ \lambda_s \end{pmatrix}$$

Let $L(\underset{\sim}{\theta} \mid N, \underset{\sim}{z}_N)$ be the likelihood function

$$L(\underset{\sim}{\theta} \mid N, \underset{\sim}{z}_N) = \frac{P_N(\lambda_s)}{1 - P_0(\lambda_s)} f_N(\underset{\sim}{z} \mid \underset{\sim}{\theta})$$

Assume $\hat{\underset{\sim}{\theta}}(N, \underset{\sim}{z}_N)$ is an unbiased estimate of $\underset{\sim}{\theta}$, i.e.,

$$\sum_{N=1}^{\infty} \int \hat{\underset{\sim}{\theta}}(N, \underset{\sim}{z}_N) \, L(\underset{\sim}{\theta} \mid N, \underset{\sim}{z}_N) \, d\underset{\sim}{z}_N = \underset{\sim}{\theta}$$

(C1)

where the integral is 2N-fold.

Assume one can differentiate under the integral in (C 1); then

$$\sum_{N=1}^{\infty} \int \hat{\theta}_j(N, \underset{\sim}{z}_N) \, \frac{\partial \ln L(\underset{\sim}{\theta} \mid N, \underset{\sim}{z}_N)}{\partial \theta_i} \, L(\underset{\sim}{\theta} \mid N, \underset{\sim}{z}_N) \, d\underset{\sim}{z}_N = \delta_{ij}$$

Let $\underset{\sim}{u}(N, \underset{\sim}{z}_N)$ be a vector with components

$$u_j(N, \underset{\sim}{z}_N) = \frac{\partial \ln L(\underset{\sim}{\theta} \mid N, \underset{\sim}{z}_N)}{\partial \theta_j}$$

Matrix transposition will be indicated by a prime. Then

$$\sum_{N=1}^{\infty} \int \hat{\underset{\sim}{\theta}}(N, \underset{\sim}{z}_N) \, \underset{\sim}{u}'(N, \underset{\sim}{z}_N) \, L(\underset{\sim}{\theta} \mid N, \underset{\sim}{z}_N) \, d\underset{\sim}{z}_N = \underset{\sim}{I}$$

where $\underset{\sim}{I}$ is a 3 x 3 identity matrix. In other words, the expected value of the matrix

$$\hat{\underset{\sim}{\theta}}(N, \underset{\sim}{z}_N) \, \underset{\sim}{u}'(N, \underset{\sim}{z}_N)$$

is the identity matrix.

Since $\underset{\sim}{L}(\underset{\sim}{\theta} \mid N, \underset{\sim}{z}_N)$ is a likelihood function

$$\sum_{N=1}^{\infty} \int L(\underset{\sim}{\theta} \mid N, \underset{\sim}{z}_N) \, d\underset{\sim}{z}_N = 1$$

Differentiating this equation with respect to θ_j, one obtains

$$\sum_{N=1}^{\infty} \int \underset{\sim}{u}(N, \underset{\sim}{z}_N) \, L(\underset{\sim}{\theta} \mid N, \underset{\sim}{z}_N) \, d\underset{\sim}{z}_N = \underset{\sim}{0}$$

i.e., the expected value of $\underset{\sim}{u}(N, \underset{\sim}{z}_N)$ is zero. Therefore, the covariance matrix between $\hat{\underset{\sim}{\theta}}(N, \underset{\sim}{z}_N)$ and $\underset{\sim}{u}(N, \underset{\sim}{z}_N)$ is

$$\underset{\sim}{\Sigma}_{\hat{\theta} u} = \sum_{N=0}^{\infty} \int [\hat{\underset{\sim}{\theta}}(N, \underset{\sim}{z}_N) - \underset{\sim}{\theta}] \, \underset{\sim}{u}'(N, \underset{\sim}{z}_N) \, L(\underset{\sim}{\theta} \mid N, \underset{\sim}{z}_N) \, d\underset{\sim}{z}_N =$$

$$\sum_{N=0}^{\infty} \int \hat{\underset{\sim}{\theta}}(N, \underset{\sim}{z}_N) \, \underset{\sim}{u}'(N, \underset{\sim}{z}_N) \, L(\underset{\sim}{\theta} \mid N, \underset{\sim}{z}_N) \, d\underset{\sim}{z}_N = \underset{\sim}{I}$$

Next define the 6-vector

$$\underset{\sim}{w}(N, \underset{\sim}{z}_N) = \begin{pmatrix} \hat{\underset{\sim}{\theta}}(N, \underset{\sim}{z}_N) \\ \underset{\sim}{u}(N, \underset{\sim}{z}_N) \end{pmatrix}$$

The covariance matrix of $\underset{\sim}{w}(N, \underset{\sim}{z}_N)$ is

$$\underset{\sim}{\Sigma}_{ww} = \begin{pmatrix} \underset{\sim}{\Sigma}_{\theta\theta} & \underset{\sim}{I} \\ \underset{\sim}{I} & \underset{\sim}{\Sigma}_{uu} \end{pmatrix}$$

where $\underset{\sim}{\Sigma}_{\theta\theta}$ and $\underset{\sim}{\Sigma}_{uu}$ are the covariance matrices of $\hat{\underset{\sim}{\theta}}(N, \underset{\sim}{z}_N)$ and $\underset{\sim}{u}(N, \underset{\sim}{z}_N)$.

Assume $\underset{\sim}{\Sigma}_{uu}$ is non-singular. Let $\underset{\sim}{\alpha}$ and $\underset{\sim}{\beta}$ be arbitrary 3-vectors, which are not random. Then

$$(\underset{\sim}{\alpha}'\underset{\sim}{\beta})^2 = \text{Cov}^2\left[\underset{\sim}{\alpha}'\hat{\underset{\sim}{\theta}}(N, \underset{\sim}{z}_N), \underset{\sim}{\beta}'\underset{\sim}{u}(N, \underset{\sim}{z}_N)\right] \le$$

$$\text{Var}\left[\underset{\sim}{\alpha}'\hat{\underset{\sim}{\theta}}(N, \underset{\sim}{z}_N)\right] \text{Var}\left[\underset{\sim}{\beta}'\underset{\sim}{u}(N, \underset{\sim}{z}_N)\right] =$$

$$(\underset{\sim}{\alpha}'\underset{\sim}{\Sigma}_{\theta\theta}\underset{\sim}{\alpha})(\underset{\sim}{\beta}'\underset{\sim}{\Sigma}_{uu}\underset{\sim}{\beta}) \qquad (C2)$$

Let $\underset{\sim}{\beta} = \underset{\sim}{\Sigma}_{uu}^{-1}\underset{\sim}{\alpha}$,   then

$$\underset{\sim}{\alpha}'\underset{\sim}{\Sigma}_{uu}^{-1}\underset{\sim}{\alpha} \le \underset{\sim}{\alpha}'\underset{\sim}{\Sigma}_{\theta\theta}\underset{\sim}{\alpha}$$

for all $\underset{\sim}{\alpha} \ne \underset{\sim}{0}$. Therefore,

$$\frac{\pi^{3/2}}{\Gamma(\frac{5}{2})}\frac{1}{\sqrt{|\underset{\sim}{\Sigma}_{uu}^{-1}|}} = \int_{\underset{\sim}{\alpha}'\underset{\sim}{\Sigma}_{uu}^{-1}\underset{\sim}{\alpha} \le 1} d\underset{\sim}{\alpha} \ge \int_{\underset{\sim}{\alpha}'\underset{\sim}{\Sigma}_{\theta\theta}\underset{\sim}{\alpha} \le 1} d\underset{\sim}{\alpha} = \frac{\pi^{3/2}}{\Gamma(\frac{5}{2})}\frac{1}{\sqrt{|\underset{\sim}{\Sigma}_{\theta\theta}|}}$$

and $\quad |\underset{\sim}{\Sigma}_{\theta\theta}| \geqslant |\underset{\sim}{\Sigma}_{uu}|^{-1}$

This is the fundamental bound on the variability of estimators of x_o, y_o, and λ_s since $|\underset{\sim}{\Sigma}_{uu}|$ does not depend on the estimator $\underset{\sim}{\hat{\theta}}$.

The matrix $\underset{\sim}{\Sigma}_{uu}$ can be simplified. First

$$\ln L(\underset{\sim}{\theta}|N, \underset{\sim}{z}_N) = P_N(\theta_3) - \ln[1 - P_o(\theta_3)] - N \ln(\theta_3 + \lambda_b)$$
$$+ \sum_{j=1}^{N} \ln[\theta_3 G_s(x_j - \theta_1, y_j - \theta_2) + \lambda_b G_b(x_j, y_j)]$$

then

$$u_1 = \sum_{j=1}^{N} \frac{-\theta_3 \partial_1 G_s(x_j - \theta_1, y_j - \theta_2)}{\theta_3 G_s(x_j - \theta_1, y_j - \theta_2) + \lambda_b G_b(x_j, y_j)}$$

$$u_2 = \sum_{j=1}^{N} \frac{-\theta_3 \partial_2 G_s(x_j - \theta_1, y_j - \theta_2)}{\theta_3 G_s(x_j - \theta_1, y_j - \theta_2) + \lambda_b G_b(x_j, y_j)}$$

$$u_3 = \sum_{j=1}^{N} \frac{G_s(x_j - \theta_1, y_j - \theta_2)}{\theta_3 G_s(x_j - \theta_1, y_j - \theta_2) + \lambda_b G_b(x_j, y_j)} - \frac{\epsilon_o \epsilon_q T}{1 - P_o(\theta_3)}$$

where

$$\partial_1 G(x, y) = \frac{\partial G(x, y)}{\partial x}$$
$$\partial_2 G(x, y) = \frac{\partial G(x, y)}{\partial y}$$

Without loss of generality, one can set $\theta_1 = \theta_2 = 0$ in the bound. Then the entries in $\underset{\sim}{\Sigma}_{uu}$ become

$$E(u_1)^2 = \frac{\bar{N}}{1-P_o} E\left[\frac{\partial_1 G_s(x,y)}{G_s(x,y) + \lambda_b G_b(x,y)/\theta_3}\right]^2$$

$$E(u_1 u_2) = \frac{\bar{N}}{1-P_o} E\left[\frac{\partial_1 G_s(x,y)\, \partial_2 G_s(x,y)}{(G_s(x,y) + \lambda_b G_b(x,y)/\theta_3)^2}\right]$$

$$E(u_2)^2 = \frac{\bar{N}}{1-P_o} E\left[\frac{\partial_2 G_s(x,y)}{G_s(x,y) + \lambda_b G_b(x,y)/\theta_3}\right]^2$$

$$E(u_1 u_3) = \frac{-\bar{N}}{\theta_3(1-P_o)} E\left[\frac{G_s(x,y)\, \partial_1 G_s(x,y)}{(G_s(x,y) + \lambda_b G_b(x,y)/\theta_3)^2}\right]$$

$$E(u_2 u_3) = \frac{-\bar{N}}{\theta_3(1-P_o)} E\left[\frac{G_s(x,y)\, \partial_2 G_s(x,y)}{(G_s(x,y) + \lambda_b G_b(x,y)/\theta_3)^2}\right]$$

$$E(u_3)^2 = \frac{\bar{N}}{\theta_3^2(1-P_o)} E\left[\frac{G_s(x,y)}{G_s(x,y) + \lambda_b G_b(x,y)/\theta_3}\right]^2$$

By setting

$$\underset{\sim}{\alpha} = \begin{pmatrix} 0 \\ 0 \\ 1 \end{pmatrix} \qquad \underset{\sim}{\beta} = \begin{pmatrix} 0 \\ 0 \\ 1 \end{pmatrix}$$

in Equation (C2) one obtains a bound on Var $\hat{\theta}_3$, i.e.,

$$\text{Var } \hat{\theta}_3 \geqslant \left[E(u_3)^2\right]^{-1}.$$

By setting

$$\underset{\sim}{\alpha} = \begin{pmatrix} \alpha_1 \\ \alpha_2 \\ 0 \end{pmatrix} \qquad \underset{\sim}{\beta} = \begin{pmatrix} \beta_1 \\ \beta_2 \\ 0 \end{pmatrix}$$

IV-61

in Equation (C2) one obtains a bound on the generalized variance S, i.e.,

$$S \geq \left[E(u_1)^2 E(u_2)^2 - E^2(u_1 u_2) \right]^{-1}$$

Note that the above results can be applied to an arbitrary image and background since G_s and G_b are general intensity functions.

V.   PHOTODETECTORS FOR SPACE NAVIGATIONAL SYSTEMS

For a scanning optical system, a photodetector is required to efficiently convert radiant energy from a class of navigational stars into electrical signals which have sufficient magnitude to override any noise source signals so reliable signal detection can be performed. Various types of photodetecotrs will be discussed, and it will be shown that the photomultiplier is superior to non-multiplying photodetectors. This is followed by a detailed discussion of typical photomultiplier characteristics.

A.   Energy Distribution of Navigational Stars

If the 100 brightest stars are considered and if the number of stars of a given spectral class are plotted against spectral class, the resulting graph is strongly peaked at class A, see Figure 1. It is, therefore, logical to consider the response of photodetectors to Type A stars.
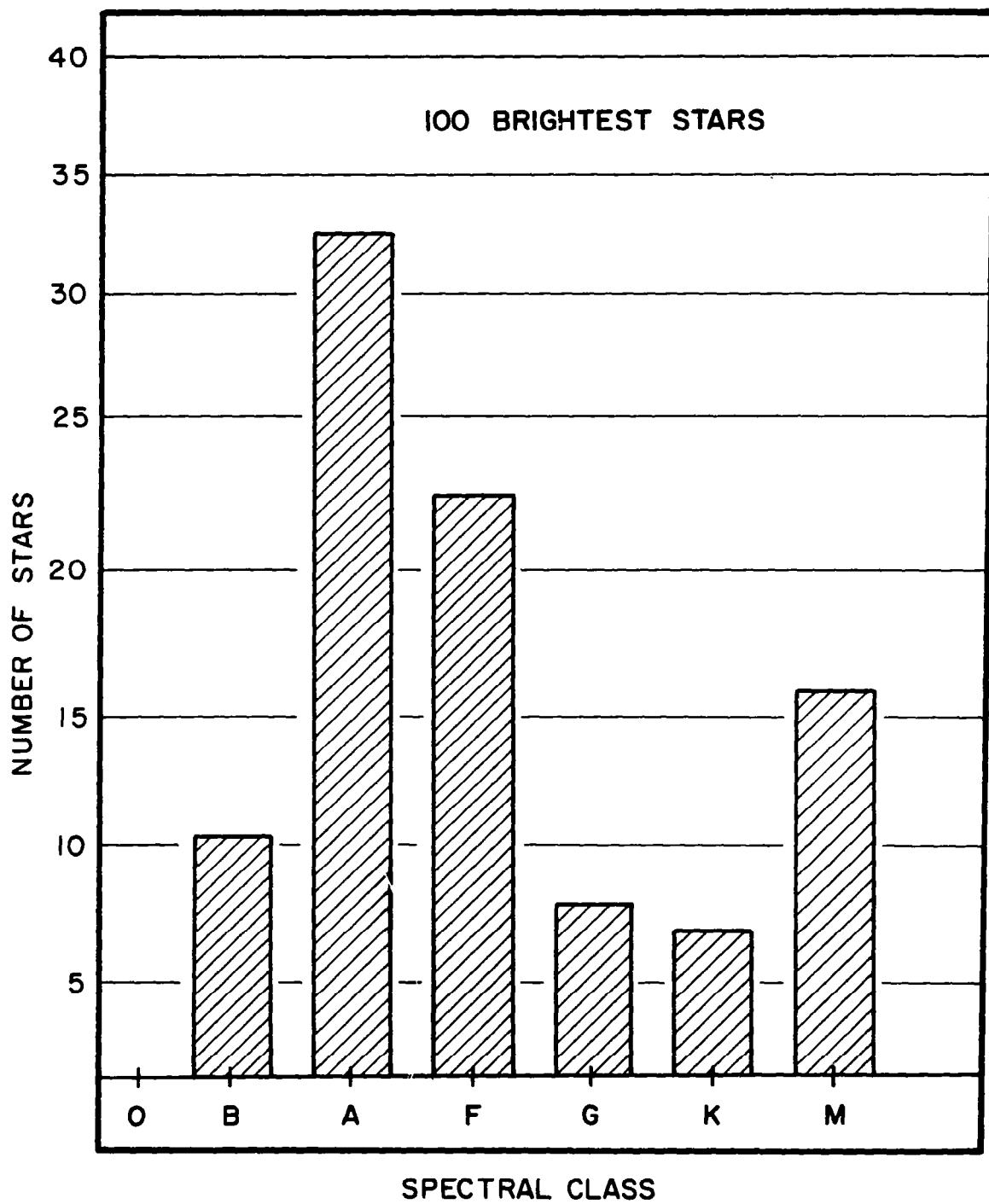
FIGURE I : SPECTRAL DISTRIBUTION OF STARS

B.   Energy Available from Type A Star

Code (1960) has tabulated the monochromatic magnitudes of Vega (α Lyr) per unit frequency interval, $m(1/\lambda)$, relative to $1/\lambda = 1.80$ for a band pass of 10 Angstroms, where Vega is a type A_0V star. These magnitudes per frequency interval can be converted into magnitudes per wavelength interval by the transformation, Norton (1964).

$$m(\lambda) \approx m(\tfrac{1}{\lambda}) + 5 \log_{10}\left[\frac{\lambda}{\lambda_.}\right]$$

The absolute spectral energy distribution of Vega can be obtained from

$$f(\lambda) = f(\lambda_.) \times 10^{-.4\,m(\lambda)}$$

where $f(\lambda_0) = f(.5560) = 3.66 \times 10^{-12}$ watts per square centimeter micron. The energy available per square centimeter to a photodetector with an S_4 response can be obtained by numerically evaluating the integral

$$\int_{\lambda_1}^{\lambda_2} f(\lambda) \cdot S_4(\lambda) \cdot d\lambda$$

where $S_4(\lambda)$ is the S4 response characteristic. $f(\lambda)$ is plotted in Figure 2, the S4 response is shown in Figure 3, and $f(\lambda) \cdot S_4(\lambda)$ is plotted in Figure 4. The area under $f(\lambda) \cdot S_4(\lambda)$ was evaluated numerically between $\lambda_1 = .34$ micron and $\lambda_2 = .66$ micron as 1.027×10^{-12} watts/cm^2. For a one inch aperture and a 75 per cent optical efficiency, the effective energy rate from Vega becomes 5.15×10^{-12} watts. The visual magnitude
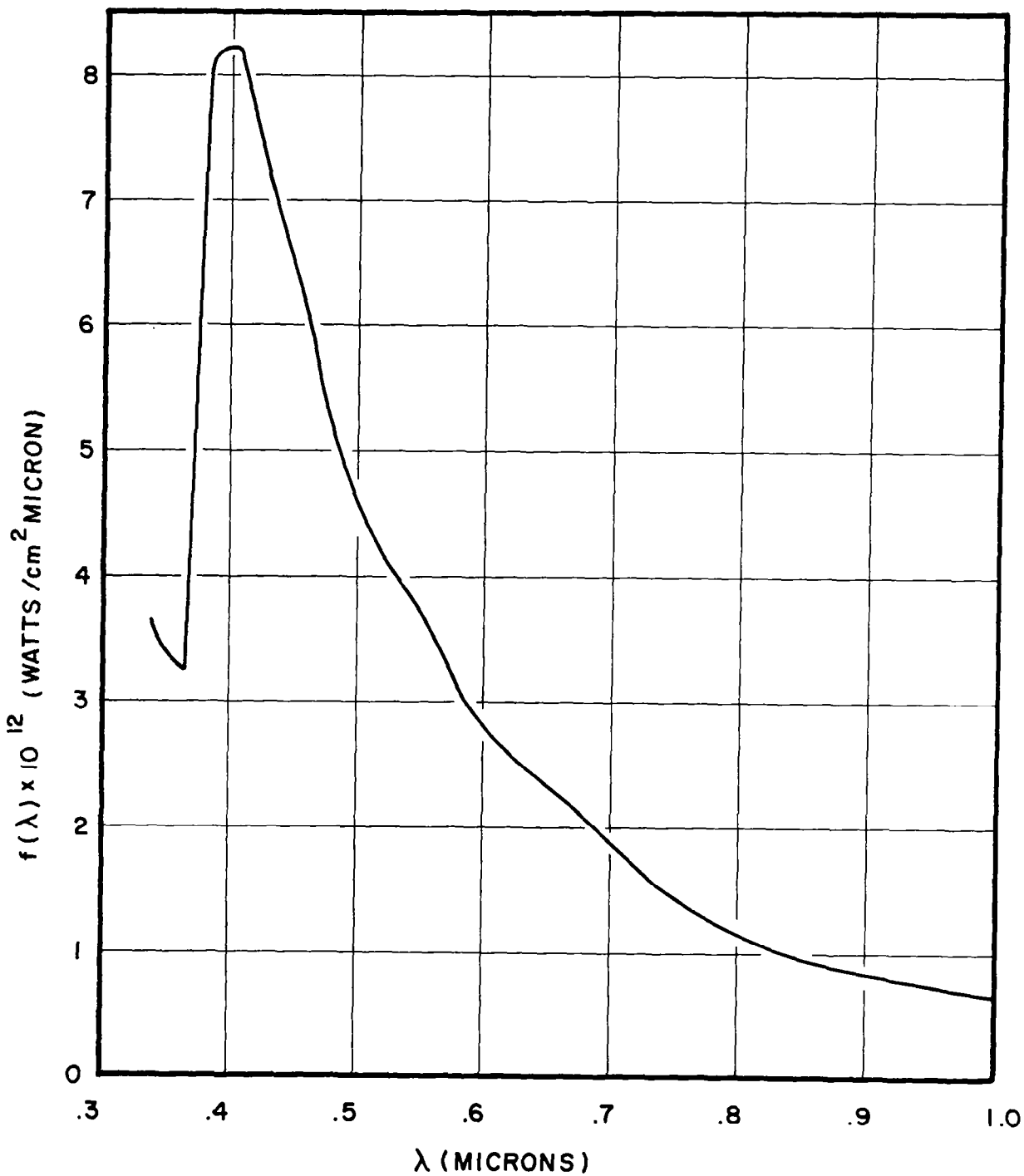
FIGURE 2: ABSOLUTE SPECTRAL ENERGY DISTRIBUTION FOR VEGA
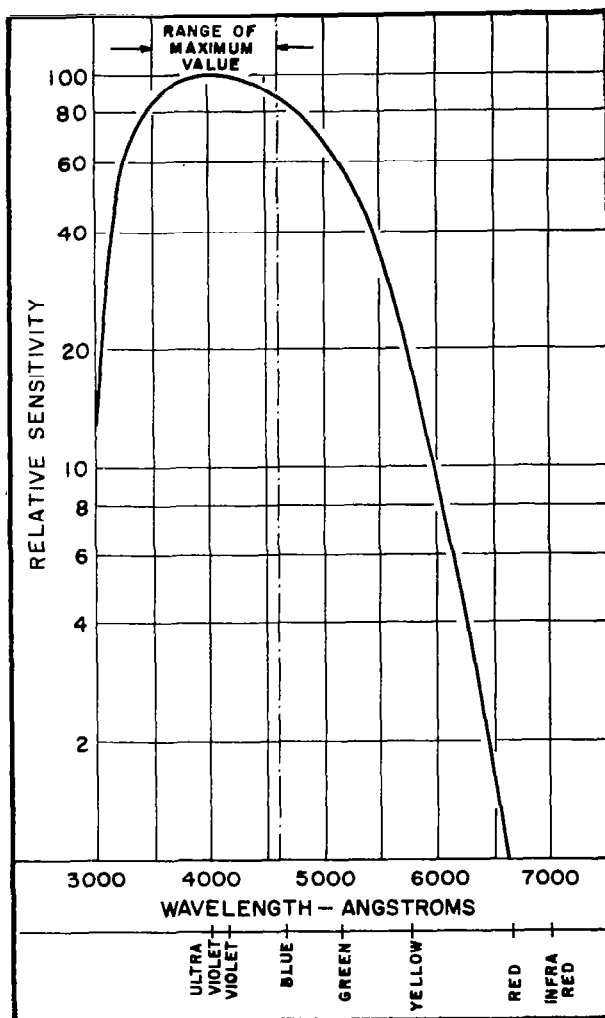
FIGURE 3: SEMI-LOGARITHMIC PRESENTATION
OF S-4 RESPONSE
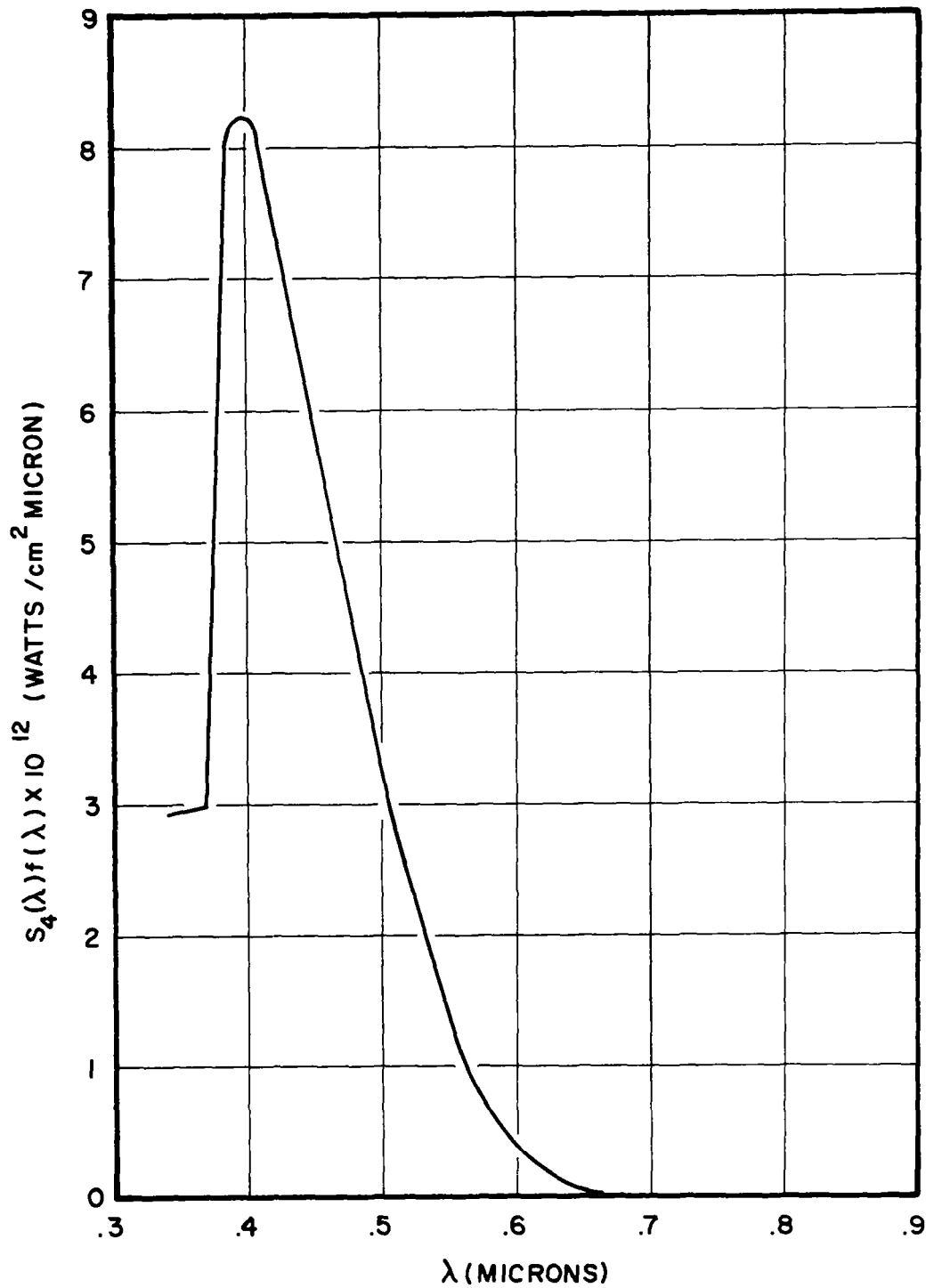
FIGURE 4: EFFECTIVE ENERGY DISTRIBUTION FROM VEGA
FOR S-4 PHOTODETECTOR

of Vega is +.04, so the approximate energy rate for a different magnitude
type A star can be obtained from Allen (1963), p. 192.

$$f_1 = f_2 \cdot 10^{-.4(m_1 - m_2)}$$

The effective energy rate from a third magnitude type A_0V star was found
to be 2.52×10^{-13} watts for an S4 response, a one inch optical aperture,
and a 75% optical efficiency.

Figure 5 gives a spectral response curve, $S_D(\lambda)$, for a silicon photo-
diode [Williams (1962)]. Figure 6 shows the plot of $f(\lambda) \cdot S_D(\lambda)$ from
which the integral

$$\int_{\lambda_1 = .4}^{\lambda_2 = 1.0} f(\lambda) \cdot S_D(\lambda) \cdot d\lambda$$

is numerically evaluated as $.75 \times 10^{-12}$ watts per square centimeter. The
effective energy rate from a third magnitude type A_0V star was found to be
1.51×10^{-13} watts for photodiode response, a one inch optical aperture and
a 75% optical efficiency. The results are presented in Table 1. The relative
response of various photomultipliers to stars in different spectral classes
is described in Subsection II.D.
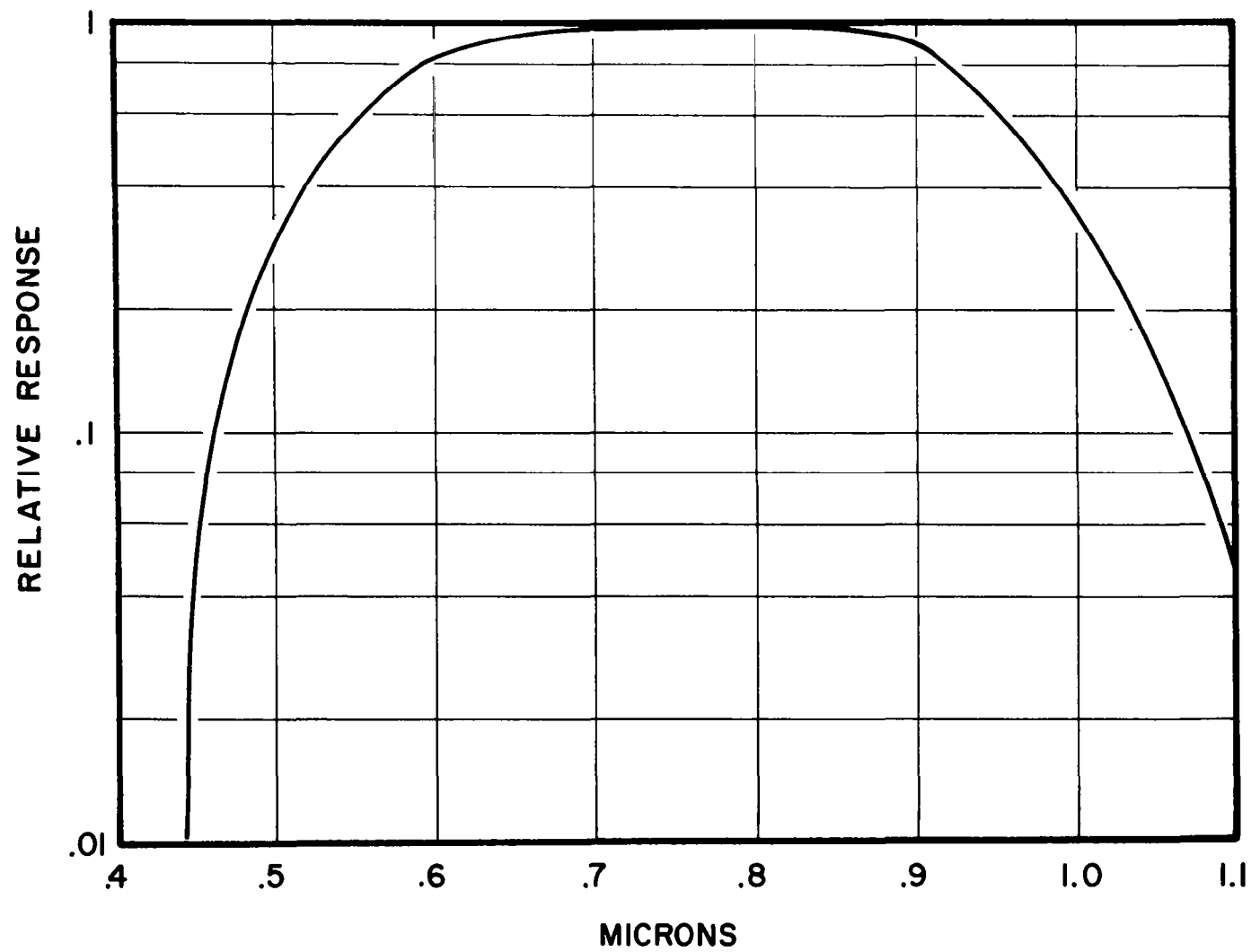
FIGURE 5: PHOTO DIODE RESPONSE
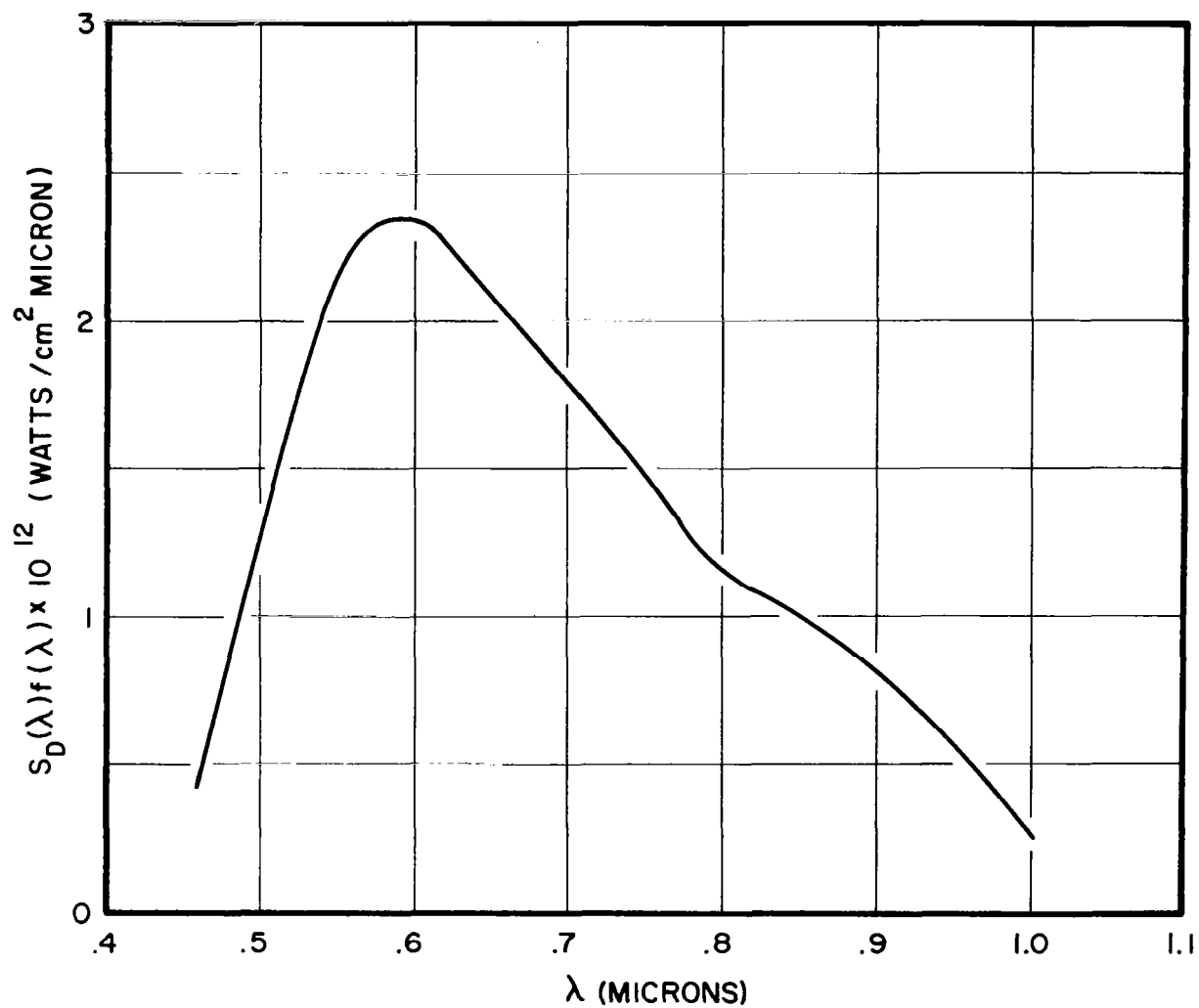
FIGURE 6 : EFFECTIVE ENERGY DISTRIBUTION FROM VEGA FOR PHOTODIODE RESPONSE

TABLE 1

EFFECTIVE ENERGY RESPONSE OF PHOTODETECTORS

Response	λ_1 microns	λ_2 microns	$\int_{\lambda_2}^{\lambda_1} f(\lambda) \cdot S(\lambda) d\lambda$	Effective energy rate from Vega with 1" aperture	Effective energy rate from third magnitude Type A star with 1" aperture and 75% optical efficiency
S-4	.34	.66	1.027×10^{-12}	5.15×10^{-12}	2.52×10^{-13}
Photodiode	.4	1.00	$.75 \times 10^{-12}$	3.08×10^{-12}	1.51×10^{-13}
			(watts/cm^2)	(watts)	(watts)

C.   Figure of Merit

A figure of merit often given for photodetectors is the "noise equivalent power per unit band width" (N.E.P. or P_N) which is the input signal needed to give an output signal-to-noise ratio of unity in a one cps band. Since the noise contains contributions from both device and back-ground, it is evident that measurement conditions must be specified in the evaluation of P_N. In addition, the noise from solid state detectors is frequency dependent.

D. Sky Background

The sky background of faint stars depends on galactic latitude and longitude; a nominal value is 180 tenth magnitude stars per square degree, Allen (1963). If these are assumed Vega type stars and a slit of 20 degrees by one minute of arc is used in the assumed optical system, the effective background reaching the detector is,

$$F_b = (.75)(5.15 \times 10^{-12}) 10^{-.4(10-.04)} \times \frac{20}{60} \times 180$$

$$= 2.4 \times 10^{-13} \text{ watts}$$

For a given photodetector, the minimum energy of a monochromatic signal which can be "detected" is that which causes a signal equal to the shot noise. From the discussion of Smith (1957), the shot noise is given by the equation

$$I_{RMS} = \sqrt{2e I_{dc} \Delta f}$$

but

$$I_{dc} = \bar{n} \cdot Q_e \cdot e$$

where $\bar{n}$ = sky background photon rate

Q_e = quantum efficiency of photocathode

e = electron charge

Hence

$$I_{RMS} = \sqrt{2 e^2 Q_e \bar{n} \, \Delta f}$$ = shot noise due to sky background

The product $\dfrac{Q_e \cdot e}{hv}$ has the units of ampere per watt, where h is Planck's constant and v is the light frequency. So light radiation of W_L watts from a star can be converted by a photocathode into a signal current of

$$\frac{W_L \cdot Q_e \cdot e}{h v}$$ ampere.

Equating the signal current to the RMS shot-noise current yields

$$W_L = \frac{hv}{Q_e} \sqrt{2 Q_e \bar{n} \, \Delta f}$$

$$= hv \sqrt{\frac{2 \bar{n} \, \Delta f}{Q_e}}$$

but $\bar{n} = \dfrac{F_b}{hv}$ so $\dfrac{W_L}{\sqrt{\Delta f}} = \sqrt{\dfrac{2 h v F_b}{Q_e}}$

For a quantum efficiency of .1 and at the frequency of the peak S4 response, we obtain

$$\frac{W_L}{\sqrt{\Delta f}} = 1.55 \times 10^{-15} \frac{watts}{(cps)^{\frac{1}{2}}}$$

Since the device noise has not been included and the required slit area may be larger by at least a factor of five, it is conceivable that a photodetector could be limited by sky background, particularly for detection of stars weaker than third magnitude at fast scan rates.

E. Electrical Bandwidth

The minimum signal which can be detected will depend upon the electrical bandwidth of the detecting apparatus. This, in turn, depends upon the rise and fall times of the signal pulses.

Let it be assumed that the star "blur circle" is Gaussian and traverses the slit in Δt seconds. If the detecting system is not bandwidth limited the signal in the time domain will be,

$$G(t) = \frac{1}{\sqrt{2\pi\sigma^2}} \, e^{-\frac{t^2}{2\sigma^2}} \tag{1}$$

The Fourier transform (spectrum) of Equation (1) is

$$\mathcal{G}(j\omega) = \sqrt{2} \, e^{-\frac{\sigma^2\omega^2}{2}} \tag{2}$$

The signal has fallen to 1/e in a time,

$$t = \pm \sqrt{2} \, \sigma \tag{3}$$

The response falls to 1/e at frequency,

$$\omega = \frac{\sqrt{2}}{\sigma} = \Delta\omega \tag{4}$$

From Equation (3)

$$\Delta t = 2 \sqrt{2} \ \sigma$$

and from Equation (4)

$$\Delta \omega = 2 \pi \Delta f = \frac{4}{\Delta t}$$

or the minimum necessary bandwidth is

$$\Delta f = \frac{2}{\pi \Delta t}$$

For the case where the optical axis is perpendicular to the spin axis, the star transit time is approximately

$$\Delta t = \frac{B_c T}{21,600}$$

where B_c equals the blur circle in minutes of arc and T is the scan period in seconds. So for this case the

$$\Delta f = \frac{2 \cdot 21,600}{\pi B_c T}$$

For a typical B_c = 3 minutes of arc and a typical T = 10 seconds, Δf = 425 cycles per second.

F.   Suitable Detectors

P_N is usually given in units of watts per $cps^{\frac{1}{2}}$. We can now check whether a given device can be used simply by comparing the quantity,

$$P_N = P_N \sqrt{\Delta f} \ \ watts$$

with the energy available from a star.

R. L. Williams (1962) reports a silicon photodiode with

$$P_N = 1.8 \times 10^{-13} \frac{watts}{\sqrt{cps}}$$

This diode using a 425 cps bandwidth can detect a signal of

$$P_N = 3.71 \times 10^{-12} \ watts$$

and falls short by an order of magnitude in the required sensitivity.

It could just be used to detect a third magnitude Type A star if the aperture were increased to

$$D = \sqrt{\frac{37.1}{1.51}} \cong 5 \ inches.$$

Here the signal to noise ratio would be unity assuming the sky background is negligible.

G. Use of Gas Phototube

G. Kron (1952) has reported on the use of gas phototubes for infrared photometery in the .8 micron region. (This region is at the peak of the S1 response and Kron's work was motivated by the lack of domestic photomultipliers with S1 response.)

The principal sources of noise in a phototube will be the shot noise of the tube (which in turn depends on the convection current and the leakage conduction current) and the Johnson noise of the load resistor. Let i_o be the tube current, σ be the gas multiplication factor, and R be the load resistance. Neglecting the leakage current, the mean square fluctuation in the output voltage is

$$\overline{N^2} = 2 e i_o \sigma^2 R^2 \Delta f + 4 k T R \Delta f$$

where k is Boltzmann's constant, T is absolute temperature of the resistor, and e is the electronic charge (see Smith (1957)).

The noise in the tube exceeds the resistor noise when

$$R \geq \frac{2 k T}{e \sigma^2 i_o} \tag{5}$$

For example, if T is 300°K, $i_o = 10^{-12}$ amp, and $\sigma = 1$ (vacuum photodiode) $2kT/e\sigma^2 i_o \cong 5 \times 10^{10}$ ohms. So for tube noise to be comparable to resistor

noise, the load resistor must be very large.

In our case we will not want to degrade the response by making the time constant of the input circuit too large. A half-power bandwidth of 425 cycles in an RC filter requires a time constant of

$$RC = \frac{1}{2\pi \Delta f} = 3.75 \times 10^{-4} \text{ second.}$$

It is possible to reduce the input capacity to about 5×10^{-12} fd. Thus we can make R as large as

$$R = 75 \text{ megohms}$$

If we take the effective energy rate from a third magnitude star from Table I for an S4 response the number of quanta incident on the photo-cell is

$$\bar{n} = \frac{2.52 \times 10^{-13}}{h\nu} = 5.06 \times 10^{5} \text{ photons per second.}$$

With a quantum efficiency of 10% the signal current is

$$i_s = e\, Q_e\, \bar{n} = 8.1 \times 10^{-15} \text{ amp}$$

We temporarily neglect the gas amplification factor σ since it affects both signal and dark current noise signal equally. The dark current noise must not exceed the signal current. Thus,

$$i_s \gtrsim \sqrt{\overline{i^2}} = \sqrt{2\, e\, i_d\, \Delta f}$$

which requires

$$i_d \gtrsim \frac{i_s^2}{2e \Delta f} = 4.82 \times 10^{-13} \text{ ampere}$$

This value can easily be obtained.

For efficient operation of the phototube we have by Equation (5)

$$\sigma^2 \gtrsim \frac{2kT}{e i_d R_L}$$

$$\sigma \gtrsim 33$$

Potassium hydride gas filled photocells have been successfully operated at gas multiplying factors of 50 without an increase in signal to noise ration, Steinke (1936). G. Kron (1952) gives a design for a gas phototube which can be operated at gas multiplying factors up to 100.

Under the assumed conditions the signal voltage due to a third magnitude Type A star will be

$$i_s \sigma R = 20.2 \text{ microvolts}$$

At room temperature the Johnson noise of the load resistor will be

$$\sqrt{\overline{n^2}} = \sqrt{4kTR \Delta f} = 23 \text{ microvolts}$$

Therefore the input resistance of the amplifier adds as much noise and the system is marginal.

However, improvement of signal to noise ratio by a factor 4 is possible by doubling the aperture. Further improvement can be had by cooling the load resistor. Indeed, the phototube and its associated circuitry may both be cooled to advantage, Kron (1952). This cooling might be simply done by insulating the detector from the rest of the vehicle and allowing the detector to radiate thermally to the $3.1^{o}K$ space background.

It thus appears feasible to use gas phototubes as the light sensitive element. Internal sources of noise must be carefully suppressed. A two inch aperture at 75% transmission may be necessary, and it will be desirable to cool the load resistor and phototube.

H.   Some Other Detectors

F. Low (1961) has described a low temperature germanium bolometer, which appears "potentially competitive with phototubes." At a temperature of 7^OK and if the conductivity to the surroundings were as low as 10^{-7} watts per ^{O}K, this device has a noise equivalent power of

$$P_N = 3 \times 10^{-14} \frac{watts}{(cps)^{\frac{1}{2}}}$$

Over a 425 cps band the minimum detectable energy flux into the one inch aperture system would be

$$P_N = 6.18 \times 10^{-13} \ watts$$

Low calculates a time constant of .32 second for his device for these assumed conditions, but it is also likely that germanium bolometers with smaller time constants can be designed.

W. Franzen (1963) describes a non-isothermal superconducting bolometer. A current passed through the sensitive element (which is an evaporated tin strip on a 1000 Angstrom thick Al_2O_3 substrate) heats the element enough to keep the center of the element above the superconducting transition. The ends are cooled below the transition. Incident radiation heating the element increases the length of the element above the transition resulting in a resistance change. Franzen estimates that a noise equivalent power can be as low as

$$P_N = 2.8 \times 10^{-14} \frac{watts}{(cps)^{\frac{1}{2}}}$$

It is, however, yet but a laboratory device and to the authors' knowledge has not yet been actually built.

The use of p-n junctions as both a photodetector and as a parametric amplifier has been suggested, Saito (1962). Modulated light falls on the diode as a pumping voltage is simultaneously applied, see Figure 7.

The advantage of this device is that the noise contribution of the following amplifier is significantly reduced. Garbrecht (1964) and Saito (1964) have compared this arrangement to a photodiode followed by a parametric amplifier.

A more promising approach would seem to be the use of avalanche multiplication in a reverse biased photodiode. Current gains as large as 1000 have been theoretically predicted, Haitz (1963). Di Domenico, et al. (1965) report a signal enhancement by 25 db when mixing modulated laser light with R.F. by means of a point contact silicon photodiode when operated near avalanche breakdown. They point out that this enhancement was obtained without an increase in the noise power and suggest the possibility of shot noise limited operation.
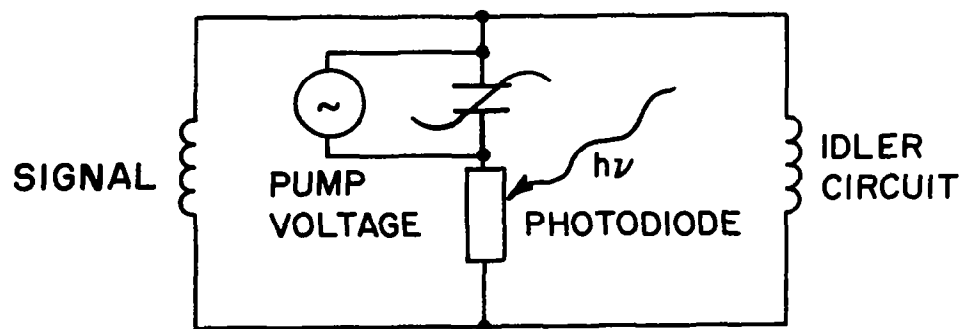
FIGURE 7: PN JUNCTION PARAMETRIC
AMPLIFIER PHOTODETECTOR

PHOTODETECTORS

I.   Superiority of Photomultipliers over Phototubes

There is no question that photomultipliers can be used. For example, a 9502-S E.M.I. photomultiplier with

$$P_N = 3.3 \times 10^{-17} \frac{watts}{(cps)^{\frac{1}{2}}}$$

is available. Thus in a 425 cycle band this can detect a signal of

$$P_N = 6.80 \times 10^{-16} \ watts$$

With an S4 response (see Table I) and the assumed optical system this power level corresponds to a 9.5 magnitude Type A star, neglecting sky background.

Lallemand (1960) has demonstrated the superiority of shot noise limited detectors to those limited by the input circuit to the electronics. The argument is specifically applied to photomultipliers versus photo-tubes, but will hold for any multiplying device as against its non-multiplying equivalent, e.g., gas phototube versus vacuum phototube, avalanche photodiode or parametric-amplifier photodiode as against simple photodiode.

The argument is worth repeating here. Let I_m be the minimum signal detectable at signal to noise ratio S_n, for a photomultiplier and let I_p be the same quantity for a phototube. Then if the photomultiplier is shot noise limited

V-25

$$I_m = S_n \sqrt{2 e i_d \Delta f} \tag{6}$$

i_d = dark current in amperes

$e = 1.602 \times 10^{-19}$ coulombs-electronic charge

Δf = bandwidth, cps.

Assuming the phototube limited by the input circuitry,

$$I_p = S_n \sqrt{4 k T \frac{\Delta f}{R}} \tag{7}$$

where T is in $^\circ$K and R is the value of the input resistor in ohms.

Define a modulation factor by

$$\Gamma = \sqrt{2} \, \frac{I_m}{i_d} \tag{8}$$

Then Equations (6) and (8) give

$$I_m = 2 \sqrt{2} \, e \, S_n^2 \, \frac{\Delta f}{\Gamma} \tag{9}$$

Then, the minimum detectable signal ratio is

$$G = \frac{I_p}{I_m} = \frac{\Gamma}{S_n e} \sqrt{\frac{k T}{2 R \Delta f}} \tag{10}$$

But R will inevitably be in shunt with some input capacity C which, indeed,

sets the bandwidth as,

$$\Delta f = \frac{1}{2\pi RC} \tag{11}$$

The use of Equation (11) in (10) leads to

$$G = \frac{\Gamma}{S_n e} \sqrt{\pi k T C} \tag{12}$$

which depends only on temperature T, capacity C, modulation factor Γ, and

the signal to noise ratio S_n. C can be as small as 5 pfd. Taking

$T = 300^{\circ}K$, $S_n = 2$,

$$G \approx 800 \cdot \Gamma \tag{13}$$

If $\Gamma = 1$, $(\sqrt{2}\ I_m = i_d$, not an unreasonable condition) $G = 800$. And the

multiplier is almost three orders of magnitude better!

J. Photomultiplier Characteristics

With the performance superiority of photomultipliers over non-multiplying phototubes established, it is appropriate to further discuss some of the important characteristics of photomultipliers as related to star detection.

In a photomultiplier, each photoelectron emitted from the photocathode undergoes cascade multiplication inside the tube and comes out of the tube as a pulse of many (about 10^6) electrons. If the photoelectrons were multiplied by this process to form pulses of exactly equal sizes, they would continue to contribute equally to the signal current, but in actual photomultipliers the amount of multiplication is very different from one photoelectron to another. Consequently, the stream of pulses coming out of a photomultiplier tube has a very broad range of amplitudes, some of the pulses contributing ten times as much to the photocurrent as others.* Since the pulses are not of equal size, it is evident that the signal-to-noise performance of a photomultiplier will be lower when used in combination with an ordinary current measuring or charge collecting (condenser-integrator) system than when used in a system that counts the pulses with equal weight redardless of these sizes.** However, the current measuring method is easier to implement for scanning optical systems. Because of the very high rate of photoemission for bright stars, a pulse counting

---

*   Discussed by Engstrom (1947) and Tusting (1962).

** See the discussion by Baum (1962) p.23, Farrell and Zimmerman (1965), and Section VI.B of this report.

technique would require a system of high capacity, high speed counters which become somewhat impractical for low power satellite applications. So far as is known, a pulse counting system has not yet been implemented for a satellite system.

1.   Photomultiplier Cathode Emission*

An electron may be ejected from the surface of certain metals if the energy of electromagnetic radiation striking the surface exceeds the surface potential barrier. The number of electrons ejected per incident photon is termed the quantum efficiency. Because of electron scattering and reflection at the surface during the energy transfer, the quantum efficiency is less than unity.

Figure 8 shows the electron potential energy level diagram at the inteface between a solid and a vacuum. Electrons in the conduction band can move through the solid when a potential difference is applied across the solid. If the energy of electromagnetic radiation striking the surface exceeds the surface potential barrier, a conduction electron may be sufficiently excited and be ejected from the surface of certain metals. Other electrons not in the conduction band are more tightly bound in a lower energy level and the gap between the conduction band and the lower level valence band represents the energy required to raise an electron into the conduction energy level band.

---

*   Sharpe, J. (1961)
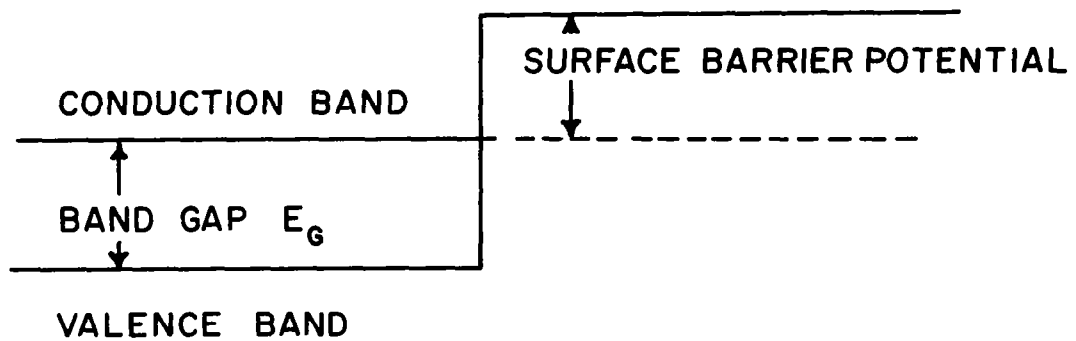
FIGURE 8: THE ENERGY LEVELS OF SEMICONDUCTORS

For a semiconductor material such as an antimony-cesium alloy, Cs_3Sb, photons must provide enough energy to an electron to raise its energy level above the conduction level and the surface potential barrier before the electron is ejected as a photoelectron. In Cs_3Sb, this energy is approximately 1.9 eV which corresponds to a long wavelength threshold of .66 micron. Because it is relatively easy for free electrons to escape, at room temperature the thermionic emission rate of Cs_3Sb ranges from 10^2 to 10^4 per square centimeter per second. This rate can be drastically reduced by cooling the material.

Above the threshold wavelength the quantum efficiency rises to a maximum (as the excess energy supplied to the electron increases) until the optical absorption of the photosurface and any window material causes the excess energy and therefore the quantum efficiency to decrease. The maximum quantum efficiency depends upon the cathode material and ranges from .07 to 0.25.

Figure 9 shows spectral response curves for various types of available photocathodes. The influence of the window cut-off in the ultraviolet region is also shown. Table 2 shows a tabulation of photosensitivity values in microamperes per lumen of tungsten light at $2870^\circ K$.

As can be seen, no photoemissive surface is available with sensitivity above 1.2 microns. At the opposite end of the spectrum, normal glass envelopes cause a radiation cut-off at about 0.35 micron. Special ultraviolet transmitting glasses cut off radiation at approximately .22 micron and fused-silica glass cut-off at .165 micron. Consequently,
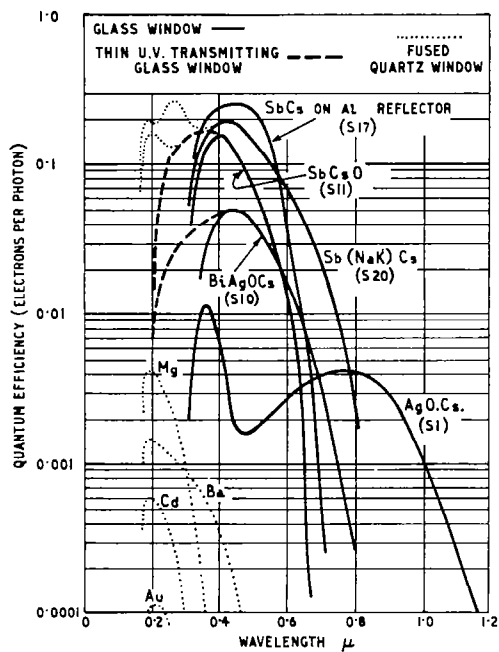
FIGURE 9 : *Spectral response of various photocathodes*

TABLE II
TYPICAL PHOTOCATHODES
(Glass windows except where noted†)

Photocathode	Form	Peak Sensitivity		Long Wavelength Threshold	Typical Sensitivity (2870 °K lamp)
		λ	Quantum Efficiency		
		μ	Electrons/ photon	μ	μA/L
SbCsO (S–11) ..	Semi transparent	0·42	0·15	0·67	60
SbCs (S–4)	Opaque	0·45	0·10	0·7	40
SbCs (EMI 'S') ..	Semi-transparent	0·42	0·12	0·65	40
Sb(NaK)Cs (S–20) ..	,,	0·44	0·20	0·85	150
BiAgOCs (S–10) ..	,,	0·45	0·05	0·8	35
AgOCs (S–1) ..	,,	0·8 (also	0·004 in blue)	1·2	15
†Mg (quartz window)	,,	<0·2	0·004	0·39	—
†Au (quartz window)	,,	<0·2	0·0001 to 0·00001	0·27	—

photoemissive surfaces are commercially obtainable over a wavelength range from .165 micron to 1.2 microns. Type A stars fall within this spectral range.

2. Photomultiplier Secondary Emission

An electron with a few hundred electron volts of energy which strikes the surface of a solid-vacuum interface will impart some of its energy to a few adjacent electrons in the solid. Some of the excited electrons may then have enough energy to overcome the surface potential barrier and be ejected as secondary electrons. The number of electrons ejected depends upon the energy loss rate of the incident electron and the energy imparted to the secondary electrons. An electron with low incident velocity cannot impart high energies to adjacent electrons, while a high incident velocity causes the electron to penetrate deeper into the solid where excited electrons find it more difficult to escape. Consequently, there is an optimum incident energy which produces a maximum number of secondaries, σ, per incident electron. Figure 10 shows curves of σ versus voltage curves for photomultiplier secondary emission materials. A single stage of secondary emission will multiply the current by about a factor of σ, and for n stages the photocurrent is multiplied by σ^n.

Various geometries can be employed for a secondary emission multiplier assembly. The design problem is to ensure that electrons strike the secondary emission element (called a dynode) at points where the electric field is directed away from the dynode and toward the next dynode. Four

FIGURE 10: g_1, σ *voltage curves for various materials*
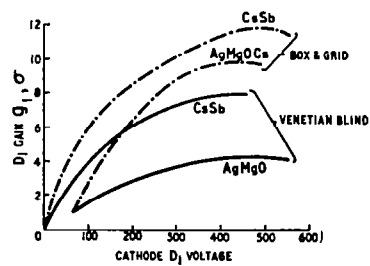
useful geometries are shown in Figure 11.

All four types in Figure 11 are electrostatically operated and may be placed in two classes determined by the strength of the electric field at the surface of the dynode. For the venetian-blind (Figure 11c) and the box-grid (Figure 11-d) structures, the directing field at the dynode surface is comparatively weak so the initial velocity of the secondary electrons largely determines the landing position on the next dynode. Since there is little relationship between the emission point of one dynode and the arrival point of the next dynode, the multiplier assembly is said to be unfocussed. Generally the box and grid structure is physically smaller than the venetian-blind structure. Figures 11a and 11b show focussed structures with strong directing fields constraining the secondaries to paths with little position spread resulting in less transit time spread compared to the unfocussed structures. Larger currents may be drawn since the high electric fields reduce space charge effects.

Each secondary electron emitted from one dynode is not successful in producing secondary electrons at the succeeding dynode.* Therefore, the stage gain depends upon the value of σ which is characteristic of the secondary emission element and the dynode collection efficiency, g. Both σ and g are voltage dependent. Figure 12 indicates the high efficiency of the box-grid structure using the SbCs surface while an AgMgO material must be prepared with cesium to achieve a high secondary emission.

---

* The effect of losing electrons between the cathode and anode has been investigated by Gadsten (1965).
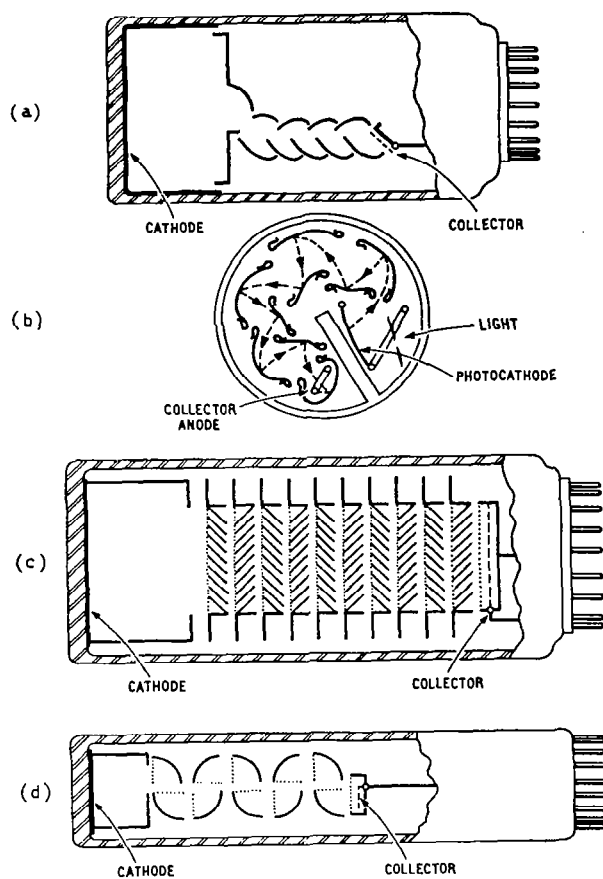
FIGURE 11 *Electrostatic dynode systems; (a) focused structure, (b) compact focused structure, (c) venetian-blind structure, (d) box-and-grid structure*
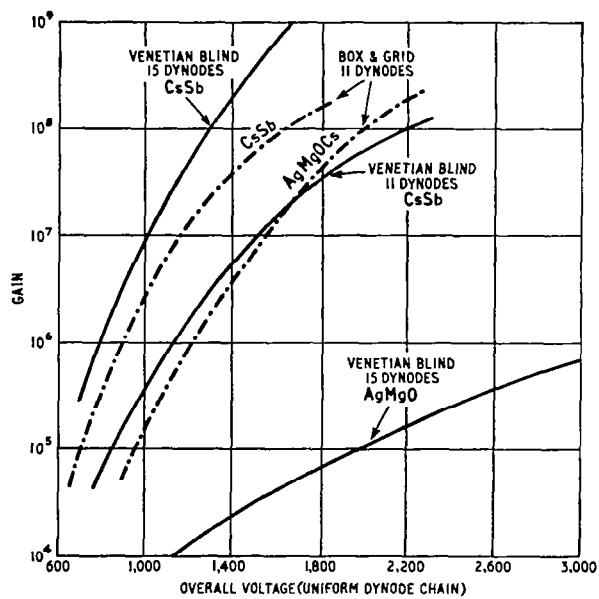
FIGURE 12 : *Gain vs voltage curves for various dynode systems and secondary emitting surfaces*

3.   Typical Photomultiplier Gain, Sensitivity, and Dark Current Curves

Photomultiplier sensitivity is specified at a given overall voltage in terms of amperes per lumen, while the cathode sensitivity is specified in microamperes per lumen. Figure 13 shows how photomultiplier sensitivity varies with different dynode structures and dynode materials.

When the photomultiplier is completely blacked out, cathode thermionic emission is multiplied by the dynode assembly in the same manner as cathode photoelectrons resulting in a tube dark current. Photomultiplier dark current may be specified either as the anode dark current at a specified photomultiplier sensitivity or as the equivalent light input in lumens which gives the equivalent value of dark current. If no anode to cathode feedback occurs, the equivalent dark current input is independent of tube gain up to some limiting value, see Figure 14. Above a certain gain, the equivalent light input increases and increasing the voltage ultimately causes the tube to become unstable. The rapid rise in anode dark current with gain is due to optical and ionic anode to cathode feedback. The box and grid dynode structure has a limiting gain value which is generally independent of the number of stages. The venetian-blind structure characterizes a higher value of limiting gain before feedback begins and is increased by a factor of two for each additional pair of dynodes. Dark current also increases with cathode area.

In any application of the photomultiplier to star detection, one of the most important considerations is the tube dark current. Depending upon what voltage is applied to the tube, there are three dominating types of
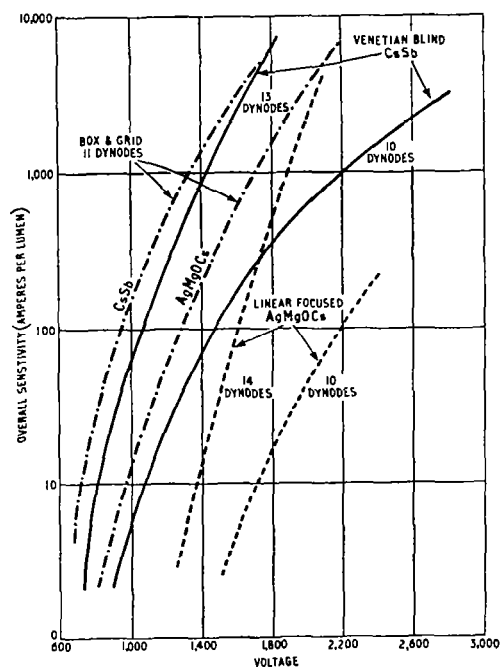
FIGURE 13: *Overall sensitivity vs overall voltage*
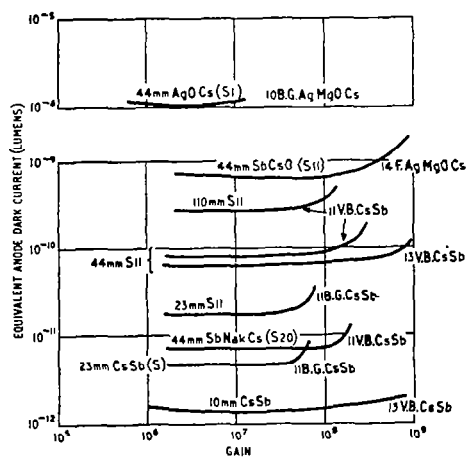
FIGURE 14: *Dark current at 23 °C vs gain for various cathode sizes and types and various dynode structures. Typical sensitivities are: S11, 60–70 μA/L; SbCs, 40–60 μA/L; S1, 15–30 μA/L, and S20, 120–140 μA/L. F = focused, V.B. = venetian blind, B.G. = box and grid dynodes*

dark current, ohmic leakage, thermionic emission, and regenerative ioniza-
tion. At low voltage ohmic leakage caused by slight conduction in
insulating materials is dominant. At high voltages regenerative ionization
caused by anode to cathode feedback of ionized gas ions or by light
emission from ionized gas becomes dominant. At normal operating voltages,
the dominant noise source is thermionic emission.* Thermionic emissions
from the dynodes contribute only about 3% of the total thermionic emission
noise. Thermionic cathode emissions are amplified by the multiplier
dynode chain in the same manner as photo emissions. Associated with
cathode thermionic emission is a shot noise resulting from randomly
emitted electrons, which is variably multiplied by the dynodes. The RMS
variation in the thermionic emission current is expressed by the basic
shot noise equation.

$$I_{RMS} = \sqrt{2 e I_{av} \Delta f}$$

where $e = 1.6 \times 10^{-19}$ coulomb = electron charge

I_{av} = average value of the cathode current

Δf = electrical bandwidth in cycles per second.

If a cathode material has a simple thermionic work function, then
thermionic emission will fall with absolute temperature according to
Richardson's Law

---

* Engstrom, Ralph W., (1947)

$$J_k = AT^2 e^{\frac{-E}{kT}}$$

where J_k = thermionic current density in amperes per cm^2

   A = amp/cm^{2}T^2 = constant depending on cathode material

   E = work function of material in volts

   T = absolute temperature in degrees Kelvin

Hence, the most obvious way of decreasing the thermionic emission is by cooling the cathode. It has been reported by ITT-Federal Laboratories (1964) that the dark current of their photomultipliers falls about one order of magnitude per 10°C of cooling and that the dark noise falls about an order of magnitude for each 20°C of cooling. Since cathode materials exhibit multiple work function characteristics, Richardson's Law does not hold at low temperatures. It has been reported, Sharpe (1964), that the decrease of dark current with temperature apparently flattens out at -40°C and any further cooling does not decrease dark current.

4.   Photomultiplier Noise [Eberhardt,(1959)]

At the cathode the RMS variation in cathode emission current is expressed by $I_{RMS} = i_k = \sqrt{2eI_k \Delta f}$ where I_k is the average or DC value of the cathode signal current. From this equation a cathode signal-to-noise power ratio can be expressed as

$$\left(\frac{S}{N}\right)_k = \frac{I_k^2}{i_k^2} = \frac{I_k}{2e \Delta f} \tag{14}$$

where $\quad e = 1.6 \times 10^{-19}$ coulomb = electron charge

Δf = bandwidth in cycles per second.

At the first dynode, most of the electrons emitted from the cathode are collected while the remaining electrons are lost in traveling from the cathode to first dynode. The electrons collected at dynode, D1, cause an input current I_1 which has an RMS variation approximately $i_1 = \sqrt{2eI_1\Delta f}$. So at the input to the first dynode D1, the signal-to-noise power ratio is

$$\left(\frac{S}{N}\right)_1 = \frac{I_1^2}{i_1^2} = \frac{I_1}{2e\Delta f} = \frac{\epsilon I_k}{2e\Delta f} = \epsilon \left(\frac{S}{N}\right)_k \qquad (15)$$

where ϵ is the percentage of emitted cathode electrons collected at the first dynode. $\epsilon = I_1/I_k$ is also termed the collection efficiency.

Equation (15) indicates a photomultiplier should have a high collection efficiency, i.e., the electron loss between cathode and first dynode must be minimized. At the first dynode, each incident electron liberates an average of σ additional electrons because of the secondary emission process. So the average current from the first dynode $I_2 = \sigma_1 I_1$. The RMS variation of the current into the first dynode is multiplied by the multiplication factor and is $i_{2K} = \sigma_1 i_1$. Since the secondary emission process is assumed to be a Poisson process, there is an additional shot noise component, $i_{2s} = (2eI_2\Delta f)^{\frac{1}{2}}$. Since both noise components are assumed independent, the mean square components may be summed

$$i_2^2 = (i_{2s})^2 + (i_{2k})^2 = 2e I_2 \Delta f + \sigma_1^2 \, 2e I_1 \Delta f$$

$$= 2e \Delta f (I_2 + \sigma_1 I_2)$$

$$= 2e \Delta f \, I_2 (1 + \sigma_1) \tag{16}$$

Consequently, the signal-to-noise power ratio at the output from dynode D1 equals

$$\left(\frac{S}{N}\right)_2 = \frac{I_2^2}{i_2^2} = \frac{I_2^2}{2e \Delta f \, I_2 (1+\sigma_1)} = \frac{\sigma_1 I_1}{(1+\sigma_1) 2e \Delta f} = \frac{\sigma_1}{(1+\sigma_1)} \left(\frac{S}{N}\right)_1 \tag{17}$$

Thus the signal-to-noise ratio is degraded by a factor of $\sigma_1/(1+\sigma_1)$ due to the multiplication process. For a typical $\sigma = 4$, this factor becomes $4/5 = .80$, so a typical 20% loss in signal-to-noise ratio is caused by electron secondary emission multiplication.

The noise generation process at the second dynode is similar to that described for the first dynode. So

$$i_3^2 = \underbrace{2e I_3 \Delta f}_{\substack{\text{shot noise} \\ \text{due to secondary} \\ \text{emission}}} + \underbrace{\sigma_2^2 i_2^2}_{\substack{\text{amplified noise} \\ \text{from first dynode}}} \tag{18}$$

But $I_3 = \sigma_2 I_2$, so

$$\sigma_2^2 \, i_2^2 \;=\; \sigma_2^2 \,(1 + \sigma_1')\, 2e \,\Delta f \, I_2$$

$$=\; \sigma_2'\,(1 + \sigma_1')\, 2e \,\Delta f \, I_3$$

$$i_3^2 \;=\; 2e\, I_3 \,\Delta f \left[\, 1 + \sigma_2'\,(1 + \sigma_1')\,\right]$$

$$\left(\frac{S}{N}\right)_3 = \frac{I_3^2}{i_3^2} = \frac{I_3\,\sigma_2'\,(1 + \sigma_1')}{2e\,\Delta f \left[1 + \sigma_2'\,(1 + \sigma_1')\right]\sigma_2'\,(1+\sigma_1')} = \frac{\sigma_2'\,(1+\sigma_1')}{\left[1 + \sigma_2'\,(1+\sigma_1')\right]}\left(\frac{S}{N}\right)_2 \quad (19)$$

With $\sigma_1 = \sigma_2 = 4$ as before,

$$\frac{\left(\frac{S}{N}\right)_3}{\left(\frac{S}{N}\right)_2} \approx \frac{4(1+4)}{\left[1 + 4(5)\right]} = \frac{20}{21} = .95$$

So for a typical photomultiplier there is only about 5% reduction in signal-to-noise ratio at the second dynode.

At the third dynode, the mean square noise current can be expressed by

$$i_4^2 = 2e\, I_4 \,\Delta f \;+\; \sigma_3'^2 \, i_3^2 \;=\; 2e\, I_4 \,\Delta f \;+\; \sigma_3'^2 \left[1 + \sigma_2'\,(1 + \sigma_1')\right] 2e\, I_3 \,\Delta f$$

but

$$I_4 \;=\; \sigma_3'\, I_3$$

so

$$i_4^2 = 2e\,I_4\,\Delta f\left[1 + \sigma_3 + \sigma_3\sigma_2 + \sigma_3\sigma_2\sigma_1\right]$$

(20)

If $\sigma_1 = \sigma_2 = \sigma_3 = \sigma$, Equation (20) becomes

$$i_4^2 = 2e\,I_4\,\Delta f\left[1 + \sigma + \sigma^2 + \sigma^3\right]$$

Extending the above argument, it is easy to see for the nth dynode

$$i_{n+1}^2 = 2e\,I_{n+1}\,\Delta f\left[1 + \sigma + \sigma^2 + \sigma^3 \cdots\cdots + \sigma^n\right]$$

The last dynode is the nth stage and is termed the anode, so the signal-to-noise ratio at the anode is

$$\left(\frac{S}{N}\right)_a = \frac{I_a^2}{i_a^2} = \frac{I_a^2}{2e\,I_a\,\Delta f\left[1 + \sigma + \sigma^2 + \cdots\cdots + \sigma^n\right]}$$

$$I_a = \sigma^n I_1$$

so

$$\left(\frac{S}{N}\right)_a = \frac{\sigma^{2n} I_1}{2e\,\sigma^n\,\Delta f\left[1 + \sigma + \sigma^2 + \cdots\cdots + \sigma^n\right]}$$

(21)

substituting $\sigma^{n+1} - 1 = (\sigma-1)(\sigma^n + \sigma^{n-1} + \ldots + 1)$ Equation (21) becomes

$$\left(\frac{S}{N}\right)_a = \frac{\sigma^{2n}(\sigma-1)\,I_1}{2\,e\,\Delta f\,\sigma^n\,(\sigma^{n+1}-1)} = \frac{\sigma^{2n}(\sigma-1)}{\sigma^n\,(\sigma^{n+1}-1)}\left(\frac{S}{N}\right)_1$$

$$= \frac{\left(1-\frac{1}{\sigma}\right)}{\left(1-\frac{1}{\sigma^{n+1}}\right)}\left(\frac{S}{N}\right)_1$$

If $n \geq 6$ and $\sigma \gg 2$, $1/\sigma^{n+1} \ll 1$, so

$$\left(\frac{S}{N}\right)_a = \frac{\sigma-1}{\sigma}\left(\frac{S}{N}\right)_1 \tag{22}$$

Consequently, the total reduction in signal-to-noise ratio is independent of the number of dynodes. Therefore, it is possible to use as many dynodes as necessary to raise the signal level above other noise sources.

For a $\sigma = 4$, the overall signal-to-noise is reduced by a factor $4-1/4 = .75$ which indicates a 25% loss. Recalling that there was a 20% loss at the first dynode and a 5% loss at the second dynode indicates that the remaining dynodes contribute negligible reduction in the signal-to-noise ratio.

From Equations (15) and (22), a relationship between the cathode and anode signal-to-noise ratios can be obtained

$$\left(\frac{S}{N}\right)_a = \left(\frac{\sigma-1}{\sigma}\right)\left(\frac{S}{N}\right)_1 = \frac{\epsilon\,(\sigma-1)}{\sigma}\left(\frac{S}{N}\right)_k \tag{23}$$

From Equation (21),

$$\frac{I_a^2}{i_a^2} = \frac{(\sigma-1)}{\sigma} \frac{I_1^2}{i_1^2}$$

so the mean square output noise current is

$$i_a^2 = \frac{\sigma}{(\sigma-1)} \left(\frac{I_a}{I_1}\right)^2 i_1^2$$

If $G = I_a/I_1$ = current gain of the dynode structure, then

$$i_a^2 = \frac{\sigma}{(\sigma-1)} G^2 i_1^2 = \frac{\sigma}{(\sigma-1)} G \cdot 2 e \Delta f I_a \tag{24}$$

Therefore, the RMS noise current at the anode is $\sqrt{\sigma G/(\sigma-1)}$ higher than for a normal DC current I_a.

5. Calculation of Equivalent Noise Input

A signal-to-dark noise ratio may be defined as the ratio of the mean square value of the fundamental component of a chopped, square wave signal current to the mean square value of noise current for a 1 cps bandwidth (IRE Standards on Electron Tubes, 1962). The mean square photocathode dark current noise for Δf = 1 cps is given by

$$i_k^2 = 2 e I_k = 2 e A_k j_k$$

where A_k is the cathode area

j_k is the dark current density.

The mean square value of the fundamental of a square wave signal current is

$$I_k^2 = \left(\frac{\sqrt{2}}{\pi} \, S \cdot F \right)^2$$

where S is the cathode sensitivity

F is the DC value of the input flux prior to chopping

$\sqrt{2/\pi}$ is the RMS value of the fundamental component of a square wave.

The cathode signal-to-dark noise ratio can be determined as

$$\left(\frac{S}{N} \right)_k = \frac{\left(\frac{\sqrt{2}}{\pi} \, S \cdot F \right)^2}{2 \, e \, A_k j_k}$$

From Equation (23) the output signal-to-dark noise ratio becomes

$$\left(\frac{S}{N} \right)_a = \frac{\epsilon (\sigma - 1)}{\sigma} \, \frac{\left(\frac{\sqrt{2}}{\pi} \, S \cdot F \right)^2}{2 \, e \, A_k j_k} \tag{25}$$

The equivalent noise input, ENI, is defined as the value of input flux necessary to give a unity signal-to-noise ratio. From Equation (25)

$$ENI = F \Big|_{\frac{S}{N} = 1} = \frac{\pi}{S} \sqrt{\frac{e \, A_k j_k}{\epsilon} \, \frac{\sigma}{(\sigma - 1)}} \tag{26}$$

From Equation (26), it is clear that for minimum equivalent noise input the cathode sensitivity, S, and collection efficiency, ϵ, should be as large as possible while the cathode area, A_k, dark emission, j_k, and dynode multiplication, σ, should be as small as possible.

In the laboratory, the ENI can be determined by measuring the anode dark current noise in a 1000 cps bandwidth and the anode sensitivity. From Equation (24)

$$i_a^2 = 2e\frac{\sigma}{(\sigma-1)}\,G\cdot{}^\Delta f\cdot I_a = 2e\frac{\sigma}{(\sigma-1)}\cdot{}^\Delta f\cdot G^2\epsilon I_k = 2e\frac{\sigma}{(\sigma-1)}\cdot{}^\Delta f\cdot G^2\epsilon A_k j_k \tag{27}$$

Let A = the anode sensitivity = $I_a/F = \left(G\epsilon\, I_k/F\right) = S_\epsilon G$ (amperes /(lumen).

$$\tag{28}$$

Substituting Equations (27) and (28) into Equation (26) yields

$$ENI = \frac{\pi}{S}\sqrt{\frac{1}{\epsilon}\,\frac{i_a^2}{2\cdot{}^\Delta f\cdot\epsilon\,G^2}} \;=\; \frac{i_a}{S_\epsilon G}\sqrt{\frac{\pi^2}{2\cdot{}^\Delta f}} \;=\; \frac{i_a}{A}\sqrt{\frac{\pi^2}{2\cdot{}^\Delta f}}$$

For Δf = 1000 cps,

$$ENI = \frac{i_a}{14.2\cdot A}$$

VI. SIGNAL PROCESSING

The basic components of the scanning optical system are lens, slotted reticle, and photomultiplier. A star field is focussed on the reticle, which is fixed relative to the lens and photomultiplier. The entire system rotates; consequently, the image of the star field moves across the slit. See Figure 1. (The following results apply equally to systems in which the reticle moves relative to a stationary lens and photomultiplier.) As the star field image moves across the reticle, the amount of radiation reaching the photomultiplier fluctuates with a corresponding fluctuation in its output. The output from a bright star represents a signal; the output from the background radiation represents noise.

There are several sources of randomness in the photomultiplier output. The signal has a random component since photoelectric emission and electron multiplication are stochastic in nature. Also, the photomultiplier produces a dark current, which appears as shot noise in the output. The noise produced by the background radiation has basically three "noise" components.[*] First, it has a high frequency component from the stochastic nature of photoelectric emission and from the dark current. Second, it has a low frequency component from the "random" spatial distribution of the background stars. Third, the background noise has a very low frequency component from the general variation in background radiation over the scanning region.

---

[*] Noise from the background radiation is also discussed in Section III.

PHOTO-
MULTIPLIER

FIGURE I: SCANNING SYSTEM

VI-2
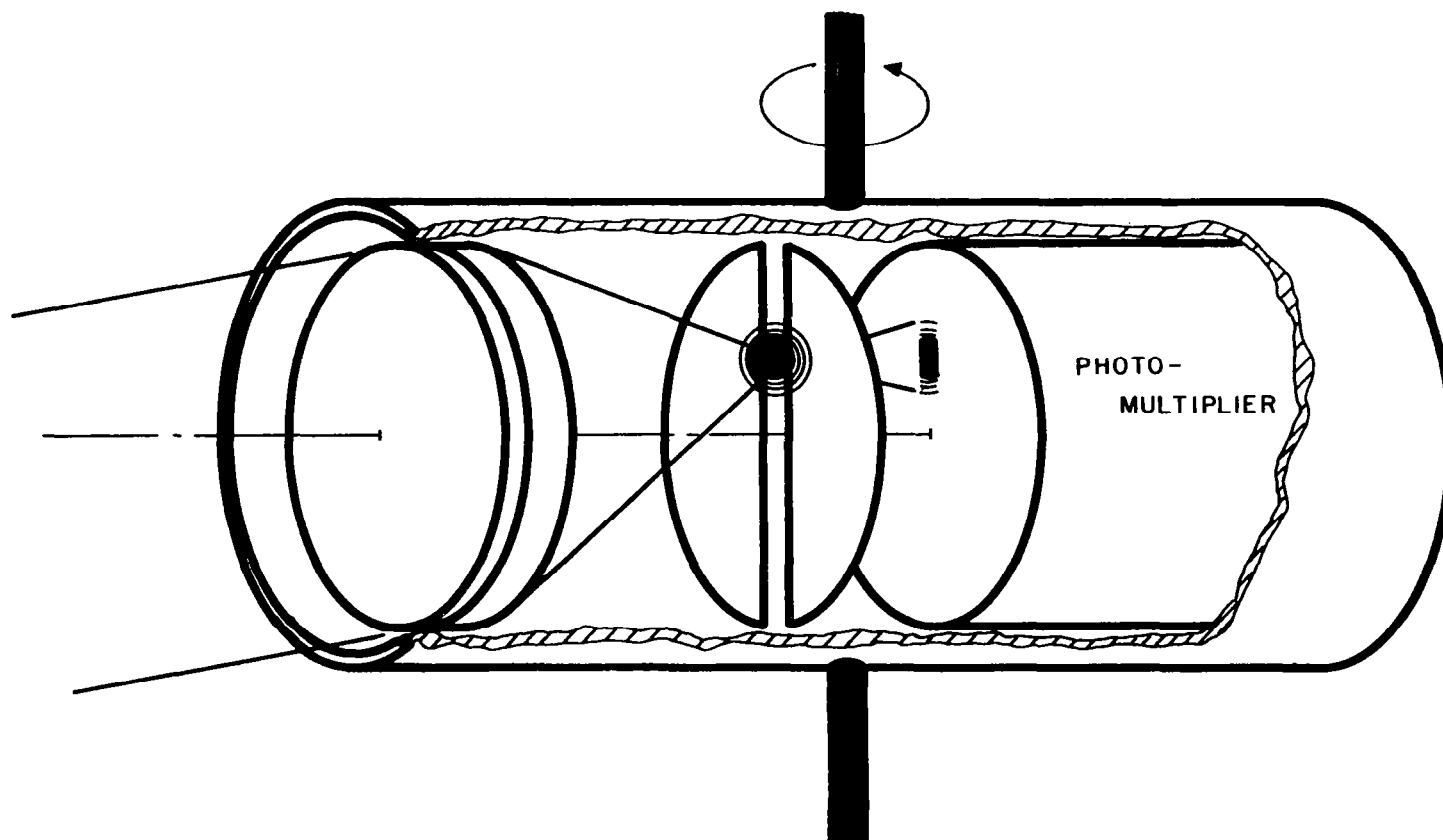
The photomultiplier output must be "processed" to discriminate against the noise and detect the bright star signals, and to determine the time at which the star is centered in the slit. In this section, we will describe several processing techniques in detail. Signal detection and parameter estimation have been studied intensively for radar and communication systems. Several of the basic ideas can be used for scanning optical systems. On the other hand, most of the specific results must be developed independently. Processing techniques for scanning optical sensors have been studied previously by Farrell and Zimmerman (1965), Harrington (1963), Kenimer and Walsh (1964), Lillestrand and Carroll (1961). In the following paragraphs we extend these earlier investigations by using more sophisticated noise and signal models (subsection A). In addition, we discuss several new processing techniques for detection (subsection B) and estimation of the star transit time (subsection C). Possible implementations are also discussed.

A. Signal and Noise Models

Let $I_s(\lambda) \, \Delta\lambda$ be the amount of radiation from the transiting star in wavelength interval $(\lambda, \lambda + \Delta\lambda)$, entering a unit area of the optical aperture. Assume $I_s(\lambda)$ is expressed in photons per second. The optical system produces an aberrated image. Assume it is Gaussian in shape; i.e. the radiation per unit area on the reticle is given by

$$\frac{AT(\lambda) I_s(\lambda) \Delta\lambda}{2\pi\sigma^2} \exp\left[-\frac{1}{2} \frac{x^2 + y^2}{\sigma^2}\right]$$

in the wavelength interval $(\lambda, \lambda + \Delta\lambda)$, where A is the aperture area, where $T(\lambda)$ is the transmittance of the optical system, and where σ defines the optical resolution. Let t_s denote the time when the star is centered in the slit, and T_s the time required for the star to cross the slit. Then the star radiation passing the slit at time t is

$$I_s(t, \lambda) \Delta\lambda = AT(\lambda) I_s(\lambda) G(t - t_s) \Delta\lambda$$

in wavelength interval $(\lambda, \lambda + \Delta\lambda)$, where

$$G(t) = \Phi\left(\frac{t}{\sigma} + \frac{T_s}{2\sigma}\right) - \Phi\left(\frac{t}{\sigma} - \frac{T_s}{2\sigma}\right)$$

$$\Phi(t) = \frac{1}{\sqrt{2\pi}} \int_{-\infty}^{t} e^{-x^2/2} \, dx \, .$$

With the star centered in the slit, eighty percent of the radiation passes the slit when $T_s/2\sigma = 1.28$. This slit width is defined as the image diameter D.

Radiation from weak stars forms the stellar background. The weak star images are assumed to be randomly distributed across the reticle with a two-dimensional Poisson distribution. Hence, the times at which weak stars enter the slit form a stationary Poisson process. Let ν denote the rate of weak star transits, and t_1, t_2, t_3, ... denote the times when weak stars are centered in the slit. Let $I_j(\lambda)\, \Delta\lambda$ be the amount of radiation from the jth weak star in wavelength interval $(\lambda, \lambda + \Delta\lambda)$, entering a unit area of the optical aperture. Assume $I_j(\lambda)$ is expressed in photons per second. The variation of $I_j(\lambda)$ between successive stars, and the rate ν, depend on the region of the sky one is scanning. The total background radiation passing the slit at time t is

$$I_b(t,\lambda)\, \Delta\lambda = A\, T(\lambda) \sum_j I_j(\lambda)\, G(t-t_j)\, \Delta\lambda$$

in the wavelength interval $(\lambda, \lambda + \Delta\lambda)$.

In addition to stellar background, there may be an ambient background radiation from zodiacal radiation or airglow, when observations are made from Earth. Let $I_0(\lambda)$ denote this ambient radiation. Assume $I_0(\lambda)$ is expressed in photons per second entering a unit area of the aperture and a unit solid angle. Let Ψ denote the solid angle formed by the slit. Then the total radiation passing the slit at time t is

$$I_s(t,\lambda)\, \Delta\lambda + I_b(t,\lambda)\, \Delta\lambda + A\, \Psi\, T(\lambda)\, I_0(\lambda)\, \Delta\lambda$$

The radiation incident on the photocathode produces electron emissions. These emissions form a non-stationary Poisson process with an instantaneous emission rate of

$$\mu(t) = \int_0^\infty Q(\lambda)\left[I_s(t,\lambda) + I_b(t,\lambda) + A\Psi T(\lambda)I_o(\lambda)\right]d\lambda$$

where $Q(\lambda)$ is the quantum efficiency at wavelength λ.[*] Substituting for I_s, I_b, and I_o, the rate becomes

$$\mu(t) = AI_s^* G(t-t_s) + A\sum_j I_j^* G(t-t_j) + A\Psi I_o^*$$

where I_s^*, I_j^*, and I_o^* are the effective intensities

$$I_s^* = \int_0^\infty Q(\lambda)T(\lambda)I(\lambda)\,d\lambda$$

$$I_j^* = \int_0^\infty Q(\lambda)T(\lambda)I_j(\lambda)\,d\lambda$$

$$I_o^* = \int_0^\infty Q(\lambda)T(\lambda)I_o(\lambda)\,d\lambda.$$

---

[*] For the intensity and spectral characteristics of stellar radiation, these assumptions are physically reasonable. The characteristics of photoelectric emissions are discussed by L. Mandel (1958, 1959), and in Section II of this report.

Let τ_1, τ_2, ..., τ_k denote the times at which photoelectron emissions occur. Corresponding to the kth emission, one obtains a pulse at the output of the photomultiplier. Let $a_k\, p_k(t - \tau_k)$ denote the instantaneous current at time t resulting from the kth emission. Assume

$$\int_{-\infty}^{\infty} p_k(t)\, dt = 1$$

so that a_k is the total charge resulting from the kth primary electron emission. The charge a_k varies between successive pulses since the electron multiplication is random. Let $f_a(-)$ be the statistical density function of the pulse amplitude distribution. The shape of the pulse $p_k(t)$ varies between successive pulses since the relative arrival times of the secondary electrons in each cascade fluctuate.

The photomultiplier dark current introduces additional noise. The dark current is the sum of several currents: thermionic emission from the photo-cathode, thermionic emission from the dynodes, and ohmic leakage. It can be represented as shot noise. In particular, pulses are produced at random times with random amplitudes. The mean pulse rate is assumed to be constant, say I_d. Let $d_k\, \hat{p}_k(t - \hat{\tau}_k)$ denote the instantaneous current at time t resulting from the kth pulse. Assume

$$\int_{-\infty}^{\infty} \hat{p}_k(t)\, dt = 1$$

so that a_k is the charge in the kth pulse. Note that the pulse shape varies.

Let $f_d(-)$ be the statistical density function of the pulse amplitude distribution. The statistical characteristics of the output from the photomultiplier are discussed in detail by Engstrom (1947) and Tusting (1962); also see Section V of this report.

The composite output from the photomultiplier is filtered to improve the signal-to-noise relationship. Assume the filter has an impulse response $w(t)$. In cases of interest $w(t)$ has a much longer duration than $p_k(t)$ and $\hat{p}_k(t)$. Hence, the filter output is simply,

$$X(t) = \sum_k a_k w(t - \tau_k) + \sum_k d_k w(t - \hat{\tau}_k)$$

where the τ_k's form a non-stationary Poisson process with an instantaneous rate $\mu(t)$, and where the $\hat{\tau}_k$'s form a stationary Poisson process with rate I_d. In certain situations, $X(t)$ can be approximated by a non-stationary Gaussian process. This approximation is helpful in solving certain more complicated problems. Parzen (1962) page 157, and Rice (1944) page 305 develop this result in some detail.

With these models for the signal and noise, we can investigate various detection techniques. This is the subject of the following paragraphs.

B.   Star Detection Techniques

The function of a detection technique is to discriminate between desired
signals and undesired signals. The optimum detection technique depends on
the characteristics of the signals. In scanning optical systems, we encounter
three operating situations.

In the first situation, the detection technique must discriminate against
"false" star detections, i.e. detections resulting from dark current, zodiacal
light, "very weak" stars   (stars with intensities several stellar magnitudes
below that of the weakest star of interest), and radiation from the atmosphere,
when observations are made from Earth. The sporatic detections of "weak" stars
(i.e. stars with stellar magnitudes near that of the weakest star of interest)
are acceptable in this operating situation. The optimum technique maximizes
the probability of detecting the weakest star of interest with a fixed proba-
bility of detecting a false star. In this case, the output of the photo-
multiplier forms a stationary random process in the absence of a star signal.

In the second operating situation, the detection technique must discrimi-
nate against weak stars. False star detections can be neglected. The stars
of interest are relatively bright. Hence, weak star detections are widely
spaced in time and are statistically independent. The optimum technique
maximizes the probability of detecting the weakest star of interest with a
fixed probability of detecting the brightest weak star that we must discrimi-
nate against.

In the third operating situation the detection technique must discriminate
against weak stars; but in this case, the detections are not independent.

The stars of interest are relatively weak. The primary cause of variability in the photomultiplier output (in the absence of bright stars) is the variability in the spatial distribution of weak stars. In this situation the goal is to select a detection filter that maximizes the ratio of the output signal level to output rms noise level. One can formally derive a detection technique that is optimum for the criterion used in the first situation. The technique is complex; it is impractical for real applications.

In the following paragraphs these three operating situations will be considered in detail. The optimum techniques will be developed. In applying these results, one must estimate the relative significance of various interferring signals, and select the appropriate detection technique.

1. Discrimination Against False Star Detections

To simplify the discussion we will assume that the star transit time t_s is known. Later this assumption will be relaxed. The output of the photomultiplier is observed for a period $-T + t_s$ to $T + t_s$, with 2T much larger than the time required for the star to cross the slit. Assume that at most, one bright star crosses the slit in this period, at t_s. Let $v_1 < v_2 < \ldots$ represent the times at which pulses are observed at the output of the photomultiplier; let b_1, b_2, $\ldots$ represent their amplitudes. The decision as to whether or not a star is present is based on the number of pulses observed N, the times $(v_1, v_2, \ldots, v_N)$ and the amplitudes $(b_1, b_2, \ldots, b_N)$. There is no practical way of using the pulse shapes to discriminate between the star signal and noise.

Detection is basically a statistical problem of testing the hypothesis that "no star is present, i.e. $I_s^* = 0$," as opposed to "a star is present with intensity $I_s^* = I_{so}^*$." There are two types of errors: Type I--the star is "detected" when it is not present, Type II--the star is not detected when it is present, see Figure 2. In practice, false star detections can be eliminated by comparison to star charts. On the other hand, if a star is missed, the system accuracy is reduced; and it may be impossible to obtain the required attitude estimates. Hence, the goal is to select a detection technique that minimizes the probability of a Type II for a fixed probability of a Type I error.

The optimum detection technique is based on the joint likelihood function of N, v_1, v_2, ..., v_N, b_1, b_2, ..., b_N given I_s^* and t_s. Let $\mathcal{L}(N, v_1, ..., v_N, b_1, ..., b_N \mid I_s^*, t_s)$ denote this function. Let $\mathcal{J}$ denote the ratio

$$\mathcal{J} = \frac{\mathcal{L}(N, v_1, \cdots, v_N, b_1, \cdots, b_N \mid I_{so}^*, t_s)}{\mathcal{L}(N, v_1, \cdots, v_N, b_1, \cdots, b_N \mid 0, t_s)}$$

The optimum detection technique is the following. If $\mathcal{J}$ is larger than a specified constant C_p, a star is present. If $\mathcal{J}$ is less than C_p, a star is not present. The constant C_p is selected so that the probability of a Type I error is P. The probability of a Type II error is minimized with this technique. The proof of optimality is given in subsection G of this section. In the following paragraphs, explicit equations are derived for the likelihood function $\mathcal{L}$ and the test statistic $\mathcal{J}$.

STATE OF NATURE

	NO STAR PRESENT	STAR PRESENT
NO STAR PRESENT		TYPE II ERROR
STAR PRESENT	TYPE I ERROR	

DECISION

FIGURE 2 : DETECTION ERRORS

One can show that the joint density function of the v_j's and b_j's conditional on observing N pulses at the output of the photomultiplier is[*]

$$\frac{N!}{\overline{N}^N} \prod_{j=1}^{N} \left[\mu(v_j) f_a(b_j) + I_d f_d(b_j) \right] \quad,$$

where $\overline{N}$ is the average number of pulses observed

$$\overline{N} = \int_{-T}^{T} \mu(t) \, dt \; + \; 2TI_d \quad.$$

Therefore, the joint likelihood function is

$$\mathcal{L} = \prod_{j=1}^{N} \left[\mu(v_j) f_a(b_j) + I_d f_d(b_j) \right] e^{-\overline{N}} \quad.$$

Since we are concerned with false star detections the effective background radiation is assumed to be constant; the quantity

$$A \sum_{j} I_j^* G(t - t_j)$$

in $\mu(t)$ can be replaced by its average value

$$A \overline{I_b^*} \, \nu T_s \quad.$$

---

[*]   The derivation follows closely one given by Parzen (1962), p. 139ff.

Since 2T is assumed to be much larger than T_s,[*]

$$\int_{-T}^{T} G(t - t_j)\, dt \approx \int_{-\infty}^{\infty} G(t - t_j)\, dt = T_s \;.$$

The test statistic $\mathcal{J}$ becomes

$$\mathcal{J} = \prod_{j=1}^{N} \left\{ \frac{[AI_{so}^* G(v_j - t_s) + A\overline{I_b^*}\nu T_s + A\Psi I_o^*]\, f_\alpha(b_j) + I_d f_d(b_j)}{[A\overline{I_b^*}\nu T_s + A\Psi I_o^*]\, f_\alpha(b_j) + I_d f_d(b_j)} \right\} e^{-AI_{so}^* T_s}$$

Note that $\mathcal{J}$ is independent of the duration of observation 2T. The detection technique based on $\mathcal{J}$ is equivalent to a technique based on the logarithm of $\mathcal{J}$. On the other hand, it is easier to implement a technique based on the logarithm. Let

$$\mathcal{J}' = \ln \mathcal{J} + AI_{so}^* T_s = \sum_{j=1}^{N} \ln \left\{ \rho(b_j) G(v_j - t_s) + 1 \right\}$$

where

$$\rho(b_j) = \frac{AI_{so}^* f_\alpha(b_j)}{[A\overline{I_b^*}\nu T_s + A\Psi I_o^*]\, f_\alpha(b_j) + I_d f_d(b_j)}$$

The constant $AI_{so}^* T_s$ does not change the technique since $\mathcal{J}'$ is compared to a constant, say C'_p.

---

[*]   A derivation is given by Farrell and Zimmerman (1965).

The general term in $\mathcal{J}'$

$$\ln\left[\rho(b)\,G(v)+1\right]$$

describes how pulses occurring at different times with various amplitudes influence the detection decision. First, consider the factor $\rho(b)$. The quantities AI_{so}^{*}, $AI_{b}^{*}\; v\; T_{s}+A\Psi I_{o}^{*}$, and I_{d} represent the effective intensities of the star radiation, interferring radiation, and dark current. Graphs of $AI_{so}^{*}\; f_{a}(b)$, $[\overline{AI_{b}^{*}}\; v\; T_{s}+A\Psi I_{o}^{*}]\; f_{a}(b)$, and $I_{d}\; f_{d}(b)$ appear in Figure 3; the corresponding graph of $\rho(b)$ is in Figure 4. The magnitude and shape of $\rho(b)$ changes significantly from one photomultiplier to another. There is a threshold value of b, say b_{t}, such that $\rho(b)$ is "small" for values of $b < b_{t}$. The effect of this threshold is to discriminate against pulses from secondary dynodes and ohmic leakage. The function $G(v)$ is a simple bell-shaped function. Note that

$$\ln\left[\rho(b)\,G(v)+1\right]\approx\rho(b)\,G(v)$$

when

$$\rho(b)\,G(v)\;<\;.2$$

and that

$$\ln\left[\rho(b)\,G(v)+1\right]\approx\ln\rho(b)+\ln G(v)$$
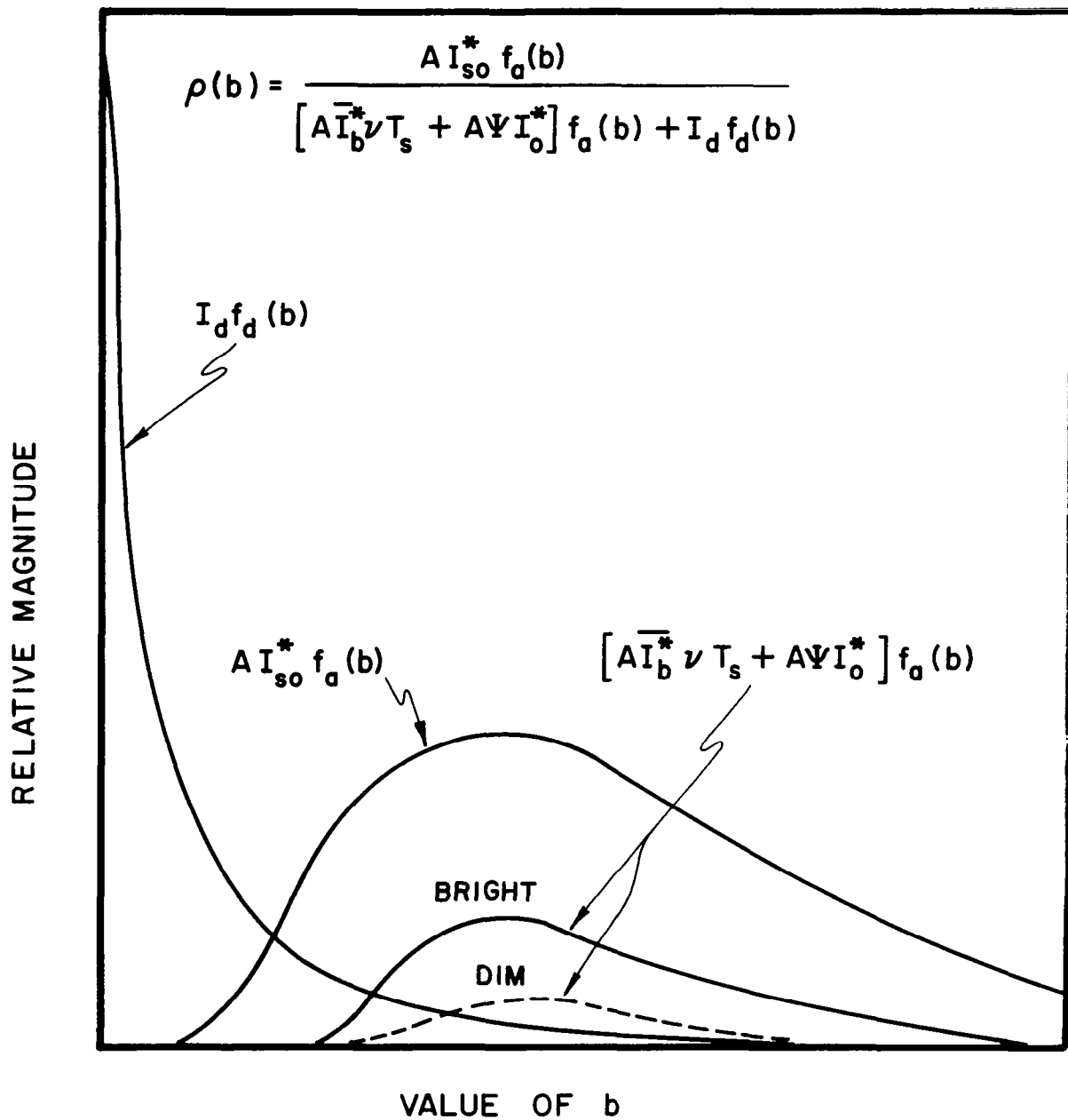
FIGURE 3: RELATIVE MAGNITUDE OF TERMS IN $\rho(b)$
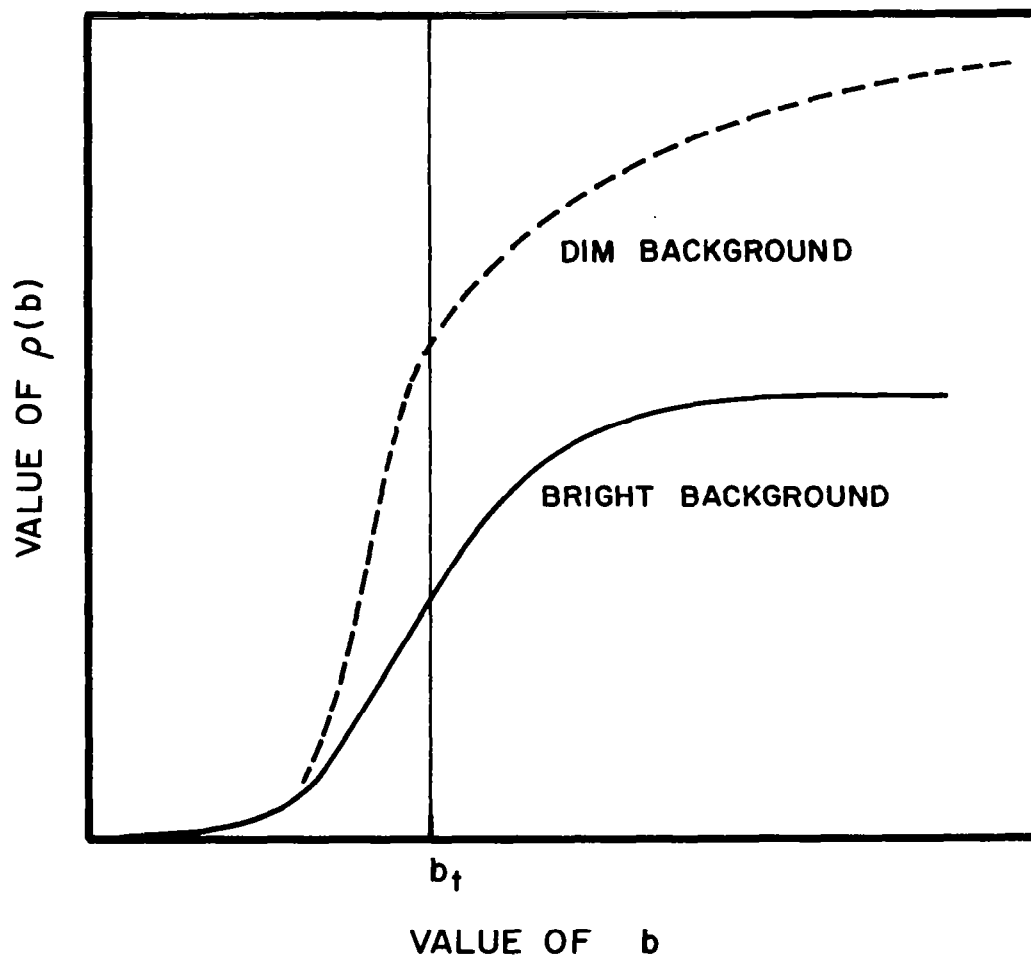
FIGURE 4 : FUNCTIONAL FORM OF ρ (b)

when

$$P(b) \, G(v) > 10.$$

The term

$$\ln \left[\rho(b) \, G(v) + 1 \right]$$

is graphed in Figure 5. From these remarks, we find that $\mathcal{J}'$, and consequently the detection, is only influenced by large pulses near t_s.

In most situations the star transit time t_s is unknown. Then the detection technique becomes the following. If the value of

$$\mathcal{J}'(t) = \sum_{j=1}^{N} \ln \left\{ \rho(b_j) \, G(v_j - t) + 1 \right\}$$

exceeds C_p' continuously between times t_1 and t_2, a star is present. The time $\hat{t}_s$ between t_1 and t_2 at which $\mathcal{J}'(t)$ achieves its maximum value is the most likely value of t_s; i.e. it is the maximum likelihood estimate of t_s.[*] This detection technique is a likelihood ratio test with parameter t.[**]

The quantity $\mathcal{J}'(t)$ as a function of time can be interpreted as the output of a non-linear invariant filter. The response to an impulse at

---

[*]   See Willis (1962), p. 360.

[**] See Wilks (1962), p. 402ff.

RELATIVE MAGNITUDE
OF $\ln\left[\rho(b)\,G(v)+1\right]$

b

t_s

v

b_t
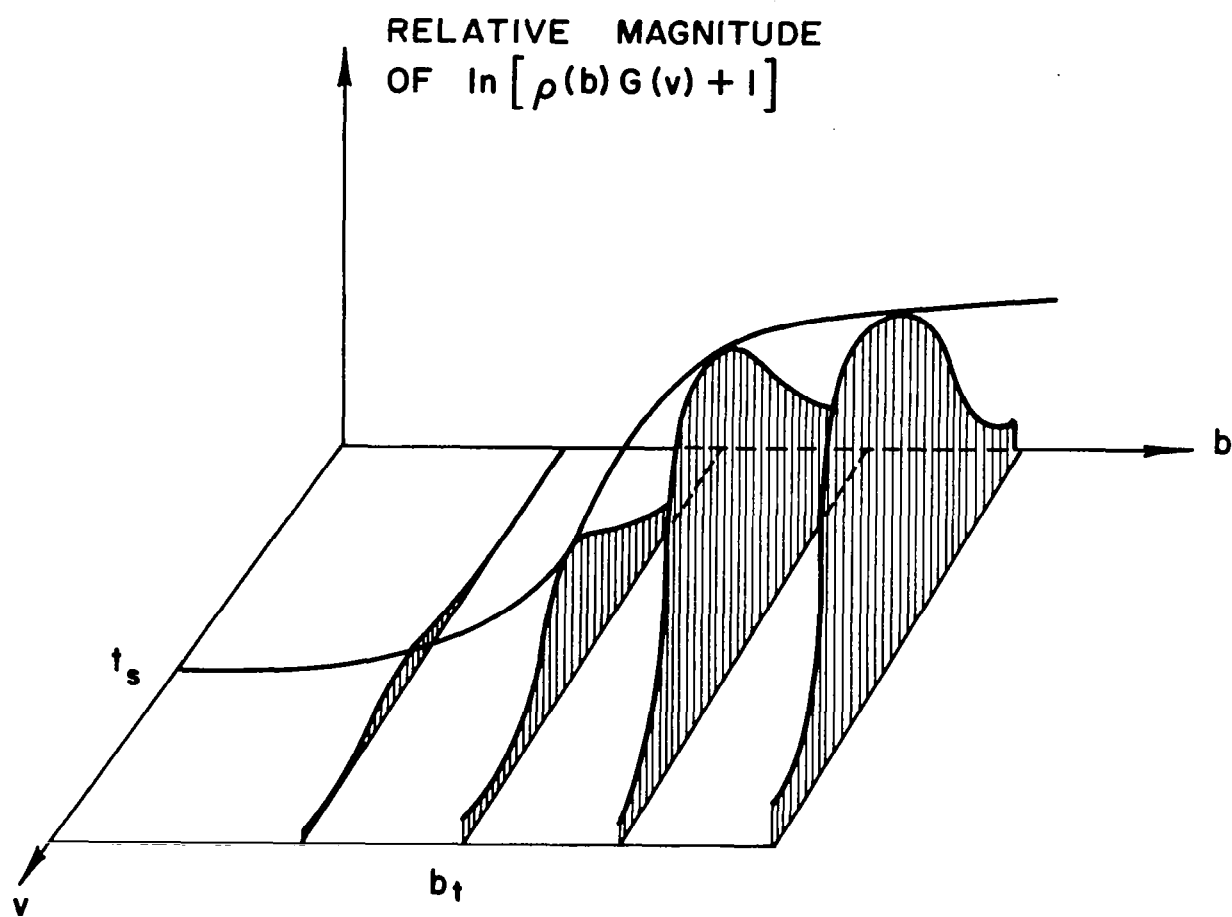
FIGURE 5: GRAPH OF $\ln\left[\rho(b)\,G(v)+1\right]$

time v with amplitude b is

$$\ln \left[\rho(b) \, G(t-v) + 1 \right] .$$

This response is graphed in Figure 6. It is not practical to implement the filter in the above form. A reasonable approximation is illustrated in Figure 7. The amplitudes of the input pulse train $(b_1, b_2, \ldots)$ are modified by a non-linear amplifier. Strong pulses are amplified; weak pulses are attenuated. The jth input pulse becomes a pulse with amplitude

$$\frac{\ln \left[\rho(b_j) \, G(t') + 1 \right]}{\ln \left[\rho(b') \, G(t') + 1 \right]} .$$

The parameters b' and t' are defined below. The modified pulse is then filtered to produce an output

$$\frac{\ln \left[\rho(b_j) \, G(t') + 1 \right]}{\ln \left[\rho(b') \, G(t') + 1 \right]} \ \ln \left[\rho(b') \, G(t-v_j) + 1 \right] .$$

This approximation is also graphed in Figure 6. Note that the approximation equals the optimum response when $t - v_j = t'$ (for all b_j) and when $b_j = b'$ (for all t). The parameter t' and b' are selected to minimize the "separation" between the correct function and the approximation. In some situations, it may be adequate to delete low level pulses, below b_t, and normalize pulses above b_t to unity. This type of normalization was used by Farrell and Zimmerman (1965). Possible implementations are discussed in Subsection VI.E.
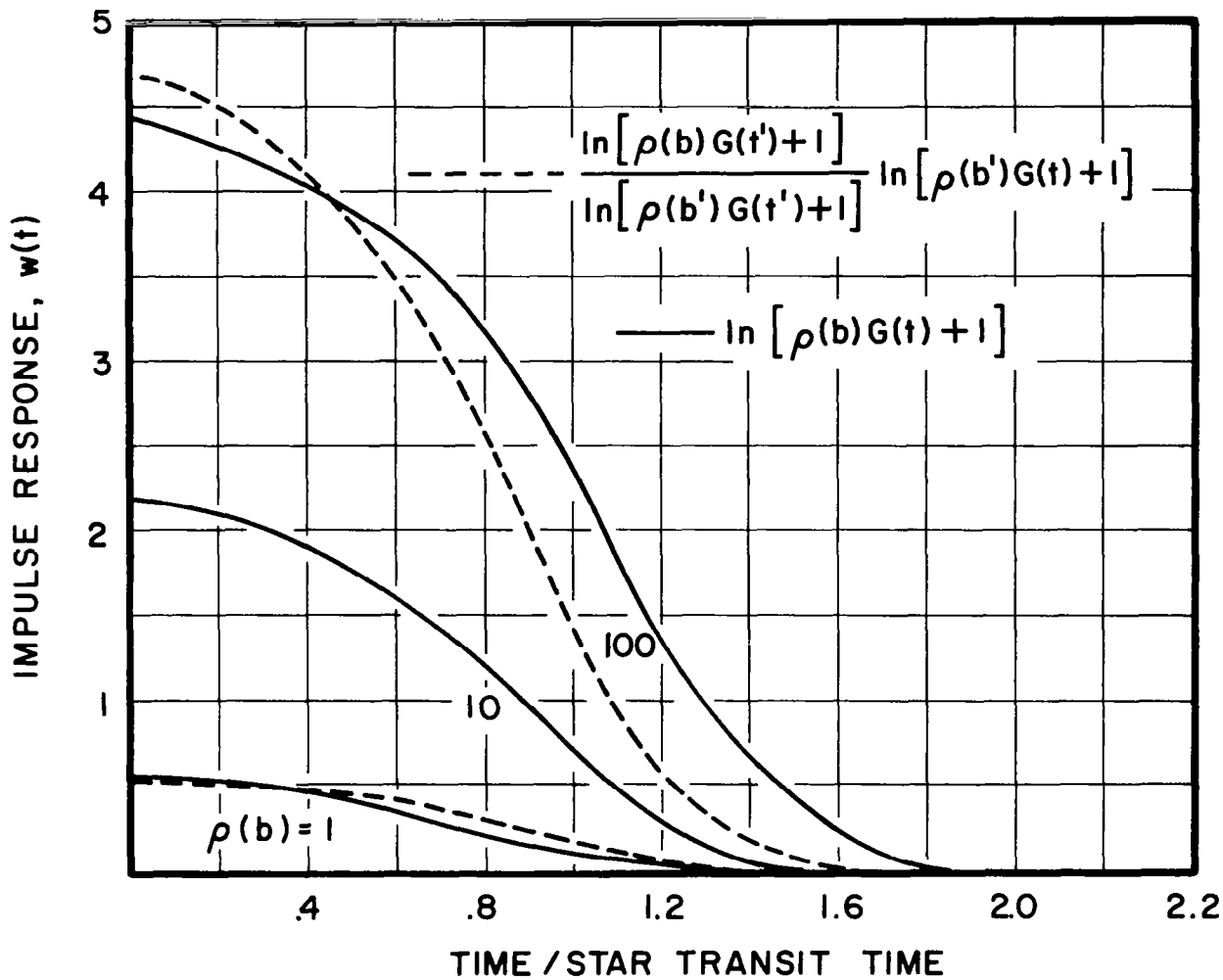
FIGURE 6: IMPULSE RESPONSE AND APPROXIMATION

IMPULSE RESPONSE

$$w(t) = \ln\left[\rho(b')G(t) + 1\right]$$

```
┌──────────────┐   ┌──────────────┐   ┌──────────┐   ┌──────────────┐
│   PHOTO -    │   │ NON LINEAR   │   │ LINEAR   │   │  THRESHOLD   │
│ MULTIPLIER   │──▶│  WIDE BAND   │──▶│ FILTER   │──▶│  DETECTION   │
│              │   │  AMPLIFIER   │   │          │   │              │
└──────────────┘   └──────────────┘   └──────────┘   └──────────────┘
```

$X(t)$

OUTPUT

$$\frac{\ln\left[\rho(b)G(t') + 1\right]}{\ln\left[\rho(b')G(t') + 1\right]}$$

1

b'   INPUT
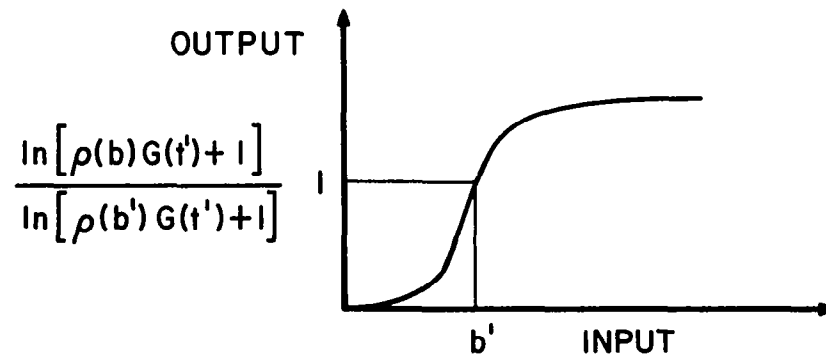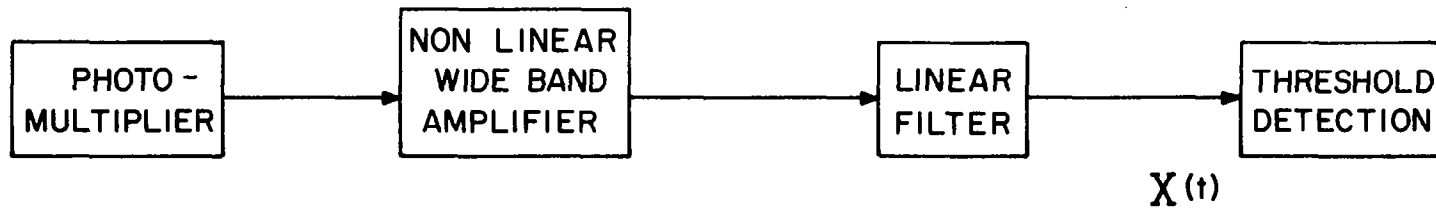
FIGURE 7 : FILTERING TECHNIQUE

The impulse response

$$w(t) = \ln\left[\rho(b')G(t) + 1\right]$$

is graphed in Figure 8 for several values of slit width with a fixed image diameter. In Figure 9, w(t) is graphed for several values of image diameter with a fixed slit width. In Figure 10, w(t) is graphed for several values of $\rho(b')$ with fixed image diameter and slit width. When the slit width is comparable to the image diameter, w(t) can be approximated by a simple Gaussian impulse response. This approximation will be used extensively in the following discussion. Note that the filter output is insensitive to changes in the input pulse shapes, $p_k(t)$ and $\hat{p}_k(t)$, since the filter response time is much longer than the duration of the input pulses.

The remaining problem is to determine the probability of detection with a detection threshold C'_p. The probability of detection is the probability that the filter output, say $X(t)$, exceeds C'_p. The probability of detection is greater than the probability that $X(t_s) \geq C'_p$. In practice, this lower bound is close to the actual probability of detection. We will use this bound as the probability of detection. Since the distribution of $X(t_s)$ cannot be expressed in closed form, it is convenient to evaluate the probability of detection by assuming $X(t_s)$ has a gamma distribution with the same mean and variance as $X(t_s)$.

The mean and variance of $X(t_s)$ can be expressed in terms of the Fourier transforms of $G(t)$ and $w(t)$, denoted by $\mathcal{G}(f)$ and $\mathcal{W}(f)$. The mean of $X(t_s)$ is
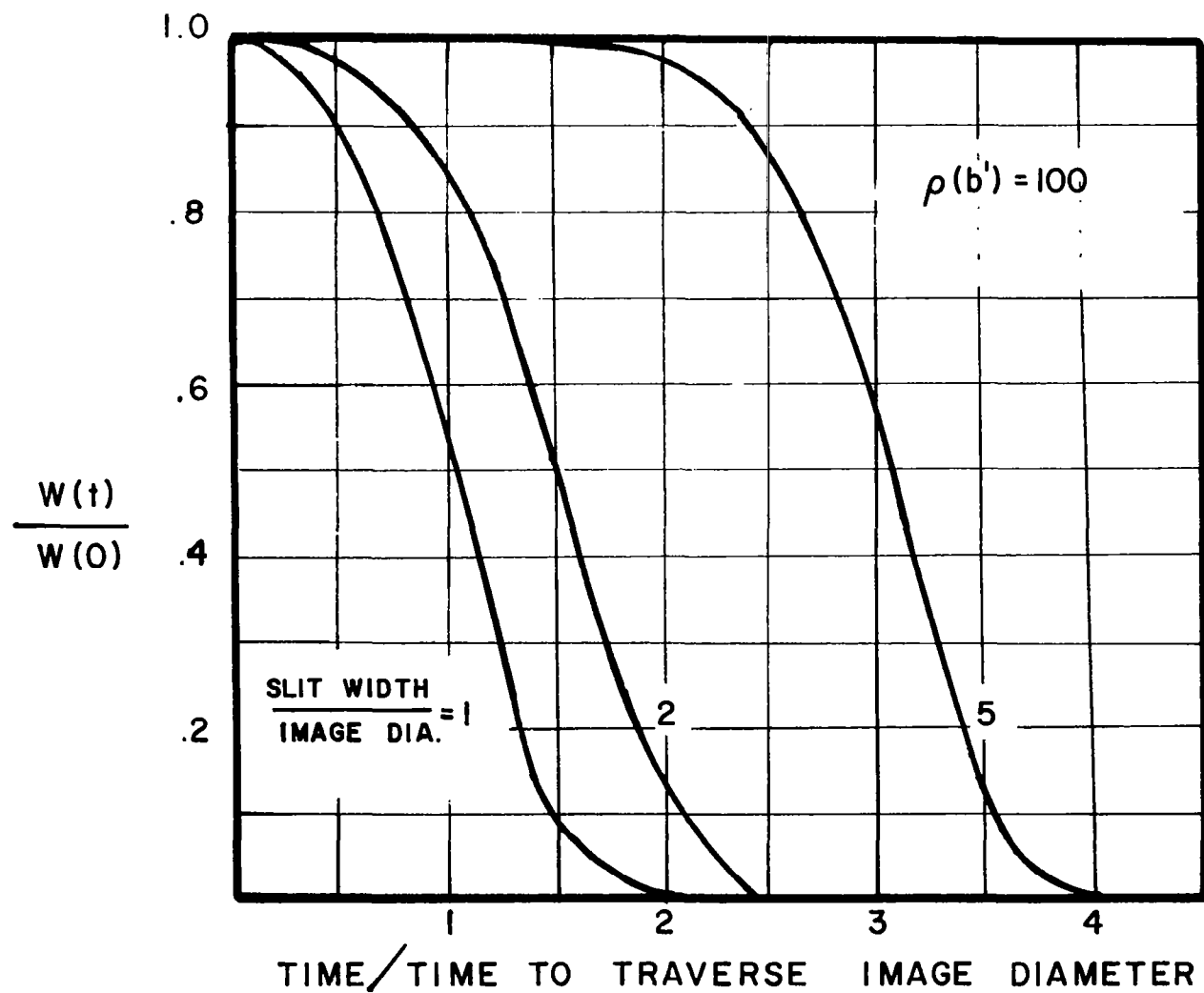
FIGURE 8: NORMALIZED IMPULSE RESPONSE, VARIABLE
SLIT WIDTH AND FIXED IMAGE DIAMETER
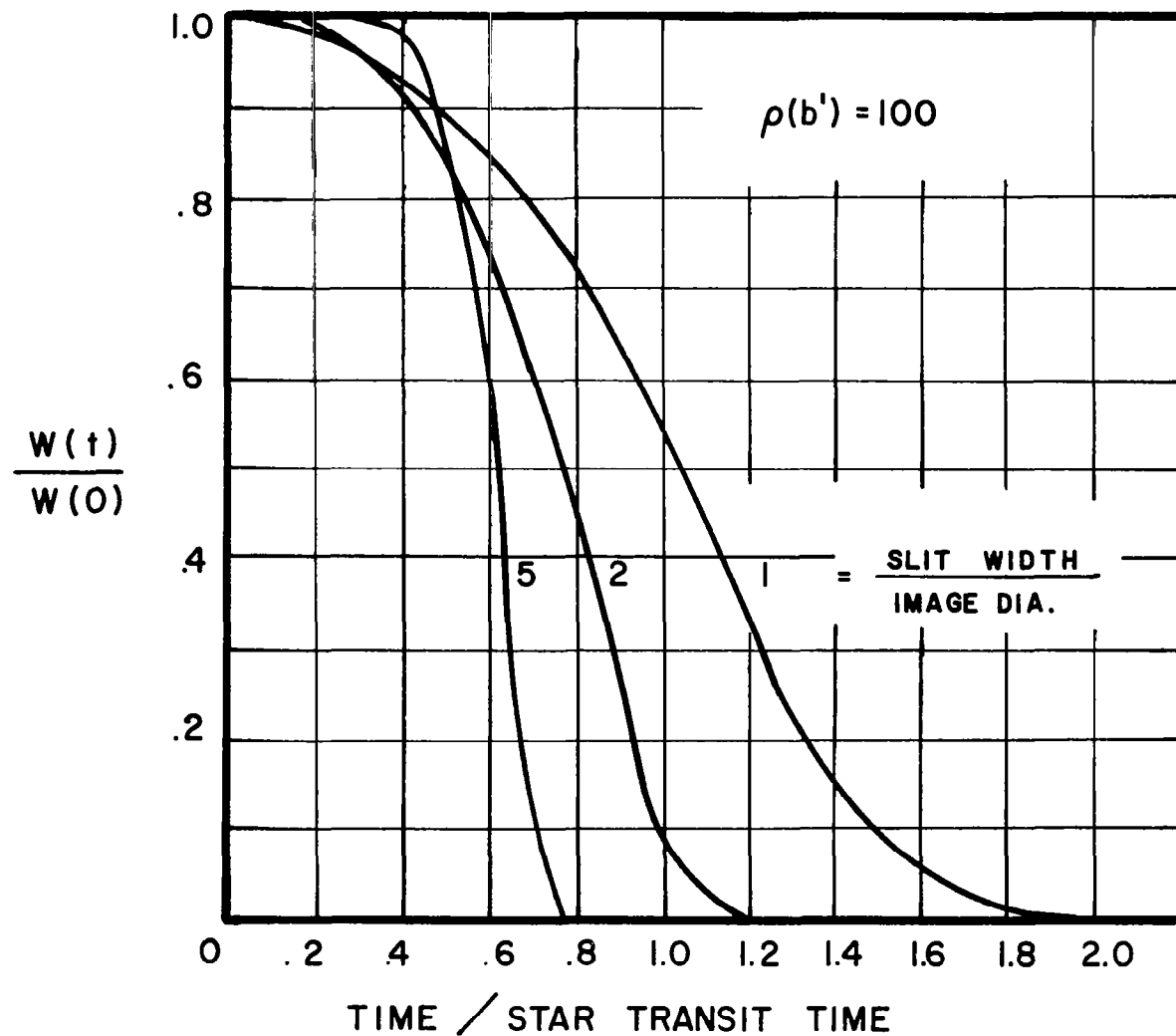
FIGURE 9 : NORMALIZED IMPULSE RESPONSE, VARIABLE IMAGE DIAMETER AND FIXED SLIT WIDTH
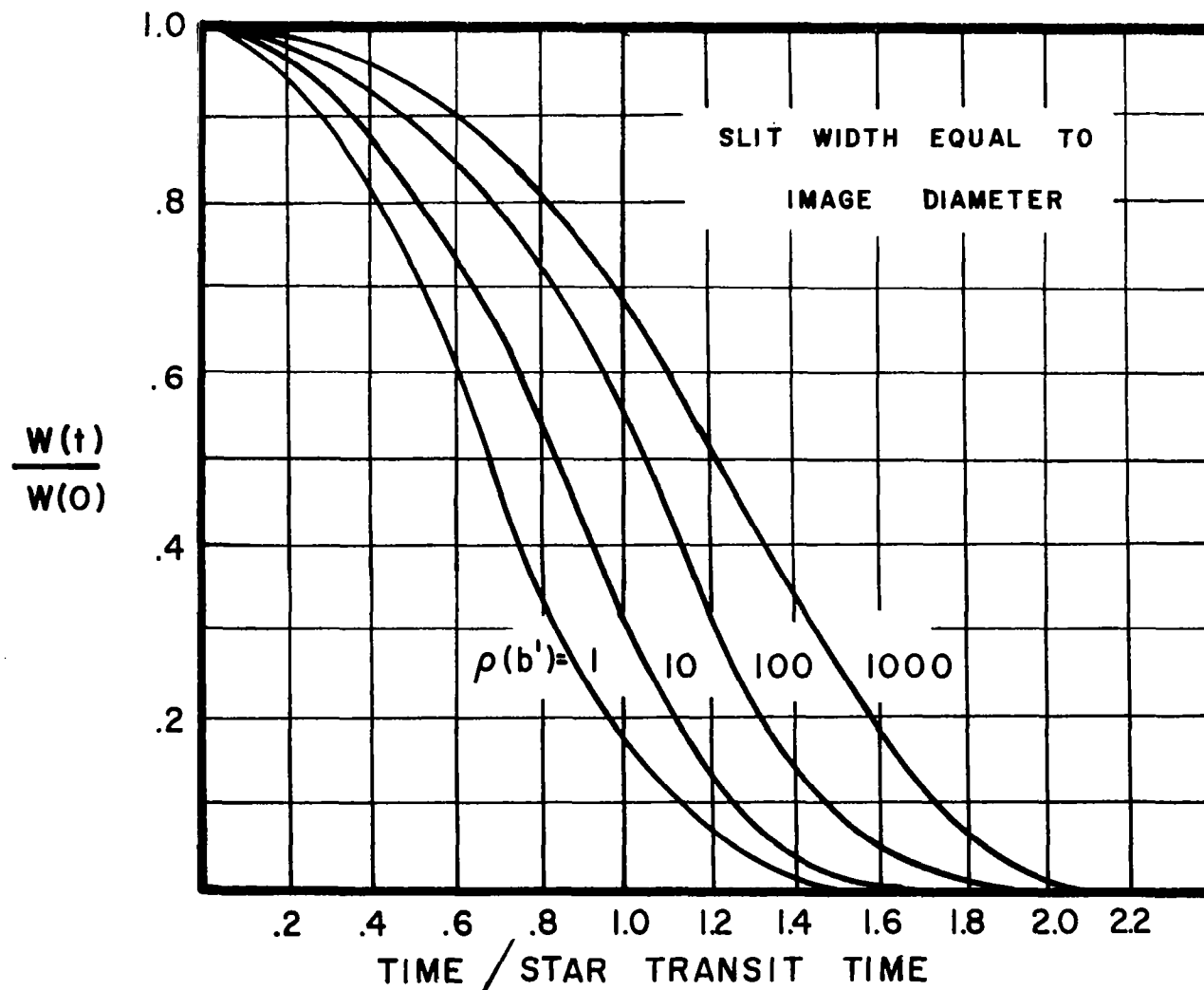
FIGURE 10: NORMALIZED IMPULSE RESPONSE, VARIABLE SIGNAL TO NOISE RATIO

$$E \, X(t_s) = \bar{a} \, A \, I_s^* \int_{-\infty}^{\infty} \mathcal{D}(f) \, \mathcal{W}(f) \, df$$

$$+ \left[\bar{a} \, A \, \overrightarrow{I_b^*} \, \nu T_s + \bar{a} \, A \, \Psi I_o^* + \bar{d} \, I_d \right] \mathcal{W}(0).$$

The variance of $X(t_s)$ is

$$Var \, X(t_s) = \overline{a^2} \, A \, I_s^* \int_{-\infty}^{\infty} G(t) \, [w(t)]^2 \, dt$$

$$+ \left[\overline{a^2} \, A \, \overline{I_b^*} \, \nu T_s + \overline{a^2} \, A \, \Psi I_o^* + \overline{d^2} \, I_d \right] \int_{-\infty}^{\infty} |\mathcal{W}(f)|^2 \, df.$$

Assume $w(t)$ is a Gaussian-shaped impulse response function, i.e.,

$$w(t) = w_o \, e^{-\frac{1}{2}(tf_o)^2}.$$

Then the Fourier transform is

$$\mathcal{W}(f) = \frac{\sqrt{2\pi} \, w_o}{f_o} \, e^{-2\pi^2 f^2 / f_o^2}.$$

The half-power frequency is $.133 f_o$. Also one can show that

$$\mathcal{Y}(f) = \frac{1}{\pi f} \sin(\pi f T_s) \, e^{-2(\pi f \sigma)^2}$$

The mean and variance can now be evaluated in closed form. Namely,

$$E \, X(t_s) = \sqrt{2\pi} \; \bar{a} A I_s^* \frac{w_o}{f_o} \left[1 - 2 \Phi \left(\frac{-T_s f_o}{2\sqrt{1 + \sigma^2 f_o^2}} \right) \right]$$

$$+ \sqrt{2\pi} \left[\bar{a} A \overline{I_b^*} \nu T_s + \bar{a} A \Psi I_o^* + \bar{d} I_d \right] w_o / f_o$$

$$\text{Var} \, X(t_s) = \sqrt{\pi} \; \overline{a^2} A I_s^* \frac{w_o^2}{f_o} \left[1 - 2 \Phi \left(\frac{-T_s f_o}{2\sqrt{1/2 + \sigma^2 f_o^2}} \right) \right]$$

$$+ \sqrt{\pi} \left[\overline{a^2} A \overline{I_b^*} \nu T_s + \overline{a^2} A \Psi I_o^* + \overline{d^2} I_d \right] w_o^2 / f_o$$

Using this mean and variance, we can determine the probability of detecting a star with intensity I_{so}^* and the probability of a false star detection. In the first case E X and Var X are evaluated with $I_s^* = I_{so}^*$, in the second case with $I_s = 0$. The expected number of false star detections is approximately

equal to scan period divided by T_s times the probability of a false star detection.

As mentioned previously, the ambient background radiation passing the slit fluctuates during one scan period, in some cases more than an order of magnitude. Consequently, to maintain the probability of detecting a third magnitude star at .9, for example, we must change the detection threshold C'_p during the scan. An analog method is described in Subsection VI.E.

2. Discrimination Against Independent Weak Star Detections

In this subsection we will consider a second operating situation in which the detection technique must discriminate against independent weak star detections. False star detections can be neglected. The effective intensity of the interferring radiation and dark current is much less than the star intensities. The optimum technique maximizes the probability of detecting the weakest star of interest, with a fixed probability of detecting the brightest weak star that we must discriminate against.

Many of the results on false-star detections can be applied to weak-star detections. The optimum technique is based on the ratio

$$\mathcal{J} = \frac{\mathcal{L}(N, v_1, \cdots, v_N, b_1, \cdots, b_N \mid I_{s0}^*, t_s)}{\mathcal{L}(N, v_1, \cdots, v_N, b_1, \cdots, b_N \mid I_{s1}^*, t_s)} \quad ,$$

where I_{s0}^* is the intensity of the weakest star of interest, and where I_{s1}^* is the intensity of the brightest weak star that we must discriminate against. If $\mathcal{J}$ is larger than a specified constant C_p, a star is present. If $\mathcal{J}$ is

less than C_p, a star is not present. The constant C_p is selected so that the probability of detecting a star with intensity I_{s1}^* is P. The probability of detecting a star with intensity I_s^* is then maximized. The proof of optimality is very similar to that given in subsection G of this section.

The detection technique based on $\mathcal{J}$ is equivalent to a technique based on the logarithm of $\mathcal{J}$. Substituting for the likelihood function, we obtain

$$\mathcal{J}' \equiv \ln \mathcal{J} + A(I_{so}^* - I_{s1}^*)T_s =$$

$$\sum_{j=1}^{N} \ln \left\{ \frac{[AI_{so}^* G(v_j - t_s) + A\overline{I_b^*}\nu T_s + A\Psi I_o^*]f_a(b_j) + I_d f_d(b_j)}{[AI_{s1}^* G(v_j - t_s) + A\overline{I_b^*}\nu T_s + A\Psi I_o^*]f_a(b_j) + I_d f_d(b_j)} \right\}$$

Since ninety-eight percent of the signal pulses occur in the interval $(t_s - T_s, t_s + T_s)$, pulses for which $|v_j - t_s| > T_s$ can be ignored with no significant degradation in the detection technique. Further, the terms involving $A\overline{I_b^*} \nu T_s$ and $A\Psi I_o^*$ can be deleted because the intensity of the interferring radiation is assumed to be much less than the star intensity, nominally by a factor one hundred. Note that $G(T_s) \approx .1$ when the slit width is equal to the blur circle diameter. Also, the value of $\mathcal{J}'$ is influenced only by large "large" pulses. The terms in $\mathcal{J}'$ corresponding to these pulses have essentially the same magnitude, namely

$$\ln\left(I_{so}^* / I_{s1}^*\right).$$

The detection technique based on $\mathcal{J}$' can be implemented with a wide-band non-linear amplifier followed by a linear filter with a rectangular impulse response. The optimum holding time depends on the relative magnitude of the signal and noise. This approximation to $\mathcal{J}$' also minimizes the relative error in the star intensity measurements; see Subsection VI.D.

3.   Discrimination Against Dependent Weak Star Detections

In this subsection we will consider a third operating situation in which the detection technique must discriminate against dependent weak star detections. The stars of interest are relatively dim. Consequently, the "weak stars" are closely spaced, and detections are not independent of one another. The primary cause of variability in the photomultiplier output is the variability in the spatial distribution of the weak stars.[*] The goal is to select a detection filter that maximizes the ratio of the output signal level to the output rms noise level.

Let w(t) denote the impulse response of the filter. Then the mean signal level at the output of the detection filter is

$$E\ X(t_s) = \bar{a}\ A\ I_s^* \int_{-\infty}^{\infty} \mathcal{D}(f)\ \mathcal{W}(f)\ df.$$

---

[*]   The noise generated by scanning a "random" stellar background is similar to radar clutter noise, see Urkowitz (1953) and Wainstein and Zubakov (1962) p. 110.

In the absence of a signal, the rms variation of the output about the dc level is the square root of

$$\bar{a}^2 A^2 \overline{I_b^{*2}} \, \nu \int_{-\infty}^{\infty} |W(f)|^2 \, |\mathcal{Y}(f)|^2 df$$

$$+ \left[\bar{a}^2 A \left(\overline{I_b^*} \, \nu T_s + \Psi I_o^* \right) + \bar{d}^2 I_d \right] \int_{-\infty}^{\infty} |W(f)|^2 df .$$

Therefore, the optimum filter frequency response $W(f)$ is one that maximizes the ratio

$$\frac{\left[\bar{a} A I_s^* \int_{-\infty}^{\infty} \mathcal{Y}(f) W(f) \, df \right]^2}{\int_{-\infty}^{\infty} \left(\bar{a}^2 A^2 \overline{I_b^{*2}} \, \nu |\mathcal{Y}(f)|^2 + \bar{a}^2 A \overline{I_b^*} \, \nu T_s + \bar{a}^2 A \Psi I_o^* + \bar{d}^2 I_d \right) |W(f)|^2 df}$$

We can show that the ratio is minimized with[*]

$$W(f) = \frac{\bar{a} A I_s^* \, \mathcal{Y}(f)}{\bar{a}^2 A^2 \overline{I_b^{*2}} \, \nu |\mathcal{Y}(f)|^2 + \bar{a}^2 A \overline{I_b^*} \, \nu T_s + \bar{a}^2 A \Psi I_o^* + \bar{d}^2 I_d}$$

---

[*]   Wainstein and Zubakov (1962), pp. 82, 83.

The first term in the denominator corresponds to the scanning noise generated by scanning the background stars. In Figure 11, the response is illustrated for several levels of scanning noise. Note that for low noise levels $\mathcal{W}(f)$ is proportional to $\mathcal{Y}(f)$. The output signal-to-noise ratio is

$$\left[\int_{-\infty}^{\infty} \frac{\bar{a}^2 A^2 I_s^{*2} |\mathcal{Y}(f)|^2 \, df}{\bar{a}^2 A^2 \overline{I_b^{*2}} \nu |\mathcal{Y}(f)|^2 + \bar{a}^2 A \overline{I_b^*} \nu T_s + \bar{a}^2 A \Psi I_o^* + \bar{d}^2 I_d} \right]^{\frac{1}{2}}$$

The probability of detection can be evaluated using a gamma distribution, as described above.

The optimum filter to discriminate against dependent weak star detections is a band-pass filter. On the other hand, a low-pass filter is best for false star detections. For independent weak star detections, the optimum filter has a frequency response function $\dfrac{\sin 4\pi T_s f}{\pi f}$.
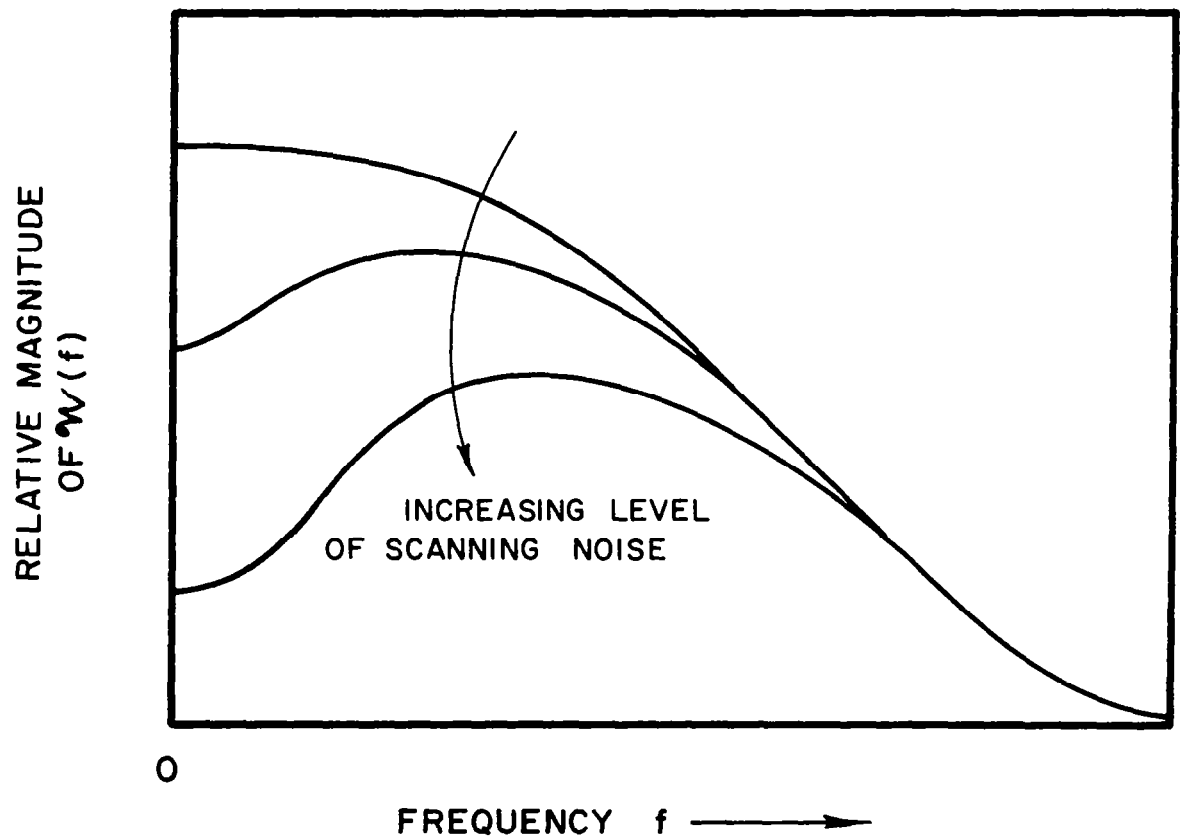
FIGURE II: OPTIMUM FREQUENCY RESPONSE FOR
DIFFERENT NOISE LEVELS

C. Accuracy of Image Location

In the discussion on false star detections, we point out that the maximum likelihood estimate of t_s is the time at which the filter output achieves its maximum value. Also, one can estimate t_s with the average of the first and last time that the filter output crosses a fixed threshold. In this section, we will determine the variance of both estimates. Special cases are considered in detail using a Gaussian impulse response function. In many cases of interest, the optimum impulse response can be approximated by a Gaussian impulse response, see Figures 8, 9, and 10. At the end of this section the effect of angle quantization and image instability, such as that caused by atmospheric seeing, is considered.

1. Accuracy of Peak-Value Technique

Let $\hat{t}_s$ denote the time at which the filter output $X(t)$ achieves its maximum value. The maximazation is over an interval "around" a star detection; $\hat{t}_s$ is determined for each star detection. In the following paragraphs, a general expression for the variance of $\hat{t}_s$ is derived. It is evaluated for a Gaussian impulse response in closed form.

To determine the variance of $\hat{t}_s$, it is convenient to expand the filter output $X(t)$ in a power series about t_s; namely

$$X(t) = X(t_s) + X'(t_s)(t-t_s) + X''(t_s)(t-t_s)^2 + o(t-t_s)^2$$

For the following discussion, it is sufficient that the filter impulse $w(t)$

have a bound third order derivative. Since X(t) achieves its maximum value at $\hat{t}_s$, the first order derivative must be zero, i.e.,

$$X'(\hat{t}_s) = X'(t_s) + X''(t_s)(\hat{t}_s - t_s) + o(\hat{t}_s - t_s)^2 = 0.$$

In general, the filter has an impulse response whose "duration" is comparable to the time the star is in the slit. Hence, X(t) is slowly changing like $E\,X(t)$; X(t) is essentially quadratic in an interval about t_s. Consequently,

$$\hat{t}_s \approx t_s - \frac{X'(t_s)}{X''(t_s)}$$

If one obtains a "large" number of primary photoelectrons from the transiting star, the variance of $X''(t_s)$ is small relative to its mean. Using a simple first order approximation, one observes that

$$\hat{t}_s \approx t_s - \frac{X'(t_s)}{E\,X''(t_s)}\left[1 - \frac{X''(t_s) - E\,X''(t_s)}{E\,X''(t_s)}\right] \approx t_s - \frac{X'(t_s)}{E\,X''(t_s)}$$

when the relative variation of $X''(t_s)$ is small. In other words, the shape of the quadratic approximation essentially fixed. The maximum is displaced in time and amplitude. Then the variance of $\hat{t}_s$ is[*]

$$\text{Var}\,\hat{t}_s \approx \text{Var}\,X'(t_s)\,/\,[E\,X''(t_s)]^2$$

---

[*] A similar result is obtained by Halstrom (1964), p. 284, for two-dimensional images.

Note that this equation is valid when X(t) is quadratic near t_s and when

$$\text{Var } X''(t_s) \ll [EX''(t_s)]^2 .$$

The second condition is discussed later in more detail.

To evaluate the variance of $\hat{t}_s$, it is necessary to find the mean of $X''(t_s)$ and the variance of $X'(t_s)$. In general, the jth derivative of X(t) is

$$X^{(j)}(t) = \sum_k a'_k w^{(j)}(t-\tau_k) + \sum_k d'_k w^{(j)}(t-\hat{\tau}_k) .$$

where a'_k and d'_k are the pulse amplitudes at the output of the non-linear amplifier, see Figure 7, and where w(t) is the impulse response function. The mean and variance of $X^{(j)}(t_s)$ are

$$E X^{(j)}(t_s) = \overline{a'} A I_s^* \int_{-\infty}^{\infty} (-i 2\pi f)^j \mathcal{Y}(f) \mathcal{W}(f) \, df$$

$$\text{Var } X^{(j)}(t_s) = \overline{a'^2} A I_s^* \int_{-\infty}^{\infty} G(t) [w^{(j)}(t)]^2 \, dt$$

$$+ \overline{a'}^2 A^2 \overline{I_b^{*2}} \nu \int_{-\infty}^{\infty} (2\pi f)^{2j} |\mathcal{Y}(f)|^2 |\mathcal{W}(f)|^2 \, df$$

$$+ \left[\overline{a'^2} A \left(\overline{I_b^*} \nu T_s + \Psi I_o^* \right) + \overline{d'^2} I_d \right] \int_{-\infty}^{\infty} (2\pi f)^{2j} |\mathcal{W}(f)|^2 \, df$$

where j = 1, 2.

Assume $w(t)$ is a Gaussian-shaped impulse response function, i.e.,

$$w(t) = w_o \, e^{-\frac{1}{2}(t f_o)^2}$$

Note that

$$W(f) = \frac{\sqrt{2\pi} \, w_o}{f_o} \, e^{-2\pi^2 f^2 / f_o^2}$$

and that half-power frequency is $.133 f_o$. Also one can show that

$$\mathcal{Y}(f) = \frac{1}{\pi f} \sin(\pi f T_s) \, e^{-2(\pi f \sigma)^2}$$

The mean of $X^{(j)}(t_s)$ becomes

$$E X^{(j)}(t_s) = (-2\pi i)^j \, \overline{a'} \, A I_s^* \int_{-\infty}^{\infty} f^j \left[\frac{\sin \pi f T_s}{\pi f} \, e^{-2\pi^2 \sigma^2 f^2} \right]$$

$$\left[\frac{\sqrt{2\pi} \, w_o}{f_o} \, e^{-2\pi^2 f^2 / f_o^2} \right] df$$

The means of all odd order derivatives are zero. Hence, the expected value of $\hat{t}_s$ is t_s. The mean of the second derivative is

$$E X''(t_s) = -\overline{a'} \, A I_s^* w_o \, \frac{1}{f_o T_s^2} \, c^{3/2} \, e^{-c/8}$$

where

$$c = \frac{(f_o T_s)^2}{(f_o \sigma)^2 + 1} \quad .$$

A detailed evaluation is presented in subsection VI.F.2. Note that $0 < c < 1$.

The variance of $X'(t_s)$ becomes

$$\text{Var } X'(t_s) = \overline{a'^2} A I_s^* \int_{-\infty}^{\infty} G(t) \, w_o^2 \, (t \, f_o^2)^2 \, e^{-(t \, f_o)^2} \, dt$$

$$+ \overline{a'}^2 A^2 \overline{I_b^{*2}} \, \nu \int_{-\infty}^{\infty} (2\pi f)^2 \left[\frac{1}{\pi f} \sin(\pi f T_s) \, e^{-2(\pi f \sigma)^2} \right]^2$$

$$\cdot \left[\frac{\sqrt{2\pi} \, w_o}{f_o} \, e^{-2\pi^2 f^2 / f_o^2} \right]^2 df$$

$$\left[\overline{a'^2} A (\overline{I_b^*} \nu T_s + \Psi I_o^*) + \overline{d'^2} I_d \right] \int_{-\infty}^{\infty} (2\pi f)^2 \left[\frac{\sqrt{2\pi} \, w_o}{f_o} \right.$$

$$\left. \cdot e^{-2\pi^2 f^2 / f_o^2} \right]^2 df.$$

In subsection VI.F.3, these integrals are evaluated, and

$$\text{Var } X'(t_s) = \overline{a'^2} A I_s^* w_o^2 f_o F_1(T_s f_o, \sigma f_o)$$

$$+ \overline{a'^2} A^2 \left(\frac{\overline{I_b^{*2}}}{\overline{I_b^*}} \right) (\overline{I_b^*} \nu T_s) w_o^2 F_2(T_s f_o, \sigma f_o)$$

$$+ \frac{\sqrt{\pi}}{2} \left[\overline{a'^2} A (\overline{I_b^*} \nu T_s + \Psi I_o^*) + \overline{d'^2} I_d \right] w_o^2 f_o$$

where the functions F_1 and F_2 are

$$F_1(\alpha, \beta) = \frac{1}{2} \left[\sqrt{\pi} - 2\sqrt{\pi} \, \Phi \left(\frac{-\alpha}{\sqrt{2 + 4\beta^2}} \right) \right.$$

$$\left. - \frac{\alpha}{(1 + 2\beta^2)^{3/2}} \, \exp\left(-\frac{1}{4} \, \frac{\alpha^2}{1 + 2\beta^2} \right) \right]$$

$$F(\alpha, \beta) = \frac{2\pi}{\alpha\sqrt{1 + \beta^2}} \left[1 - \frac{1}{2\sqrt{\pi}} \, \exp\left(-\frac{1}{4} \, \frac{\alpha^2}{1 + \beta^2} \right) \right]$$

Note that F_1 and F_2 are unitless; also the intensity ratio $\overline{I_b^{*2}}/\overline{I_b^*}$ and the average intensity $\overline{I_b^*} \; \nu \; T_s$ have been previously evaluated in subsection III.C. With these results one can evaluate

$$\operatorname{Var} \hat{t}_s \approx \operatorname{Var} X'(t_s) \Big/ \left[E X''(t_s) \right]^2 .$$

It remains to show that the standard deviation of $X''(t_s)$ is small relative to its mean. To do this, an upper bound will be derived for $\operatorname{Var} X''(t_s)$. The ratio of the bound to $\left[E X''(t_s) \right]^2$ is small for cases of interest. Also, we will show that the bound on the variance is close to the true value.

The expression for $\operatorname{Var} X''(t_s)$ is the sum of three integrals; upper bounds will be derived for each term. The first term is

$$\overline{a'^2} \, A \, I_s^* \int_{-\infty}^{\infty} G(t) \left[w''(t) \right]^2 dt .$$

Since $0 < G(t) < 1$, this term is bounded by

$$\overline{a'^2} \, A I_s^* \int_{-\infty}^{\infty} (2\pi f)^4 \, |W(f)|^2 df =$$

$$\frac{3}{4} \sqrt{\pi} \; \overline{a'^2} \, A \, I_s^* \, f_o^3 \, w_o^2 .$$

The function $G(t)$ is significant for $t < 2\sigma$. On the other hand, $\left[w''(t) \right]^2$ is

zero at $t = 1/f_o$. In most cases of interest, $\sigma \geq 1/f_o$. Hence, the bound is near the true value.

The second term in Var $X''(t_s)$ is

$$\overline{a'}^2 A^2 \overline{I_b^{*2}} \nu \int_{-\infty}^{\infty} (2\pi f)^4 |\mathsf{G}(f)|^2 |W(f)|^2 \, df.$$

By replacing

$$\left| \frac{\sin(\pi f T_s)}{\pi f} \right|$$

with its maximum value T_s, in the expression for $|G(f)|$, one obtains an upper bound: viz.,

$$\overline{a'}^2 A^2 \overline{I_b^{*2}} \nu \int_{-\infty}^{\infty} (2\pi f)^4 T_s^2 e^{-4(\pi f \sigma)^2} \frac{2\pi w_o^2}{f_o^2} e^{-4(\pi f/f_o)^2} df$$

$$= \frac{3}{4} \sqrt{\pi} \, \overline{a'}^2 A \overline{I_b^{*2}} \nu T_s^2 f_o^3 w_o^2 \Big/ (1 + \sigma^2 f_o^2)^{5/2}$$

When the diameter of the star image and slit width are comparable, G(t) can be approximated by a Gaussian density function. Hence, the Fourier transform of G(t) is proportional to W(f) and the above bound is close to the true value.

The third term in Var $X''(t_s)$ can be evaluated explicitly; namely,

$$\left[\overline{a'^2} A \left(\overline{I_b^*} \nu T_s + \Psi I_o^* \right) + \overline{d'^2} I_d \right] \int_{-\infty}^{\infty} (2\pi f)^4 \, |\mathcal{W}(f)|^2 \, df =$$

$$\frac{3}{4} \sqrt{\pi} \left[\overline{a'^2} A \left(\overline{I_b^*} \nu T_s + \Psi I_o^* \right) + \overline{d'^2} I_d \right] f_o^3 w_o^2$$

Combining the four bounds one obtains

$$\mathrm{Var}\, X''(t_s) \leq \frac{3}{4} \sqrt{\pi} \, \overline{a'^2} A I_s^* f_o^3 w_o^2$$

$$+ \frac{3}{4} \sqrt{\pi} \, \overline{a'^2} A^2 \overline{I_b^{*2}} \nu T_s^2 f_o^3 w_o^2 \Big/ \left(1 + \sigma^2 f_o^2 \right)^{\frac{5}{2}}$$

$$+ \frac{3}{4} \sqrt{\pi} \left[\overline{a'^2} A \left(\overline{I_b^*} \nu T_s + \Psi I_o^* \right) + \overline{d'^2} I_d \right] f_o^3 w_o^2$$

The problem is to show that

$$\mathrm{Var}\, X''(t_s) \ll \left[E\, X''(t_s) \right]^2$$

and consequently that

$$\mathrm{Var}\,\hat{t}_s \approx \mathrm{Var}\,X'(t_s)\Big/\left[E\,X''(t_s)\right]^2$$

By direct substitution one can show that

$$\frac{\mathrm{Var}\,X''(t_s)}{\left[E\,X''(t_s)\right]^2} \leq \frac{3}{4}\,\frac{\sqrt{\pi}}{A I_s^* T_s}\,(f_o T_s)^5\,c^{-3}\,e^{c/4}$$

$$\left[\frac{\overline{a'^2}}{\overline{a'}^2} + A T_s\,\frac{\overline{I_b^{*2}}}{\overline{I_b^*}}\,\frac{\overline{I_b^*}\,\nu T_s}{I_s^*}\,\frac{1}{(1+\sigma^2 f_o^2)^{5/2}}\right.$$

$$\left. + \frac{\overline{a'^2}}{\overline{a'}^2}\,\frac{\overline{I_b^*}\,\nu T_s}{I_s^*} + \frac{\overline{a'^2}}{\overline{a'}^2}\,\frac{\Psi I_o^*}{I_s^*} + \frac{\overline{a'^2}}{\overline{a'}^2}\,\frac{\overline{d^2 I_d}}{\overline{a'^2}\,A I_s^*}\right]$$

The terms have been arranged for easy evaluation. The significance of various terms are as follows:

(i) $A I_s^* T_s$ is the mean number of photoelectrons emitted during the star transit time.

(ii) $\overline{a'^2}\big/\overline{a'}^2$ depends on the photomultiplier characteristics.

(iii) The ratio $\overline{I_b^{*2}}/\overline{I_b^*}$ is determined by the variability of the stellar background.[*]

---

[*]   This quantity is evaluated in subsection III.C.

(iv) $\overline{I_b^*} \, \nu \, T_s / I_s^*$ is the ratio of the average stellar background in the slit to the star radiation entering the sensor.[*]

(v) $\Psi I_o^* / I_s^*$ is the ratio of the ambient radiation entering the sensor to the star radiation entering the sensor.

(vi) $\overline{d^2} \, I_d \Big/ \overline{a'^2} \, AI_s^*$ is the ratio of the ac power in the dark current to the ac power in the star signal with the slit removed.

To use the basic equation

$$\text{Var}\,\hat{f}_s = \text{Var}\,X'(t_s) \Big/ \big[E X''(t_s) \big]^2$$

one must verify that

$$\text{Var}\,X'(t_s) \ll \big[E X''(t_s) \big]^2$$

and that $X(t)$ is quadratic near t_s. Implementations of this technique of measuring t_s are described in subsection VI.E.

2. Accuracy of Threshold Technique

The "threshold technique" of estimating the time at which the star is centered in the slit is based on threshold crossings. In particular, an amplitude threshold is selected, say x_0. Assume $X(t)$ crosses x_0 at times u_1 and u_2. The estimate of t_s is then

$$\tilde{f}_s = \frac{1}{2}(u_1 + u_2).$$

---

[*] This quantity is evaluated in subsection III.C.

Note that x_0 is not necessarily the same threshold as used for detection, c'_p.

To determine the variance of $\widetilde{t}_s$, it is convenient to expand the filter output $X(t)$ in a power series. Let $\bar{u}_1$ and $\bar{u}_2$ denote the times at which $E\, X(t) = x_0$, and $\bar{u}_1 \leq \bar{u}_2$. The expansion of $X(t)$ about $\bar{u}_1$ is

$$X(t) = X(\bar{u}_1) + X'(\bar{u}_1)(t - \bar{u}_1) + \cdots$$

Since $X(t)$ crosses x_0 at u_1,

$$X(u_1) = x_0 = X(\bar{u}_1) + X'(\bar{u}_1)(u_1 - \bar{u}_1) + \cdots$$

In general, the filter has an impulse response whose duration is comparable to the time the star is in the slit. Hence, $X(t)$ is slowly changing like $E\, X(t)$; $X(t)$ is essentially linear in an interval about $\bar{u}_1$. Consequently,

$$u_1 \approx \bar{u}_1 + \frac{x_0 - X(\bar{u}_1)}{X'(\bar{u}_1)} .$$

If one obtains a "large" number of primary photoelectrons from the transiting star, the variance of $X'(\bar{u}_1)$ is small relative to its mean. Using a simple first order approximation, one observes that

$$u_1 \approx \bar{u}_1 + \frac{x_0 - X(\bar{u}_1)}{E\, X'(\bar{u}_1)} \left[1 - \frac{X'(\bar{u}_1) - E\, X'(\bar{u}_1)}{E\, X'(\bar{u}_1)} \right]$$

$$\approx \bar{u}_1 + \frac{x_0 - X(\bar{u}_1)}{E\, X'(\bar{u}_1)} .$$

In other words, the slope of the linear approximation is essentially fixed; its intercept changes. Similarly, one can show that

$$U_2 \approx \overline{U}_2 + \frac{x_o - X(\overline{u}_2)}{E\,X'(\overline{u}_2)} \quad .$$

Hence, the variance of $\tilde{t}_s$ is

$$\text{Var } \tilde{t}_s \approx \text{Var}\left[\frac{X(\overline{u}_2) - X(\overline{u}_1)}{2\,E\,X'(\overline{u}_1)}\right] =$$

$$\frac{\text{Var } X(\overline{u}_1) - \text{Cov}\left[X(\overline{u}_1), X(\overline{u}_2)\right]}{2\left[E\,X'(\overline{u}_1)\right]^2} \quad .$$

Note that this equation is valid when $X(t)$ is linear near $\overline{u}_1$, and when

$$\text{Var } X'(\overline{u}_1) \ll \left[E\,X'(\overline{u}_1)\right]^2 \quad .$$

The second condition is discussed in more detail later.

To evaluate the variance of $\tilde{t}_s$ it is necessary to find the variance of $X(\bar{u}_1)$, the covariance between $X(\bar{u}_1)$ and $X(\bar{u}_2)$, and the mean of $X'(\bar{u}_1)$. One can show directly that

$$Var\, X(t) = A I_s^* \overline{a'^2} \int_{-\infty}^{\infty} G(t') \left[w(t-t_s-t') \right]^2 dt'$$

$$+ \overline{a'}^2 A^2 \overline{I_b^{*2}} \nu \int_{-\infty}^{\infty} |W(f)|^2 |\mathcal{Y}(f)|^2 \, df$$

$$+ \left[\overline{a'^2} A (\overline{I_b^*} \nu T_s + \Psi I_o^*) + \overline{d'^2} I_d \right] \int_{-\infty}^{\infty} |W(f)|^2 df$$

$$E\, X'(t) = -2\pi A I_s^* \overline{a'} \int_{-\infty}^{\infty} f \, \sin\left[2\pi f(t-t_s)\right] W(f) \mathcal{Y}(f) \, df$$

Assume $w(t)$ is a Gaussian-shaped impulse response function, i.e.

$$w(t) = w_o \, e^{-\frac{1}{2}(t f_o)^2}$$

and

$$W(f) = \frac{\sqrt{2\pi} \, w_o}{f_o} \, e^{-2\pi^2 f^2/f_o^2}$$

The variance of X(t) and the mean of X'(t) can be evaluated in closed form.

$$Var \, X(t) = A I_s^* \, \overline{a'^2} \, \frac{w_o^2}{f_o} \, F_3(T_s f_o, \sigma f_o, (t-t_s)f_o)$$

$$+ \, \overline{a'^2} A^2 \overline{I_b^{*2}} \, \nu \, \frac{w_o^2}{f_o^3} \, F_4(T_s f_o, \sigma f_o)$$

$$+ \, \sqrt{\pi} \left[\overline{a'^2} A(\overline{I_b^*} \nu T_s + \Psi I_o^*) + \overline{d'^2} I_d \right] w_o^2/f_o$$

where

$$F_3(\alpha, \beta, \gamma) = \frac{\sqrt{\pi}}{2} \left[\Phi\left(\frac{\alpha/2 - \gamma}{\sqrt{1/2 + \beta^2}}\right) - \Phi\left(-\frac{\alpha/2 - \gamma}{\sqrt{1/2 + \beta^2}}\right) \right.$$

$$\left. + \, \Phi\left(\frac{\alpha/2 + \gamma}{\sqrt{1/2 + \beta^2}}\right) - \Phi\left(-\frac{\alpha/2 + \gamma}{\sqrt{1/2 + \beta^2}}\right) \right]$$

$$F_4(\alpha, \beta) = 4\pi\alpha \left[\frac{1}{2} - \Phi\left(\frac{-\alpha}{\sqrt{2(1+\beta^2)}} \right) \right]$$

$$-2\sqrt{2\pi}\sqrt{2(1+\beta^2)} \left[1 - \exp\left(-\frac{1}{4}\frac{\alpha^2}{1+\beta^2} \right) \right]$$

The detail evaluations of the integrals are presented in subsection VI.F.4. Further, we show that

$$E\,X'(t) = \frac{A\,I_s^*\,\overline{\alpha'}\,w_o}{\sqrt{1 + f_o^2\sigma^2}} \left\{ \exp\left[-\frac{f_o^2(t - t_s + T_s/2)^2}{2(f_o^2\sigma^2 + 1)} \right] \right.$$

$$\left. - \exp\left[-\frac{f_o^2(t - t_s - T_s/2)^2}{2(f_o^2\sigma^2 + 1)} \right] \right\}$$

in subsection VI.F.5. In addition, the covariance between $X(t_1)$ and $X(t_2)$, for arbitrary times t_1 and t_2, can be expressed in terms of the variance of $X(t)$; namely,

$$\text{Cov}\big(X(t_1), X(t_2)\big) = e^{-\frac{1}{4}f_o^2(t_1 - t_2)^2}\,\text{Var}\,X\left(\frac{t_1 + t_2}{2} \right)$$

See subsection VI.F.6.

It remains to show that the standard deviation of $X'(\bar{u}_1)$ is small relative to its mean. The variance of $X'(t)$ can be evaluated directly; it is

$$
\operatorname{Var} X'(t) = A I_s^* \overline{a'^2} w_o^2 f_o F_5(T_s f_o, \sigma f_o, (t-t_s)f_o)
$$

$$
+ \overline{a'}^2 A^2 \overline{I_b^{*2}} \nu T_s w_o^2 F_2(T_s f_o, \sigma f_o)
$$

$$
+ \frac{\sqrt{\pi}}{2} \left[\overline{a'^2} A(\overline{I_b^*}\nu T_s + \Psi I_o^*) + \overline{d'^2} I_d \right] w_o^2 f_o
$$

where

$$
F_5(\alpha, \beta, \gamma) = \frac{\sqrt{\pi}}{4} \left[\Phi\left(\frac{\alpha/2 + \gamma}{\sqrt{1/2 + \beta^2}}\right) - \Phi\left(-\frac{\alpha/2 + \gamma}{\sqrt{1/2 + \beta^2}}\right) \right.
$$

$$
\left. + \Phi\left(\frac{\alpha/2 - \gamma}{\sqrt{1/2 + \beta^2}}\right) - \Phi\left(-\frac{\alpha/2 - \gamma}{\sqrt{1/2 + \beta^2}}\right) \right]
$$

$$
- \frac{1}{2(2\beta^2 + 1)^{3/2}} \left\{ (\alpha/2 - \gamma) \exp\left[-\frac{(\alpha/2 - \gamma)^2}{2(1/2 + \beta^2)}\right] \right.
$$

$$
\left. (\alpha/2 + \gamma) \exp\left[-\frac{(\alpha/2 + \gamma)^2}{2(1/2 + \beta^2)}\right]\right\} .
$$

The details are presented in subsection VI.F.7.

To use the basic equation

$$\mathrm{Var}\ \tilde{t}_s = \frac{\mathrm{Var}\ X(\bar{u}_1) - \mathrm{Cov}[X(\bar{u}_1), X(\bar{u}_2)]}{2[E\ X'(\bar{u}_1)]^2}$$

one must verify that

$$\mathrm{Var}\ X'(\bar{u}_1) \ll [E\ X'(\bar{u}_1)]^2$$

and that X(t) is linear "near" $\bar{u}_1$. Possible implementations of the threshold technique are discussed in Section VI.E.

3.   Quantization Error

In most applications the output of the sensor is expressed in digital form and used in a computer. Consequently, there is a quantization error in addition to random errors. In some applications, the sensor output is the star transit time obtained from a digital clock. In other applications, the sensor output is the angular position of the reticle when a star is centered in the slit; the angle is measured with an angle encoder. In the following discussion, the first application will be considered. The results also apply to applications in which an angle encoder is used.

The relation between the input and output of the "time encoder" are illustrated in Figure 12. The input time estimate $\hat{t}_s$ is quantized to obtain $Q\hat{t}_s$. Note that Δ is the quantization interval. The rms error is then
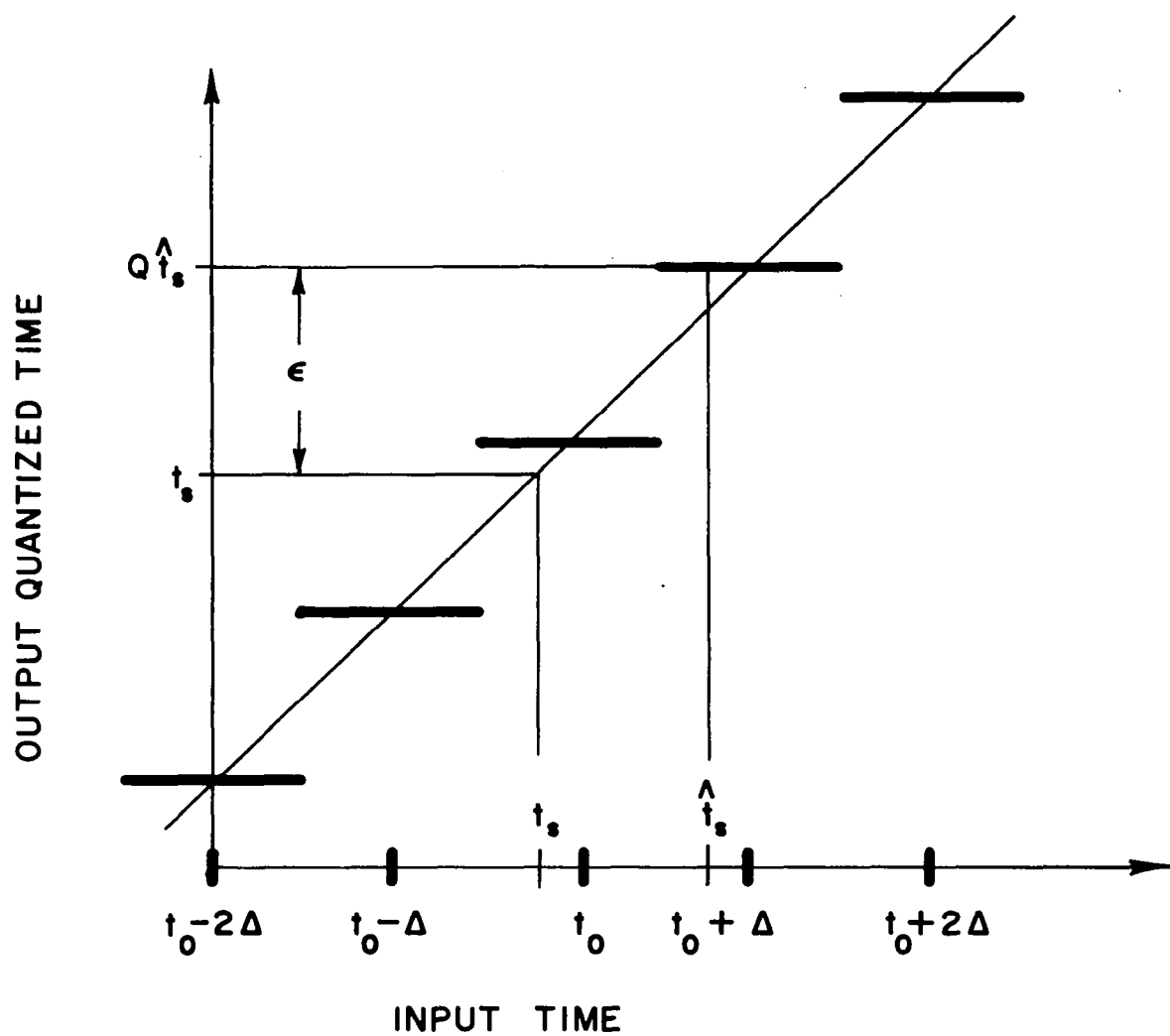
FIGURE 12: OPERATION OF TIME QUANTIZER

$$\epsilon = \left[\int_{-\infty}^{\infty} (Qt - t_s)^2 \, \phi\left(\frac{t-\mu}{\nu}\right) \, dt \right]^{1/2}$$

where

$$\mu = E \, \hat{t}_s$$

$$\nu^2 = Var \, \hat{t}_s .$$

To estimate the effect of quantization we have assumed $\hat{t}_s$ is normally distributed. Also, we will assume that there is no systematic error in measuring t_s, i.e., $E \hat{t}_s = t_s$. We can show directly that

$$\epsilon^2 = \sum_{j=-\infty}^{\infty} (t_o - t_s + j\Delta)^2 \left[\Phi\left(\frac{t_o - t_s + j\Delta}{\nu} + \frac{\Delta}{2\nu}\right) - \Phi\left(\frac{t_o - t_s + j\Delta}{\nu} - \frac{\Delta}{2\nu}\right) \right]$$

The factor in the brackets is functionally identical to $G(t)$ with T_s replaced with Δ and σ replaced by ν. Note that as ν approaches zero, ϵ^2 approaches $(t_o - t_s)^2$.

When $\Delta < \sigma$, we can bound ϵ^2. Farrell and Zimmerman (1965) have shown that

$$\Phi\left(\frac{t_o - t_s + j\Delta}{\nu} + \frac{\Delta}{2\nu}\right) - \Phi\left(\frac{t_o - t_s + j\Delta}{\nu} - \frac{\Delta}{2\nu}\right) \approx$$

$$\frac{\Delta}{\nu} \, \phi\left(\frac{t_o - t_s + j\Delta}{\nu}\right) .$$

Hence, ϵ^2 is approximately

$$\epsilon^2 \approx \sum_{j=-\infty}^{\infty} (t_0 - t_s + j\Delta)^2 \frac{\Delta}{\nu} \phi\left(\frac{t_0 - t_s + j\Delta}{\nu}\right)$$

Note that as Δ approaches zero as ϵ^2 approaches σ^2, i.e., the summation converges to an integral.

4. Effect of Atmospheric Seeing

If observations are made from Earth, atmospheric seeing causes the star images to move randomly in the field of view. Consequently, a star transit time t_s varies from scan to scan. In such a situation we must average ϵ^2 with respect to t_s to obtain the total rms error: random error, quantization error, and seeing error.

D.   Accuracy of Intensity Measurement

The relative error in the intensity measurement is the ratio of the rms noise level to signal level when the output signal is a maximum. In this section the background radiation is assumed to be homogeneous. We use the model described in subsection VI.B.1 for false star detections. The relative error is

$$\frac{\left\{\int_{-\infty}^{\infty}\left[\overline{a^2}AI_s^*G(t) + \overline{a^2}A\overline{I_b^*}\nu T_s + \overline{a^2}A\Psi I_o^* + \overline{d^2}I_d\right]w^2(t)\,dt\right\}^{1/2}}{\overline{a}AI_s^*\int_{-\infty}^{\infty}G(t)\,w(t)\,dt}$$

This ratio is minimized when[*]

$$w(t) = \frac{\overline{a}AI_s^*G(t)}{\overline{a^2}AI_s^*G(t) + \overline{a^2}A\overline{I_b^*}\nu T_s + \overline{a^2}A\Psi I_o^* + \overline{d^2}I_d}$$

The corresponding minimum relative error is

$$\left[\int_{-\infty}^{\infty}\frac{\left[\overline{a}AI_s^*G(t)\right]^2}{\overline{a^2}AI_s^*G(t) + \overline{a^2}A\overline{I_b^*}\nu T_s + \overline{a^2}A\Psi I_o^* + \overline{d^2}I_d}\,dt\right]^{-1/2}$$

If the magnitude of the interferring radiation and dark current are small relative to the star signal, the impulse response w(t) is essentially constant over a long interval, relative to the star transit time T_s. Since 98 percent of the signal pulses occur in the interval $(t_s - T_s, t_s + T_s)$, we can restrict the effective duration of the impulse response to $2T_s$ without a significant loss of information. Hence, the optimum filter can be approximated by a

___

[*]   See discussion by Wainstein and Zubakov (1962), pp. 82, 83.

filter which has a rectangular impulse response. Note that a filter which minimizes the relative error in the intensity measurement is optimum in discrimination against weak star detections. See subsection VI.B.2. With a high signal-to-noise ratio, the minimum relative error is inversely proportional to the square root of the mean number of primary photoelectrons generated by the star: viz., $AI_s^* T_s$.

Assume $w(t)$ is a rectangular impulse response, i.e.,

$$w(t) = \begin{cases} w_o & |t| < T/2 \\ 0 & |t| \geqslant T/2 \end{cases}$$

where T is the duration of the impulse response function. Then the relative intensity error becomes

$$\frac{\left\{\overline{a^2}AI_s^* \int_{-T/2}^{T/2} G(t)\,dt + T\left[\overline{a^2}A\overline{I_b^*}\nu T_s + \overline{a^2}A\Psi I_o^* + \overline{d^2}I_d\right]\right\}^{1/2}}{\overline{a}\,AI_s^* \int_{-T/2}^{T/2} G(t)\,dt}$$

We can select a holding time T which minimizes the relative error by differentiating. The best value of T is the value which satisfies the following equation,

$$1 = G(T/2)\left[\frac{\overline{a^2}AI_s^*}{\overline{a^2}A\overline{I_b^*}\nu T_s + \overline{a^2}A\Psi I_o + \overline{d^2}I_d} + \frac{2T}{\int_{-T/2}^{T/2} G(x)\,dx}\right].$$

E.   Implementation of Signal Processing Technique

The techniques described in the preceding paragraphs have relatively simple implementations. We will present several electronic designs suitable for satellite systems. The basic functions of the electronic processing are signal filtering, detection of bright stars, discrimination against weak stars, measurement of image position, and measurement of signal intensity. These functions are related in Figure 13. The intensity and position measurements are not initiated until a detection is obtained. Also the detection threshold is selected for optimum discrimination against weak stars. Figure 14 shows the electronics block diagram for the peak-value method, and Figure 15 shows the block diagram for the threshold method.

1.   Signal Filtering

A typical output signal from a photomultiplier is shown in Figure 16a. This signal is characterized by many randomly occurring small amplitude noise pulses, and signal pulses whose amplitudes vary randomly. The duration of a typical elementary anode current pulse due to a single photocathode emission has been experimentally determined as 10×10^{-9} second, Tanasescu (1960). The width of the pulse is largely determined by the RC time constant of the photomultiplier output circuit. The voltage amplitude of the pulse is approximately determined by $\Delta V = \Delta Q/C_s$ where C_s is the stray capacitance at the output of the photomultiplier and ΔQ is the total charge collected at the anode. If the gain of the photomultiplier is 10^6, then one

OPTIMUM DETECTION THRESHOLD FOR
WEAK STAR DISCRIMINATION

SIGNAL FROM
PHOTOMULTIPLIER → SIGNAL FILTERING → DETECTION

INITIATION PULSE

POSITION MEASURE-MENT ← → INTENSITY MEASURE-MENT

OUTPUT DATA TO TELEMETRY OR COMPUTER
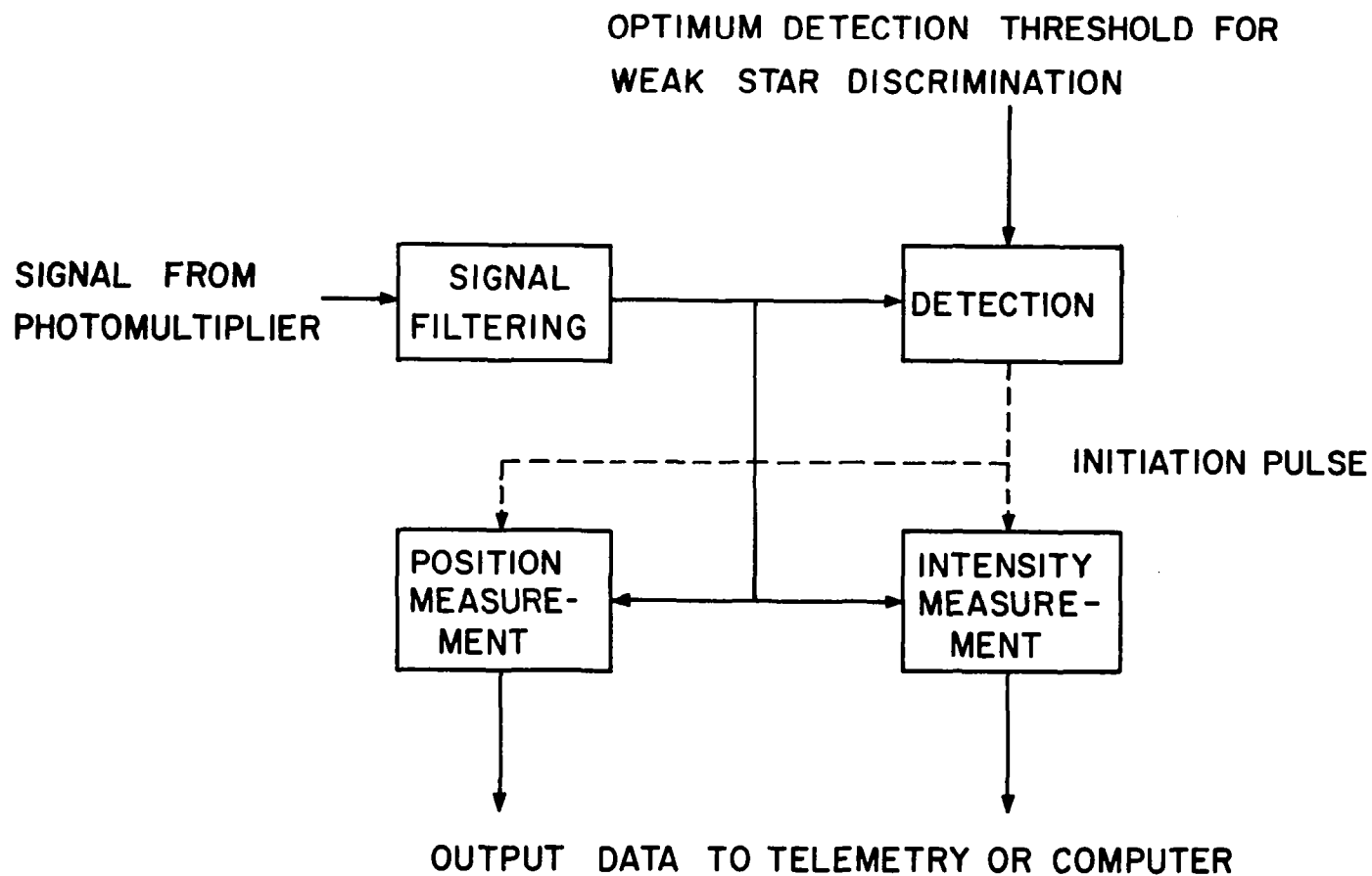
FIGURE 13 : BASIC FUNCTIONS OF ELECTRONIC PROCESSING
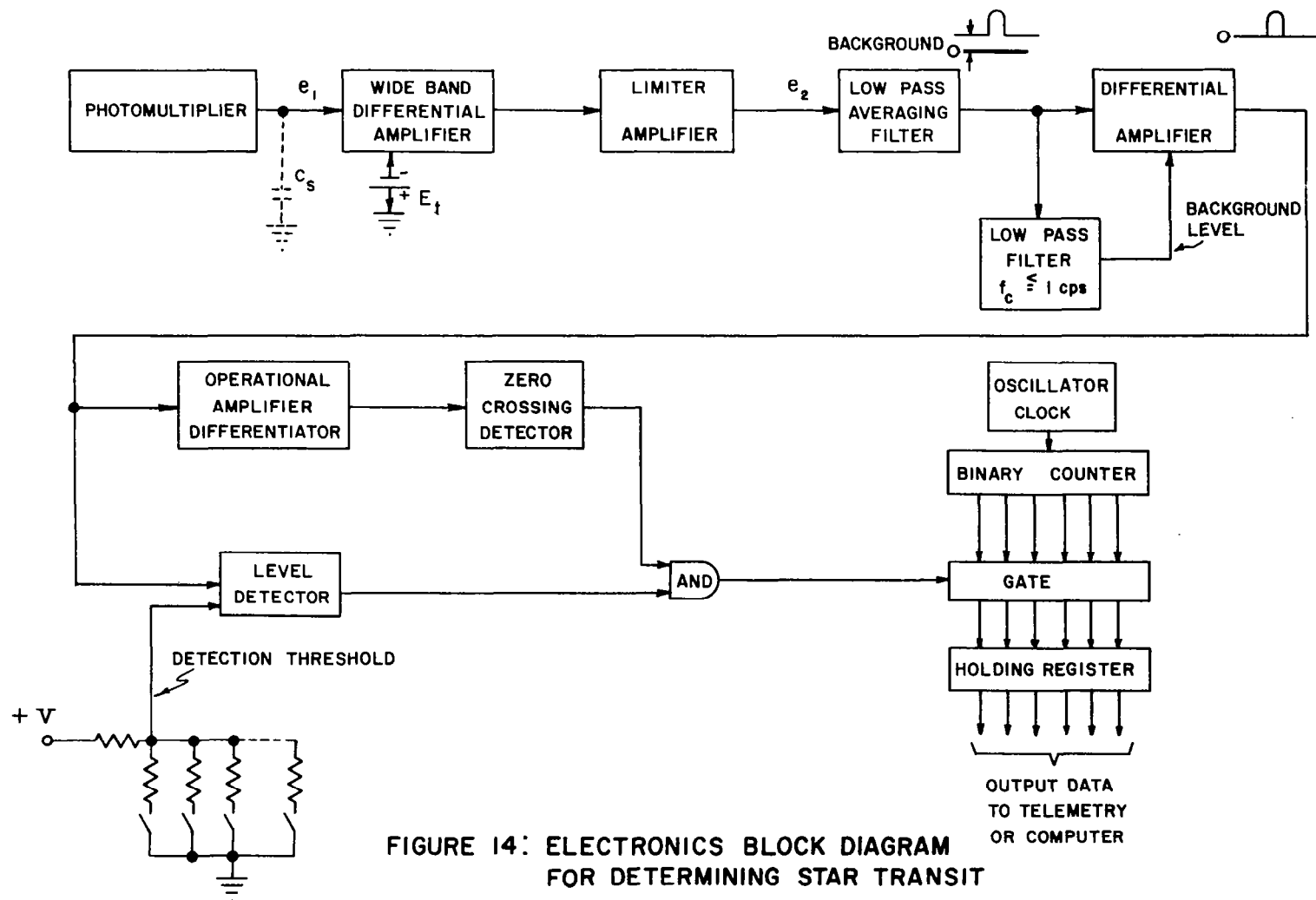
FIGURE 14: ELECTRONICS BLOCK DIAGRAM
FOR DETERMINING STAR TRANSIT
TIME WITH THE PEAK VALUE
TECHNIQUE
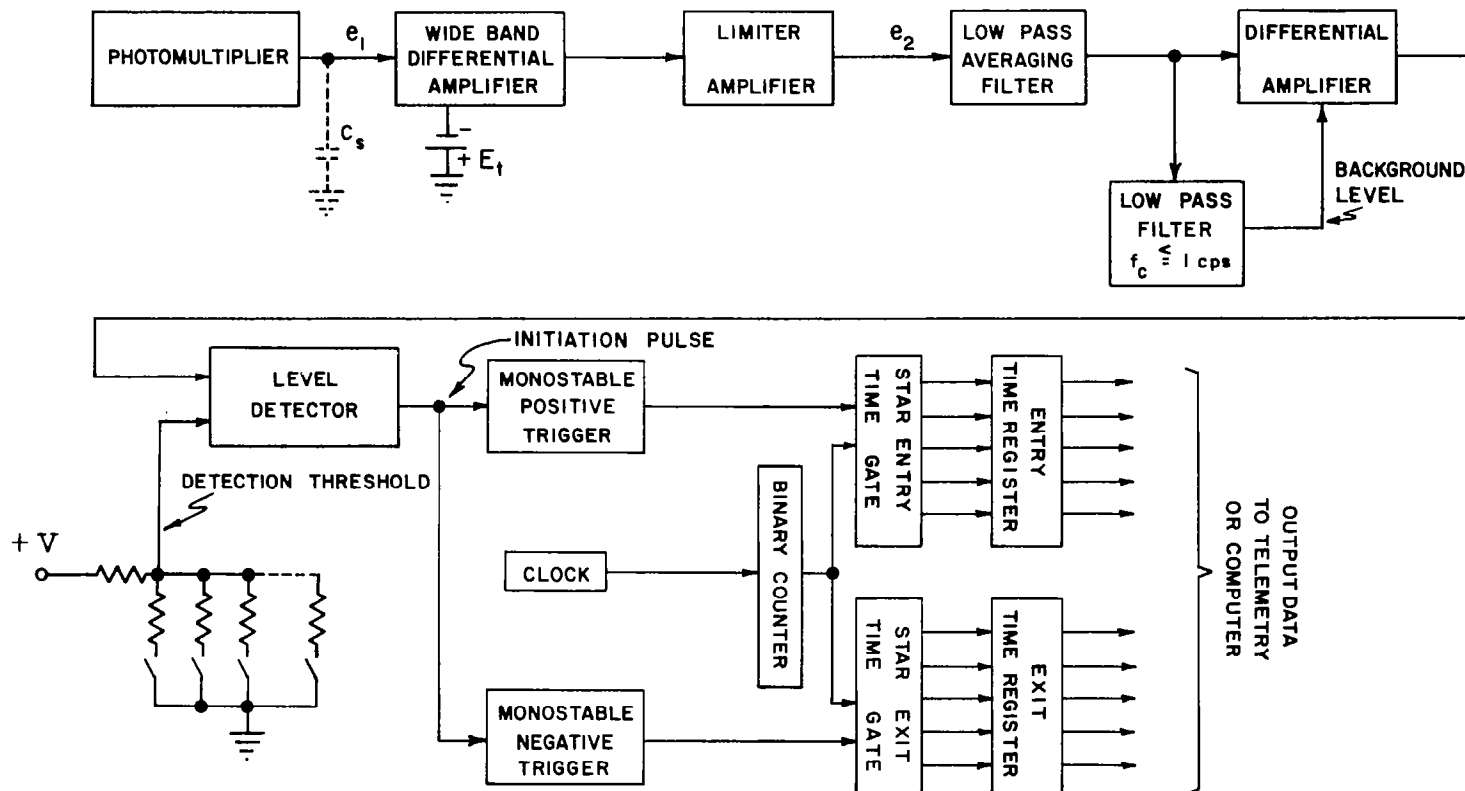
FIGURE 15 : ELECTRONICS BLOCK DIAGRAM FOR DETERMINING STAR TRANSIT TIME
WITH THE THRESHOLD TECHNIQUE
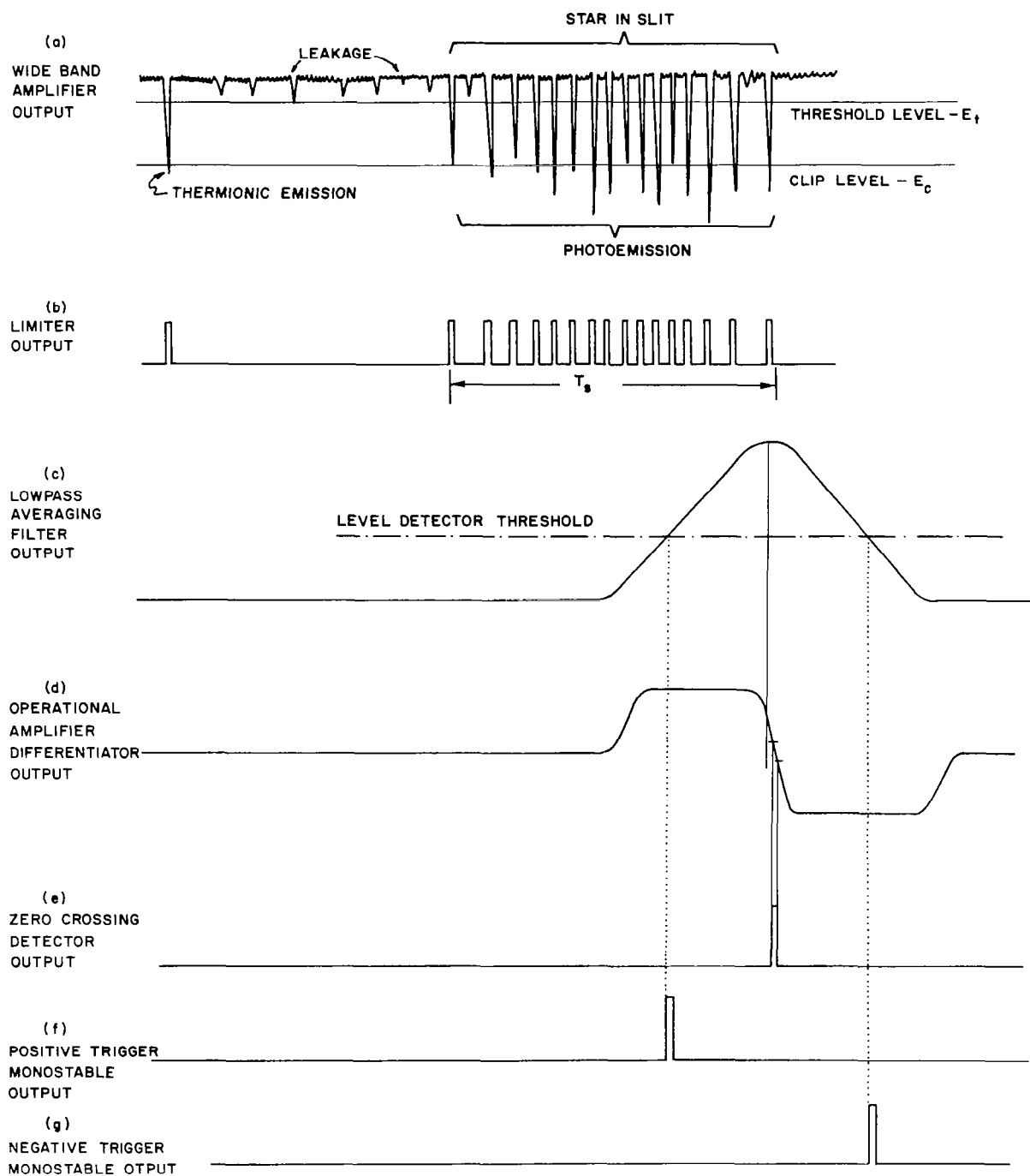
FIGURE 16 : TYPICAL WAVE FORMS

photoelectron will cause a burst of approximately 10^6 electrons to be

collected at the anode. So for a typical $C_s = 10^{-11}$ farads and

$\Delta Q \approx 10^6 \times 1.6 \times 10^{-19}$ coulombs, $\Delta V = 16$ millivolts. With a one inch

optical aperture, there is approximately 10^6 photons per second arriving

at the photocathode for a zero magnitude star. Assuming a cathode quantum

efficiency of 0.1 electron per photon, the average photoelectron rate

becomes 10^5 electrons per second. To minimize the possiblity of overlapping

anode pulses, the bandwidth of the anode output circuit and amplifier

should be much greater than the expected average frequency of anode

pulses. If we choose a factor of 100, the required bandwidth becomes

10^7 cycles per second. The half-power cut-off frequency for an RC low

pass filter is $f = 1/2\pi RC$, so the input resistance to the amplifier must

be $R_{in} \leq 1/f2\pi C_s = 1/10^7 \times 2\pi \times 10^{-11} = 1.59 \times 10^3$ ohms for $C_s = 10^{-11}$ farads.

In subsection VI.B, we show that "detectability" is optimized by

discriminating against the small amplitude noise pulses and by

reducing the variation of the signal pulses. The effect of noise can

be reduced by choosing an amplifier threshold level, E_t, such that a

large percentage of noise pulses have amplitudes less than E_t. The

variation in signal pulses received at the anode can be reduced by clipping

the pulse peaks with a suitable limiting amplifier. Clipping the signal

pulses also reduces the effects of drift in photomultiplier gain,

Brimhall and Page (1965). The signal output from the limiter amplifier

should appear as in Figure 16b. The desired voltage transfer characteristic

for amplification of the photomultiplier output is shown in Figure 17. The
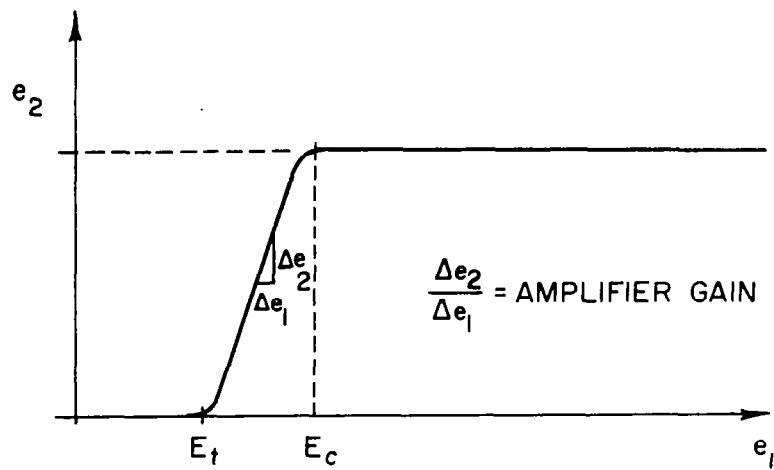
FIGURE 17 : VOLTAGE TRANSFER CHARACTERISTIC FOR AMPLIFICATION OF PHOTOMULTIPLIER OUTPUT

threshold function can be performed by a differential input amplifier
whose output is clamped to a fixed level (preferably zero) for all signal
inputs less than E_t. For a satellite system the amplifier should be
an integrated circuit. Examples of suitable commercially available
integrated circuit RF amplifiers are the types CA3005 and CA3006 recently
announced by Radio Corporation of American (RCA Application Note
ICAN-5022 (1965). The CA3004 and CA3006 feature differential input,
frequency response from DC to 10^8 cycles per second, high gain, and sharp
limiting characteristics. Versatility in the operation of the CA3005 and
CA3006 is made possible by the availability of internal circuit points
to which external circuit elements may be connected to alter the basic
circuit configuration. To realize the voltage transfer characteristic
of Figure 17, no more than two stages of the CA3005 or the CA3006 will
be required. The 16 millivolt photomultiplier anode pulses are sufficient
to drive the input stage.

Following the amplifier of Figure 14 is shown a low pass averaging
filter whose purpose is to integrate the limiter output for some fixed
period T. It is not necessary to have the averaging period T greater
than twice the time period that the star appears in the slit. Ninety-
eight percent of the signal occurs in this interval. The output signal
from the low pass averaging filter will appear as shown in Figure 16c.
The finite time averaging process is described by $e_o = 1/T \int_{t-T}^{t} e_{in}(t) \, dt$.
The design problem is to realize a filter which approximates the time
averaging process. An approximate filter transfer function has been given as

$$A(s) = E_o(s)/E_{in}(s) =$$

$$\frac{\left[1 + \left(\frac{s}{\omega_c}\right)^2\right]\left[1 + \frac{1}{4}\left(\frac{s}{\omega_c}\right)^2\right]\cdots\left[1 + \left(\frac{2}{n-2}\right)^2\left(\frac{s}{\omega_c}\right)^2\right]}{\left\{\left[1 + 4\left(\frac{s}{\omega_c}\right)^2\right]\left[1 + \frac{4}{9}\left(\frac{s}{\omega_c}\right)^2\right]\cdots\left[1 + \left(\frac{2}{n-1}\right)^2\left(\frac{s}{\omega_c}\right)^2\right]\right\} + \left\{a_n\frac{s}{\omega_c}\left[1 + \left(\frac{s}{\omega_c}\right)^2\right]\cdots\left[1 + \left(\frac{2}{n-2}\right)^2\left(\frac{s}{\omega_c}\right)^2\right]\right\}}$$

where $\quad a_n = 3 \qquad a_n = a_{n-2}\dfrac{1 - [2(n-1)]^{-2}}{1 - [2(n-1)]^{-2}}$

$$n = 4, 6, 8, \cdots$$

This tranfer function is presented by Hansen (1965).

The $|A| = 1$ when $\frac{\omega}{\omega_c} = 0$ and $|A| = 0$ when $\frac{\omega}{\omega_c} = 1, 2, \ldots (\frac{n}{2} - 1)$.

For

$$\frac{\omega}{\omega_c} \gg \left(\frac{n}{2} - 1\right)$$

$$|A| = \frac{1 \cdot 3 \cdot 5 \cdots (n-1)}{1 \cdot 2 \cdot 3 \cdots (n/2 - 1) \, 2^{n/2}} \left(\frac{\omega}{\omega_c}\right)^2$$

Any order transfer function can be factored into quadratic terms, so the averaging filter may be realized by a series of cascaded quadratic stages. Two circuit configurations for realizing the quadratic sections of the averaging filter are shown in Figures 18 and 19, Sallen and Key (1955). Most quadratic sections can be realized practically with an
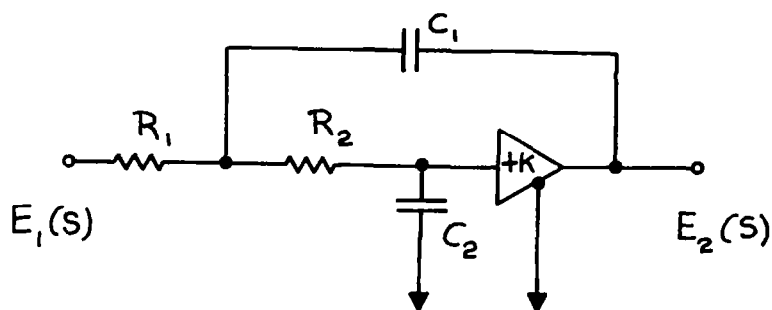
Transfer function $\dfrac{E_2(s)}{E_1(s)} = \dfrac{K}{\left\{ S^2 + S\left[\dfrac{\left(1+\dfrac{R_1}{R_2}\right)}{R_1 C_1} + R_1 C_1(1-K)\right] + 1 \right\}}$

Figure 18: Circuit for realizing transfer functions of form $\dfrac{K}{S^2 + dS + 1}$
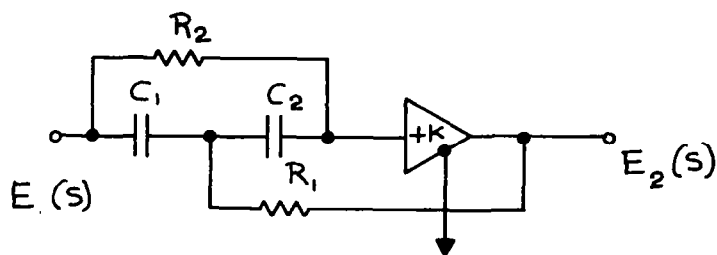
$\dfrac{E_2(s)}{E_1(s)} = K \cdot \dfrac{S^2 + S\left[\dfrac{1}{R_2 C_2} + R_1 C_2\right] + 1}{\left\{ S^2 + S\left[\dfrac{\left(1+\dfrac{R_1}{R_2}\right)}{R_1 C_1} + R_1 C_1(1-K)\right] + 1 \right\}}$

Figure 19: Circuit for realizing transfer function of form

$K \dfrac{S^2 + bS + 1}{S^2 + dS + 1}$

emitter follower amplifier whose gain K $\stackrel{\sim}{=}$ 1.

An averaging filter is optimum for discrimination against weak star detection (VI.B.2). In many satellite applications this is the basic "noise" problem. To discriminate against false star detections and dependent weak star detections other types of filters are optimum, as described in subsections VI.B.1 and VI.B.3.

Following the averaging filter, Figure 14 shows a differential input amplifier, and a lowpass filter with a very low cut-off frequency driving one input to the amplifier. The other amplifier input and the filter input is driven by the averaging filter output. The purpose of this configuration is to eliminate the slowly varying, almost DC, background signal caused by the stellar background of very weak stars. Depending upon the pointing direction of the optical system, the integrated stellar background may vary more than an order of magnitude. The lowpass filter with a cutoff frequency less than 1 cps attenuates the star pulse portion of the composite background-star signal and passes the background signal into one input to the amplifier. The other input to the amplifier is driven by the composite background-star signal from the averaging filter. The output of the differential amplifier is an amplified star pulse rising from a zero background level.

2. Detection and Measurement of Image Position

First we will describe a design that implements the peak-value technique, VI.C.1. The star pulse output from the differential amplifier

drives a differentiator, see Figure 14. The zero crossing of the differ-
entiated pulse occurs very close to the peak time of the star pulse, as shown
in Figure 16d. The zero crossing would occur exactly at the star pulse peak only
if the differentiator were perfect. Probably the best practical differenti-
ator employs a high gain operational amplifier. One of the difficulties
of differentiation is that any high frequency noise is enhanced, hence
differentiator design should include high frequency response limiting.
Figure 20 shows a low-noise operational amplifier-differentiator with
double high frequency cutoff, see Burr-Brown Handbook of Operational
Amplifier Applications (1963). To further reduce the noise susceptibility
of the differentiator, it would also be possible to add more stages to
the averaging filter to improve the attenuation of high frequency noise
components in the stop band.

The zero crossing detector (Figure 14) should have an output signal
as shown in Figure 16e. As the input signal approaches zero volts, the
output rises to a level sufficient to drive a logic gate. The zero crossing
detector can simply be realized by a high gain amplifier followed by a
monostable circuit which triggers when the amplifier input approaches
zero.

Since the zero crossing detector of Figure 14 will have an output
for each weak star, it is desirable to gate the zero-crossing detector
output so only the brightest stars initiate the output data. To
accomplish this, Figure 14 shows a two input level detector circuit. One
input is driven by the star pulse while the other input is driven by a

$$e_2 = -R_0 C_1 \frac{de_1}{dt}$$
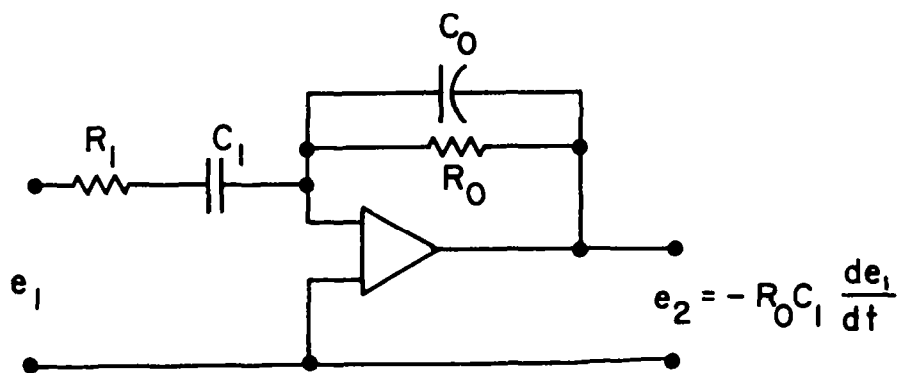
FIGURE 20 : LOW NOISE OPERATIONAL AMPLIFIER DIFFERENTIATOR

voltage divider threshold circuit. The level detector circuit has an output whenever the star pulse exceeds the threshold voltage level. The level detector output drives an AND gate which gates the zero crossing detector output. The number of times star transit data is generated per scan is determined by the threshold-voltage-divider setting. A suitable integrated-circuit level-detector would be the μ A-710 manufactured by Fairchild Semiconductor.

Star transit time data is generated for bright stars when the zero crossing detector of Figure 14 gates the output of a continuously stepping binary counter into a holding register. The binary counter is continuously stepped by a stable oscillator clock whose frequency is determined by the scan rate and the required angular accuracy of each bright star transit. The number of stages in the binary counter is determined by the required angular resolution to achieve the star transit accuracy.

Next we will describe a design that will implement the threshold technique, VI.C.2. Figure 15 shows a block diagram for gathering star transit data with the threshold technique. The amplification and filtering is similar to that already described in Figure 14 for peak detection. For the threshold technique, a level detector is employed as described for Figure 14, except the level detector output drives both a positive-trigger monostable and a negative-trigger monostable. The positive monostable will trigger when the leading edge of the star pulse begins to exceed the threshold level as shown in Figure 16f. The pulse from the positive monostable will gate the output of a continously stepping

binary counter into a star entry time holding register. As the trailing edge of the star pulse falls below the level detector threshold, the negative monostable will trigger (see Figure 16g). The pulse from the negative monostable will gate the output of the continuously stepping counter into an exit time register. If the star pulse can be assumed to be symmetrical, then the star pulse peak occurs midway between the entry time and the exit time.

3. Discimination Against Weak Stars

The voltage divider that establishes the threshold voltage at one input to the level detector can be automated so that only the brightest stars exceed the threshold level for each scan. Basic to automating the threshold level is a voltage divider as shown in Figure 21.

This voltage divider, as shown in Figure 21, consists of a reference voltage, V_R, a fixed resistor, R, and a set of multiple valued resistors (R_0, R_1, R_2, ..., R_n) which can be switched in or out of the divider with transistor switches. At any one instant, only one of the resistors is active in the divider, which means the transistor switch controlling that resistor is ON while all remaining transistor switches are OFF. The ON transistor is driven by the ON output from the command decode matrix, while the remaining switches are held OFF by corresponding decode matrix outputs.

The transistor switches must be operated in inverted connection (i.e.,
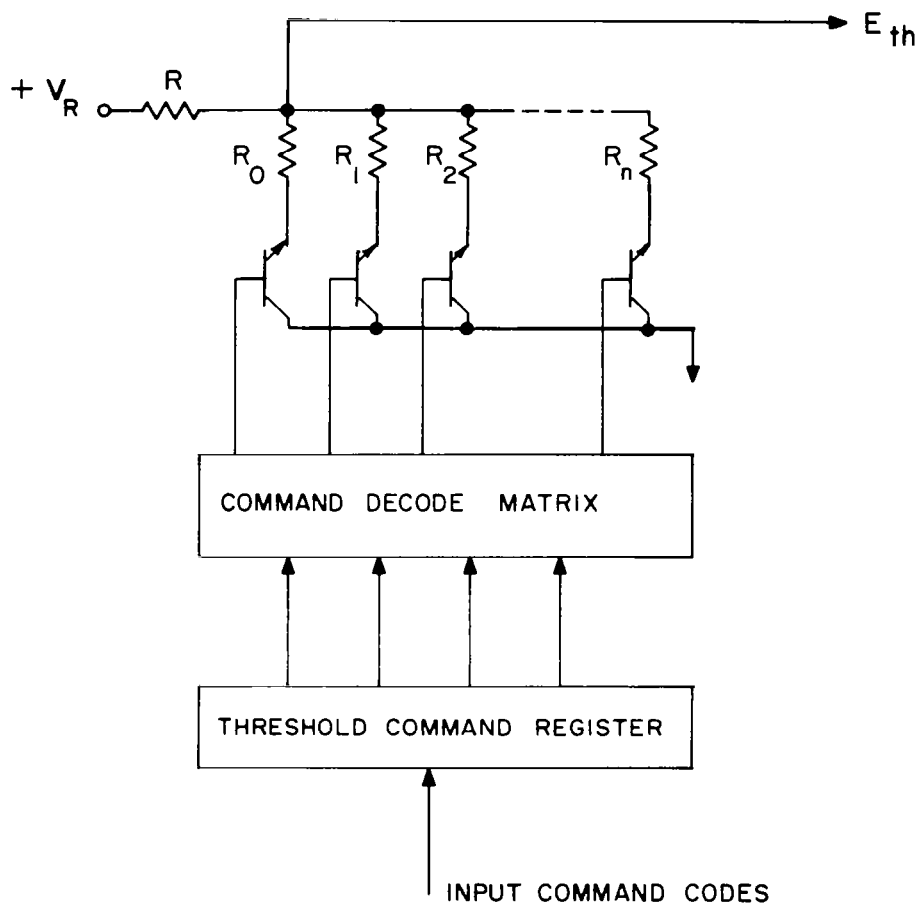
FIGURE 21: BLOCK DIAGRAM FOR AUTOMATING
THRESHOLD LEVEL

collector operated as emitter and vice versa) so the typical 1 to 3 milli-volt inverted emitter-collector saturation voltage can be neglected.

Calculation of the values for the divider components is relatively simple. To prevent loading of the divider output, the amplifier input impedance must be much greater than the equivalent divider output resistance.

Figure 21 shows a matrix for decoding the command codes stored in the command register. The matrix consists of an interconnection of logic gates which converts each combination of binary coded input signals into a unique signal at one of the matrix output terminals. The number of logic gates required to perform the decoding is fixed by the number of subdivisions of the star magnitude intervals.

Figure 22 shows a possible distribution of 2^4 = 16 subdivisions of the interval from star magnitude 0 to star magnitude 4. The decoding matrix has 2^4 = 16 outputs. Sixteen subdivisions were chosen because 16 is a power of 2 and also because 16 subdivisions would provide considerable resolution. More resolution could be obtained by assigning 2^5 = 32 sub-intervals, but the decoding logic increases in complexity.

In Figure 22, twice as many subdivisions were arbitrarily assigned between star magnitudes 3 and 4 than between star magnitudes 2 and 3 because the latter interval has approximately one-half as many stars in the celestial sphere as the interval between magnitudes 3 and 4. Figure 22 also shows a binary code assignment for the threshold commands which can be used for control of the star pulse detection threshold.

Figure 21 shows a threshold command register which stores the

Star Magnitude	Subdivision of Magnitude Intervals	n	Binary Coding
0	————————		————
	——	15	1111
1	————————	14	0111
	——	13	1011
2	————————	12	0011
	——	11	1101
	——	10	0101
	——	9	1001
3	————————	8	0001
	——	7	1110
	——	6	0110
	——	5	1010
	——	4	0010
	——	3	1100
	——	2	0100
	——	1	1000
4	————————	0	0000

Figure 22: A Subdivision of the Star Magnitude Intervals

threshold commands during decoding. For space applications, the input codes

to the threshold command register can be recieved from a ground tracking

station via telemetry or can be logically generated internally from a counter

which counts the number of star transits per scan.

4. Measurement of Signal Intensity

To assist in star pattern recognition for determination of sensor point-

ing direction, it is desirable to know the relative intensities of the transited

stars. For long distance communication to Earth from space or for on-board

satellite computer computation, it is desirable to encode the relative

intensity of each transited star.

A technique for star intensity encoding can be implemented with a dif-

ferential amplifier, Schmitt trigger, voltage divider, counter, and decoder

as shown in Figure 23. The Schmitt trigger level is set at .5 volt, with the

amplifier gain set at 2000. Initially, before a star pulse appears at the

positive (+) input terminal of the amplifier, the four stage binary counter

must be reset to state 0000, causing the decode matrix output to appear at

terminal L_0. Resister R_0 is switched into the voltage divider. When the star

pulse appears at the positive amplifier input, the amplifier output will be

negative initially, because the star pulse is less than the threshold formed

with R_0 in the voltage divider. As the star pulse increases and exceeds the

threshold by .25 millivolt, the amplifier output becomes .5 volt. The Schmitt

trigger will then step the binary counter; and the decode matrix will switch

R_1 into the voltage divider. This establishes a new threshold level which is

STAR PULSE

+

GAIN=2000

DIFFERENTIAL
INPUT OPERATIONAL
AMPLIFIER

SCHMITT
TRIGGER—
LEVEL=.5 VOLTS

$+ V_R$

R_0 R_1 R_2 R_{14} R_{15}

L_0 L_1 L_2 L_{14} L_{15}

DECODE MATRIX

4 STAGE BINARY COUNTER

COUNTER STEP

COUNTER
RESET

MONOSTABLE
NEGATIVE
TRIGGER

MONOSTABLE
POSITIVE
TRIGGER

PULSE DURATION
TWICE STAR
TRANSIT TIME
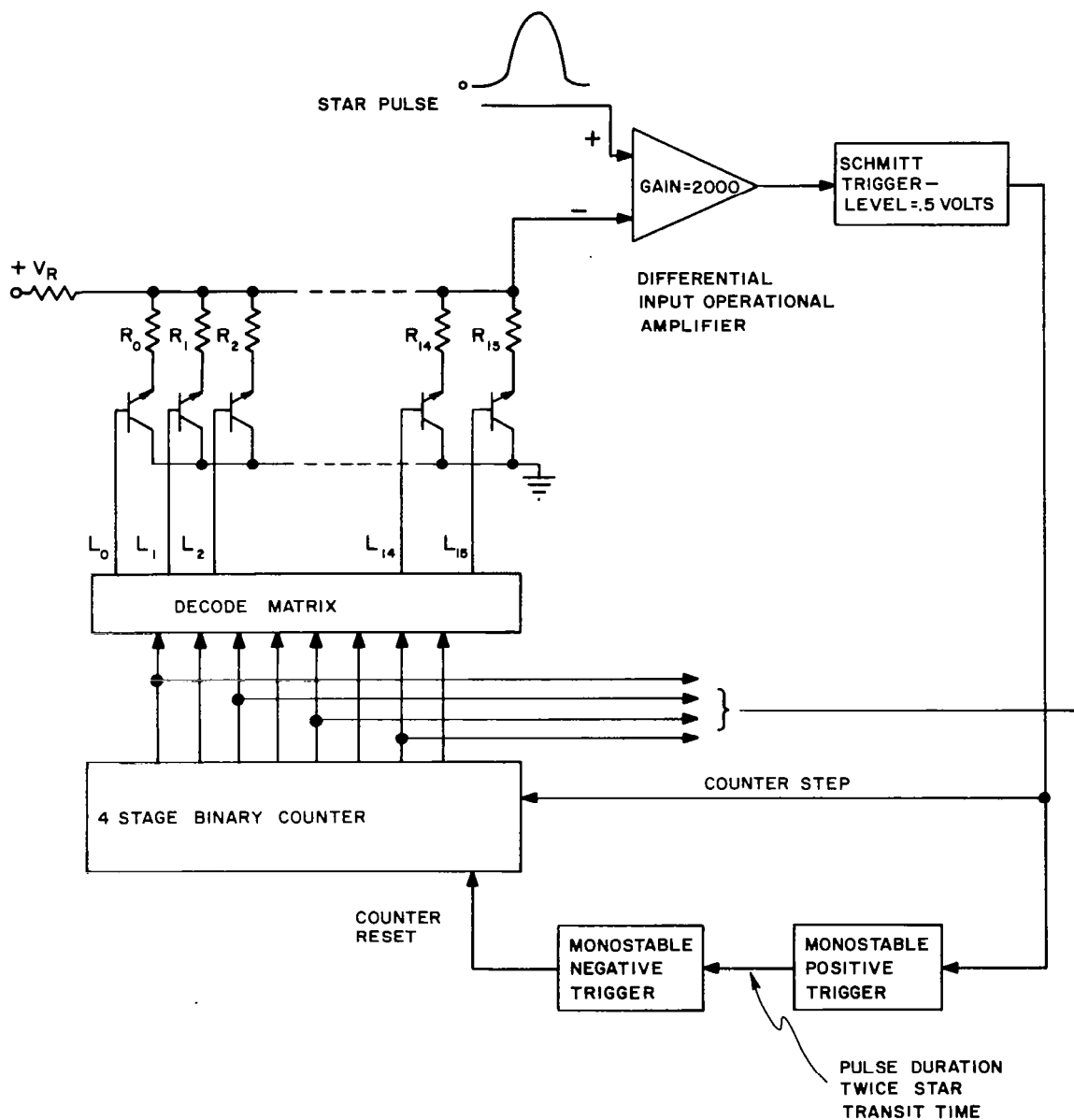
FIGURE 23 : BLOCK DIAGRAM FOR ENCODING OF STAR INTENSITY

greater than the previous level. This level change occurs before the star

pulse can change substantially since the circuit response time is much less

than the rise time of the star pulse. If the star pulse continues to increase,

it will again exceed the new threshold by .25 millivolt. The Schmitt trigger

switches again and steps the counter to the next state. If the star pulse

does not increase beyond the newest threshold set by the voltage divider, the

Schmitt trigger will not trigger and the counter will rest in the state which

is the binary encoded equivalent of the star pulse amplitude. After a delay

equal to twice the duration of the star pulse, starting when R_1 is switched

into the divider, the counter contents are gated into a storage register.

The counter is reset for the next star pulse.

The resolution of the encoded intensity is determined by the number of

stages in the counter. Figure 23 shows a four stage counter and $2^4 = 16$

levels of encoding. A typical encoding schedule for 16 levels is shown in

Figure 22. More resolution can be obtained by adding more counter states,

i.e., adding more bits in the coee. Increasing the resolution increases the

complexity of the decoding matrix, but the resolution is ultimately limited

by the relative noise level and the temperature stability of the electronics.

F. Special Derivation

To simplify the preceding discussion, several derivations have been put in this subsection. They are arranged in the order they appear in the section.

1. Optimality of Likelihood Ratio Detection Technique

A detection technique is characterized by a sequence of sets ω_2, ω_4, ... , ω_{2N}, ... in Euclidean space of two dimensions, four dimensions, ... , 2N dimensions, etc. If N pulses are observed, a star is present when

$$\left(v_1, v_2, \cdots, v_N, b_1, \cdots, b_N\right) \in \omega_{2N} \quad .$$

Let $\underset{\sim}{X}$ denote this 2N-vector. The probability of a type I error is

$$\sum_{N=1}^{\infty} \int_{\omega_{2N}} \mathcal{L}(N, \underset{\sim}{x} \mid 0, t_s) \, d\underset{\sim}{x} = P$$

and the probability of detection is

$$\sum_{N=1}^{\infty} \int_{\omega_{2N}} \mathcal{L}(N, \underset{\sim}{x} \mid I_{so}^{*}, t_s) \, d\underset{\sim}{x} .$$

Let ω_{2N}^{*} be the set such that

$$\frac{\mathcal{L}(N, \underset{\sim}{x} \mid I^*_{s_0}, t_s)}{\mathcal{L}(N, \underset{\sim}{x} \mid 0, t_s)} \geqslant C_P$$

where Cp is selected so that

$$\sum_{N=1}^{\infty} \int_{\omega^*_{2N}} \mathcal{L}(N, \underset{\sim}{x} \mid 0, t_s) \, d\underset{\sim}{x} = P.$$

The sequence ω^*_2, ω^*_4, ... defines a detection technique that minimizes

the probability of a type II error, and hence maximizes the probability

of detection. Let $\bar{\omega}_{2N}$ denote the compliment of ω_{2N}. Then

$$\sum_{N=1}^{\infty} \int_{\omega^*_{2N} \cap \omega_{2N}} \mathcal{L}(N, \underset{\sim}{x} \mid 0, t_s) \, d\underset{\sim}{x} + \sum_{N=1}^{\infty} \int_{\omega^*_{2N} \cap \bar{\omega}_{2N}} \mathcal{L}(N, \underset{\sim}{x} \mid 0, t_s) \, d\underset{\sim}{x} = P =$$

$$\sum_{N=1}^{\infty} \int_{\omega_{2N} \cap \omega^*_{2N}} \mathcal{L}(N, \underset{\sim}{x} \mid 0, t_s) \, d\underset{\sim}{x} + \sum_{N=1}^{\infty} \int_{\omega_{2N} \cap \overline{\omega^*_{2N}}} \mathcal{L}(N, \underset{\sim}{x} \mid 0, t_s) \, d\underset{\sim}{x}.$$

and hence

$$\sum_{N=1}^{\infty} \int_{\omega^*_{2N} \cap \bar{\omega}_{2N}} \mathcal{L}(N, \underset{\sim}{x} \mid 0, t_s) \, d\underset{\sim}{x} = \sum_{N=1}^{\infty} \int_{\omega_{2N} \cap \overline{\omega^*_{2N}}} \mathcal{L}(N, \underset{\sim}{x} \mid 0, t_s) \, d\underset{\sim}{x}.$$

The probability of detection using ω^*_{2N} is

$$\sum_{N=1}^{\infty} \int_{\omega_{2N}^* \cap \omega_{2N}} \mathcal{L}(N, \underset{\sim}{x} \mid I_{so}^*, t_s) \, d\underset{\sim}{x} + \sum_{N=1}^{\infty} \int_{\omega_{2N}^* \cap \overline{\omega}_{2N}} \mathcal{L}(N, \underset{\sim}{x} \mid I_{so}^*, t_s) \, d\underset{\sim}{x} \geqslant$$

$$\sum_{N=1}^{\infty} \int_{\omega_{2N}^* \cap \omega_{2N}} \mathcal{L}(N, \underset{\sim}{x} \mid I_{so}^*, t_s) \, d\underset{\sim}{x} + \sum_{N=1}^{\infty} C_P \int_{\omega_{2N}^* \cap \overline{\omega}_{2N}} \mathcal{L}(N, \underset{\sim}{x} \mid 0, t_s) \, d\underset{\sim}{x} =$$

$$\sum_{N=1}^{\infty} \int_{\omega_{2N}^* \cap \omega_{2N}} \mathcal{L}(N, \underset{\sim}{x} \mid I_{so}^*, t_s) \, d\underset{\sim}{x} + \sum_{N=1}^{\infty} C_P \int_{\omega_{2N} \cap \overline{\omega}_{2N}^*} \mathcal{L}(N, \underset{\sim}{x} \mid 0, t_s) \geqslant$$

$$\sum_{N=1}^{\infty} \int_{\omega_{2N}^* \cap \omega_{2N}} \mathcal{L}(N, \underset{\sim}{x} \mid I_{so}^*, t_s) \, d\underset{\sim}{x} + \sum_{N=1}^{\infty} \int_{\omega_{2N} \cap \overline{\omega}_{2N}^*} \mathcal{L}(N, \underset{\sim}{x} \mid I_{so}^*, t_s) \, d\underset{\sim}{x} =$$

$$\sum_{N=1}^{\infty} \int_{\omega_{2N}} \mathcal{L}(N, \underset{\sim}{x} \mid I_{so}^*, t_s) \, d\underset{\sim}{x}.$$

Therefore, ω_2^*, ω_4^*, ... maximizes the probability of detection.

2. Mean of X" (t_s)

The mean of X"(t_s) is evaluated for a Gaussion-shaped impulse response.

The basic equation is

$$E \, X''(t_s) = -2^{5/2} \pi^{3/2} \, \overline{a'} A I_s^* \, \frac{w_o}{f_o} \int_{-\infty}^{\infty} f \, \sin(\pi f T_s) \, \bar{e}^{\beta f^2} df \, ,$$

where

$$\beta = 2\pi^2 \sigma^2 + \frac{2\pi^2}{f_o^2} \quad .$$

The interval can be evaluated by parts,

$$\int_{-\infty}^{\infty} f \, \sin(\pi f T_s) \, \bar{e}^{\beta f^2} df = \frac{\pi T_s}{2\beta} \int_{-\infty}^{\infty} \cos(\pi f T_s) \, \bar{e}^{\beta f^2} df =$$

$$\frac{T_s}{2} \left(\frac{\pi}{\beta} \right)^{3/2} \exp\left(-\frac{\pi^2 T_s^2}{4\beta} \right) \quad .$$

Hence

$$E \, X''(t_s) = -\overline{a'} A I_s^* \, w_o \, \frac{1}{f_o T_s^2} \, C^{3/2} \, \bar{e}^{-C/8}$$

where

$$C = \frac{(f_o T_s)^2}{1 + (f_o \sigma)^2} \quad .$$

3.   Variance of $X'(t_s)$

The basic equation for Var $X'(t_s)$ is given in VI.C.1. It involves three indefinite integrals. The first integral is

$$I_1 = \int_{-\infty}^{\infty} G(t) \, w_o^2 \, (t + f_o^2)^2 \, e^{-(t + f_o)^2} \, dt ,$$

where

$$G(t) = \Phi\left(\frac{t}{\sigma} + \frac{T_s}{2\sigma}\right) - \Phi\left(\frac{t}{\sigma} - \frac{T_s}{2\sigma}\right) .$$

Integrating by parts, one obtains

$$I_1 = -\frac{(w_o f_o)^2}{2}\left[G(t) \, t \, e^{-(t + f_o)^2} \Big|_{-\infty}^{\infty} - \int_{-\infty}^{\infty} G(t) \, e^{-(t + f_o)^2} \, dt \right.$$

$$\left. - \int_{-\infty}^{\infty} t \, G'(t) \, e^{-(t + f_o)^2} \, dt \right] =$$

$$\frac{(w_o f_o)^2}{2}\left[\int_{-\infty}^{\infty} g(f) \, \frac{\sqrt{\pi}}{f_o} \, e^{-(\pi f / f_o)^2} \, df \; + \right.$$

$$\int_{-\infty}^{\infty} t \, \phi\left(\frac{t}{\sigma} + \frac{T_s}{2\sigma}\right) \frac{1}{\sigma} \, e^{-(t + f_o)^2} \, dt \; - \int_{-\infty}^{\infty} t \, \phi\left(\frac{t}{\sigma} - \frac{T_s}{2\sigma}\right) \frac{1}{\sigma} \, e^{-(t + f_o)^2} \, dt \left. \right] =$$

$$\frac{(w_o f_o)^2}{2} \left[\int_{-\infty}^{\infty} \frac{\sin(\pi f T_s)}{\pi f} e^{2(\pi f \sigma)^2} \frac{\sqrt{\pi}}{f_o} e^{-(\pi f/f_o)^2} df \right.$$

$$+ \int_{-\infty}^{\infty} t \frac{1}{\sqrt{2\pi}} e^{-\frac{1}{2}\left(\frac{t}{\sigma} + \frac{T_s}{2\sigma}\right)^2} \frac{1}{\sigma} e^{-(t f_o)^2} dt$$

$$\left. - \int_{-\infty}^{\infty} t \frac{1}{\sqrt{2\pi}} e^{-\frac{1}{2}\left(\frac{t}{\sigma} - \frac{T_s}{2\sigma}\right)^2} \frac{1}{\sigma} e^{-(t f_o)^2} dt \right].$$

The first term is the integral of $\measuredangle$ (f) with σ^2 replaced by

$$\left(\sigma^2 + \frac{1}{2 f_o^2} \right)^{1/2}$$

The second and third terms are means of normal random variables. Hence

$$I_1 = \frac{(w_o f_o)^2}{2} \left\{ \frac{\sqrt{\pi}}{f_o} \left[\Phi\left(\frac{T_s}{2\sqrt{\sigma^2 + 1/2 f_o^2}} \right) - \Phi\left(\frac{-T_s}{2\sqrt{\sigma^2 + 1/2 f_o^2}} \right) \right] \right.$$

$$\left. - \frac{T_s}{(1 + 2\sigma^2 f_o^2)^{3/2}} \exp\left(-\frac{1}{4} \frac{(T_s f_o)^2}{1 + 2(\sigma f_o)^2} \right) \right\} = w_o^2 f_o F_1 (T_s f_o, \sigma f_o).$$

The second integral in Var X' (t_s) is

$$I_2 = \frac{8\pi w_0^2}{f_0^2} \int_{-\infty}^{\infty} \sin^2(\pi f T_s)\, e^{-4\pi^2(\sigma^2 + f_0^{-2})f^2}\, df$$

$$= \frac{4\pi w_0^2}{f_0^2} \int_{-\infty}^{\infty} [1 - \cos(2\pi f T_s)]\, e^{-4\pi^2(\sigma^2 + f_0^{-2})f^2}\, df$$

$$= \frac{2\pi w_0^2}{f_0 \sqrt{1 + \sigma^2 f_0^2}} \left[1 - \frac{1}{2\sqrt{\pi}}\, \exp\left(-\frac{1}{4}\, \frac{T_s^2 f_0^2}{1 + \sigma^2 f_0^2}\right) \right]$$

$$= w_0^2 T_s\, F_2(T_s f_0, \sigma f_0).$$

The third integral in Var X'(t_S) is·

$$I_3 = \frac{8\pi^3 w_o^2}{f_o^2} \int_{-\infty}^{\infty} f^2 e^{-(2\pi f/f_o)^2} df = \frac{\sqrt{\pi}}{2} w_o^2 f_o \; .$$

Combining these integrals one obtains the required result.

$$\text{Var } X'(t_s) = \overline{a'^2} A I_s^* w_o^2 f_o F_1(T_s f_o, \sigma f_o)$$

$$+ \overline{a'}^2 A \overline{I_b^{*2}} \nu \frac{w_o^2}{f_o} F_2(T_s f_o, \sigma f_o)$$

$$+ \frac{\sqrt{\pi}}{2} \left[\overline{a'^2} A (\overline{I_b^4} \nu T_s + \Psi I_o^*) + \overline{d'^2} I_d \right] w_o^2 f_o$$

4. Variance of X (t)

The basic equation for the variance of X (t) is

$$\text{Var } X(t) = A I_s^* \,\overline{a'^2} \int_{-\infty}^{\infty} G(t')\left[w(t-t_s-t')\right]^2 dt'$$

$$+ \,\overline{a'}^2 A^2 \,\overline{I_b^{*2}}\, \nu \int_{-\infty}^{\infty} |W(f)|^2\, |\mathcal{Y}(f)|^2 df$$

$$+\left[\,\overline{a'^2} A \left(\overline{I_b^*}\,\nu T_s + \Psi I_o^*\right) + \overline{d'^2} I_d\right] \int_{-\infty}^{\infty} |W(f)|^2 df \, .$$

The integral in the first term can be evaluated by using Parseval's

theorem:

$$\int_{-\infty}^{\infty} G(t'-t+t_s)\, w_o\, e^{-(t'f_o)^2} dt' =$$

$$\int_{-\infty}^{\infty} \frac{1}{\pi f} \sin(\pi f T_s)\, e^{-2(\pi f \sigma)^2} e^{i 2\pi f(t_s-t)} \frac{\sqrt{\pi}\, w_o^2}{f_o}\, e^{-\pi^2 f^2/f_o^2}\, df =$$

$$\frac{\sqrt{\pi}\, w_o^2}{2 f_o}\left[\Phi\!\left(\frac{T_s f_o/2 - (t-t_s)f_o}{\sqrt{1/2 + \sigma^2 f_o^2}}\right) - \Phi\!\left(-\,\frac{T_s f_o/2 - (t-t_s) f_o}{\sqrt{1/2 + \sigma^2 f_o^2}}\right)\right.$$

$$\left. +\, \Phi\!\left(\frac{T_s f_o/2 + (t-t_s)f_o}{\sqrt{1/2 + \sigma^2 f_o^2}}\right) - \Phi\!\left(-\,\frac{T_s f_o/2 + (t-t_s) f_o}{\sqrt{1/2 + \sigma^2 f_o^2}}\right)\right]$$

$$= \frac{w_o^2}{f_o}\, F_3\left[T_s f_o,\, \sigma f_o,\, (t-t_s)f_o\right]\, .$$

The last step uses the Fourier transform $\aleph(f)$. Next consider the integral in the second term of Var X (t); it can be rewritten as

$$\frac{\sqrt{2\pi}\,w_0 T_s}{f_0^2 \sqrt{2(f_0^{-2}+\sigma^2)}} \int_{-\infty}^{\infty} \frac{1}{\pi^2 f^2 T_s} \sin^2(\pi f T_s)$$

$$\cdot \sqrt{2\pi}\,w_0 \sqrt{2(f_0^{-2}+\sigma^2)}\; e^{-4\pi^2 f^2 (\sigma^2 + f_0^{-2})}\, df$$

$$= \frac{2\sqrt{2\pi}\,w_0 T_s}{f_0^2 \sqrt{2(f_0^{-2}+\sigma^2)}} \int_{-T_s}^{0} \left(1+\frac{t}{T_s}\right) w_0\, e^{-\frac{1}{4}t^2/(f_0^{-2}+\sigma^2)}\, dt$$

$$= \frac{4\pi w_0^2 T_s}{f_0^2}\left[\frac{1}{2} - \Phi\!\left(\frac{-T_s f_0}{\sqrt{2(1+\sigma^2 f_0^2)}}\right)\right]$$

$$-\frac{2\sqrt{2\pi}\,w_0^2}{f_0^3}\sqrt{2(1+\sigma^2 f_0^2)}\left[1 - \exp\!\left(\frac{-T_s^2 f_0^2}{4(1+\sigma^2 f_0^2)}\right)\right]$$

$$= \frac{w_0^2}{f_0^3}\, F_4(T_s f_0,\, \sigma f_0).$$

The last integral in the expression for Var X (t) can be directly

$$\int_{-\infty}^{\infty} |\mathcal{W}(f)|^2 df = \int_{-\infty}^{\infty} w_o^2 \, \bar{e}^{(tf_o)^2} \, dt = \frac{w_o^2}{f_o} \sqrt{\pi}$$

5. Mean of X' (t)

The basic steps in the evaluation are

$$E X'(t) = -2\pi A I_s^* \bar{a}' \int_{-\infty}^{\infty} f \, \sin[2\pi f(t-t_s)] \, \mathcal{Y}(f) \, \mathcal{W}(f) \, df$$

$$= A I_s^* \bar{a}' \int_{-\infty}^{\infty} \cos[2\pi f(t-t_s+T_s/2)] \, e^{-2(\pi f \sigma)^2} \mathcal{W}(f) \, df$$

$$- A I_s^* \bar{a}' \int_{-\infty}^{\infty} \cos[2\pi f(t-t_s-T_s/2)] \, e^{-2(\pi f \sigma)^2} \mathcal{W}(f) \, df$$

$$= \frac{A I_s^* \bar{a}'}{\sqrt{1+\sigma^2 f_o^2}} \left\{ \exp\left[-\frac{f_o^2 (t-t_s+T_s/2)^2}{2(1+\sigma^2 f_o^2)}\right] \right.$$

$$\left. - \exp\left[-\frac{f_o^2 (t-t_s-T_s/2)^2}{2(1+\sigma^2 f_o^2)}\right] \right\}$$

6. Covariance Between X (t_1) and X (t_2).

Using the fact that the impulse response is Gaussian, one can express

the covariance between $X(t_1)$ and $X(t_2)$ in terms of the variance function. In particular

$$Cov[X(t_1), X(t_2)] = \overline{a'^2} \int_{-\infty}^{\infty} \mu(\tau)\, w(t_1 - \tau)\, w(t_2 - \tau)\, d\tau,$$

but

$$w(t_1 - \tau)\, w(t_2 - \tau) = w_0^2 \exp\left[-\frac{1}{2} f_0^2 (t_1 - \tau)^2 - \frac{1}{2} f_0^2 (t_2 - \tau)^2\right]$$

$$= w_0^2 \exp\left[-f_0^2 \left(\tau - \frac{t_1 + t_2}{2}\right)^2\right]$$

$$\cdot \exp\left[-\frac{f_0^2 (t_1 - t_2)^2}{4}\right]$$

$$= \left[w\left(\frac{t_1 + t_2}{2} - \tau\right)\right]^2 \exp\left[-\frac{f_0^2 (t_1 - t_2)^2}{4}\right].$$

Therefore,

$$Cov[X(t_1), X(t_2)] = \overline{a'^2} \exp\left[-\frac{f_0^2 (t_1 - t_2)^2}{4}\right] \int_{-\infty}^{\infty} \mu(\tau)\left[w\left(\frac{t_1 + t_2}{2} - \tau\right)\right]^2 d\tau$$

$$= \exp\left[-\frac{f_0^2 (t_1 - t_2)^2}{4}\right] Var\, X\left(\frac{t_1 + t_2}{2}\right)$$

7.   Variance of X'(t)

The basic equation for the variance of X'(t) is

$$
\text{Var } X'(t) = \overline{a'^2} A I_s^* \int_{-\infty}^{\infty} G(t') \left[w'(t - t_s - t') \right]^2 dt'
$$

$$
+ \overline{a'}^2 A^2 \overline{I_b^{*2}} \, v \int_{-\infty}^{\infty} (2\pi f)^{2j} \, |\mathcal{Y}(f)|^2 \, |\mathcal{W}(f)|^2 \, df
$$

$$
+ \left[\overline{a'^2} A (\overline{I_b^*} \, v T_s + \Psi I_o^*) + \overline{d'^2} I_d \right] \int_{-\infty}^{\infty} (2\pi f)^{2j} \, |\mathcal{W}(f)|^2 \, df.
$$

The last two terms are the same as the last two terms of Var X'(t$_s$),
which are evaluated in VI. F.3. The first term of Var X'(t) is
evaluated similar to the way in which the first term of Var X' (t$_s$)
was evaluated.

VII. MULTIPLE OBSERVATION TECHNIQUES

Multiple observation techniques can be used to reduce the uncertainty in the measured image position and intensity, and to reduce the number of false star detections. By "combining" several position measurements, we can obtain an accurate estimate of the image position. Accurate intensity measurements facilitate recognition of the star pattern. Sporatic false-star detections (detections resulting from photomultiplier dark current, ambient radiation, and electronic noise) significantly complicate the star pattern recognition.

There are basically two techniques: multiple scan and multiple slit. The first technique "combines" data obtained from several successive scans with a single slit. The second technique "combines" data obtained from several closely spaced slits crossing a star image, in one scan period. In sophisticated systems these techniques can be combined. By directly averaging (or correlating) the multiple observations, we can minimize the variance of the position and intensity measurements. On the other hand, data averaging requires holding-registers, special gating and timing, etc. In some applications, the hardware required for this averaging is not warranted. Sufficient accuracy is obtained if the data is converted into a binary sequence of ones and zeros, where a one indicates the presence of a star. Using binary techniques, we lose all intensity information.

In addition to accuracy and detection requirements, we must consider several physical restrictions. Limitations on weight, size, and power restrict the complexity of the electronics that can be in the system. Precession and

nutation of a satellite complicate the signal processing. If these motions
are large, multiple scan techniques are not practical. In addition, we must
consider the capacity of the communication channel for ground-based processing
of satellite data. These physical restrictions are important factors in
selecting a multiple observation technique; in some applications they dominate
the selection.

The technique described by Kenimer and Walsh (1964) uses a single scan
with a multiple slit. A recent program at Control Data has involved the
fabrication and test of a celestial sensing system, which is discussed in
Section I. Several multiple observation techniques were investigated. For
a detailed description see "Final Report: Feasibility Investigation of a
Wide Angle Celestial Reference for Space Navigation," submitted to Air Force
Avionics Laboratory, Wright-Patterson Air Force Base, Contract No. AF 33(615)-
1428.

In the following paragraphs we compare a single-slit multiple-scan
technique using averaging to a single-slit multiple-scan technique using
binary sequences. In particular, we compare expected numbers of weak star
detections. In subsection B, the design of coded multiple slits is discussed.
In the last subsection, C, we briefly describe the effect of vehicle motion
on the attitude measurement and results of task 5 in this study.

A.   Scan-to-Scan Comparison

In this section we will compare three methods of star detection. Consider the system illustrated in Figure 1. Assume that the direction of the spin axis is fixed and that the scan period is one second. Thus, a star centered in the slit at time t, will be centered in the slit at time t+1 seconds. The detection electronics is illustrated on page III-13.

The number of pulses in the holding filter, y(t), resulting from a star in the center of the slit at time t, is assumed to be random with mean[*]

$$\mu = \alpha \, \epsilon_0 \, \epsilon_q \left[\; \lambda_s \int_{-\frac{T_f}{2}}^{\frac{T_f}{2}} G(x) \, dx \; + \; \lambda_b T_f \right] + \; \alpha \, T_f \, \lambda_d$$

where α = fraction of photoelectric pulses transmitted by threshold clamp

ϵ_0 = optical efficiency of lens system

ϵ_q = quantum efficiency of photomultiplier

λ_b = average number of photons received from the background per second

λ_d = dark current expressed in equivalent number of photoelectrons per second

λ_s = average number of photons received from a star per second

T_f = time duration of holding filter

T_s = time for star to cross slit

$$G(t) = \Phi\left(\frac{t}{\sigma} + \frac{T_s}{2\sigma}\right) - \Phi\left(\frac{t}{\sigma} - \frac{T_s}{2\sigma}\right)$$

$$\Phi(x) = \frac{1}{\sqrt{2\pi}} \int_{-\infty}^{x} e^{-\frac{1}{2}s^2} \, ds$$

---

[*]   For derivation see Farrell and Zimmerman (1965) pp. 641-644.

PHOTO-MULTIPLIER
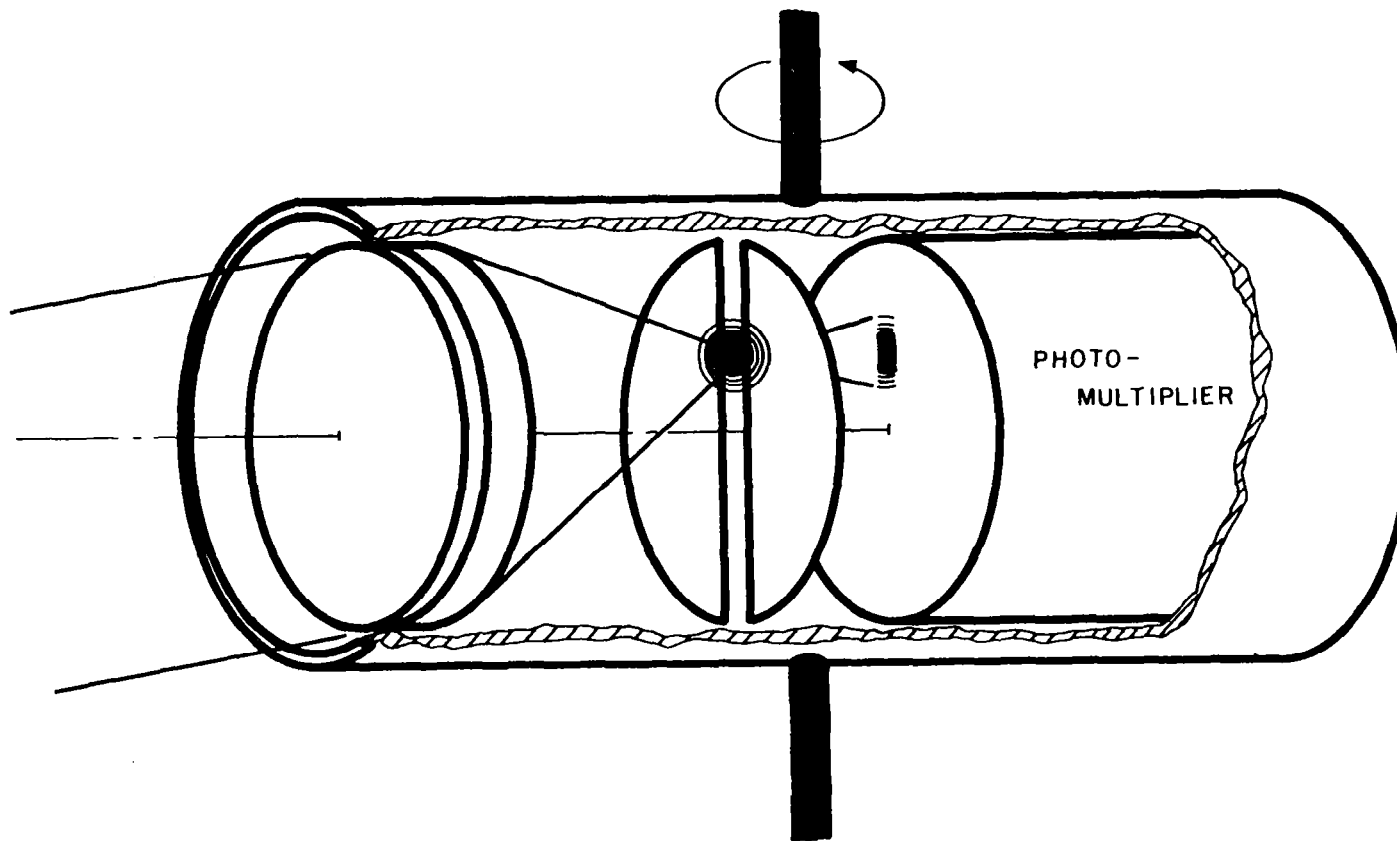
FIGURE I: SCANNING SYSTEMS

The three methods of star detection are:

Simple Method--A star detection occurs when $y(t) > \tau$.

Compare Method--A star detection occurs when $y(t-1) > \tau$ and $y(t) > \tau$.

Sum Method--A star detection occurs when $y(t) + y(t-1) > \tau$.

In order to compare these three methods, the detection threshold τ is selected so that the probability of detecting a star of fourth magnitude is .9. The following quantities will be computed:

(1) $\Pr\left\{y(t) > \tau \,/\, n^{th} \text{ magnitude star in slit at time } t\right\}$ (n = 2, 3, ...7).

(2) Expected number of star detections of nth magnitude in a one second scan. (n = 3, 4, ... 7).

For the Simple Method the probability of detecting a star that is in the center of the slit at time t is

$$P_\tau = \sum_{k=\tau+1}^{\infty} p_k$$

where p_k is the probability of k pulses in holding filter when filter is centered on the signal. Note that

$$p_k = \frac{\mu^k}{k!} e^{-\mu}$$

If we assume that the slit passes eighty percent of the star radiation when the image is centered in the slit and $T_f = T_s$, then

$$G(0) = .8 \qquad\qquad T_s/2\sigma = 1.28$$

$$\frac{1}{T_s} \int_{-\frac{T_f}{2}}^{\frac{T_f}{2}} G(x)\,dx = .69$$

VII-5

Hence,

$$\mu = \alpha T_s \left\{ \epsilon_o \epsilon_q \left[(.69) \lambda_s + \lambda_b \right] + \lambda_d \right\}$$

In order to evaluate (1) and (2) a particular system must be considered.

Let α = 1

ϵ_o = .8

ϵ_q = .1

λ_d = 8000 pulses per second

slit width = 2.4 minutes of arc

slit length = 4 degrees

background = 100 tenth magnitude stars per square degree

Then

$T_s = T_f = .107$ ms

$\lambda_b = .14$ pulses per second

Thus

$$\mu = (.107 \times 10^{-3}) \left\{ (.08) \left[(.69) \lambda_s + .14 \right] + 8 \times 10^3 \right\}$$

Tabulations of μ for stars of magnitude 1 through 9 appear in Table 1.

For the Simple Method and a star of fourth magnitude, the value of τ for which P_τ is closest to .9 is τ = 7. This value of τ is used to calculate P_τ for stars of other magnitudes. The General Electric Company (1962) has published a table of the Poisson distribution.

TABLE 1

MEAN NUMBER OF PULSES FROM STARS

Magnitude of Star	1	2	3	4	5	6	7	8	9
λ_s (photons/second	3.25×10^7	1.3×10^7	5×10^6	2×10^6	8.2×10^5	3.3×10^5	1.3×10^5	5.2×10^4	2.1×10^4
μ	192.6	77.6	30.4	12.7	5.7	2.805	1.623	1.164	.981

For the Compare Method, let

$$_1\pi_n = \text{Pr (detecting an } n^{th} \text{ magnitude star centered in the slit)}$$

Then

$$_1\pi_n = \text{Pr (detecting an } n^{th} \text{ magnitude star on first scan)}$$

$$\cdot \text{ Pr (detecting an } n^{th} \text{ magnitude star on second scan)}$$

$$= \left[\sum_{k=\tau+1}^{\infty} p_k \right]^2$$

The value of τ for which $_1\pi_4$ is closest to .9 is $\tau = 6$; $_1\pi_4 = .937$ for $\tau = 6$. This value of τ is used in evaluating $_1\pi_n$ for other values of n.* .

For the Sum Method, let $y_2(t) = y(t) + y(t-1)$. Assume $y(t)$, $y(t-1)$ are independent Poisson processes with common parameters $\mu(t)$. Then $y_2(t)$ is Poisson with parameter $2\mu(t)$. Let

$$_2\pi_n = \text{Pr (detecting a star of } n^{th} \text{ magnitude which is at the center of the slit at time t-1 and t)}$$

Then

$$_2\pi_n = \sum_{k=\tau+1}^{\infty} e^{-2\mu} \frac{(2\mu)^k}{k!}$$

The value of τ for which $_2\pi_4$ is closest to .9 is $\tau = 17$; $_2\pi_4 = .925$ for $\tau = 17$. This value of τ is used to evaluate $_2\pi_n$ for other values of n.

In one scan the slit covers 1440 square degrees. Based on data from

---

$*$ A convenient table of the Poisson distribution has been published by General Electric Company (1962).

Allen (1963) we can estimate the number of stars in the scanned region. See Table 2. The expected number of detections in one scan is the product of the number of stars and the probability of detection. The probability of detection and expected number of detections are presented in Table 3 and Figures 2, 3, and 4.

A comparison was also carried out for the system described in Table 3 of Section VIII (page VIII-36). The OPSCAN program was used to design the system using the Compare Method and the Simple Method of star detection. This was done for ten photomultipliers. Figures 5 and 6 indicate the results of this automatic design program by comparing the expected number of weak star detections and the aperture diameter as a function of photomultiplier and star detection method.

TABLE 2

DENSITY OF STARS

n	Number of Stars Per Square Degree Between Magnitudes $(n-\frac{1}{2},\ n+\frac{1}{2})$	Number of Stars Per Scan Between Magnitudes $(n-\frac{1}{2},\ n+\frac{1}{2})$
1	3.83×10^{-4}	.522
2	1.4×10^{-3}	2.02
3	4.9×10^{-3}	7.06
4	1.57×10^{-2}	22.6
5	4.75×10^{-2}	68.4
6	1.45×10^{-1}	209
7	3.9×10^{-1}	562
8	10.95×10^{-1}	1577
9	3.2	4608

TABLE 3

COMPARISON OF DETECTION METHODS

Star (n) Magnitude	Probability of Detection			Expected Number of Star Detections in One Scan			Expected Number of Star Detections of Magnitude $\geq$ n		
	Simple	Compare	Sum	Simple	Compare	Sum	Simple	Compare	Sum
1	1	1	1	.552	.552	.552	46.7	38.3	32.9
2	1	1	1	2.02	2.02	2.02	46.1	37.7	32.4
3	$1-4.4 \times 10^{-7}$	$1-6.4 \times 10^{-15}$	1	7.06	7.06	7.06	44.1	35.7	30.4
4	.93	.937	.925	20.3	20.3	20.3	37.1	28.6	23.3
5	.217	.12	4.4×10^{-2}	14.8	8.21	3.01	16.8	8.34	3.01
6	8.22×10^{-3}	6.05×10^{-4}	2.73×10^{-5}	1.72	1.26×10^{-1}	1.26×10^{-1}	1.70	1.27×10^{-1}	5.71×10^{-3}
7	2.87×10^{-4}	2.13×10^{-6}	$< 10^{-8}$	1.61×10^{-1}	1.20×10^{-3}	$<5.62 \times 10^{-6}$	2.50×10^{-1}	1.30×10^{-3}	$<5.62 \times 10^{-6}$
8	3.02×10^{-5}	4.45×10^{-8}	-	4.76×10^{-2}	7.02×10^{-5}	-	8.88×10^{-2}	9.55×10^{-5}	-
9	8.94×10^{-6}	5.48×10^{-9}	-	4.12×10^{-2}	2.53×10^{-5}	-	4.12×10^{-2}	2.53×10^{-5}	-

$\tau+1 = 8$ $\qquad$ $\tau+1 = 7$ $\qquad$ $\tau+1 = 8$
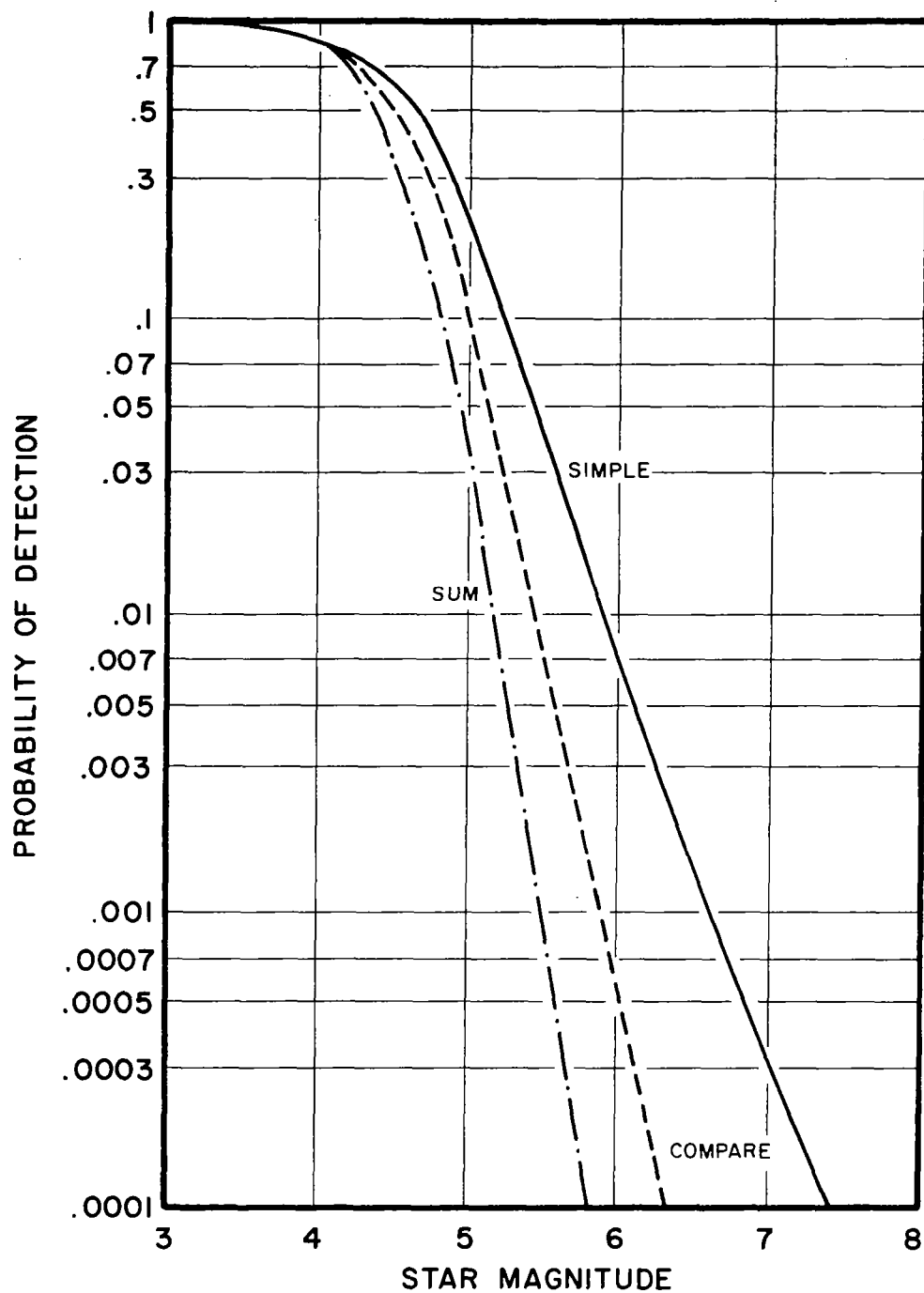
FIGURE 2: PROBABILITY OF STAR DETECTION
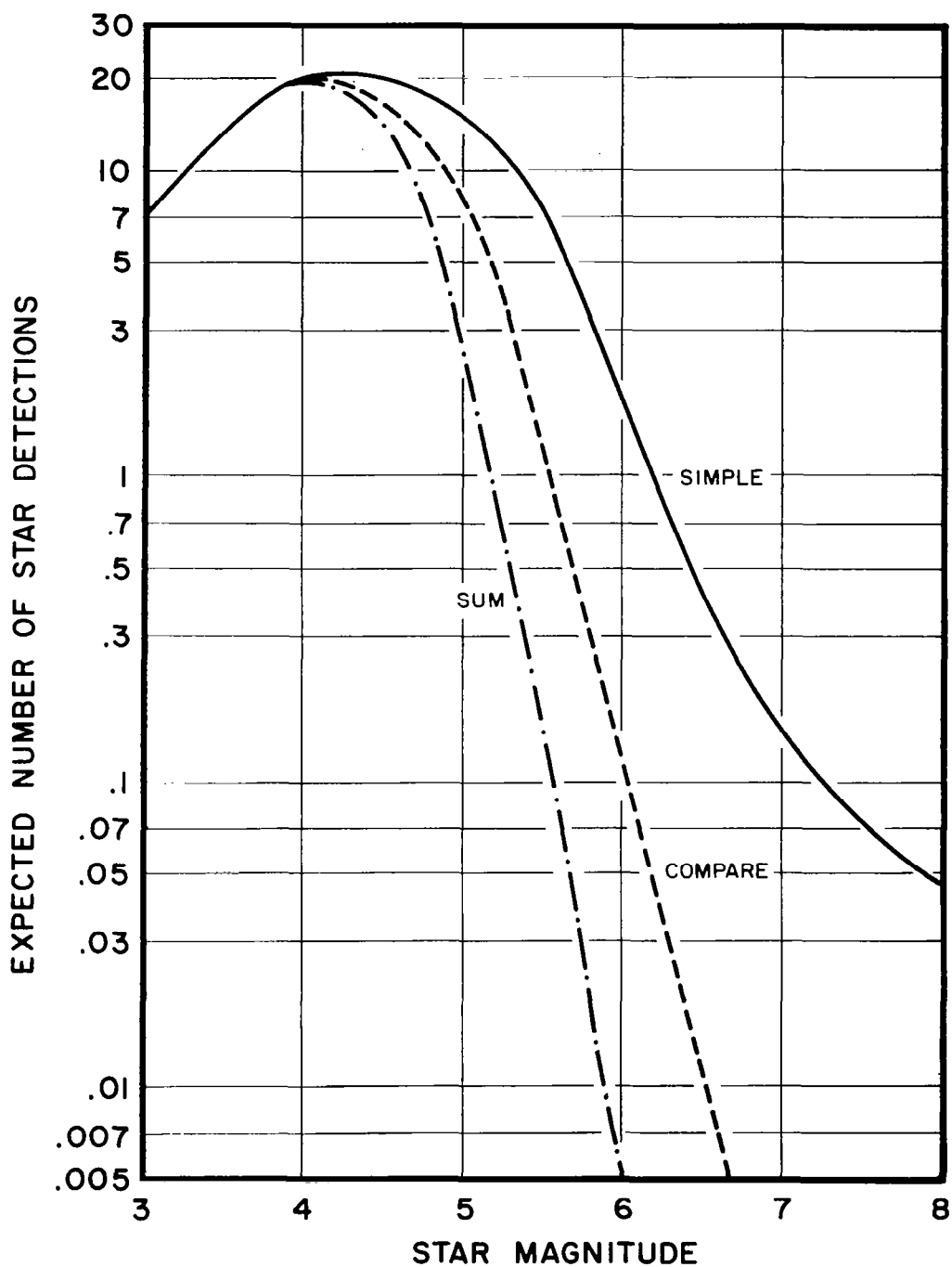
FIGURE 3: EXPECTED NUMBER OF STAR DETECTIONS
IN ONE SCAN
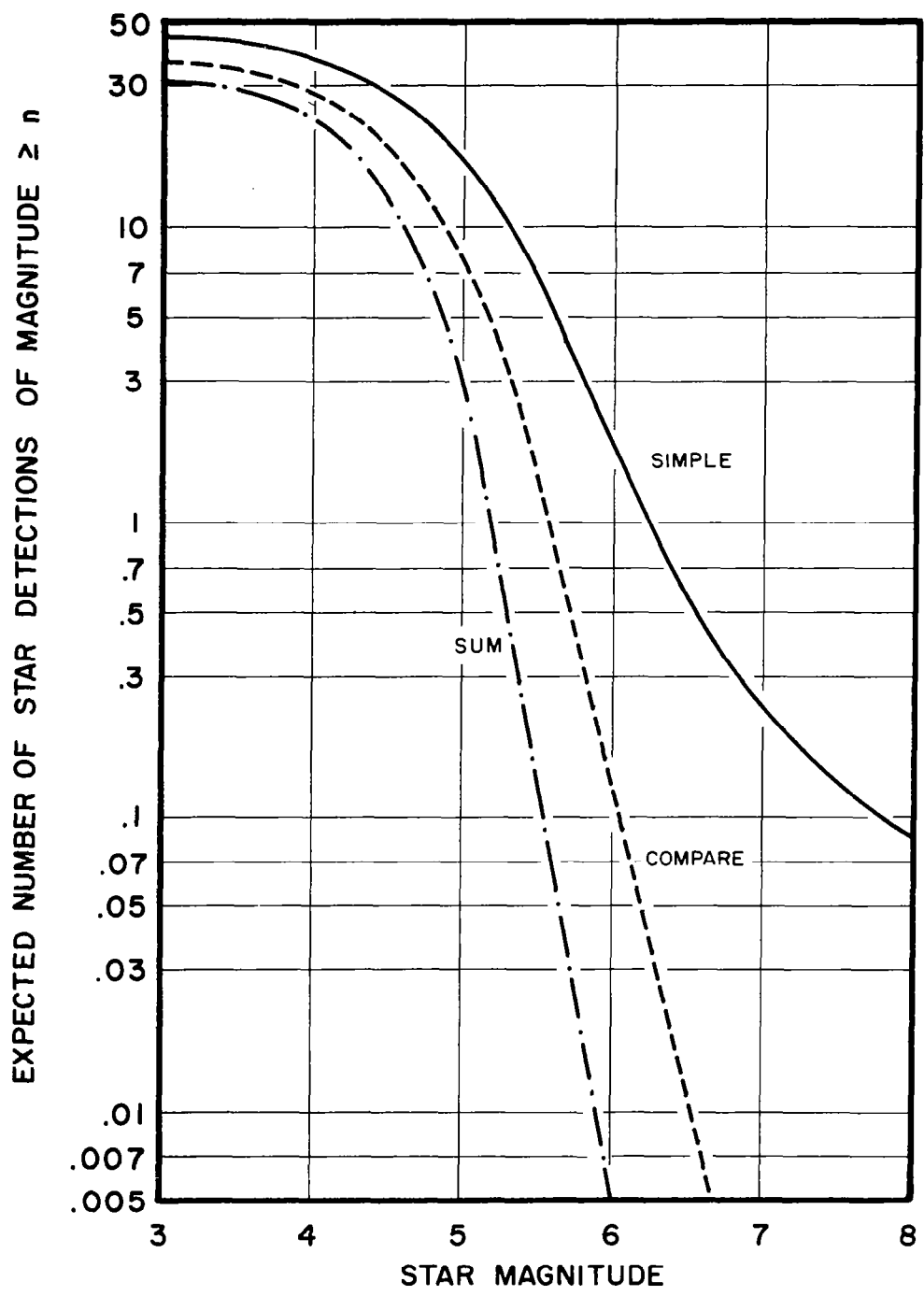
FIGURE 4: EXPECTED NUMBER OF STAR DETECTIONS
OF MAGNITUDE ≥ n
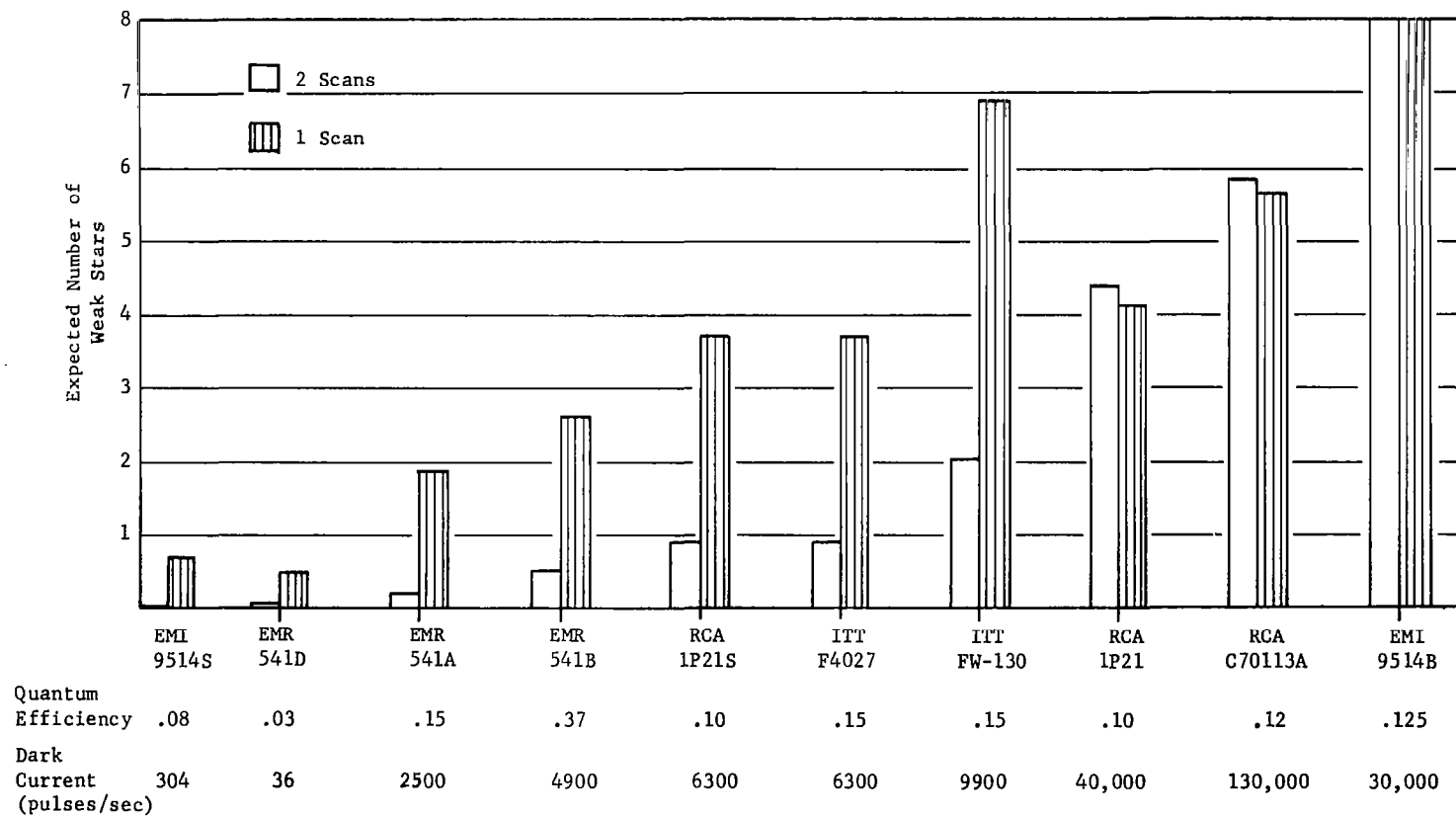
Figure 5: Expected Number of Weak Star Detections as a Function of
Photomultiplier and Detection Method

	EMI 9514S	EMR 541D	EMR 541A	EMR 541B	RCA 1P21S	ITT F4027	ITT FW-130	RCA 1P21	RCA C70113A	EMI 9514B
Quantum Efficiency	.08	.03	.15	.37	.10	.15	.15	.10	.12	.125
Dark Current (pulses/sec)	304	36	2500	4900	6300	6300	9900	40,000	130,000	30,000

B. Multiple Slit Techniques

From a theoretical point of view, the slit width and angle accuracy are directly related. Thus, by decreasing the slit width and the blur circle diameter, one obtains better angle accuracy. In practice this is not always the case. If the slit width is decreased, the optical aperture must be increased or the scan period must be increased to insure that a sufficient number of photons are obtained. To obtain an angle accuracy less than ten arc seconds, the aperture and scan period are prohibitively large in many cases of interest. Also a narrow slit requires high optical resolution.

An alternate approach to obtain high angle accuracy is to use multiple slits with a correlation technique. In this way one can obtain high angle accuracy with a reasonable aperture and scan period. The basic technique is to correlate the output of the photodetector with an electrical replica of the multiple slit pattern. If the peak output of the correlator exceeds a preassigned detection threshold, a star is to be present at the time corresponding to the peak output.

When designing a multiple slit scanning system, a basic problem to solve is the arrangement of the slit pattern. The number of slits is determined by the signal requirements; the slit widths are determined by the required angle accuracy. These problems are considered by Andreyev (1963a, b) and Jauregui (1962).

A slit pattern is selected so that the autocorrelation function has a relatively simple form. A multiple peaked correlation function significantly complicates star pattern recognition. Listed below are some desirable features of the autocorrelation function:

Condition 1)   The autocorrelation function R(t) should increase to its

peak value and then decrease.

Condition 2)   The central peak should have the narrowest possible width.

The central peak should resemble the correlation function of one

slit with itself.

Condition 3)   The entire length of the pattern should be as short as

possible. A trade-off exists between low off-peak correlation

values and short pattern length.

The task of finding a suitable slit pattern f(t) having these autocorrelation

properties is complicated by the fact that f(t) must be non-negative.[*]   One

example of a binary sequence satisfying the above listed requirements is

f(t; m, n, k) = 1100101, with n = 7, m = 4, and k = 1. The parameter n

signifies length of the sequence and m the number of 1's. The parameter k

signifies the maximum off-peak correlation value. The autocorrelation

function of this sequence when interpreted as a series of adjacent pulses of

unit width is shown in Figure 7.

The autocorrelation function shown in Figure 7 has all of the desirable

features set forth earlier:

(1)   It is monotonically decreasing as one proceeds from the peak
value.

(2)   The central peak could be narrower only if R(-1) = R(1) were
equal to zero. For binary sequences f(t; m, n, k) the factor
of increase in the central peak width of R(t) over what it
would be for the autocorrelation function of a single pulse of
unit width is $m/(m-R(1))$. One way to remove this increased
width is to make R(1) = R(-1) = 0. This precludes satisfying
Condition 1.

---

[*]   Construction of specific autocorrelation functions is described by Hofstetter
(1964).
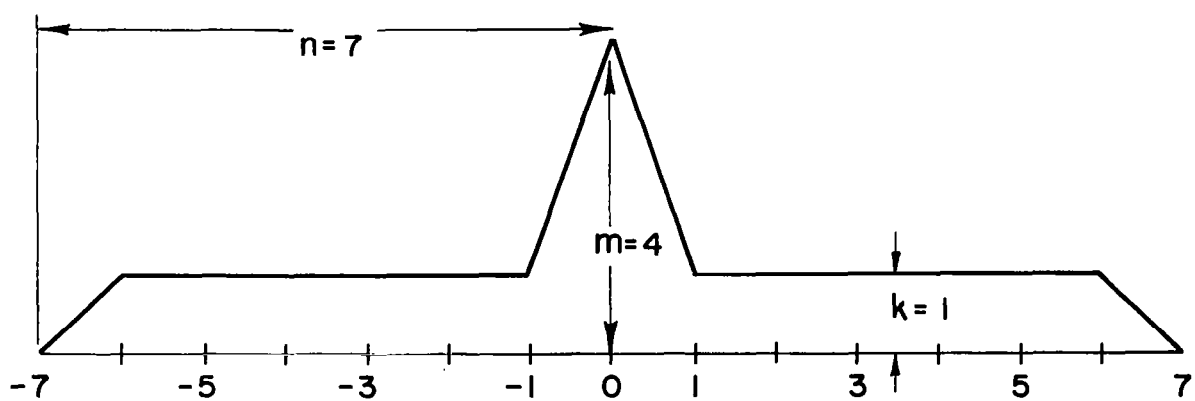
FIGURE 7 : AUTOCORRELATION FUNCTION
R(t) OF f(t,4,7,1)

(3) The length of the pattern shown in Figure 7 is the least possible for the given values of n, m, and k. A formula may be obtained which relates n, m, and k. This formula assumes that the autocorrelation function has the form 0, 0, 0, 1, 2, 3, ... k-1, k, k ... k, m, k, k, ... k, k-1, ... 2, 1, 0, 0, 0. Under these restrictions

$$n = \frac{m(m-1) + k(k+1)}{2k} \qquad (1)$$

Table 4 shows some results of Equation (1) for selected values of k and m. It must be remembered that this formula may represent binary sequences which do not exist. For example, it is known that it is impossible to achieve n = 11, m = 5, k = 1 as a binary sequence. While n = 12, m = 5, k = 1 does exist, it does not satisfy Condition 1 stated earlier. However, there may be a number of situations in which this condition can be relaxed.

Table 4 also shows the results of a construction algorithm which has been used to generate binary sequences. The resulting sequences do not satisfy Condition 1 in many cases but do satisfy Conditions 2 and 3. These sequences have a central peak in their respective autocorrelation functions which are wider by a factor of $m/(m-k)$ than the correlation function of a single unit pulse.

The algorithm begins with a pair of adjacent 1's. For example, suppose that we wish to construct a sequence which contains seven ones and whose maximum off-peak correlation value is 2. Start with

x_1 x_2 ....

1   1   ....

TABLE 4

AUTOCORRELATION CODES

m Number of Slits and Autocorrelation Peak	k Specified Autocorrelation Noise	n Actual Code Length	$n = \dfrac{m(m-1)+k(k+1)}{2K}$
1	0	1	---
2	1	2	2
3	1	4	4
4	1	7	7
5	1	12	11
6	1	21	16
7	2	14	12
7	1	31	21
8	2	23	16
8	1	45	29
10	2	39	24
10	1	81	46
20	4	99	50
30	5	196	90
50	10	358	128

The length of the sequence will be called ℓ, which is 2 in this case. For

the value of t > 0 at which R(t) is for the first time less than the specified

off-peak maximum, which in this case is 2, make the following addition. Let

$x_{t+1} = 1$. The new value of ℓ is now changed so that the new ℓ is the sum of

the old value of ℓ and t. Following this approach, one produces 11101001100001.

The process is terminated as soon as seven ones have been employed. According

to Equation (1), the sequence might possibly have had a length of 11 instead

of the length 14, which was obtained. It has been found that modifications

to the above procedure can be made to produce shorter sequences. However,

no systematic method of improving the process has yet been descovered. It

appears that the greatest potential improvement exists in the range

100 < n < 400 and 1 < k < 10. Table 4 shows that in this area the method

described falls far short of what may be expected with respect to length of

sequences for a specified off-peak maxima. Furthermore, these binary

sequences almost invariably fail to have monotonically decreasing autocor-

relation function.

In general, for photon-limited operation, $m\,D^2\,T$ is constant. Thus, if

a system involving m = 10 slits were employed, it would be possible to reduce

the optical aperture D to about 1/3. Alternatively, the scan period T could

be reduced by a factor of 10, and this would represent an important advantage

for guidance systems for which high sampling rates are required. It is to be

noted that these improvements resulting from the use of multiple slits are

achieved with no loss in angle accuracy, as would result if a single slit were

widened by a factor of 10 to compensate for a reduced D or T. As shown in

Table 4, the length of a code with a maximum off-peak correlation of one, $k = 1$, would be 81 elements long.

C. Correction for Sensor Motion

If the frame to which the scanning sensor is mounted is undergoing random changes in orientation as a function of time, then it is undoubtedly impossible to compensate analytically for this random motion. However, if the frame is undergoing some systematic change of orientation, then it is possible to account for such changes.

In a previous study,* which was supported as Task 5 under the same contract as the present study, it is assumed that the scanning slit(s) was rigidly attached to a body. The body itself was that assumed to be rigid, torque-free, and nearly symmetric. Under these assumptions, it was shown that it is possible to analytically compensate for the vehicle's orientation motion.

The effect of sensor motion is pictured in Figure 8. For this figure we assume rigid body torque-free motion with a half-cone angle or precession angle of $\theta = 2^{\circ}$. From this figure, we note that the time between successive transits of the same star, $t_{i+1} - t_i$, is not constant. This fact may cause some concern if scan-to-scan correlation techniques are utilized. For $\theta = 6^{\circ}$ the effect is about ten times greater than that shown in Figure 8.

---

*   For a complete discussion see "Final Report: Starmapper Attitude Determination," prepared for NASA Langley Research Center by Control Data Corporation, 1965.

FIG 8 : EFFECT OF PRECESSION ON TIME BETWEEN
SUCCESSIVE TRANSITS
$\theta = 2°$
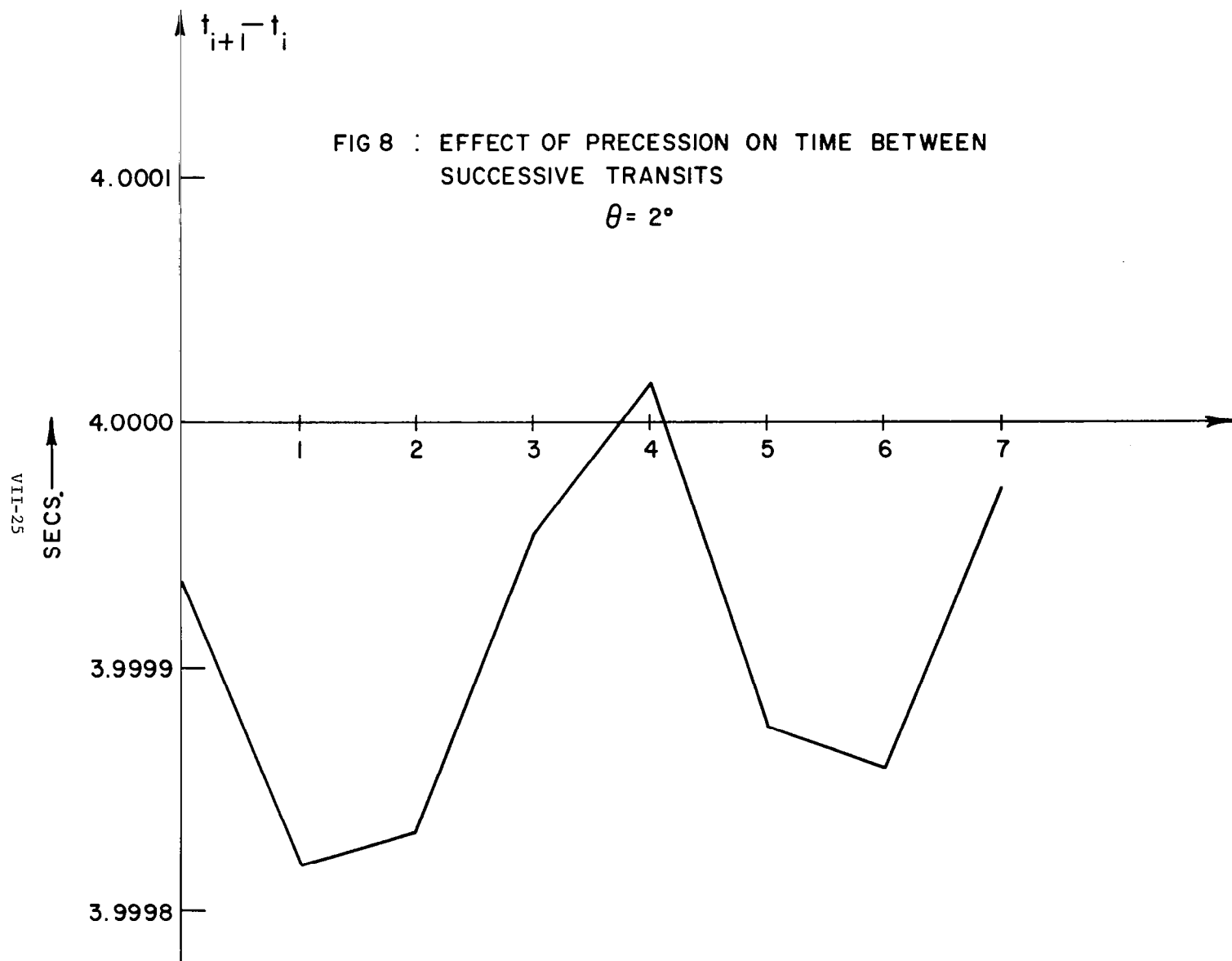
VIII. SYSTEM DESIGN

Once the instrumentation is defined and the radiation environment is known, it is possible to tabulate a primary set of parameters, as shown in Figure 1. For systems of the type we are considering, this set might number between twenty and fifty quantities. Proceeding to the left in Figure 1, the primary set of parameters can be used to devine the gross system characteristics, i.e., weight, size, power, cost, and reliability. Proceeding to the right, the primary set of parameters can be used to derive a set of signal and noise parameters, i.e., number of photoelectrons from star, effective number noise photoelectrons, detection threshold, etc. From these quantities, the characteristics of individual star transits can be evaluated. These characteristics are (1) the probability of relative detection, (2) the expected number of false detections per scan, (3) rms accuracy of the star transit measurement, and (4) the rms accuracy of the intensity measurement. Finally, a set of system performance characteristics are established. This set contains two characteristics--the rms angle accuracy about the three attitude axes (σ_T) and the probability of making the correct celestial pattern recognition (P_p). When proceeding in the direction of the arrows in Figure 1, one always passes in the direction of fewer parameters:

$$\{5\} \Leftarrow \{50\} \Rightarrow \{8\} \Rightarrow \{4\} \Rightarrow \{2\}$$

This occurs because of the inherent nature of analysis; i.e., no design freedom exists once the problem is defined. When proceeding in this manner our

VIII-3

Primary Parameters

Optical Aperture
Resolution
Field of View
Spectral Transmission
Focal Length
Optical Efficiency
Optical Arrangement
Slit Width
Slit Length
Number of Slits
Slit Code Pattern
Relative Slit Arrangement
Type of Detector
Detector Noise Level
Spectral Response of Detector
Quantum Efficiency
Scan Period
Scanning Geometry
Required Number of Star
  Detections
Number of Scans Which
  are Correlated
  .
  .
  .

Cross
System
Characteristics

Size
Weight
Power
Reliability
Cost

Signal and Noise
Parameters

Photoelectrons
  From Star
Photoelectrons
  From Background
Effective Detector
  Noise
Detection Threshold
  .
  .
  .

Characteristics
of Star Transit

Probability of
  Detection
Number of False
  Detections
RMS Transit Time
  Accuracy
RMS Intensity
  Accuracy

System Performance
Characteristics

Attitude Accuracy
Probability of Star
  Pattern Recognition

Figure 1: Diagram of System Analysis

principal concern is the adequacy of the mathematical transformations repre-
sented symbolically by the arrows ($\Longrightarrow$).

If we proceed in a direction opposite to that indicated by the arrows, a
problem of system SYNTHESIS presents itself. Because of the nature of the
synthetic process, more than one set of primary parameters can be used to
obtain the system characteristics, extreme right or left.

$$\{5\} \Longleftarrow \{50\} \Longrightarrow \{8\} \Longrightarrow \{4\} \Longrightarrow \{2\}$$
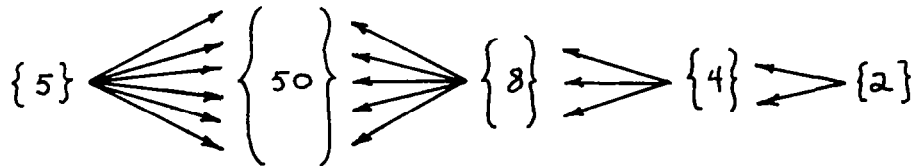
It is obvious that a high degree of arbitrariness exists when synthesizing
new systems, and any number of designs might adequately meet the requirements
established at the extreme right or left of Figure 1.

In practice, one designs a sensor using a hybrid analysis--synthesis
technique. Any type of parameter can serve as a starting point. Values of
certain parameters are specified; bounds are placed on other parameters. One
then tries to optimize the system. In subsection B we have developed a computer
program that implements this concept and efficiently designs scanning optical
systems. A simplified flow chart is shown in Figure 2. In this program,
values are specified for,

> (1) number of photoelectrons from limiting magnitude star during
>   the slit transit,
>
> (2) scan period and scanning geometry,
>
> (3) quantum efficiency,
>
> (4) optical efficiency,
>
> (5) ratio of image diameter to slit width,

(6)   number of star detections required per scan,

(7)   probability of detecting required number of stars, and

(8)   number of scans which are correlated.

Upper bounds are placed on the expected number of false star detections and the rms star transit error. With these constraints the optical aperture is minimized. Consequently, volume and weight are minimized. With this program one can derive and analyze a design in a few minutes, considering many pointing directions.

The basic relationships between signal and noise are illustrated in Figure 3 relative to slit width and optical aperture. All of the sensor parameters are fixed except slit width and optical aperture; the image diameter is always equal to the slit width. In the region marked "dark current noise" the photomultiplier dark current noise is the dominant source of noise. Similarly, signal photon noise and stellar background noise dominate in the regions so marked. For values of slit width and optical aperture in the "operating domain" the signal-to-noise ratio is sufficiently large to permit reliable discrimination between signal and noise. Iteration steps of the automatic design program are marked in Figure 3. Initially, the design is noise limited. The slit width is decreased and the aperture is increased, maintaining a constant signal level. The iteration stops when the operating domain is reached. The aperture has the minimum value in the operating domain. A particular example is discussed in subsection A.
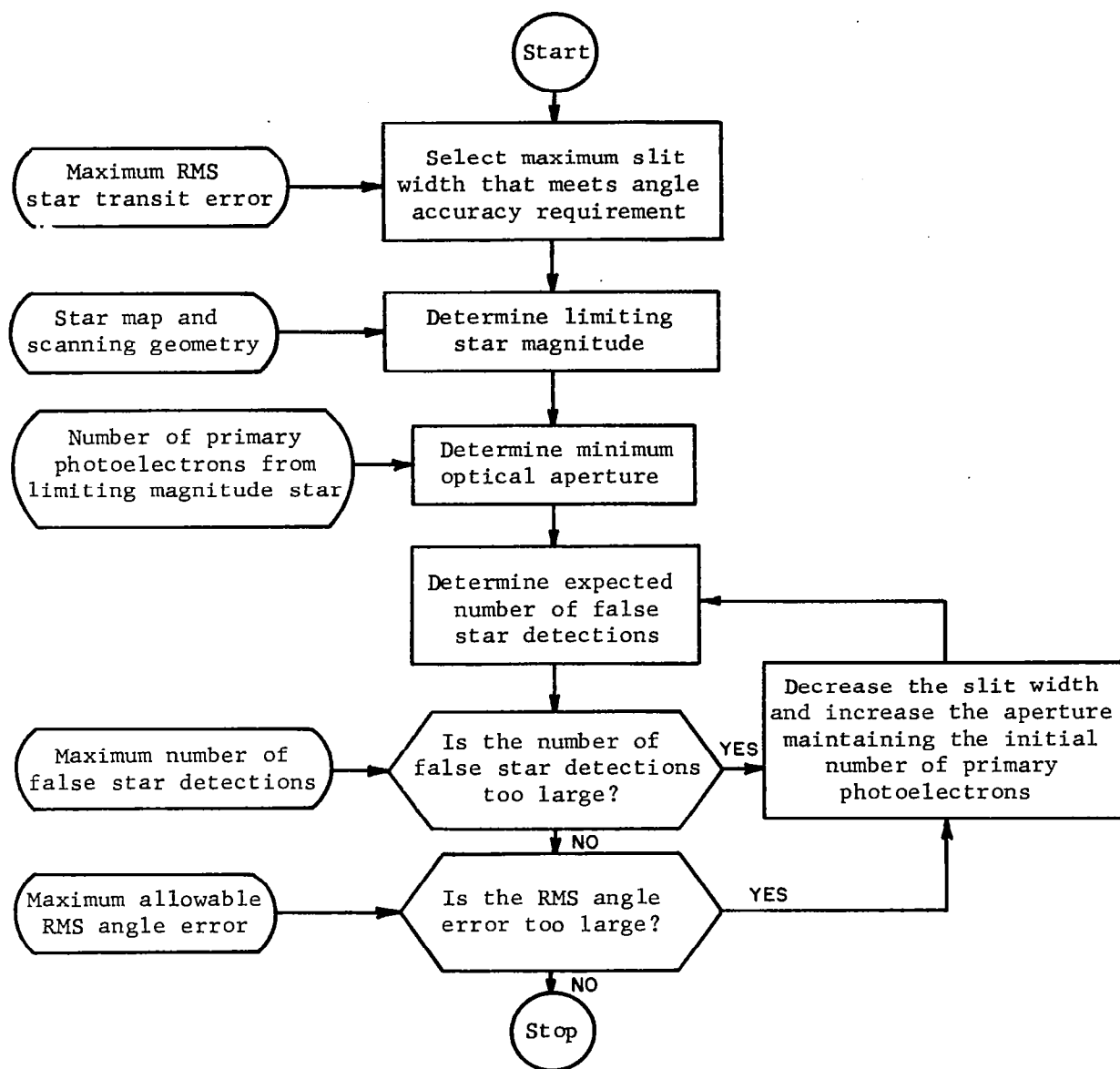
Figure 2: Basic Steps in Automatic Design Program
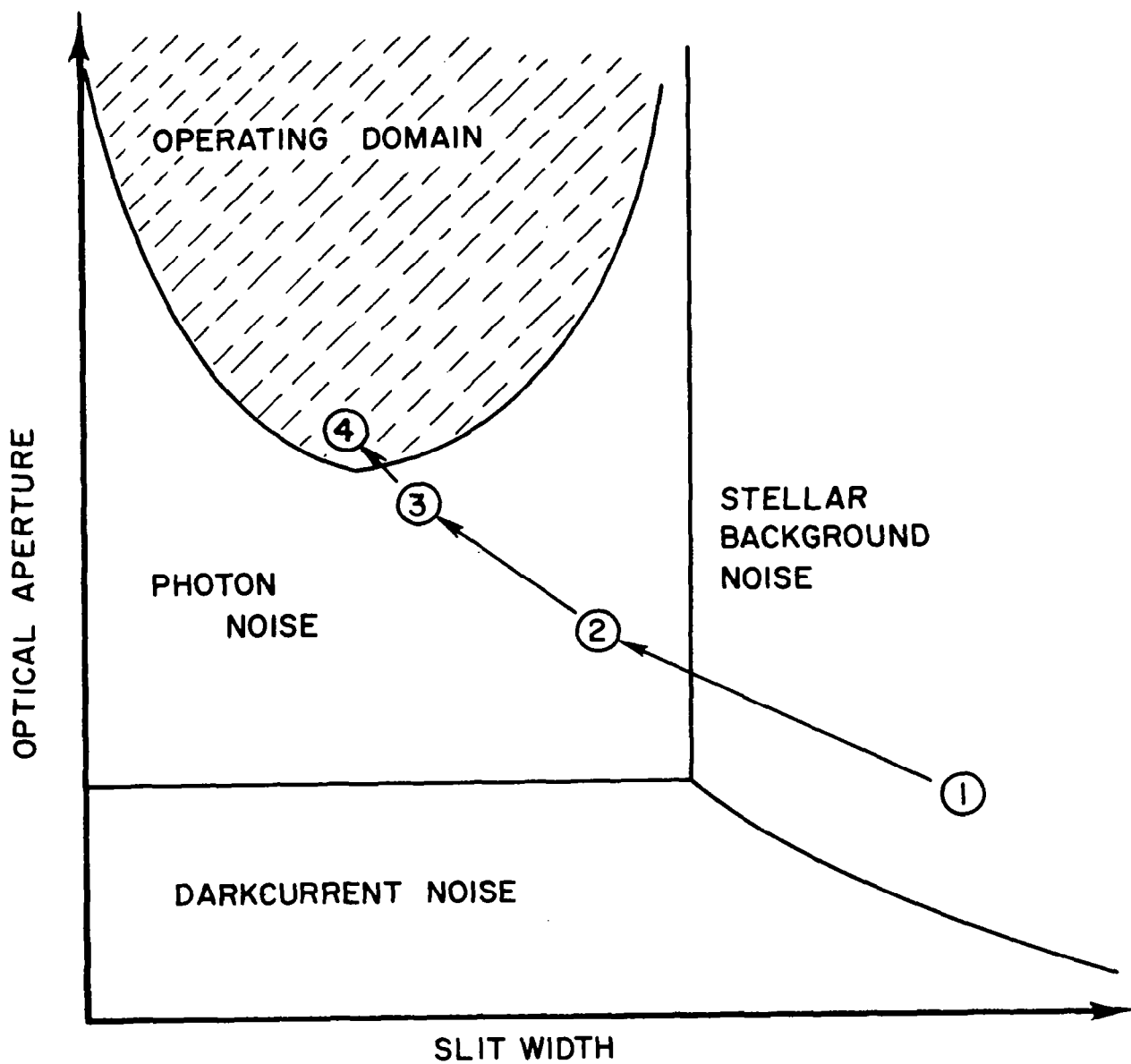
FIGURE 3 : SIGNAL AND NOISE RELATIONSHIPS

A. Operating Domains

In the design of a scanning optical system the two basic parameters which govern the relationship between signal and noise are the aperture diameter (D) and slit width (SW). Thus, restrictions must be placed on D and SW so that we have sufficient signal strangth along with a desirable signal-to-noise ratio.

The composite signal has three components:

m_s = mean number of star pulses (signal)

m_d = mean number of dark current pulses (noise)

m_b = mean number of background pulses (noise)

The relationships between the system parameters (D and SW) and the composite signal components are

$$m_s = k_1 D^2 (SW)$$

$$m_d = k_2 (SW)$$

$$m_b = k_3 D^2 (SW)^2 \tag{1}$$

where k_1, k_2, k_3 are constants which are independent of D and SW.

In the (aperture diameter)-(slit width) plane, several curves are of interest. These are curves corresponding to the equations,

$$m_s = m_d \quad \text{and } m_s/(m_b + m_d) = C_1$$

$$m_s = m_b \qquad m_s = C_2$$

$$m_b = m_d \tag{2}$$

where C_1 is desired signal-to-noise ratio; C_2 is desired constant value for m_s.

These equations produce the desired operating domain for the design, and can be expressed in terms of the slit width and aperture diameter by utilizing the equations in (1).

Thus,

$$m_s = m_d \rightarrow D^2 = k_2/k_1 \qquad m_s = m_b \rightarrow SW = k_1/k_3$$

$$m_b = m_d \rightarrow D^2 = \frac{k_2}{k_3(SW)} \qquad m_s = C_2 \rightarrow D^2 = \frac{C_2}{k_1(SW)} \qquad\qquad (3)$$

$$\frac{m_s}{m_b + m_d} = C_1 \quad\longrightarrow\quad D^2 = \frac{k_2}{k_3\left(\frac{k_1}{C_1 k_3} - SW\right)}$$

In order to determine explicit curves for the different relationships, it is necessary to consider a numerical example using specific values of k_1, k_2, k_3, C_1, and C_2. For the numerical example given in subsection B we find that

$$k_1 = 24.6 \qquad\qquad C_1 = 2$$
$$k_2 = 34.9 \qquad\qquad C_2 = 30$$
$$k_3 = .689$$

Thus, the equations in (3) above become

$$m_s = m_d \rightarrow D^2 = 1.418 \qquad m_s = m_b \rightarrow SW = 35.7$$

$$m_b = m_d \rightarrow D^2 = 50.7/SW \qquad m_s = 30 \rightarrow D^2 = 1.22/SW$$

$$\frac{m_s}{m_b + m_d} = 2 \rightarrow D^2 = 50.7/(17.84 - SW)$$

The graphs of these equations are illustrated in Figure 4. In the area to the left of the vertical line at SW = 35.7, $m_s > m_b$ and in the area above the horizontal line at D = 1.19, $m_s > m_d$. In the area above the curve $m_b = m_d$, $m_b > m_d$. In the area above the hyberbolic curve, $m_s/(m_b + m_d) = 2$, $m_s/(m_b + m_d) > 2$. In the area above the curve, $m_s = 30$, $m_s > 30$.

Thus, in the area above the curves $m_s = 30$ and $[m_s/(m_b + m_d)] = 2$ the signal-to-noise ratio, $m_s/(m_b + m_d)$, is greater than 2 and the mean number of star pulses, m_s, is greater than 30.

These principals are incorporated in the automatic design technique to be described in subsection B. This technique uses a constant m_s as an input parameter along with an initial determination of the slit width based on accuracy requirements. Rather than use the signal-to-noise ratio to determine the acceptability of the design, the expected number of false star detections in one scan, E_f, is used. The signal-to-noise ratio is not as direct a measure of system acceptability as is E_f. On the other hand, E_f is more complicated computationally.
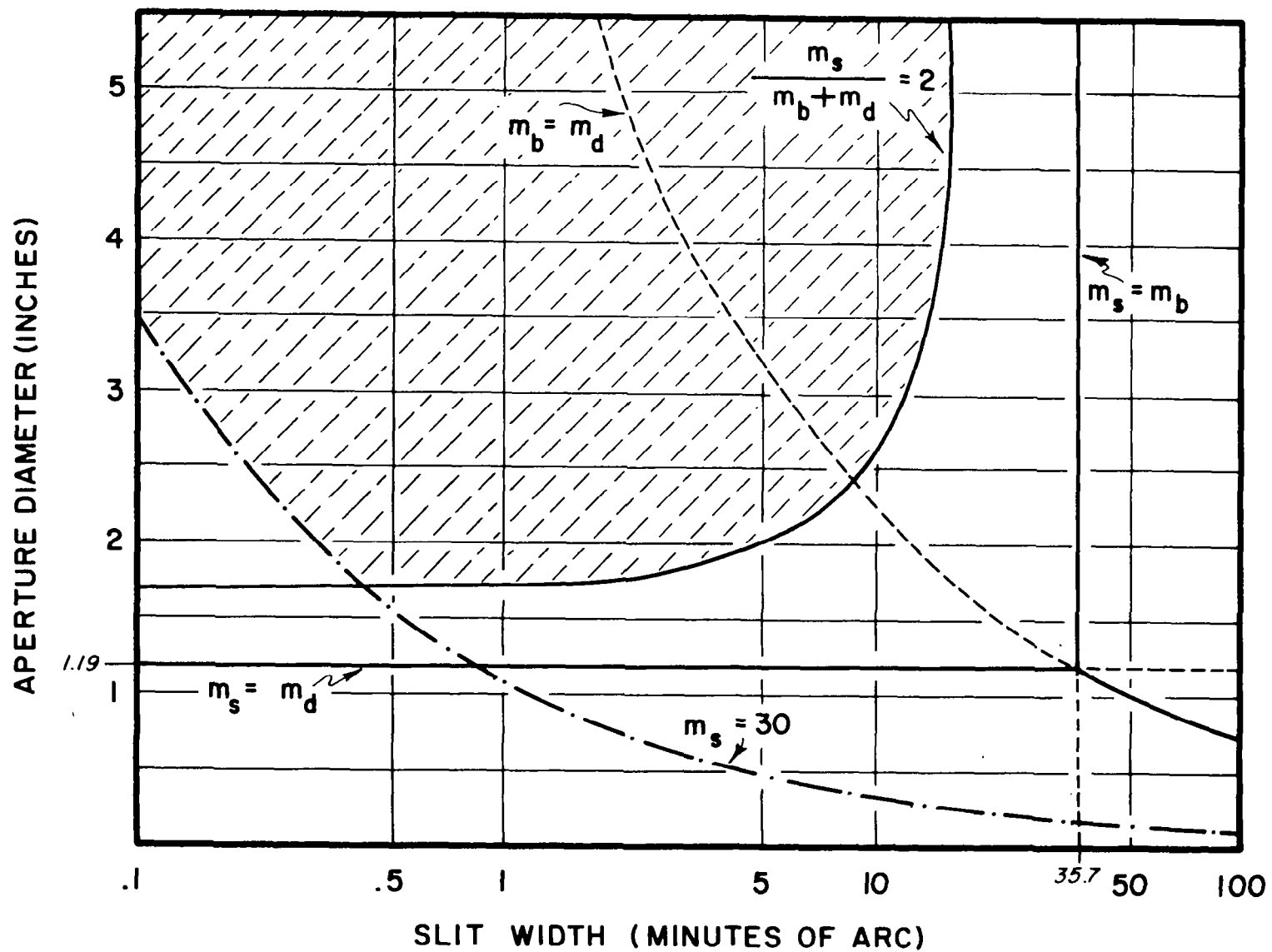
FIGURE 4 : OPERATING DOMAINS

B.   An Automatic Optimum Design Technique

The design of a scanning optical system is a complex problem in that there exist many complex non-linear relationships among the various system design and performance parameters. System design is basically the technique of determining the design parameters after the performance parameters are specified. The design parameters can be represented as a specific set of functions of the performance parameters. In many cases these are implicit functional relationships. In addition to performance specifications, design constraints may necessarily be imposed as not all solutions are acceptable.

The design problem thus reduces to solving a specified set of functions of the performance parameters within specified constraints. It is possible then to conceive of an automatic design program for a digital computer to determine the design. By its very nature, i.e., solution of mathematical functions, the problem becomes amenable in implementation on a computer system. System design would thus be achieved optimally and with much less time than by conventional methods.

The OPSCAN (OPtimum SCANner) program uses a number of performance parameters to design an optical scanning system. In addition to the performance parameters, design constraints are imposed on the calculated design parameters.

Some of the supplied parameters are maximum rms angle error, number of star detections required, probability of obtaining this many detections, the maximum number of false star detections, field of view, and scan period. Using these values the program designs a system with a minimum aperture for a specified number of primary photoelectrons. Many pointing directions are

examined to determine the smallest aperture necessary to operate for any pointing angle. Note that the pointing direction determines the signal-to-noise ratio. In many cases the initial determinations of the aperture diameter and slit width yield an unacceptable signal-to-noise ratio (E_f is too large). This can be corrected by decreasing the slit width and increasing the aperture diameter (see Equation (1) in subsection A).

Different optimum designs can be determined with different fields of view and scan periods. The program does not attempt to find an optimum design among these because qualitative factors must be taken into consideration; such as, interception of bright objects in the field of view, vehicle motion, feasibility of optical design. Engineering judgment must be employed to select the appropriate final design. Thus, the program provides several optimum designs from which the evaluator may choose.

The programming philosophy employed was to maintain functional modularity so that the basic functions could be easily modified. At the present time, several functions are being calculated by simple, approximate techniques. At a later time these functions will be replaced by more sophisticated and exact methods. The program organization will, therefore, allow these changes to be made with a minimum of difficulty.

1.   Program Description

The general flow diagram of the OPSCAN program is shown in Figure 5. The program is organized around nine basic functions which are:

(1)   determination of maximum slit width,
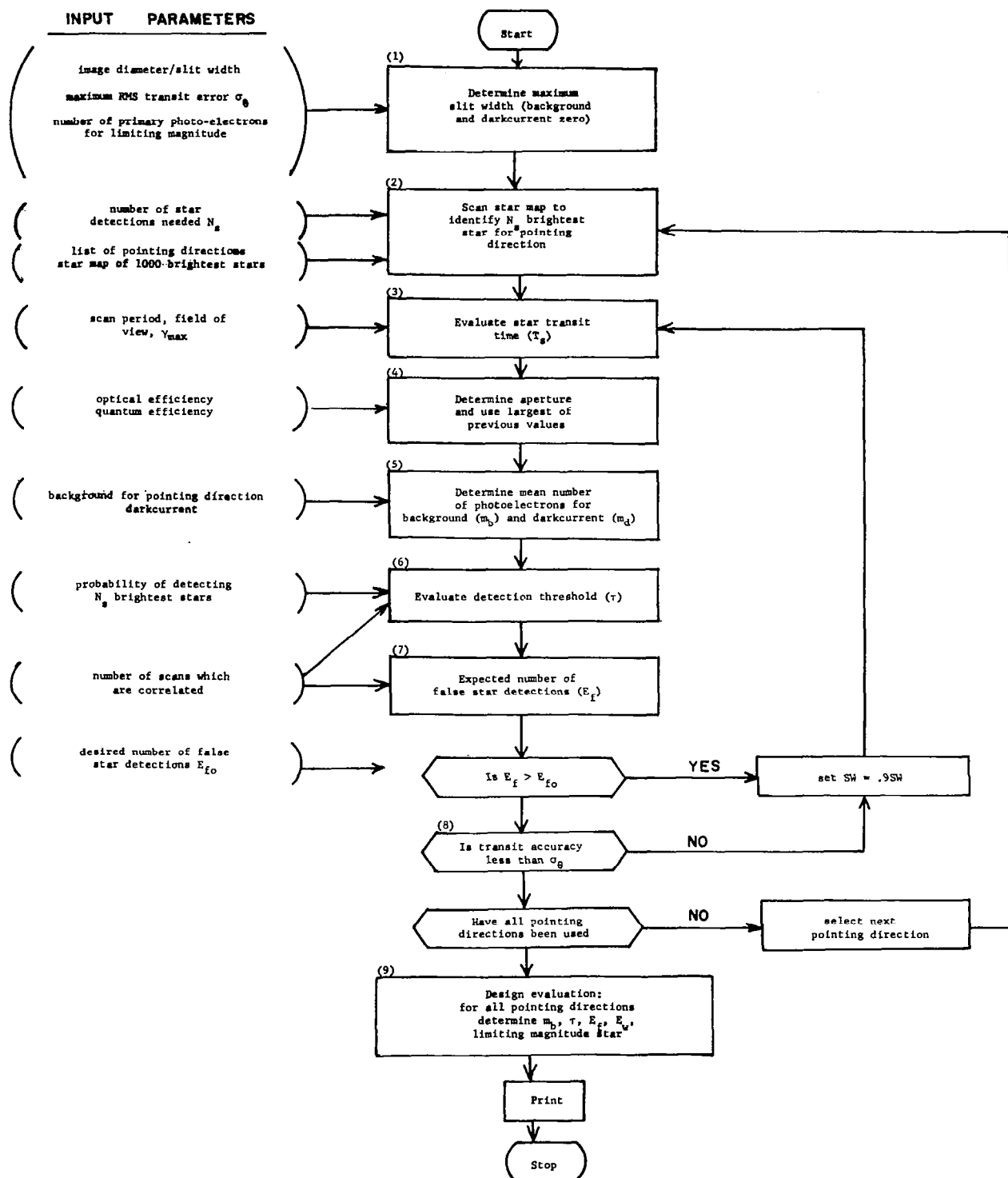
FIGURE 5 : OPSCAN FLOW DIAGRAM

(2) identification of the bright stars in the scanned area,

(3) determination of transit time,

(4) determination of aperture,

(5) determination of average number of background and dark current photoelectrons,

(6) determination of detection threshold,

(7) determination of expected number of false detections,

(8) determination of final rms transit error, and

(9) design evaluation.

The equations used in this section were developed by Farrell and Zimmerman, (1965). Table 1 contains a symbol and definition list which is necessary for the following material.

Determination of Maximum Slit Width (1)[*] Given the average number of photoelectrons from the limiting magnitude star, the ratio of image diameter to slit width, and the maximum accuracy, the maximum slit width can be determined. In the present program the maximum slit width is simply set equal to a multiple of the maximum rms transit error. In the most general case, however, a more complicated function of all three variables would be involved. In these computations the background and dark current are assumed to be zero. Consequently, the computed slit width is the maximum slit width with the specified rms transit error. Stellar background and dark current decrease the angle accuracy.

---

[*] The numbers in parentheses, such as (1), refer to boxes in Figure 5.

TABLE 1

SYMBOL LIST

T_s = transit time in seconds

SW = slit width in minutes of arc

γ = inclination angle in degrees

T = scan period in seconds

FOV = field of view in degrees

γ_{max} = maximum inclination in degrees

m_s = average number of photoelectrons from limiting magnitude star

D = aperture diameter, in inches

α = fraction of pulses transmitted by threshold clamp

ϵ_q = effective quantum efficiency relative to an S-4 response

ϵ_o = optical efficiency

C = constant = 1.2×10^7

M_L = limiting magnitude (photographic)

m_{sp} = previous value of average number of photoelectrons from limiting magnitude star

D_p = previous aperture diameter

m_b = average number of background photoelectrons during star transit

N_{SL} = number of slits

N_T = number of tenth magnitude stars per square degree

m_d = average number of effective dark current pulses

λ_d = effective dark current photoelectron rate

p_o = specified minimum probability of detection

p_i = probability of detecting a star of magnitude i

τ = detection threshold

N_s = number of stars needed in the scanned area

m_{si} = average number of photoelectrons from the ith star in the scanned area

m_{bi} = average number of background photoelectrons from the stellar background near the ith star

E_f = expected number of false star detections

E_w = expected number of weak star detections

σ_θ = maximum rms transit error in minutes of arc

N_p = number of slit positions in the scanned area

SA = scanned area (square degrees)

N_i = number of ith magnitude stars in scanned area

One such possible function is

$$SW_{max} = k\sigma_\theta \left[\frac{(2t+3)P_{2t+2}}{m_s^2 P_t} - \frac{(t+2)P_{t+2}}{m_s^2 P_t} + \frac{P_{t+1} - P_{t+2}}{m_s P_t} \right]$$

where SW_{max} = maximum slit width in minutes of arc

σ_θ = maximum rms transit error in minutes of arc

t = largest value of t_1 for which

$$P_0 \leq 1 - \sum_{j=0}^{t_1} \frac{m_s^j}{j!} e^{-m_s}$$

p_0 = specified minimum probability of detection for the limiting magnitude star with no background or dark current

$$P_T = 1 - \sum_{j=0}^{T} \frac{m_s^j}{j!} e^{-m_s} \qquad \text{where} \qquad T = t, t+1, t+2, 2t+1, 2t+2$$

m_s = average number of photoelectrons from limiting magnitude star

The slit width and rms transit accuracy as angles are measured across the center of the field of view with the vertex at the intersection of the spin axis and optical axis. This is depected in Figure 6, where SW' represents the slit width as measured by this technique and SW represents the slit width measured in a plane orthogonal to the spin axis. In the latter case, the slit width measurement is independent of this inclination, γ.

Identification of Bright Stars in Field of View (2) To identify the N_s brightest stars in the scanned area a stored star map is used. N is an input

SW' = SW • SIN γ
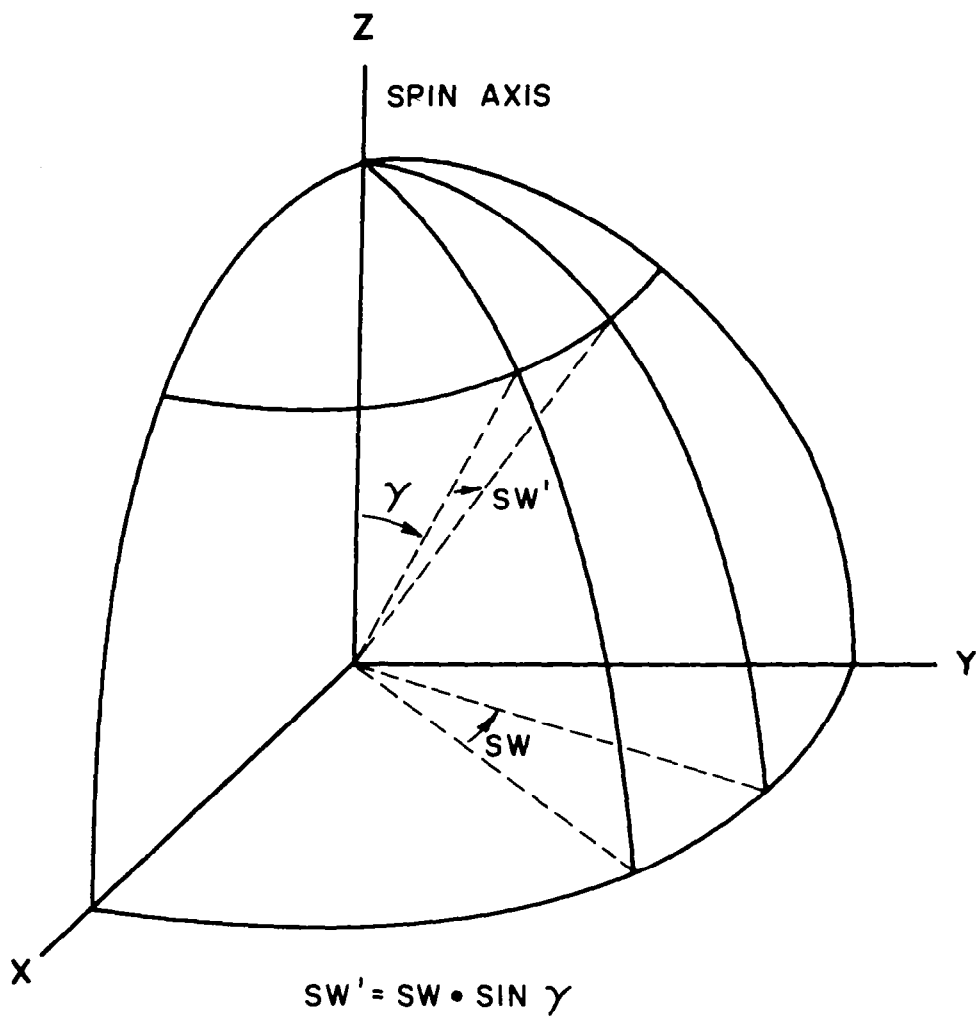
FIGURE 6: RELATION BETWEEN SLIT WIDTH AS
MEASURED FROM SPIN AXIS (SW) AND
LENS (SW')

parameter. The scanned area is defined by the pointing direction, $\hat{p}$, inclination angle, γ, i.e., the angle between the optical axis and spin axis, and the field of view, FOV. The scanned area can be defined by the two angles $\gamma + FOV/2$ and $\gamma - FOV/2$. See Figure 7.

To determine whether a star is in the scanned area, the direction cosines (p_x, p_y, p_z) of the pointing direction are expressed in galactic coordinates. The direction cosines of the star (s_x, s_y, s_z) are determined and the inner product $\hat{p} \cdot \hat{s}$ is calculated. The star is in the scanned area if the inner product is greater than $\cos(\gamma + FOV/2)$ but less than $\cos(\gamma - FOV/2)$. The pro cedure is depicted in Figure 8. Summary of procedure:

(1) Calculate p_x, p_y, p_z.

(2) Read in s_x, s_y, s_z.

(3) Calculate $\hat{p} \cdot \hat{s} = p_x s_x + p_y s_y + p_z s_z$.

(4) If $\cos(\gamma + FOV/2) < \hat{p} \cdot \hat{s} < \cos(\gamma - FOV/2)$ go to 5; otherwise go to next star, begin at Step 2.

(5) Add 1 to N (N = number of stars located in scanned area).

(6) If $N > N_s$ terminate procedure; otherwise, go to next star, begin at Step 2.

All stars in the scanned area are temporarily stored and the procedure is repeated until N_s stars are identified in the scanned area. The limiting magnitude is set equal to the magnitude of the dimmest star in this list of N_s stars.

Determination of Transit Time (3)   The star transit time is calculated using the following equations:

$$\gamma = \gamma_{max} - FOV/2$$

$$T_s = (SW) \; T \Big/ \big[(21600)(\sin \gamma)\big]$$

The angular relationships between the spin axis, the optical axis, and the field of view are depicted in Figure 7.

Determination of Aperture (4)   The basic equation by which the aperture diameter is determined is

$$m_s = \alpha \, \varepsilon_q \, \varepsilon_o \, C D^2 \, T_s \, 10^{-.4 M_L}$$

This equation results from the fact that the average number of photons per second, λ_s, striking an optical system with aperture, D, is proportional to $D^2 \, 10^{-.4 M_L}$ or

$$\lambda_s = C D^2 \, 10^{-.4 M_L}$$

During the time of transit of the limiting magnitude star the average number
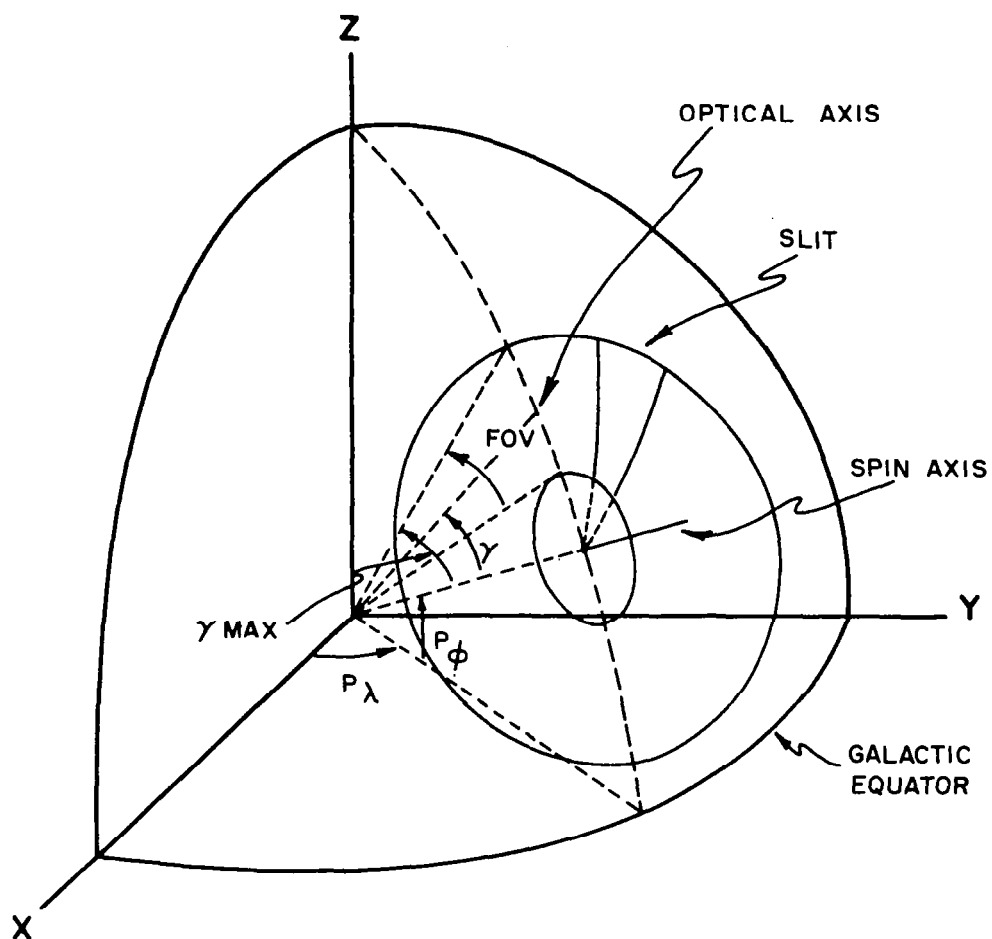
FIGURE 7: ANGULAR RELATIONSHIPS AMONG SPIN AXIS,
OPTICAL AXIS, AND THE FIELD OF VIEW

ENTER

COMPUTE P_x, P_y, P_z
SELECT FIRST
STAR SET N = 0

READ IN
S_x, S_y, S_z

COMPUTE
$\hat{P} \cdot \hat{S}$

SELECT
NEXT
STAR

NO

$A < \hat{P} \cdot \hat{S} < B$

YES

STORE STAR No.
$N + 1 \longrightarrow N$

$A = \cos\left(\gamma + \dfrac{FOV}{2}\right)$

$B = \cos\left(\gamma - \dfrac{FOV}{2}\right)$

NO

$N \geq N_s$

YES

EXIT
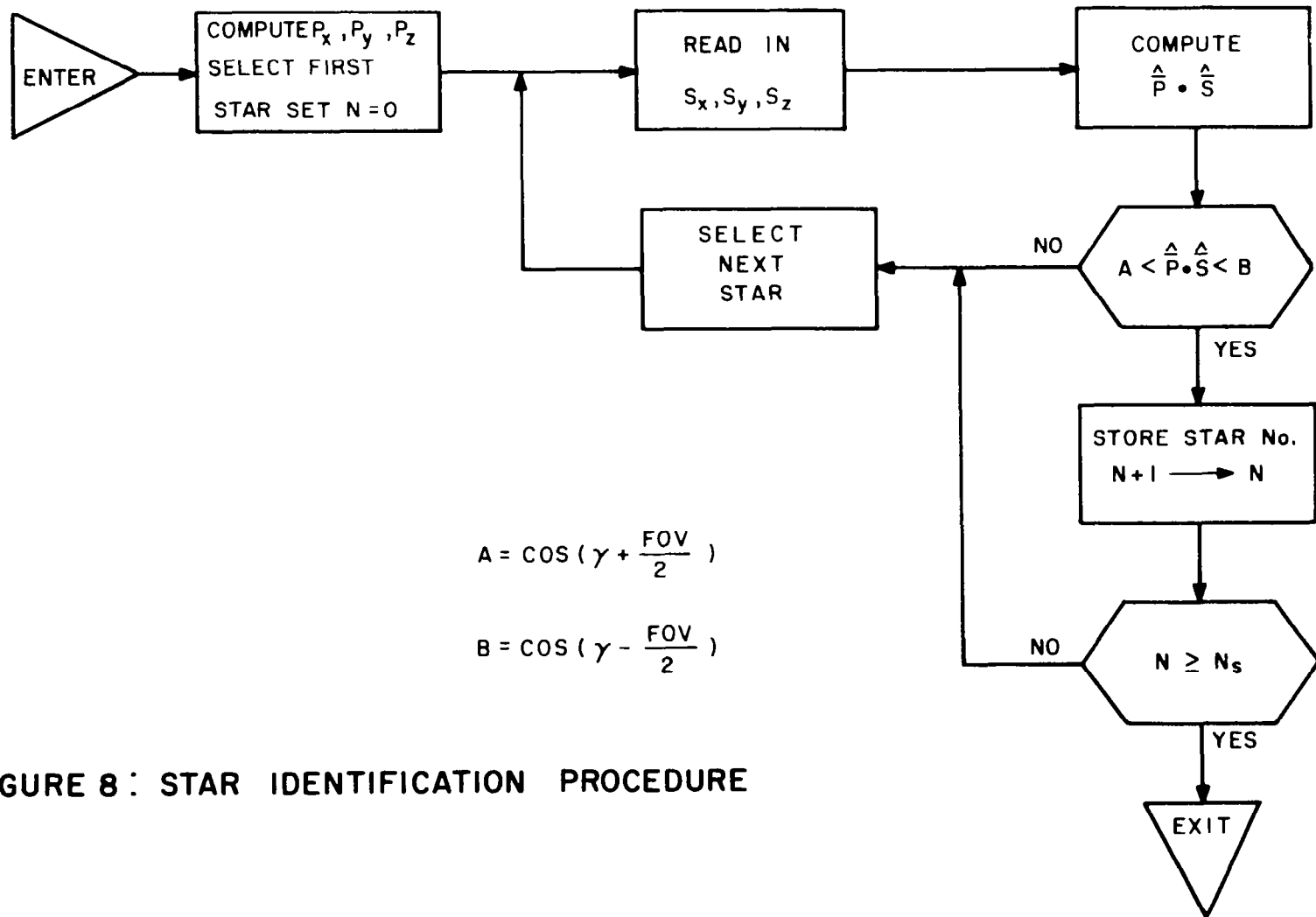
FIGURE 8: STAR IDENTIFICATION PROCEDURE

of photons striking the system will be $T_s \, CD^2 \, 10^{-.4M}L$. The proportion of
photons transmitted by the lens is the optical efficiency so the number of
photons from the limiting magnitude star transmitted through the lens is

$$\varepsilon_{\bullet} \, T_s \, C D^2 \, 10^{-.4M_L}$$

The proportion of photons converted to photoelectric pulses is the quantum
efficiency. The photoelectric output of the limiting magnitude star is

$$\varepsilon_{\mathfrak{q}} \, \varepsilon_{\circ} \, T_s \, C \, D^2 \, 10^{-.4 M_L}$$

The effect of the noise generated by the photomultiplier can be reduced by
using a threshold clamp at the output of the photomultiplier. This device
transmits only those pulses exceeding a fixed threshold; the output pulses
are clamped to a standard level. See subsection VI.B. If α is the fraction
of the pulses transmitted, then

$$m_s = \alpha \, \varepsilon_{\mathfrak{q}} \, \varepsilon_{\circ} \, T_s \, C \, D^2 \, 10^{-.4M_L}$$

The aperture diameter is

$$D = \left[\frac{m_s}{\alpha \varepsilon_{\mathfrak{q}} \varepsilon_{\circ} \, C \, T_s \, 10^{-.4M_L}} \right]^{\frac{1}{2}}$$

The calculated aperture diameter is compared against a previously stored

value. If the new diameter is larger it will replace the previous value. Thus, the stored value represents the largest diameter determined up to that point.

If the previous aperture diameter is larger than the current value, it will remain the same and the average number of photoelectrons from the limiting magnitude star is recalculated by (ratio of diameter squared).

$$m_s = m_{sp} \frac{D_p^2}{D^2}$$

The value of D used for the last pointing direction determines the aperture diameter for the system.

Average Background and Dark Current Photoelectrons (5) The average number of background photoelectrons is calculated by

$$m_b = 20 \, N_{SL} \propto \varepsilon_q \, \varepsilon_o \, T_s \, (FOV)(SW) \, N_T \, D^2$$

The average number of dark current photoelectrons is calculated by

$$m_d = \lambda_d \, T_s$$

Determination of Detection Threshold (6)   The detection threshold is

determined from the inequality

$$p_0 \leq \prod_{i=1}^{N_s} p_i \quad \begin{cases} p_i = 1 - \sum_{k=0}^{\tau_1} \frac{m_i^{\,k}}{k!} e^{-m_i} & \text{if } m_i < 50 \\[2em] p_i = \int_{\tau_1}^{\infty} \frac{e^{-\frac{(x-m_i)^2}{2m_i}}}{\sqrt{2\pi m_i}} \, dx & \text{otherwise} \end{cases}$$

where

$$m_i = m_{si} + m_{bi} + m_d$$

The p_i represent probabilities of detection for each of the N_s stars in

the scanned area and are evaluated by calculating the Poisson function or a

normal approximation to the Poisson function. These probabilities are evaluated

for various values of τ_1 and multiplied together to compare against p_0. The

largest value of τ_1 that still results in the joint probability being greater

than p_0 is set equal to τ, the detection threshold.

To reduce the amount of time required to calculate the detection threshold,

τ, a starting value of

$$\tau_1 \doteq m_i - k \sqrt{m_i}$$

is used, where

$$m_i = m_{si} + m_{bi} + m_d$$

and K = value for which $\displaystyle\int_{-\infty}^{k} \frac{e^{-\frac{x^2}{2}}}{\sqrt{2\pi}} \, dx = p_0$

In all cases m_i is large enough so that a normal distribution gives a rough estimate of τ.

Expected Number of False Star Detections (7)   The expected number of false star detections, E_f, is calculated by determining the probability of detection of the background and dark current sources and multiplying this by the number of slit positions in the scanned area. The probability of detection of the background and dark current sources is

$$P(m_b + m_d, \tau) = 1 - \sum_{k=0}^{\tau} \frac{(m_b + m_d)^k}{k!} e^{-(m_b + m_d)}$$

The number of slit positions in the scanned area is

$$N_p = T/T_s$$

The expected number of false star detections is thus,

$$E_f = P(m_b + m_d, \tau) N_p$$

Final Transit Accuracy (8)   The final transit accuracy is determined by solving for σ_θ in the expression used to determine SW_{max} in (1). For our example we assume that the transit accuracy is proportional to the slit width.

Program Logical Structure   The program begins by calculating the maximum slit width based on the required angle accuracy, without background and dark current. Using this value of slit width, a stored star map is scanned to identify N_s stars in the scanned area, and the star transit time and aperture are calculated. If the aperture is larger than the previously calculated aperture, it is stored. If not, the average number of photoelectrons from the limiting magnitude star is calculated using the previous aperture value.

The program then calculates the average number of background and dark current photoelectrons and evaluates the detection threshold. The expected number of false star detections is calculated and compared against a desired number of false star detections. If greater than the desired number, the slit width is reduced to 90 percent of its previous value and processing is resumed at the evaluation of star transit time. The steps from the star transit time function (3) to the expected false star detection function (7) are repeated with the slit width being reduced 10 percent each time until the expected number of false star detections becomes less than the desired number.

At this point, the rms transit error is determined and compared against the maximum rms transit error. The background and dark current are included in the calculation. If the computed error is larger than the maximum, the slit width is reduced once again by 10 percent and control is returned to the star transit time evaluation. Reduction of the slit width and repetition of the steps from star transit time (3) to transit error (8) continues until the computed transit error becomes less than the maximum.

The above sequences are repeated using all pointing directions. The

largest aperture and smallest slit width from any pointing direction are the final design values. With these values the design characteristics are evaluated for all pointing directions.

Design Evaluation (9) When a design has been determined, several quantities that vary with the pointing direction are calculated and tabulated for all pointing directions. These values are the average number of background photo-electrons, the detection threshold, the expected number of false star detections, the limiting magnitude, and the expected number of weak star detections.

In computing the expected number of weak star detections we concerned ourselves only with stars whose magnitudes were several magnitudes greater than M_L. Special densities of stars in magnitude class M (M = 1, 2, 3, 4, 5, 6, 7)[*] were recorded. A star of magnitude m is in class M if $M - \frac{1}{2} \leq m \leq M + \frac{1}{2}$. The stars of class M were assumed to be uniformly distributed over the sphere. For each pointing direction two magnitude classes were used to compute the expected number of weak star detections. If we let M_L^* be the closest integer to M_L, then the two classes considered were $M_L^* + 1$ and $M_L^* + 2$. The expected number of weak stars (E_w) is then

$$E_w = (SA) \sum_{i=M_L^*+1}^{M_L^*+2} N_i \, \rho_i$$

The calculations necessary to compute the scanned area are indicated in Figure 9.

---

[*] Data taken from Allen (1963).

SPIN AXIS

$$h = \cos(\gamma_{max} - FOV) - \cos(\gamma_{max})$$
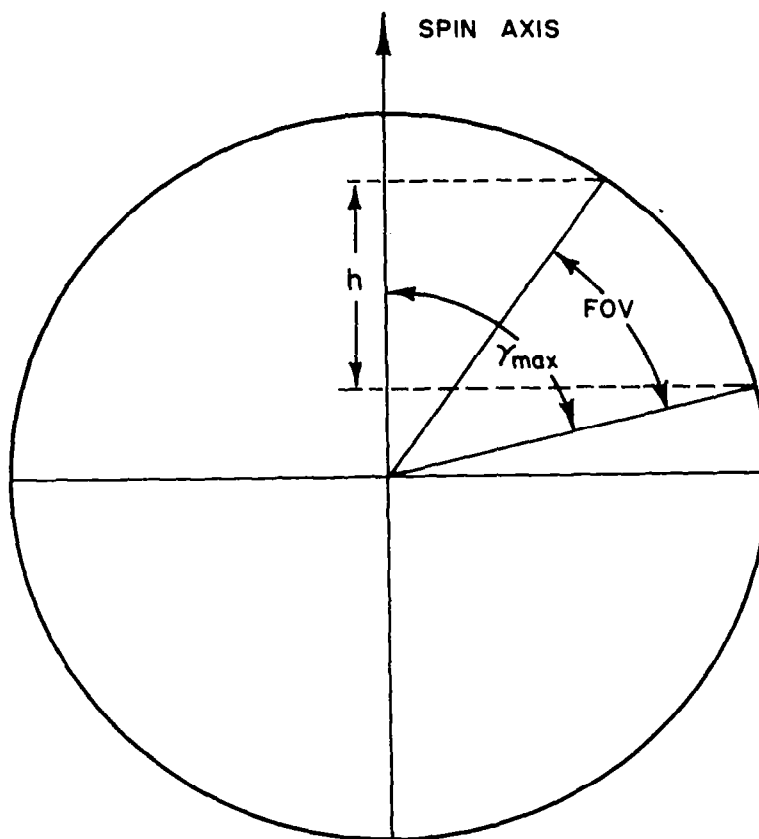
$$\text{SCANNED AREA} = h/2$$

FIGURE 9 : DERIVATION OF SCANNED AREA
CALCULATION

A more elaborate model for the stellar background has been developed in Section III and this model will be incorporated in the OPSCAN program at a later time.

Following the design evaluation, the results are printed. At this point the program is terminated.

2. Numerical Example

The following is a numerical example where a design is calculated and evaluated for a specific set of input parameters. The data are taken from Table 2 and the computer printouts in Table 3. Table 2 indicates how some of the parameters change as the program decreases the slit width and increases the optical aperture. The mean number of star pulses is fixed at 30. This looping process is carried out while examining a given pointing direction.

Maximum Slit Width (1)   A maximum slit width of SW_{max} = 1.447 minutes of arc is computed using a maximum rms transit accuracy of σ_θ = .241 minute of arc.

Identification of Bright Stars in the Scanned Area (2)   Using values of N_s = 4 for the required number of stars in the scanned area, a maximum inclination of 24 degrees, a pointing direction of 10 degrees right ascension and

TABLE 2

CHANGE IN PARAMETERS WHICH CAUSE E_f TO DECREASE

Pass No.	SW	T_s	D	m_b	m_d	τ	E_f
1	1.447	.00166	.916	1.21	50.66	67	64.4
2	1.306	.0015	.965	1.09	45.59	62	52.6
3	1.175	.00135	1.018	.98	41.03	58	34.2
4	1.058	.00121	1.073	.88	36.93	54	25.2
5	.952	.00109	1.131	.79	33.23	51	13.7
6	.857	.00098	1.192	.71	29.91	48	8.23
7	.771	.00088	1.257	.64	26.92	45	5.56
8	.694	.00080	1.325	.58	34.23	42	4.34
9	.624	.00072	1.396	.52	21.80	40	2.10
10	.562	.000641	1.472	.47	19.62	38	1.11
11	.506	.00058	1.552	.42	17.66	36	.65

The mean number of star photoelectrons is held constant at 30.

minus ten degrees declination, and a field of view of 20 degrees, four stars are identified in the scanned area. The magnitude of the dimmest of these four stars was found to be M_L = 4.3.

Star Transit Time (3) From a scan period of T = 6 seconds, a star transit time of T_s = .00167 second is calculated.

Aperture Diameter (4) Given values of quantum efficiency of ϵ_q = .125, optical efficiency of ϵ_o = .75, and the average number of photoelectrons from the limiting magnitude star of m_s = 30, an aperture diameter of D = .916 inch is computed.

Average Number of Background and Dark Current Photoelectrons (5) Given an average background of N_T = 16 tenth magnitude stars per square degree, an average number of background photoelectrons of m_b = 1.21 is computed.

Given an average dark current rate of λ_d = 30,400 pulses per second, an average dark current of m_d = 50.66 pulses is determined.

Detection Threshold (6) Using a specified maximum joint probability of detection of p_o = .9, a detection threshold of τ = 67 is computed.

Expected Number of False Star Detections (7) Given a maximum expected number of false star detections of E_{f_o} = 1.0, a computed number of expected false star detections of E_f < 64.4 is found to be too large.

As indicated by the flow diagram in Figure 4, steps 3 through 7 are repeated with the slit width being reduced by 10 percent at each repetition until the expected number of false star detections falls below the maximum specified. Table 2 gives the values calculated for the variables involved in steps 3 through 7 for 11 iterations. The last pass produced a value of $E_f = .65$, which was less than $E_{f_o} = 1.0$, and the process was terminated.

RMS Transit Accuracy (8) An rms transit accuracy of .084 minute of arc was computed and found to be less than the maximum of .241 minute of arc.

Evaluation of Printout The design for the scanning optical system is printed out in detail. The design is evaluated for all pointing directions used and the evaluation is printed for each pointing direction. Table 3 depicts the actual computer printout of the design and the design evaluation.

The OPSCAN program was used to design several systems based on the characteristics of various photomultipliers. These were done for two second and six second scan periods. The data resulting from these designs is found in Table 4.

In Figure 10, a scale of diameter cubed is drawn where one side represents a two second scan period and the other side represents a six second scan period. The photomultipliers are located on the scale according to the aperture diameter determined for them. Because the weight is proportional to the aperture cubed, the scale also represents the weight relationships.

TABLE 3

COMPUTER PRINTOUT FOR THE OPSCAN PROGRAM

* DESIGN FOR SCANNING OPTICAL SYSTEM *   NO. 1-02

* OPTICAL SYSTEM

    APERTURE DIAMETER   1.552 INCHES
    FOCAL LENGTH (MIN.)   1.552 INCHES
    IMAGE DIAMETER   0.506 ARC MINUTES
    FIELD OF VIEW   20.000 DEGREES
    FIELD OF VIEW SHAPE   CIRCULAR
    OPTICAL EFFICIENCY   0.75
    OPTICAL ARRANGEMENT   REFRACTING OPTICS

    SPECTRAL FILTER   NONE

* RETICLE CONFIGURATION

    WIDTH OF SLITS   0.506 ARC MIN   0.228 MILS
    LENGTH OF SLITS   20.000 DEGREES   0.547 IN.
    SLIT SHAPE   TRUNCATED SECTOR
    CODE PATTERN   000100000000000000000000
                      000000000000000000000000
    NUMBER OF CODE GROUPS 1
    COLOR CODE   NONE
    RELATIVE ORIENTATION ONE RADIAL SLIT
      OF CODE GROUPS

* DETECTOR

    TYPE OF DETECTOR   PHOTOMULTIPLIER EMI
                     9514 B
    DARK CURRENT   30400.00 PULSES PER SECOND
    TIME RESPONSE   50.00 NANOSECONDS
    QUANTUM EFFICIENCY   0.1250
    DETECTION TECHNIQUE   HOLDING FILTER,THRESHOLD
    RMS SPREAD OF PULSE
      AMPLITUDES TO MEAN   1.22
    CATHODE SIZE
      CATHODE DIAMETER   1.75 IN.

* MOTION

    SCAN PERIOD   6.00 SECONDS
    ANGLE BETWEEN SPIN
      AXIS AND OPTICAL AXIS 14.00 DEGREES
    STAR TRANSIT TIME
      (CENTRAL RAY)   581.08 MICROSECONDS
    POINTING DIRECTIONS
      RIGHT ASCENSION   0.00 TO 360.00 DEGREES
      DECLINATION   -10.00 TO =10.00 DEGREES

* DESIGN EVALUATION *

POINTING DIRECTION
RIGHT ASCENSION   10.00   DEGREES
DECLINATION   -10.00   DEGREES

* TARGET CHARACTERISTICS

LIMITING STAR MAGNITUDE   4.30 PHOTOGRAPHIC
SPECTRAL CLASSES   ALL
PLANETS, SUN, OR EARTH
   IN FIELD OF VIEW

SIGNIFICANCE OF EARTHS   OUTSIDE ATMOSPHERE
   ATMOSPHERE

* SIGNAL AND NOISE CHARACTERISTICS

MEAN NUMBER OF PULSES FROM LIMITING MAG
   STAR DURING STAR TRANSIT   30.00
MEAN NUMBER OF PULSES FROM STELLAR
   BACKGROUND DURING STAR TRANSIT   0.4249
MEAN NUMBER OF PULSES FROM DARK
   CURRENT DURING STAR TRANSIT   17.6648
PHOTOGRAPHIC MAG. OF NOISE   4.85
DETECTION THRESHOLD   36.00
MEAN VALUE OF OFF-PEAK MAXIMUM
   FOR CODE PATTERN   0.00

STAR TRANSIT CHARACTERISTICS FOR
LIMITING-MAGNITUDE STAR

POSITION ACCURACY   0.084 ARC MINUTES
RELATIVE INTENSITY ACCURACY 0.23
PROBABILITY OF DETECTION   0.96
EXPECTED NUMBER OF WEAK
   STARS DETECTED PER SCAN   7.9131
EXPECTED NUMBER OF FALSE
   STAR DETECTIONS PER SCAN 0.6553

* SYSTEM CHARACTERISTICS

MINIMUM NUMBER OF STARS IN FIELD
   OF VIEW WITH LIMITING MAGNITUDE
   AND BRIGHTER   4
ACCURACY OF ATTITUDE DETERMINATION   0.70 ARC MINUTES
PROBABILITY OF CORRECT STAR-PATTERN
   RECOGNITION   0.9
PATTERN RECOGNITION TECHNIQUE

MEAN NUMBER OF STEPS FOR PATTERN
   RECOGNITION

* DESIGN EVALUATION *

POINTING DIRECTION
RIGHT ASCENSION   90.00 DEGREES
DECLINATION   -10.00 DEGREES

* TARGET CHARACTERISTICS

    LIMITING STAR MAGNITUDE   1.37 PHOTOGRAPHIC
    SPECTRAL CLASSES   ALL
    PLANETS, SUN, OR EARTH
      IN FIELD OF VIEW

    SIGNIFICANCE OF EARTHS   OUTSIDE ATMOSPHERE
      ATMOSPHERE

* SIGNAL AND NOISE CHARACTERISTICS

    MEAN NUMBER OF PULSES FROM LIMITING MAG
      STAR DURING STAR TRANSIT   445.78
    MEAN NUMBER OF PULSES FROM STELLAR
      BACKGROUND DURING STAR TRANSIT   2.2575
    MEAN NUMBER OF PULSES FROM DARK
      CURRENT DURING STAR TRANSIT   17.6648
    PHOTOGRAPHIC MAG. OF NOISE   4.74
    DETECTION THRESHOLD   437.00
    MEAN VALUE OF OFF-PEAK MAXIMUM
      FOR CODE PATTERN   0.00

* STAR TRANSIT CHARACTERISTICS FOR
  LIMITING-MAGNITUDE STAR

    POSITION ACCURACY   0.084 ARC MINUTES
    RELATIVE INTENSITY ACCURACY   0.05
    PROBABILITY OF DETECTION   0.91
    EXPECTED NUMBER OF WEAK
      STARS DETECTED PER SCAN   0.0000
    EXPECTED NUMBER OF FALSE
      STAR DETECTIONS PER SCAN   0.0000

* SYSTEM CHARACTERISTICS

    MINIMUM NUMBER OF STARS IN FIELD
      OF VIEW WITH LIMITING MAGNITUDE
      AND BRIGHTER   4
    ACCURACY OF ATTITUDE DETERMINATION   0.70 ARC MINUTES
    PROBABILITY OF CORRECT STAR-PATTERN
      RECOGNITION   0.9
    PATTERN RECOGNITION TECHNIQUE

    MEAN NUMBER OF STEPS FOR PATTERN
      RECOGNITION

* DESIGN EVALUATION *

                    POINTING DIRECTION
                      RIGHT ASCENSION   150.00   DEGREES
                      DECLINATION   -10.00   DEGREES

* TARGET CHARACTERISTICS   * SIGNAL AND NOISE CHARACTERISTICS

    LIMITING STAR MAGNITUDE   3.70 PHOTOGRAPHIC   MEAN NUMBER OF PULSES FROM LIMITING MAG
    SPECTRAL CLASSES   ALL   STAR DURING STAR TRANSIT   32.13
    PLANETS, SUN, OR EARTH   MEAN NUMBER OF PULSES FROM STELLAR
      IN FIELD OF VIEW   BACKGROUND DURING STAR TRANSIT   1.1288
                                                      MEAN NUMBER OF PULSES FROM DARK
    SIGNIFICANCE OF EARTHS   OUTSIDE ATMOSPHERE   CURRENT DURING STAR TRANSIT   17.6648
      ATMOSPHERE   PHOTOGRAPHIC MAG. OF NOISE   4.81
                                                      DETECTION THRESHOLD   39.00
                                                      MEAN VALUE OF OFF-PEAK MAXIMUM
                                                        FOR CODE PATTERN   0.00

* STAR TRANSIT CHARACTERISTICS FOR   * SYSTEM CHARACTERISTICS
  LIMITING=MAGNITUDE STAR

    POSITION ACCURACY   0.384 ARC MINUTES   MINIMUM NUMBER OF STARS IN FIELD
    RELATIVE INTENSITY ACCURACY 0.16   OF VIEW WITH LIMITING MAGNITUDE
    PROBABILITY OF DETECTION   0.92   AND BRIGHTER   4
    EXPECTED NUMBER OF WEAK   ACCURACY OF ATTITUDE DETERMINATION   0.90 ARC MINUTES
      STARS DETECTED PER SCAN   0.0376   PROBABILITY OF CORRECT STAR-PATTERN
    EXPECTED NUMBER OF FALSE   RECOGNITION   0.9
      STAR DETECTIONS PER SCAN   0.0000   PATTERN RECOGNITION TECHNIQUE

                                                      MEAN NUMBER OF STEPS FOR PATTERN
                                                        RECOGNITION

* DESIGN EVALUATION *

POINTING DIRECTION
RIGHT ASCENSION   190.00 DEGREES
DECLINATION   -10.00 DEGREES

* TARGET CHARACTERISTICS

LIMITING STAR MAGNITUDE   3.07 PHOTOGRAPHIC
SPECTRAL CLASSES   ALL
PLANETS, SUN, OR EARTH
  IN FIELD OF VIEW

SIGNIFICANCE OF EARTHS   OUTSIDE ATMOSPHERE
  ATMOSPHERE

* SIGNAL AND NOISE CHARACTERISTICS

MEAN NUMBER OF PULSES FROM LIMITING MAG
  STAR DURING STAR TRANSIT   93.14
MEAN NUMBER OF PULSES FROM STELLAR
  BACKGROUND DURING STAR TRANSIT   0.5445
MEAN NUMBER OF PULSES FROM DARK
  CURRENT DURING STAR TRANSIT   17.6648
PHOTOGRAPHIC MAG. OF NOISE   4.84
DETECTION THRESHOLD   96.00
MEAN VALUE OF OFF-PEAK MAXIMUM
  FOR CODE PATTERN   0.00

* STAR TRANSIT CHARACTERISTICS FOR
  LIMITING-MAGNITUDE STAR

POSITION ACCURACY   0.084 ARC MINUTES
RELATIVE INTENSITY ACCURACY   0.11
PROBABILITY OF DETECTION   0.93
EXPECTED NUMBER OF WEAK
  STARS DETECTED PER SCAN   0.0000
EXPECTED NUMBER OF FALSE
  STAR DETECTIONS PER SCAN   0.0000

* SYSTEM CHARACTERISTICS

MINIMUM NUMBER OF STARS IN FIELD
  OF VIEW WITH LIMITING MAGNITUDE
  AND BRIGHTER   4
ACCURACY OF ATTITUDE DETERMINATION   0.60 ARC MINUTES
PROBABILITY OF CORRECT STAR-PATTERN
  RECOGNITION   0.9
PATTERN RECOGNITION TECHNIQUE

MEAN NUMBER OF STEPS FOR PATTERN
  RECOGNITION

* DESIGN EVALUATION *

POINTING DIRECTION
RIGHT ASCENSION   270.00 DEGREES
DECLINATION   -10.00 DEGREES

* TARGET CHARACTERISTICS

    LIMITING STAR MAGNITUDE   2.54 PHOTOGRAPHIC
    SPECTRAL CLASSES   ALL
    PLANETS, SUN, OR EARTH
     IN FIELD OF VIEW

    SIGNIFICANCE OF EARTHS   OUTSIDE ATMOSPHERE
     ATMOSPHERE

* SIGNAL AND NOISE CHARACTERISTICS

    MEAN NUMBER OF PULSES FROM LIMITING MAG
     STAR DURING STAR TRANSIT   151.75
    MEAN NUMBER OF PULSES FROM STELLAR
     BACKGROUND DURING STAR TRANSIT   2.1247
    MEAN NUMBER OF PULSES FROM DARK
     CURRENT DURING STAR TRANSIT   17.6648
    PHOTOGRAPHIC MAG. OF NOISE   4.75
    DETECTION THRESHOLD   154.00
    MEAN VALUE OF OFF-PEAK MAXIMUM
     FOR CODE PATTERN   0.00

* STAR TRANSIT CHARACTERISTICS FOR
  LIMITING=MAGNITUDE STAR

    POSITION ACCURACY   0.084 ARC MINUTES
    RELATIVE INTENSITY ACCURACY   0.09
    PROBABILITY OF DETECTION   0.91
    EXPECTED NUMBER OF WEAK
     STARS DETECTED PER SCAN   0.0000
    EXPECTED NUMBER OF FALSE
     STAR DETECTIONS PER SCAN   0.0000

* SYSTEM CHARACTERISTICS

    MINIMUM NUMBER OF STARS IN FIELD
     OF VIEW WITH LIMITING MAGNITUDE
     AND BRIGHTER   4
    ACCURACY OF ATTITUDE DETERMINATION   1.40 ARC MINUTES
    PROBABILITY OF CORRECT STAR-PATTERN
     RECOGNITION   0.9
    PATTERN RECOGNITION TECHNIQUE

    MEAN NUMBER OF STEPS FOR PATTERN
     RECOGNITION

TABLE 4

Summary of the System Parameters for Ten Photomultipliers

2 Second Scan Period

Photo-multiplier	D	SW	Right Ascension	M_L	m_s	m_b	m_d	M_{noise}	Tau	E_f	E_w
EMR 541B-03 Ruggedized DC = 4870/sec QE = .37	.928	1.451	10	4.3	30	1.22	2.70	6.51	24	0	1.23
			90	1.4	445.8	6.47	2.70	5.59	427	0	0
			150	3.7	52.1	3.24	2.70	6.06	48	0	0
			190	3.1	93.1	1.56	2.70	6.42	83	0	0
			270	2.5	151.7	6.09	2.70	5.63	144	0	0
EMR 541A-01-14 Ruggedized DC = 2540/sec QE = .15	1.449	1.451	10	4.3	30	1.22	1.41	6.94	23	0	.86
			90	1.4	445.8	6.47	1.41	5.75	426	0	0
			150	3.7	52.1	3.24	1.41	6.32	46	0	0
			190	3.1	93.1	1.56	1.41	6.81	82	0	0
			270	2.5	151.7	6.09	1.41	5.80	143	0	0
ITT F 4027 Not Ruggedized DC = 6340/sec QE = .15	1.449	1.451	10	4.3	30	1.22	3.52	6.30	25	0	1.24
			90	1.4	445.8	6.47	3.52	5.49	428	0	0
			150	3.7	52.1	3.24	3.52	5.92	48	0	0
			190	3.1	93.1	1.56	3.52	6.23	84	0	0
			270	2.5	151.7	6.09	3.52	5.54	145	0	0
ITT FW-130 Not Ruggedized DC = 9900/sec QE = .15	1.449	1.451	10	4.3	30	1.22	5.50	5.92	27	0	1.55
			90	1.4	445.8	6.47	5.50	5.30	430	0	0
			150	3.7	52.1	3.24	5.50	5.64	50	0	.01
			190	3.1	93.1	1.56	5.50	5.87	86	0	0
			270	2.5	151.7	6.09	5.50	5.33	146	0	0
EMI 9514B Not Ruggedized DC = 30400 QE = .125	1.587	1.451	10	4.3	30	1.22	16.89	4.85	36	.23	7.96
			90	1.4	445.8	6.47	16.89	4.57	441	0	0
			150	3.7	52.1	3.24	16.89	4.73	61	0	.07
			190	3.1	93.1	1.56	16.89	4.83	97	0	0
			270	2.5	151.7	6.09	16.89	4.59	157	0	0

2 Second Scan Period

Photo-multiplier	D	SW	Right Ascension	M_L	m_s	m_b	m_d	M_{noise}	Tau	E_f	E_w
RCA 1P21 Standard Not Ruggedized DC = 6330/sec QE = .10	1.775	1.451	10 90 150 190 270	4.3 1.4 3.7 3.1 2.5	30 445.8 52.1 93.1 151.7	1.22 6.47 3.24 1.56 6.09	3.52 3.52 3.52 3.52 3.52	6.30 5.49 5.92 6.23 5.54	25 428 48 84 145	0 0 0 0 0	1.24 0 .01 0 0
EMI 9514 S Not Ruggedized DC = 304/sec QE = .08	2.049	1.451	10 90 150 190 270	4.3 1.4 3.7 3.1 2.5	30 445.8 52.1 93.1 151.7	1.22 6.47 3.24 1.56 6.09	.17 .17 .17 .17 .17	7.64 5.94 6.66 7.40 6.00	22 425 45 81 141	0 0 0 0 0	.60 0 0 0 0
RCA C70113A Ruggedized DC = 128000/sec QE = .12	3.213	.369	10 90 150 190 270	4.3 1.4 3.7 3.1 2.5	30 445.8 52.1 93.1 151.7	.31 1.65 .82 .40 1.55	18.1 18.1 18.1 18.1 18.1	4.83 4.76 4.80 4.83 4.76	37 437 59 97 154	.58 0 0 0 0	6.44 0 .09 0 0
EMR 541D-01-14 Ruggedized DC = 35.6/sec QE = .03	3.354	1.451	10 90 150 190 270	4.3 1.4 3.7 3.1 2.5	30 445.8 52.1 93.1 151.7	1.22 6.47 3.24 1.56 6.09	.02 .02 .02 .02 .02	7.76 5.96 6.71 7.50 6.03	22 424 45 81 141	0 0 0 0 0	.53 0 0 0 0
RCA 1P21 Ruggedized DC = 405000/sec QE = .10	6.623	.104	10 90 150 190 270	4.3 1.4 3.7 3.1 2.5	30 445.8 52.1 93.1 151.7	.09 .46 .23 .11 .43	16.15 16.15 16.15 16.15 16.15	4.97 4.94 4.96 4.96 4.94	35 434 57 95 151	.80 0 0 0 0	5.56 0 .05 0 0

6 Second Scan Period

Photo-multiplier	D	SW	Right Ascension	M_L	m_s	m_b	m_d	M_{noise}	Tau	E_f	E_w
EMR 541B-03 Ruggedized DC = 4870/sec QE = .37	.536	1.451	10	4.3	30	1.22	8.12	5.57	29	0	2.6
			90	1.4	445.8	6.47	8.12	5.08	432	0	0
			150	3.7	52.1	3.24	8.12	5.36	53	0	.02
			190	3.1	93.1	1.56	8.12	5.53	88	0	0
			270	2.5	151.7	6.09	8.12	5.11	149	0	0
EMR 541A-01-14 Ruggedized DC = 2540/sec QE = .15	.837	1.451	10	4.3	30	1.22	4.23	6.15	25	0	1.91
			90	1.4	445.8	6.47	4.23	5.42	428	0	0
			150	3.7	52.1	3.24	4.23	5.81	49	0	.01
			190	3.1	93.1	1.56	4.23	6.09	85	0	0
			270	2.5	151.7	6.09	4.23	5.46	145	0	0
ITT F 4027 Not Ruggedized DC = 6340/sec QE = .15	.837	1.451	10	4.3	30	1.22	10.56	5.31	31	0	3.70
			90	1.4	445.8	6.47	10.56	4.91	435	0	0
			150	3.7	52.1	3.24	10.56	5.14	55	0	.03
			190	3.1	93.1	1.56	10.56	5.28	91	0	0
			270	2.5	151.7	6.09	10.56	4.94	151	0	0
ITT FW-130 Not Ruggedized DC = 9900/sec QE = .15	.837	1.451	10	4.3	30	1.22	16.49	4.87	36	.15	6.94
			90	1.4	445.8	6.47	16.49	4.59	440	0	0
			150	3.7	52.1	3.24	16.49	4.75	60	0	.09
			190	3.1	93.1	1.56	16.49	4.85	96	0	0
			270	2.5	151.7	6.09	16.49	4.61	157	0	0
RCA 1P21 Standard Not Ruggedized DC = 6330/sec QE = .10	1.025	1.451	10	4.3	30	1.22	10.55	5.32	31	0	3.67
			90	1.4	445.8	6.47	10.55	4.92	435	0	0
			150	3.7	52.1	3.24	10.55	5.14	55	0	.03
			190	3.1	93.1	1.56	10.55	5.28	91	0	0
			270	2.5	151.7	6.09	10.55	4.94	151	0	0

6 Second Scan Period

| Photo-multiplier	D	SW	Right Ascension	M_L	m_s	m_b	m_d	M_{noise}	Tau	E_f	E_w
EMI 9514S Not Ruggedized DC = 304/sec QE = .08	1.183	1.451	10	4.3	30	1.22	.51	7.40	22	0	.78
			90	1.4	445.8	6.47	.51	5.88	425	0	0
			150	3.7	52.1	3.24	.51	6.56	46	0	0
			190	3.1	93.1	1.56	.51	7.20	81	0	0
			270	2.5	151.7	6.09	.51	5.94	142	0	0
EMI 9514B Not Ruggedized DC = 30400/sec QE = .125	1.552	.506	10	4.3	30	.42	17.67	4.85	36	.66	7.9
			90	1.4	445.8	2.26	17.67	4.74	437	0	0
			150	3.7	52.1	1.13	17.67	4.81	59	0	.09
			190	3.1	93.1	.54	17.67	4.84	96	0	0
			270	2.5	151.7	2.12	17.67	4.75	154	0	0
EMR 541D-01-14 Ruggedized DC = 35.60/sec QE = .03	1.936	1.451	10	4.3	30	1.22	.06	7.73	22	0	.55
			90	1.4	445.8	6.47	.06	5.95	424	0	0
			150	3.7	52.1	3.24	.06	6.70	45	0	0
			190	3.1	93.1	1.56	.06	7.47	81	0	0
			270	2.5	151.7	6.09	.06	6.02	141	0	0
RCA C70113A Ruggedized DC = 128000/sec QE = .12	3.491	.104	10	4.3	30	.09	15.31	5.02	34	.63	5.64
			90	1.4	445.8	.46	15.31	5.00	433	0	0
			150	3.7	52.1	.23	15.31	5.01	56	0	.05
			190	3.1	93.1	.11	15.31	5.02	94	0	0
			270	2.5	151.7	.43	15.31	5.00	150	0	0
RCA 1P21 Ruggedized DC = 40500/sec QE = .10	7.195	.029	10	4.3	30	.02	13.68	5.15	33	.50	4.05
			90	1.4	445.8	.13	13.68	5.14	431	0	0
			150	3.7	52.1	.07	13.68	5.15	55	0	.03
			190	3.1	93.1	.03	13.68	5.15	92	0	0
			270	2.5	151.7	.12	13.68	5.14	149	0	0
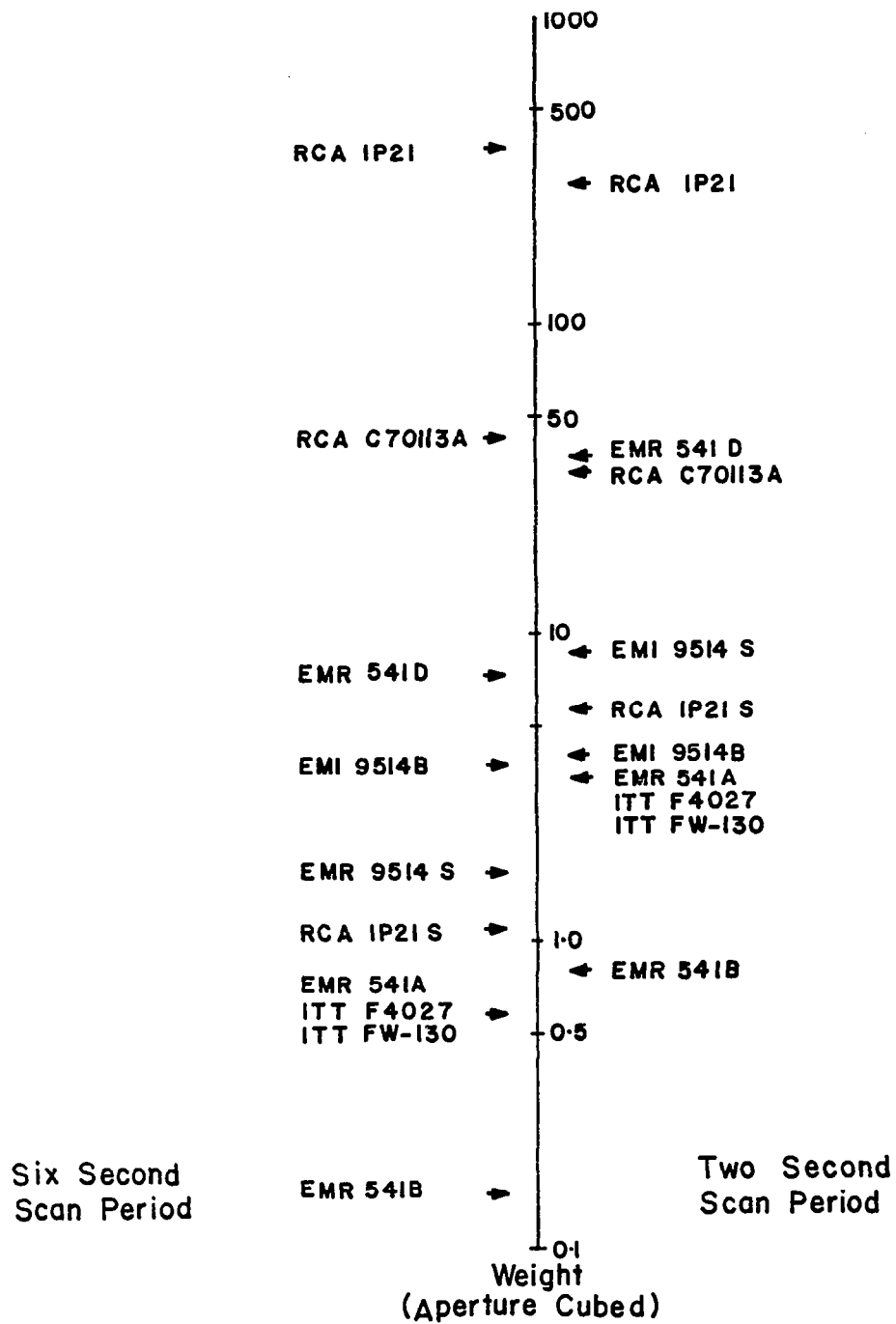
Figure 10: Relative Merit of Various Photomultipliers

3. Program Listing and Input Description

```
      COMMON NUM,D,SW,FOL,SGA,SGI,AR,FOV,CP,EO,SW1,SP,DL,AI,TIRE,EQ,T5,
     1SOAP,FML,FMS,COP,FMB,FMD,TAU,BOB,SGA1,SGI1,PTC,NS,ADD,SEN,POPS,
     2RPHI,RPHI1,DPHI,DPHI1,PT,A,BL,SW2,TS1,D1,D2,NSL,AI1,N,DFOV,NF,
     1SEN1,FMS1,NCG,PMAGN,ENFSDS,GAMM,NSCOR,SWP,WDIA
      DIMENSION P(30), F(30), N(30), AR(78), CP(8), COP(60),
     1           BAK10(30),IBS(30,30),RPH (30),DPH (30),PRD(30),
     1FMSB(30),FMBT(30) ,ADDPT(30),
     1BR(1000), X(1000), Y(1000), Z(1000),IC(1000)
      CALL INPUT
      TIRE=50.
      DTR=.01745329252U
      RTD=57.29577951B
      REWIND 3
      READ INPUT TAPE 3, 6, (IC(I), BR(I), X(I), Y(I), Z(I), I = 1,1000)
    6 FORMAT (3X, I5, F9.2, 3F13.8)
      REWIND 3
      READ 3610,TERP,FMSF,GAMM,FOV,SP,SGA,EO,A,PT,EFAL,NS,NPOINT,NSCOR
 3610 FORMAT(10(F5.2,1X),3(I5,1X))
      READ3620,(AR(I),I=34,41),DL,EQ,WDIA,(AR(I),I=71,78)
 3620 FORMAT(8A6,1X,F9.2,1X,2F6.2/8A6)
      READ3630,(RPH (I),DPH (I),BAK10(I),ADDPT(I),I=1,NPOINT)
 3630 FORMAT(4(F6.2,1X))
      SP=3.
      DO 1040 NSP=1,9
      SP=SP+3.
      RPHI=10
      RPHI1=10
      DPHI=-11
      DPHI1=-11
      DMAX=0
      AI=GAMM-FOV*.5
      AL=COSF(DTR*GAMM)
      AU=COSF(DTR*(GAMM-FOV))
      SWP=SGA*1FRP
C            SW IS MEASURED FROM SPIN AXIS
      SW=SWP/SINF(DTR*AI)
      JUMPL=0
C  LOOP ON POINTING DIRECTIONS
      DO 900 L=1,NPOINT
  161 CONTINUE
C            DETERMINE LIMITING MAGNITUDE
      CALL DIRCOS(RPH (L),DPH (L),XPHI,YPHI,ZPHI)
      NN = 0
      DO 5 I = 1,1000
      FIP = X(I)*XPHI + Y(I)*YPHI + Z(I)*ZPHI
      IF (FIP-AU) 7, 7, 3
    7 IF (FIP-AL) 3, 8, 8
```

```
    8 NN = NN + 1
      IBS(L,NN)=I
      IF (NN-NS) 3, 9, 9
    3 IF (BR(I)-4.5) 5, 158, 158
  158 PRINT 159,NN,FOV
  159 FORMAT(//,2X,I3,25H  STARS PRESENT IN FOV OF  F8.3,2X,7HDEGREES)
      GO TO 900
    5 CONTINUE
    9 FML=BR(1)
  850 TS=SW*SP/21600.
      FMS=FMSF
      SGAC=-1
      FMD=DL*TS*A
      D = SQRTF (FMS/(A*EQ*EO*1.20E7*EXPF (-.92103404*FML)*TS))
      IF (D-DMAX) 910,920,920
  910 FMS=FMS*(DMAX/D)**2
      D=DMAX
      GO TO 930
  920 DMAX=D
  930 FMB= NSL*A*EQ*EO*TS*RTD*SW*(AU-AL)*BAK10(L)*D**2*20.
C         DETERMINE THRESHOLD TAU
      DO 700 I=1,NS
      INDO=IBS(L,I)
      FMSB(I)=FMS*EXPF(2.3025850930*.4*(FML-BR(INDO)))
      FMBT(I)=FMSB(I)+FMB+FMD
  700 CONTINUE
      ITAU=FMBT(NS)-SQRTF(FMBT(NS))*1.28
      INT=0
      JNT=0
  750 TPROB=1
      DO 710 I=1,NS
      CALL PRODEC(ITAU,FMBT(I),PRD(I),NSCOR)
  710 TPROB=TPROB*PRD(I)
      IF(TPROB-PT) 730,720,740
  730 ITAU=ITAU-1
      INT=1
      IF(INT-JNT) 721,721,750
  740 JNT=1
      IF(INT-JNT) 770,720,720
  770 ITAU=ITAU+1
      GO TO 750
  721 TPROB=1
      DO 711 I=1,NS
      CALL PRODEC(ITAU,FMBT(I),PRD(I),NSCOR)
  711 TPROB=TPROB*PRD(I)
  720 CONTINUE
      PTC=PRD(NS)
      TAU=ITAU
      ITC=ITAU
      FMNOS=FMB+FMD
```

```
      CALL PRODEC(IIC,FMNOS,PFSD,NSCOR)
      ENFSUS=PFSD*SP/TS
      IF(ENFSUS-EFAL) 810,810,800
  800 CONTINUE
      SW=.9*SW
      SWP=.9*SWP
      GO TO 850
  810 CONTINUE
  820 CONTINUE
      IF(JUMPL) 900,900,1000
  900 CONTINUE
  155 CALL PRINT(0)
      SGA1=SWP/TERP
      L=0
      JUMPL=1
      GO TO 1010
 1000 ML = FML + 1.5
      ML2 = ML + 1
  116 SA = (AU - AL)/2.
      F(ML-1) = FMS
      SEN = 0.
      DO 130 I = ML, ML2
  130 F(I) = .39A*F(I-1)
      DO 150 I = ML, ML2
      F(I) = F(I) + FMB + FMD
      CALL PRODEC (ITC, F(I), P(I),NSCOR)
      EN = SA*N(I)*P(I)
  150 SEN = EN + SEN
      FLN10=2.3025850930
      PMAGN=2.5*LOGF(FMS/(FMB+FMD))/FLN10+FML
      TSDSW=TS*D**2*SW
      SG11=SQRTF(FMS+FMB+FMD)/FMS
      CALL PRINT(1)
 1010 L=L+1
      IF(L-NPOINT) 1020,1020,1030
 1020 CONTINUE
      ADD=ADDPT(L)
      RPHI=RPH(L)
      DPHI=DPH(L)
      INDO=IBS(L,NS)
      FML=BF(INDO)
      FMS=A*EQ*FO*TS*1.2E7*D**2*FXPF(-.92103404*FML)
      GO TO 930
 1030 CONTINUE
 1040 CONTINUE
      END
```

```
      SUBROUTINE DIRCOS (RA, DEC, X, Y, Z)
      DTR=.017453292520
      RAD=RA*DTR
      DECD=DEC*DTR
      CDEC=COSF (DECD)
      XT=COSF (RAD) *CDEC
      YT=SINF (RAD) *CDEC
      ZT=SINF (DECD)
      X = -.20791169*XT +  .97814760*YT
      Y = -.45921240*XT -  .09760863*YT - .88294759*ZT
      Z = -.86365307*XT -  .18357513*YT + .46947156*ZT
      RETURN
      END


      SUBROUTINE  CUMNOR(X,C,FM,FS,V)
C    V=C*PHI((X-FM)/FS)
C     C*(VALUE OF CUM. NORMAL WITH MEAN FM AND S.D. FS)
      PX=X
      PY=((PX-FM)/FS)*.70710678119
      Y=ABSF (PY)
      D=(((((((.0000430638*Y+.0002765672)*Y+.0001520143)*Y+.0092705272)*Y
     1+.0422820123)*Y+.0705230784)*Y+1.)**16
      ERF=1.-1./D
      V=.5*(1.+ERF)*C
      IF(PY) 20,30,30
   20 V=C-V
   30 RETURN
      END


      SUBROUTINE PRODEC(NTAU,FMPT,VPT,NSC)
C FMPT=MEAN  NTAU=THRESHOLD        VPT=TAIL VALUE
C   SUMS THE TAIL STARTING AT NTAU+1.NSC=NO OF SCANS CORRELATED
      IF(FMPT-50.) 30,30,40
   40 FTAU=NTAU
      SDV=SQRTF (FMPT)
      CALL CUMNOR(FTAU,1.,FMPT,SDV,VPTC)
      VPT=(1.-VPTC)**NSC
      RETURN
   30 CONTINUE
      TERM=1
      DO 10 J=1,NTAU
      DIV=NTAU-J+1
   10 TERM=TERM*FMPT/DIV+1.
      VPT=(1.-EXPF(-FMPT)*TERM)**NSC
      IF(VPT-.1E-5) 15,20,20
   15 VPT=0
   20 RETURN
      END
```

```
      SUBROUTINE INPUT
      COMMON NUM,D,SW,FOL,SGA,SGI,AR,FOV,CP,EO,SW1,SP,DL,AI,TIME,EJ,TS,
     1SOAP,FML,FMS,COP,FMB,FMD,TAU,BOB,SGA1,SGI1,PTC,NS,ADD,SEN,POPS,
     2RPHI,PPHI1,DPDI,DPHI1,PT,A,BL,SW2,TS1,D1,D2,NSL,AI1,N,DFOV,NF,
     1SEN1,FMS1,NCG,PMAGN,ENFSDS,GAMM,NSCOR,SWP,WDIA
      DIMENSION P(30), F(30), N(30), AR(78), CP(8), COP(60)
      READ 10, NUM, FOV, FOL, FMB, FMD, RPHI, DPHI, SGI, SGA, BL, DL
   10 FORMAT (A4, 4(1X, F5.1), 2(1X, F10.8), 2(1X, F5.2), 2(1X, F7.1))
      READ 20, PT, A, EO, EQ, FMS1, SP, SW1, SW2, TS1, D1, D2, NS, NSL
   20 FORMAT (4(F4.2, 1X), 7(F6.2, 1X), 2(I3, 1X))
      READ 30, AI1, (N(I), I = 1,7), DFOV, NF, SEN1
   30 FORMAT (F5.1, 7(1X, I5), 1X, F5.1, 1X, I3, 1X, F5.1)
      READ 35, POPS, BOB, TIRE, SOAP, ADD
   35 FORMAT (5(F7.3, 1X))
      READ 40, (CP(I), I = 1,8), (AR(I), I = 65,67)
   40 FORMAT (8A6,1X,3A6)
      READ 50, (AR(I), I = 1,5), NCG, (AR(I), I = 11,15)
   50 FORMAT (5A6, 1X, A4, 1X, 5A6)
      READ 60, (AR(I), I = 7,10), (AR(I), I = 16,19), (AR(I), I = 25,28)
   60 FORMAT (6A6, 1X, 4A6)
      READ 70, (AR(I), I = 20,24), (AR(I), I = 29,33)
   70 FORMAT (10A6)
      READ 80, (AR(I), I = 34,45)
   80 FORMAT (8A6, 1X, 4A6)
      READ 90, (AR(I), I = 46,57)
   90 FORMAT (4A6, 1X, 8A6)
      READ 100, (COP(I), I = 1,12)
  100 FORMAT (12A6)
      READ 110, (AR(I), I = 58,64)
  110 FORMAT (6A6, 1X, A6)
      RETURN
      END
```

```
      SUBROUTINE PRINT(NOPT)
      COMMON NUM,D,SW,FOL,SGA,SGI,AR,FOV,CP,EO,SW1,SP,DL,AI,TIRE,EJ,TS,
     1SOAP,FML,FMS,COP,FMR,FMD,TAU,BOB,SGA1,SGI1,PTC,NS,ADD,SEN,POPS,
     2RPHI,RPHI1,DPHI,DPHI1,PT,A,BL,SW2,TS1,D1,D2,NSL,AI1,N,DFOV,NF,
     1SEN1,FMS1,NCG,PMAGN,EMFSDS,GAMM,NSCOR,SWP,WDIA
      DIMENSION P(30), F(30), N(30), AR(78), CP(8), COP(60)
      IF(NOPT) 100,100,200
  100 CONTINUE
      DTR=.0174532925250
      DIM=SWP
      TSM=1.0E6*TS
      FARG1=DTR*FOV*.5
      FOL=WDIA*.5*COSF(FARG1 )/SINF(FARG1 )
      FNO=FOL/D
      SLLN=2.*FOL*SINF(FARG1)/COSF(FARG1)
      FARG2=DTR*SW*SINF(DTR*(GAMM-FOV))*.0083333333333
      SWMLMN=2000.*FOL*SINF(FARG2)/COSF(FARG2)
      FARG2=DTR*SW*SINF(DTR*GAMM)*.0083333333333
      SWMLMX=2000.*FOL*SINF(FARG2)/COSF(FARG2)
      PRINT 5, NUM
    5 FORMAT(1H1,    36X,38H* DESIGN FOR SCANNING OPTICAL SYSTEM *,15X,
     14HNO. A4, ///,2X,16H* OPTICAL SYSTEM,39X,23H* RETICLE CONFIGURATIO
     2N/)
      PRINT 10, D,SWP
   10 FORMAT(6X,17HAPERTURE DIAMETER,6X,F7.3,7H INCHES,18X,14HWIDTH OF S
     1LITS,7X,F7.3, 8H ARC MIN)
      PRINT 12,FNO,SWMLMN,SWMLMX
   12 FORMAT(6X,8HF NUMBER15X,F7.3,46X,F7.3,5X,2HTOF12.3,5H MILS)
      PRINT 15, FOL,FOV,SLLN
   15 FORMAT(6X,19HFOCAL LENGTH (MAX.), 4X,F7.3,7H INCHES,18X,15HLENGTH
     1OF SLITS,6X,F7.3,8H DEGREES,2X,F9.3,4H IN.)
      PRINT 20, DIM,(AR(I),I=1,5)
   20 FORMAT(6X,21HIMAGE DIAMETER        ,2X,F7.3,12H ARC MINUTES,13X,
     110HSLIT SHAPE,12X,5A6)
      PRINT 25, FOV,(CP(I),I=1,4)
   25 FORMAT(6X,13HFIELD OF VIEW,10X,F7.3,8H DEGREES,17X,12HCODE PATTERN,
     110X,4A6)
      PRINT 30, (AR(I),I=65,67),(CP(I),I=5,8)
   30 FORMAT(6X,19HFIELD OF VIEW SHAPE,5X,3A6,35X,4A6)
      PRINT 35, EO,NCG
   35 FORMAT(6X,18HOPTICAL EFFICIENCY,7X,F4.2,26X,22HNUMBER OF CODE GROU
     1PS ,A4)
      PRINT 40, (AR(I),I=7,24)
   40 FORMAT(6X,19HOPTICAL ARRANGEMENT,5X,4A6, 7X,10HCOLOR CODE,12X,5A6,
     1/30X,4A6, 7X,20HRELATIVE ORIENTATION,2X,5A6)
      PRINT 45, (AR(I),I=25,33)
   45 FORMAT(6X,15HSPECTRAL FILTER,9X,4A6, 9X,14HOF CODE GROUPS,6X,5A6//
     1//)
      PRINT 50,
   50 FORMAT(2X,32H* SENSOR AND DETECTION TECHNIQUE23X,8H* MOTION,/)
```

```
      PRINT 55, (AR(I),I=34,37),SP
   55 FORMAT(6X,16HTYPE OF DETECTOR,6X,4A6,9X,11HSCAN PERIOD,12X,F7.2,8H
     1 SECONDS)
      PRINT 60, (AR(I),I=38,41),DL,AI
   60 FORMAT(28X,4A6,9X,18HANGLE BETWEEN SPIN/6X,12HDARK CURRENT4X,F12.2
     1,
     118H PULSES PER SECOND,11X,21HAXIS AND OPTICAL AXIS ,F7.2,8H DEGREE
     2S)
      PRINT 65, TIRE
   65 FORMAT(6X,13HTIME RESPONSE,8X,F7.2,13H NANOSECONDS ,14X,17HSTAR TR
     1ANSIT TIME)
      PRINT 70, EQ,ISM
   70 FORMAT(6X,18HQUANTUM EFFICIENCY,6X,F6.4,27X,13H(CENTRAL RAY),5X,F1
     10.2,13H MICROSECONDS)
      PRINT 75, (AR(I),I=42,45),RPHI,RPHI1,SOAP,DPHI,DPHI1
   75 FORMAT(6X,19HDETECTION TECHNIQUE,3X,4A6,9X,19HPOINTING DIRECTIONS
     1/6X,19HRMS SPREAD OF PULSE,38X,15HRIGHT ASCENSION,6X,F7.2,4H TO ,F
     27.2,2X,7HDEGREES/8X,19HAMPLITUDES TO MEAN ,F7.2,29X,11HDECLINATION
     3,10X,F7.2,4H TO ,F7.2,2X,7HDEGREES)
      PRINT 230,(AR(I),I=71,78)
  230 FORMAT (6X,12HCATHODE SIZE/8X,8A6)
      PRINT 240,NSCOR
  240 FORMAT(6X,15HNUMBER OF SCANS/8X,10HCORRELATED 11X,I2)
      RETURN
  200 PRINT 210,RPHI,DPHI
  210 FORMAT(1H1,46X,21H* DESIGN EVALUATION *//54X,18HPOINTING DIRECTION
     1/56X,15HRIGHT ASCENSION F10.2,2X,7HDEGREES/56X,11HDECLINATION
     2F14.2,2X,7HDEGREES//)
      PRINT 80, FML
   80 FORMAT(2X,24H* TARGET CHARACTERISTICS,31X,34H* SIGNAL AND NOISE CH
     1ARACTERISTICS//6X,23HLIMITING STAR MAGNITUDE,1X,F6.2,13H PHOTOGRAP
     2HIC,12X,39HMEAN NUMBER OF PULSES FROM LIMITING MAG)
      PRINT 85, (AR(I),I=46,49),FMS
   85 FORMAT(6X,16HSPECTRAL CLASSES,8X,4A6,9X,24HSTAR DURING STAR TRANSI
     1T,15X,F8.2)
      PRINT 90,(COP(I),I=1,8),FMB,(COP(I),I=9,12)
   90 FORMAT(6X,22HPLANETS, SUN, OR EARTH,2X,4A6,7X,34HMEAN NUMBER OF PU
     1LSES FROM STELLAR,/8X,16HIN FIELD OF VIEW,6X,4A6,9X,30HBACKGROUND
     2DURING STAR TRANSIT11X,F8.4/30X,4A6,7X,31HMEAN NUMBER OF PULSES FR
     3OM DARK)
      PRINT 95, (AR(I),I=50,53),FND
   95 FORMAT(6X,24HSIGNIFICANCE OF EARTHS   ,4A6,9X,27HCURRENT DURING STA
     1R TRANSIT14X,F8.4)
      PRINT 100, (AR(I),I=54,57),PMAGN,TAU
  100 FORMAT(6X,10HATMOSPHERE,12X,4A6,7X,26HPHOTOGRAPHIC MAG. OF NOISE,
     117X,F6.2/61X,19HDETECTION THRESHOLD,22X,F8.2)
      PRINT 105,ROB
  105 FORMAT(61X,30HMEAN VALUE OF OFF-PEAK MAXIMUM/63X,16HFOR CODE PATTE
     1RN,23X,F8.2////)
```

```
      PRINT 110,
  110 FORMAT(2X,34H* STAR TRANSIT CHARACTERISTICS FOR,21X,24H* SYSTEM CH
     1ARACTERISTICS/4X,23HLIMITING-MAGNITUDE STAR/)
      PRINT 115, SG41
  115 FORMAT(6X,17HPOSITION ACCURACY,11X,F7.3,12H ARC MINUTES,7X,33H MIN
     2IMUM NUMBER OF STARS IN FIELD)
      PRINT 120, SG11
  120 FORMAT(6X,27HRELATIVE INTENSITY ACCURACY,3X,F4.2,23X,31HOF VIEW WI
     1TH LIMITING MAGNITUDE)
      PRINT 125, PTC,NS
  125 FORMAT(6X,24HPROBABILITY OF DETECTION,6X,F4.2,23X,12HAND BRIGHTER,
     122X,I2)
      PRINT 130, ADD
  130 FORMAT(6X,23HEXPECTED NUMBER OF WEAK,32X,35HACCURACY OF ATTITUDE D
     1ETERMINATION ,F6.2,12H ARC MINUTES)
      PRINT 140, SEN, POPS
  140 FORMAT(8X,23HSTARS DETECTED PER SCAN,3X,F8.4,19X,35HPROBABILITY OF
     1 CORRECT STAR-PATTERN/6X,24HEXPECTED NUMBER OF FALSE,33X,
     211HRECOGNITION,24X,F3.1)
      PRINT 145, ENFSDS,(AR(I),I=58,64)
  145 FORMAT(8X,26HSTAR DETECTIONS PER SCAN  ,F8.4,19X,29HPATTERN RECOGN
     1ITION TECHNIQUE,7X,3A6/97X,3A6/61X,32HMEAN NUMBER OF STEPS FOR PAT
     2TERN/63X,11HRECOGNITION,23X,A6)
      RETURN
      END


      Examples of card input.



SADS,16.  ,1.5  ,0.   ,0.   ,       10.00,   -10.00,.2  ,1.   ,5000.  ,380.
.9  ,.9  , .75,.1  , 5.   ,  6.00,.33333,33.  .1.0E-6,.50  ,  3.5,  4,  1
3.0  ,  11,  59,  168,  542, 1427, 4096, 8930.  4.,  3,  10.
   .9,   0.,   50.,  1.22,
0001000000000000000000000000000000000000000000,CIRCULAR
TRUNCATED SECTOR              ,  1,NONE
REFRACTING OPTICS                             ,NONE
ONE RADIAL SLIT
PHOTOMULTIPLIER   EMR   541D-01-14            ,HOLDING FILTER,THRESHOLD
ALL                      ,                    OUTSIDE ATMOSPHERE,



    6.,   30.,   24.,   20.,   6.,0.242,  .75,  1.,   .9,  1.,   4.   1,  1,
PHOTOMULTIPLIER   EMR    541A-01-14 RUGGEDIZED   2540.    .15  1.
USEFUL CATHODE DIA.  1  INCH
   10.0,  -11.,  18.,  0.55,
```

Two types of input are used: magnetic tape and punched cards. The magnetic tape contains bright star information. Stars of magnitude four or five and brighter should be included with information as described in subsection III.E.1.

The punched card input includes numerical parameters which partially specify the system along with descriptive information which describes the system and its operation. Table 5 shows the format used for the punched card input.

Not all the information indicated on cards 1-12 is used (these are the cards read in during the execution of subroutine INPUT). The following indicates which parameters are still useful to the program.

Card 1: NAME--project identification

Card 2: N_{SLITS}--number of slits in reticle

Card 3: N_M--number of stars in magnitude class M(M = 1, 2, 3, 4, 5, 6, 7)

Card 4: POPS--probability of star pattern recognition

BOB--off peak maximum for code pattern

TIRE--time response

SOAP--mean to rms amplitude

Cards 5 to 12 are self-explanatory with two exceptions. NCG refers to the number of code groups and NO. OF STEPS refers to the steps required for correct pattern recognition. These cards are of a descriptive nature and are used in the PRINT subroutine.

The cards read in through READ statements 3610, 3620, 3630 contain the numerical values of the parameters which define the system. The following is a list of symbols and definitions.

IX. SUMMARY

The investigation described in this report had two objectives:

(1) to improve the accuracy of current methods of predicting system
     performance, and

(2) to develop better techniques of signal processing.

The first objective entails selecting models that are more complete than

models currently used. With complete models, we can accurately predict

system performance. The second objective entails developing processing tech-

niques that efficiently use signals generated by the photodetector. With

efficient techniques, we can minimize the sensor size or obtain more accurate

measurements.

In particular, models of the star radiation and background radiation are

present in Sections II and III. Photodetectors are described in Section V.

The model of star radiation takes into consideration (1) complex optical

aberrations of the star image, (2) Bose-Einstein emission statistics, and

(3) the spectral distribution of the star radiation relative to the detector

response. Models of the background radiation include (1) dependence on

pointing direction, and (2) scanning noise from the "random" spatial distri-

bution of very dim stars. The description of photodetectors relates various

photodetector characteristics to the requirements of scanning optical systems

(Section V).

Signal processing techniques are developed in Sections IV, VI, and VII.

Using the radiation models described in the first part of the report, we

consider several operating situations and select an "efficient" processing

technique for each situation (Section VI). Various noise sources in the

system impose intrinsic limitations on the "processing efficiency" (Section IV). These limitations are intrinsically two-dimensional; they are independent of how the star is interrogated. Multiple observation techniques are briefly described in Section VII.

The importance of the complete models and efficient processing techniques lies in the effect they have on the gross system characteristics (size, weight, power, reliability, and cost) and the system performance characteristics (attitude accuracy, probability of star pattern recognition). On the other hand, to take full advantage of the new models and techniques in designing a system, we must manipulate several system parameters that are inter-dependent. To fascilitate the system design, an automated design program was prepared for a digital computer. In the program (described in Section VIII), relatively simple equations were used to verify the design logic. The program can be easily expanded to include complex models and processing techniques.

X. ACKNOWLEDGEMENTS

Several persons in the Research Division have contributed to this project. Significant contributions were made by R. L. Lillestrand, R. W. Peterson, J. S. Newcomb, and D. C. Harrington. In addition, technical assistance was given by personnel at Langley Research Center; in particular, Thomas Walsh and Robert Kenimer.

XI. BIBLIOGRAPHY

Publications referenced in the previous sections are listed below in alphabetical order by author, or organization when an author is not given. The objective was to prepare a complete list of publications related to scanning optical system for celestial attitude measurement.

Allen, C. W. (1963):
    Astrophysical Quantities, second edition, Athlone Press, London.

Andreyev, V. D. (1963a):
    "Transmission of a Useful Signal and a Background Signal Through a
    Radial-Slot Shutter System for Indication of Luminous Objects,"
    Engineering Cybernetics (English translation of Tekhnicheskaya
    Kibernetika) No. 3, pp. 30-40.

Andreyev, V. D. (1963b):
    "Determination or Optimum Parameters for Radial-Slot Shutters of Display
    Systems for Luminous Objects," Engineering Cybernetics (English transla-
    tion of Tekhnicheskaya Kibernetika), No. 4, pp. 78-88.

Baum, W. A. (1962):
    "The Detection and Measurements of Faint Astronomical Light Sources," in
    Astronomical Techniques, W. A. Hiltner, ed., University of Chicago Press,
    Chicago, Illinois, pp. 1-33.

Beall, W. H. (1964):
    "Statistical Analysis of Degradation in Scanned Image Systems," J. Opt.
    Soc. Am., Vol. 54, pp. 992-997.

Bolgiano, T. P., Jr. (1964):
    Quantum Electronics III, Columbia University Press.

Brimhall, James E. and Lorne A. Page (1965):
    "Particle Physics and Nuclear Decay--Cancellation of Photomultiplier Gain
    Drift Following Source Intensity Change," Technical Report No. 1, Sarah
    Mellon Scaife Radiation Laboratory, University of Pittsburgh.

Burr-Brown Research Corporation (1963):
    "Handbook of Operational Amplifier Applications," Tucson, Arizona.

BIBLIOGRAPHY

Chapman, R. M. and R. O'B. Carpenter (1959):
Effect of Night Sky Backgrounds on Optical Measurements, Geophysics
Corporation of America.

Code, A.D. (1960):
"Stellar Energy Distributions," in Stellar Atmospheres,
J. L. Greenstein, ed., Univ. Chicago Press, Chicago, Ill., p. 50.

Cramer, H. (1958):
Mathematical Methods of Statistics, Princeton University Press, Princeton,
New Jersey.

Di Domenico, M., W. M. Sharpless, and J. J. McNicol (1965):
"High Speed Photo Detection in Germanium and Silicon Cartridge Type
Point Contact Photo-Diodes," Appl. Optics, Vol. 4, No. 6, p. 677.

Eberhardt, E. H. (1959):
"Thermionic Emission in Multiplier Phototubes," Memo No. 311, ITT Indust-
rial Laboratories, Fort Wayne, Indiana.

Eberhardt, E. H. (1960):
"Noise in Multiplier Phototubes," Memo No. 309, ITT Industrial Laboratories
Fort Wayne, Indiana.

Engstrom, R. W. (1947):
"Multiplier Phototube Characteristics: Application to Low Light Levels,"
J. Opt. Soc. Am., Vol. 37, No. 6, pp. 420-431.

Farrell, E. J. and C. D. Zimmerman (1965):
"Information Limits of Scanning Optical Systems," Optical and Electro-
Optical Information Processing, J. T. Tippett, et al., ed., MIT Press,
Cambridge, Massachusetts, pp. 639-671.

Fellgett, P. B. (1949):
"On the Ultimate Sensitivity and Practical Performance of Radiation
Detectors," J. Opt. Soc. Am., Vol. 39, p. 970.

Fellgett, P. B., R. C. Jones, and R. Q. Twiss (1959):
"Fluctuations in Photon Streams," Nature, Vol. 184, pp. 967-970.

Franzen, W. (1963):
"Non-Isothermal Superconducting Bolometer: Theory of Operation," J. Opt.
Soc. Am., Vol. 53, No. 5.

Fried, D. L. (1965):
"Noise in Photoemission Current," Appl. Opt., Vol. 4, No. 1, pp. 79-80.

Gadsden, M. (1965):
"Some Statistical Properties of Pulses from Photomultipliers," Appl. Optics, Vol. 4, No. 11, pp. 1446-1452.

Garbrecht, K. and W. Heinlein (1964):
"Noise Performance of Photo-Diodes in Parametric Amplifiers," Proc. IEEE, Vol. 52, No. 2, p. 192.

Garbuny, M. (1965):
Optical Physics, Academic Press, New York, New York.

General Electric Company (1962):
Tables of the Individual and Cumulative Terms of Poisson Distribution, D. Van Nostrand Company, Inc., Princeton, New Jersey.

Grau, G. K. (1965):
"Noise in Photoemission Current," Appl. Optics, Vol. 4, No. 6, pp. 755-756.

Greaves, W. M. H. (1956):
"The Continuous Spectrum," in Vistas in Astronomy, Vol. 2, A. Beer, ed., Pergamon Press, New York, pp. 1309-1321.

Haitz, R. H., A. Goetzberger, R. M. Scarlett, and W. Shockley (1963):
"Avalanche Effects in Silicon p-n Junctions I. Localized Photomultiplication Studies on Microplasmas," J. Appl. Phys., Vol. 34, No. 6, p. 1581.

Hansen, Peter D. (1965):
"New Approaches to the Design of Active Filters," The Lightning Empiricist, Vol. 13 No. 1-2, Philbrick Researches, Inc., Dedham, Massachusetts.

Harmon, W. L., G. J. Shroyer, and K. J. Gilkey (1962):
"Optical Trackers in Space," ISA Journal, pp. 70-73.

Harrington, D. C. (1963):
"Noise Error Analysis of an Optical Star and Planet Scanner," Proceedings of the National Aerospace Electronics Conference, pp. 134-142.

Harwit, M. (1960):
"Measurement of Thermal Fluctuations in Radiation," Physical Review, Vol. 120, No. 5, pp. 1551-1556.

Helstrom, C. W. (1964):
"The Detection and Resolution of Optical Signals," IEEE Trans. on Information Theory, Vol. IT-10, pp. 275-287.

BIBLIOGRAPHY

Hiltner, W. A. ed. (1962):
   Astronomical Techniques, University of Chicago Press, Chicago, Illinois.

Hisdal, E. (1965):
   "Information Content of a Beam of Photons," J. Opt. Soc. Am., Vol. 55,
   No. 11, pp. 1446-1454.

Hodara, H. (1965):
   "Statistics of Thermal and Laser Radiation," Proc. IEEE, Vol. 53, No. 7,
   pp. 696-704.

Hofstetter, E. M. (1964):
   "Construction of Time-Limited Functions with Specified Autocorrelation
   Functions," IEEE Trans. on Information Theory, Vol. IT-10, No. 2,
   pp. 119-126.

Institute of Radio Engineers (1962):
   "IRE Standards on Electron Tubes: Methods of Testing," published by The
   Institute of Radio Engineers, Inc., New York, New York.

Iriarte, B., H. L. Johnson, R. I. Mitchell, and W. K. Wisniewski (1965):
   "Five-Color Photometry of Bright Stars," Sky and Telescope, July,
   pp. 21-31.

ITT Components and Instrument Laboratory
   "Typical Absolute Spectral Response Characteristics of Photoemissive
   Devices," Fort Wayne, Indiana, (wall chart).

ITT Industrial Laboratories (1964):
   "Threshold Sensitivity and Noise Ratings of Multiplier Phototubes,"
   Application Note E2, third edition, Fort Wayne, Indiana.

Jauregui, S. (1962):
   "A Theoretical Study of Complementary Binary Code Sequences and a Computer
   Search for New Kernels," doctoral thesis, United States Naval Postgraduate
   School, Monterey, California.

Jones, R. C. (1953):
   "Performance of Detectors for Visible and Infrared Radiation," L. Marton,
   ed., in Advances in Electronics, Vol. 5, Academic Press, pp. 1-96.

Jones, R. C. (1960a):
   "Energy Detectable by Radiation Detectors," J. Opt. Soc. Am., Vol. 50,
   pp. 883-886.

Jones, R. C. (1960b):
    "Information Capacity of Radiation Detectors," J. Opt. Soc. Am., Vol. 50,
    pp. 1166-1170.

Jones, R. C. (1962):
    "Information Capacity of a Beam of Light," J. Opt. Soc. Am., Vol. 52,
    No. 5, pp. 493-501.

Kenimer, R. L. and T. M. Walsh (1964):
    "A Star Field Mapping System for Determining the Attitude of a Spinning
    Probe," Presented at the Aerospace Electro-Technology Symposium of the
    International Conference and Exhibit on Aerospace Electro-Technology
    in April.

Kron, G. (1952):
    "Developments in the Practical Use of Photocells for Measuring Faint
    Light," Astro-Phys. Journal, Vol. 115, No. 1.

Lallemand, A. (1962):
    "Photomultipliers," in Astronomical Techniques, W. A. Hiltner, ed.,
    University of Chicago Press, Chicago, Illinois, pp. 126-156.

Lally, E. F. (1961):
    "Mosaic Guidance for Interplanetary Travel," ARS Space Flight Report to
    the Nation, October 9-15.

Levy, G., (1958):
    "Infrared System Design," Electrical Design News.

Lillestrand, R. L. and J. E. Carroll (1961):
    "Self-Contained System for Interplanetary Navigation," Presented at the
    August meeting of the American Astronautical Society.

Low, F. (1961):
    "Low-Temperature Germanium Bolometer," Jour. Opt. Soc. Am., Vol. 51,
    No. 11, p. 1300.

Lugt, A. Vander (1964):
    "Signal Detection by Complex Spatial Filtering," IEEE Trans. on Information
    Theory, Vol. IT-10, pp. 139-145.

BIBLIOGRAPHY

Mandel, L (1958):
    "Fluctuations of Photon Beams and Their Correlations," Proc. Phys. Soc.,
    Vol. 72, pp. 1037-1047.

Mandel, L. (1959):
    "Fluctuations of Photon Beams: The Distribution of the Photoelectrons,"
    Proc. Phys. Soc., Vol. 74, pp. 233-243.

Megill, L. R. and F. E. Roach (1961):
    "The Integrated Star Light Over the Sky," National Bureau of Standards,
    Boulder Laboratories, Technical Note 106.

Montgomery, W. D. and P. W. Broome (1962):
    "Spatial Filtering," J. Opt. Soc. Am., Vol. 52, pp. 1259-1275.

Norton, R. H. (1964):
    "The Absolute Spectral Energy Distribution of Canopus," Jet Propulsion
    Laboratories TR No. 32-641, California Institute of Technology.

O'Neil, E. L. (1963):
    Introduction to Statistical Optics, Addison-Wesley Publishing Company,
    Inc., Reading, Massachusetts.

Parzen, E. (1962):
    Stochastic Processes, Holden-Day, Inc., San Francisco, California.

Potter, N. S. (1960):
    "Orientation Sensing in Inertial Space by Celestial Pattern Recognition
    Techniques," Presented at the ARS 15th Annual Meeting, Shoreham Hotel,
    Washington, D. C.

Radio Corporation of America (1965):
    "Application of the RCA CA3004, CA3005, and CA 3006 Integrated Circuit
    RF Amplifiers," Application Note ICAN-5022, Radio Corporation of America,
    Electronic Components and Devices, Harrison, New Jersey.

Rice, S. O. (1944):
    "Mathematical Analysis of Random Noise," Bell System Tech. J., Vol. 23,
    pp. 282-332.

Richtmyer, F. K. and E. H. Kennard (1942):
    Introduction to Modern Physics, McGraw-Hill Book Company, New York, New
    York, third edition.

Rosenfeld, A. (1960):
    "Stellar Navigation Without Star Tracking," Presented at the East Coast
    Conference on Aeronautical and Navigational Electronics.

Saito, S., K. Kurokawa, Y. Fujii, T. Kimura, and Y. Uno (1962):
    "Detection and Amplification of the Microwave Signal in Laser Light by a
    Parametric Diode," Proc. IEEE, Vol. 50, No. 11, p. 2369.

Saito, S. and Y. Fujii (1964):
    "On the Noise Performance of a Photo-Parametric Amplifier," Proc. IEEE,
    Vol. 52, No. 8, p. 978.

Sallen, R. P. and E. L. Key (1955):
    "A Practical Method of Designing RC Active Filters, IRE Transactions on
    Circuit Theory, Vol. CT-2, No. 1, pp. 74-85.

Sharpe, J. (1961):
    "Photoelectric Cells and Photomultipliers," Electronic Technology, EMI,
    Electron Tube Division, Los Angeles, California, June-July, pp. 2-16.

Smith, R. A., F. E. Jones, and R. P. Chasmar (1957):
    The Detection and Measurement of Infrared Radiation, Oxford at the
    Clarendon Press.

Snowman, L. (1962):
    "Star-Field Tracker Gives Attitude Data," Aviation Week and Space
    Technology, Vol. 76, No. 25, pp. 52-53.

Steinke, E. (1926):
    "Natural Fluctuations of Weak Photoelectric Currents," Zeits. fur Phys.,
    Vol. 38, p. 378.

Stern, T. E. (1960):
    "Some Quantum Effects in Information Channels," IRE Trans. on Information
    Theory, Vol. IT-6, No. 4, pp. 435-440.

Swerling, P. (1962):
    "Statistical Properties of the Contours of Random Surfaces," IRE Trans. on
    Information Theory, Vol. IT-8, pp. 315-321.

BIBLIOGRAPHY

Swerling, P. (1964):
   "Parameter Estimation Accuracy Formulas," IEEE Trans. on Information Theory, Vol. IT-10, pp. 302-314.

Tanasescu, T. (1960):
   "Pulse Shape in Scintillation Counters," IRE Transactions on Nuclear Science, Vol. NS-7, No. 2-3.

Trumpler, R. J. and H. F. Weaver (1953):
   Statistical Astronomy, University of California Press.

Tusting, R. F. Q. A. Kerns, and H. K. Knudsen (1962):
   "Photomultiplier Single-Electron Statistics," IRE Trans. on Nuclear Sci., Vol. NS-9, pp. 118-123.

Urkowitz, H. (1953):
   "Filter for Detection of Small Radar Signals in Clutter," J. Appl. Phys., Vol. 24, pp. 1024-1031.

Viglione, S. S. and H. F. Wolf (1962):
   "Star Field Recognition for Space Vehicle Orientation," Paper 1.2.5, 9th Annual East Coast Conference on Aerospace and Navigational Electronics, Baltimore, Maryland.

Wainstein, L. W. and V. D. Zubakov (1962):
   Extraction of Signals from Noise, Prentice-Hall, Inc., Englewood Cliffs, New Jersey.

Wilks, S. S. (1962):
   Mathematical Statistics, John Wiley and Sons, New York, New York.

Williams, R. L. (1962):
   "Fast High-Sensitivity Silicon Photo-Diodes," J. Opt. Soc. Am., Vol. 52, No. 11, p. 1237.

"The aeronautical and space activities of the United States shall be conducted so as to contribute . . . to the expansion of human knowledge of phenomena in the atmosphere and space. The Administration shall provide for the widest practicable and appropriate dissemination of information concerning its activities and the results thereof."

—NATIONAL AERONAUTICS AND SPACE ACT OF 1958

NASA SCIENTIFIC AND TECHNICAL PUBLICATIONS

TECHNICAL REPORTS: Scientific and technical information considered important, complete, and a lasting contribution to existing knowledge.

TECHNICAL NOTES: Information less broad in scope but nevertheless of importance as a contribution to existing knowledge.

TECHNICAL MEMORANDUMS: Information receiving limited distribution because of preliminary data, security classification, or other reasons.

CONTRACTOR REPORTS: Scientific and technical information generated under a NASA contract or grant and considered an important contribution to existing knowledge.

TECHNICAL TRANSLATIONS: Information published in a foreign language considered to merit NASA distribution in English.

SPECIAL PUBLICATIONS: Information derived from or of value to NASA activities. Publications include conference proceedings, monographs, data compilations, handbooks, sourcebooks, and special bibliographies.

TECHNOLOGY UTILIZATION PUBLICATIONS: Information on technology used by NASA that may be of particular interest in commercial and other non-aerospace applications. Publications include Tech Briefs, Technology Utilization Reports and Notes, and Technology Surveys.

Details on the availability of these publications may be obtained from:

SCIENTIFIC AND TECHNICAL INFORMATION DIVISION

NATIONAL AERONAUTICS AND SPACE ADMINISTRATION

Washington, D.C. 20546